UNIVERSITY OF LIVERPOOL

A STUDY OF NOVEL ELECTROLYTE MATERIALS WITH INTERSTITIAL OXIDES AS MOBILE SPECIES

Thesis submitted in accordance with the requirements of the University of Liverpool for the degree of Doctor in Philosophy by

Maria Diaz Lopez
February 2016

To my family, Michael and Paco

'Nothing ever goes away until it teaches us what we need to know'
Pema Chodron

DECLARATION

The work presented in this thesis was carried out by myself, except where stated, at the Chemistry Department, University of Liverpool between 2011 and 2015 under the supervision of Professor Matthew J. Rosseinsky and Dr. John Claridge This work has not been submitted for any other degree at this or any other university.

Signed:_____

Date:_____

Maria Diaz Lopez

A STUDY OF NOVEL ELECTROLYTE MATERIALS WITH INTERSTITIAL OXIDES AS MOBILE SPECIES

Maria Diaz-Lopez

ABSTRACT

This thesis investigates the interstitial oxide ion accommodation, induced local deformation around interstitial defects and increase in ionic conductivity in doped $La_3Ga_5GeO_{14}$ materials with a langasite structure. The choice of langasites as a target system for oxide interstitial doping was motivated by their structural resemblance with apatite and melilite materials, which by the accommodation of up to 3.7 and 4.6 % of extra oxygen respectively increased the ionic conductivity up to 5.6×10^{-3} S·cm^{-1} in $La_{9.75}Sr_{0.25}(SiO_4)_6O_{2.875}$ and 4.1×10^{-2} S·cm^{-1} in $La_{1.54}Sr_{0.46}Ga_3O_{7.27}$ at 700 °C. The good ionic conducting properties shown by these materials lights the way for the development of novel oxide ionic conducting materials toward the doping of tunnelled structures with large voids for oxide interstitials and away from the more traditional approach based on the generation of oxygen vacancies by aliovalent doping of close-packed systems such as fluorite (*e*. *g*. YSZ, GDC) and perovskite (*e*. *g*. LSGM) type materials.

Here we show that the $La_3Ga_5GeO_{14}$ langasite is able to accommodate 5.36 % of extra oxygen in $La_3Ga_{3.75}Ge_{2.5}O_{14.75}$ by a carefully developed Pechini route. Elemental analysis in various $La_3Ga_{5-x}Ge_{1+x}O_{14+x/2}$ compositions presented in this work demonstrated the successfully substitution of Ga for Ge at the desired ratio with the consequent incorporation of extra oxygen. AC conductivity measurements were carried out on dense pellets prepared by conventional and fast Spark Plasma-assisted (SPS) sintering methods revealing an increase in the conductivity of two orders of magnitude (~4×10^{-3} S·cm^{-1} at 700 °C in $La_3Ga_5GeO_{14.25}$) when compared to the un-doped langasite ($La_3Ga_5GeO_{14}$, ~1×10^{-5} S·cm^{-1}). The location of the extra oxygen and the induced local deformation was studied by ^{71}Ga and ^{17}O Solid-State NMR and high-resolution neutron powder diffraction (NPD) techniques. The extra oxygen incorporated by doping was found to form a $(Ga/Ge)_2O_8$ unit predicted by DFT calculations. Two neighbouring tetrahedra sites bridged by oxygen are relaxed into two pseudo square-based pyramid like polyhedral sharing one edge. This unit shows a high resemblance to the Ge_2O_8 unit found in $La_3GaGe_5O_{16}$.

Two additional doping mechanisms were studied involving the partial and complete substitution of La/Ga in $La_3Ga_{5-x}Ge_{1+x}O_{14+x/2}$ for isovalent cations: $La_{3-y}Ln_yGa_{5-x}Ge_{1+x}O_{14+x/2}$ where Ln = Pr, Nd, Sm and Gd and $La_3Al_{5-y-x}Ga_yGe_{1+x}O_{14+x/2}$. Neutron powder diffraction studies carried out in these compositions revealed a $(Ge/M)_2O_8$ environment for the extra oxygen analogous to the one determined for $La_3Ga_{3.5}Ge_{2.5}O_{14.75}$ and $La_3Ga_4Ge_2O_{14.5}$. The conductivity analysis revealed a decrease in the bulk conductivity at 500 °C with the decrease in size of the large lanthanide atoms from ~2.44×10^{-5} S·cm^{-1} in $La_3Ga_{4.5}Ge_{1.5}O_{14.25}$ to 4.51×10^{-6} S·cm^{-1} in $La_{1.5}Nd_{1.5}Ga_{4.5}Ge_{1.5}O_{14.25}$. The isovalent substitution of Ga^{3+} for Al^{3+} causes a decrease in conductivity by one order of magnitude, where the highest conductivity value of 2.94×10^{-6} S·cm^{-1} is reached by $La_3Al_{4.8}Ge_{1.2}O_{14.1}$ at 500 °C.

ACKNOWLEDGEMENTS

First and foremost I would like to acknowledge my supervisors Prof. Matthew J. Rosseinsky and Dr John Claridge for providing my with the opportunity to undertake PhD studies at this world-class research group at the University of Liverpool. Over the past years I have been honoured to use their facilities and attend advanced scientific discussions in numerous group meetings enabling me to better my skills as a researcher. I am also very grateful to the EPSRC and the Ministry of Education of the Basque Country for sponsoring my studies, making all the work presented in this dissertation and the experiences lived over these years possible.

During my PhD I thankfully came across kind people who helped me with different tasks and equipment. Amongst the several members of the MJR group I would like to thank Dr Hongjun Niu, Leopoldo E. Maldonado, Dr Ming-Li, Dr Pranab Mandal and Dr Michael Pitcher in particular for his valuable input and advices while writing this dissertation and the paper that this work resulted in.

Lastly, I would like to show my most sincere appreciation to Dr Jorge Lago who mentored my studies at the University of the Basque Country. Jorge guided me when I first left to McMaster University to finish my undergrad studies, and later on while applying for PhD positions and funding. I am indebted to him for sharing his knowledge, skills and professional experiences with me and for providing me with the best advices that have been well present to me during the course of my studies. The completion of this thesis was only possible thanks to all the encouragement he extended to me.

CONTENTS

GLOSSARY OF ABBREVIATIONS, SYMBOLS AND ACRONYMS

The significance of the abbreviations and acronyms used throughout this thesis are enumerated in the following table.

$a, b, c, \alpha, \beta, \gamma$	Lattice parameters
Abs	Absorption corrections
AFC	Alkaline Fuel Cell
ASR	Area Specific Resistance
b	Neutron nuclear scattering length
$B_{eq} = 8\pi^2 U_{iso}$	'B-factor'
BiCuTiVOx	$Bi_4Cu_{0.15}Ti_{0.15}V_{1.7}O_{11-\delta}$
BiMeVOx	(Bi–bismuth, Me–dopant metal, V–vanadium, Ox–oxide)
BUTVAR	Poly Vinyl Butyral
c	Speed of light
CA	Citric Acid
ccp	Cubic close-packed
CCR	Close-Cycled Refrigerator
CGO	Gadolinium Doped Ceria, $Ce_{1-x}Gd_xO_{2-\delta}$
CHP	Combined Heat and Power systems
CIP	Cold Isostatic Pressing
CW	Constant Wavelength
d_{hkl}	Interplanar spacing between (hkl) planes
DF	Driving Force
DIR	Direct Internal Reforming
e	Charge of the electron
E_a	Activation energy
EG	Ethylene Glycol
EM	Electron Microscopy
f	X-ray scattering form factor
$F(hkl)$	Structure factor for hkl diffraction peak
fcc	Face Centered Cubic
GEM	GEneral Materials diffractometer
$G(x)$	Gaussian profile function
h	Planck's constant
HIP	Hot Isostatic Pressing
hkl	Reflection indices
HRPD	High Resolution Powder Diffractometer
HT-SOFC	High Temperature Solid Oxide Fuel Cell
IT-SOFC	Intermediate Temperature Solid Oxide Fuel Cell
k_B	Boltzmann's constant
Lp	Lorentz polarisation correction
LSGM	$La_{1-x}Sr_xGa_yMg_{1-y}O_{3-\delta}$
$L(x)$	Lorentzian profile function
M	Modulus
M_{20}	Indexing figure of merit
MCFC	Molten Carbonate Fuel Cell
MIEC	Mixed Ionic-Electronic Conductors
NMR	Nuclear Magnetic Resonance Spectroscopy
NPD	Neutron Powder Diffraction

ORR	Oxygen Reduction Reaction
PAFC	Phosporic Acid Fuel Cell
PEMFC	Proton Exchange Membrane Fuel Cell
PVA	Polyvinyl Alcohol
pO_2	Partial pressure of oxygen
$pV(x)$	Pseudo-Voigt profile function
R	Resistance
R_{exp}	Expected profile R-factor
R_{wp}	Weighted profile R-factor
s	Scale factor
S	Goodness of fit
S_y	Sum of the squared differences
SDC	Samaria Doped Ceria, $Ce_{1-x}Sm_xO_{2-\delta}$
SECA	Solid-state Energy Conversion Alliance
SEM	Scanning Electron Microscopy
SOFC	Solid Oxide Fuel Cell
SPS	Spark Plasma Sintering
SXRD	Synchrotron X-ray Diffraction
T	Temperature
t_o	Transport number
TEC	Thermal Expansion Coefficient
TEM	Transmission Electron Microscopy
TOF	Time Of Flight
TOPAS	Total Pattern Analysis Suite
TPB	Triple Phase Boundary region
YSZ	Yttrium Stabilized Zirconia, $Zr_{1-x}Y_xO_{2-x/2}$
U^{ij}	Anisotropic Displacement Parameters
V	Cell volume
ν	Speed of electron, speed of neutron
$y_{calc,i}$	Calculated count at i^{th} step
$y_{obs,i}$	Observed count at i^{th} step
Z	Impedance
ϕ	Volume fraction of a solid
γ_S	Specific surface energy
ε	Permittivity
θ	Bragg angle
λ	Wavelength
σ^2	Variance
σ_e	Electronic conductivity
σ_o	Ionic conductivity
χ^2	Measure of goodness of fit
ω	Angular frequency
$\emptyset$	Diameter

List of Appendices

1 INTRODUCTION

This chapter briefly introduces the current energy needs and prospects that motivated the search for environmentally friendly energy sources such as Solid Oxide Fuel Cells (SOFCs). Then, the challenges that the various components of a fuel cell: cathode, anode and electrolyte faced in order to ensure a proper operation are discussed. One of the limiting factors of SOFCs devices is the slow oxide ion migration at an intermediate temperature range (500-750 °C). Thus, this technology will greatly benefit from the discovery of novel electrolyte materials which allow for a fast ionic conductivity at lower temperatures. The state-of-the-art electrolyte materials are presented in this chapter with particular focus on those structures in which the oxide ion migration occurs via interstitials. A careful inspection of these materials allowed us to identify the langasites family of materials as a potential host for interstitial oxides.

1.1 Current energy demands and SOFC research motivation

One of the major challenges of Science and Engineering for the 21st century is the search for new clean technologies alternative to non-renewable fossil fuel power generation methods. This highly desired goal is motivated by the limited supply of fossil fuels which in turn entails severe environmental damage and an increase demand for energy[1,2] linked to an increase in population[3].

Amongst the existent renewable energy sources, fuel cell technology constitutes an attractive method for the decarbonisation of the future[4]. Fuel cells are electrochemical energy conversion devices which allow for a direct conversion of chemical energy from a fuel and an oxidant gas into electricity[5]. Commonly, fuel cells are referred to as a crossover point between heat engines and batteries: like combustion engines fuel cell technology uses of a chemical fuel as energy source; but like a battery, the chemical energy is directly converted into electricity. The electrochemical oxidation of a fuel can be carried out at very high efficiencies as fuel cells are no subject to the Carnot efficiency losses and can be recharged more quickly and easily compared to heat engines, which utilize a more inefficient combustion step[6,7].

There are a number of fuel cell technologies which operate over a wide range of temperatures from ambient up to 1000 °C. Amongst the several types of fuel cell technology, the five more developed type of cells are introduced in Table 1-1 as follows: polymer

(PEMFC), alkaline (AFC), phosphoric acid (PAFC), molten carbonate (MCFC) and solid oxide fuel cells (SOFC)[8]. Each cell type is named after the ion transport mechanism of the electrolyte, which in turn delimits the operational temperature of the cell.

Table 1-1 Fuel cell types

Fuel Cell Type	Operating temperature[8] (°C)	Mobile ion	Electrolyte
Proton Exchange Membrane (PEMFC)	30-100	H^+	Sulfonated polymers[9-11]
Alkaline (AFC)	50-200	OH^-	KOH solution
Phosphoric Acid (PAFC)	~220	H^+	H_3PO_4 in a SiC matrix
Molten Carbonate (MCFC)	~650	CO_3^{2-}	Li_2CO_3-K_2CO_2 in a $LiAlO_2$ matrix
Solid Oxide (SOFC)	500-1000	O^{2-}	Ceramic

It should be noted that the low temperature fuel cell technologies: PEMFC, AFC and PAFC require high purity hydrogen as fuel free from CO to avoid the poisoning of the platinum used as a catalyst. Therefore, low temperature fuel cells require of a fuel processor to remove CO from the fuel mixture which entails a degree of complexity and additional cost to these systems compared to the Pt-free higher temperatures systems: MCFC and SOFC. Due to the H_2 fuel-related issues to do with its generation and storage, the hydrogen economy remains an important technological challenge[12,13]. Alternatively, in the higher temperature cells the use of hydrocarbons[14,15] (methane, ethane, 1-butene and toluene) through Direct Internal Reforming (DIR) is also possible.

Despite of the elevated operational temperatures of up to 1000 °C, SOFCs remain in the solid state whereas this does not hold for MCFCs. In the latter devices, the hot and corrosive electrolyte melt of lithium and potassium carbonates leads to a degradation of the cell[16]. Much research is still needed to address the long-term stability issues that derive from molten electrolytes. On the other hand, the complete solid-state SOFC devices use pure oxide ionic conductor ceramic material as the electrolyte. This allows for a more simplistic design without any need for large radiators, cooling fans or pumps[17].

Over the past half century, high temperature SOFC (HT-SOFC) technology operating at 750-1000 °C was successfully developed in stationary and central power plants[18] by large multi-national companies (*e*. *g*. General Electrics, Siemens Westinghouse, Rolls Royce, *etc*.). The much-needed high operational temperatures of ~1000 °C, which allow to overcome the energy barriers for a fast oxide ion migration, have associated disadvantages such as mechanical and chemical incompatibility between components of the cell, the need of expensive interconnects and heat exchangers and extended start-up times of fuel burning to reach the operating temperature. In order to reduce the overall system cost while maintaining the DIR characteristics, the SOFC operating temperatures have been lowered into an intermediate regime 500-750 °C, in the so-called IT-SOFC. The lower-operating temperature in IT-SOFC operating in hydrocarbon-air mixtures allows to spread the use of this technology for the power generation in vehicles and micro-combined heat and power (CHP) systems [19]. The successful development of IT-SOFC by Mitsubishi materials[20], the Solid State Energy Conversion Alliance (SECA), *etc*., highlights the potential use in the near future of this technology while improvement of the design and constituents of the cells are still needed for optimal performance and affordability.

SOFC have the potential to use either an oxide ion or a proton conductor as the electrolyte. The higher conductivity of proton in comparison with oxide ions at lower temperatures is caused by the smaller size of the former element. This fact has promoted the investigation of proton conducting materials for IT-SOFC applications[21]. In those SOFC with a proton conducting electrolyte the protons produced at the anode migrate though the electrolyte to the cathode leading ultimately to the formation of water molecules. The formation of water at the cathode leads to some advantages with respect to the oxide ion conducting electrolytes, where the water is formed at the anode diluting the fuel. However, the chemical instability of these materials to H_2O or CO_2 SOFC by-products has hindered the development of a proton conducting electrolyte based technology.

1.2 SOFC explained: Unit cell components

The primary components of a SOFC are a dense electrolyte sandwiched between two porous electrodes: a cathode and anode. Figure 1-1 shows a very simple representation of a single SOFC unit, in which the oxygen present in air enters the cell through the porous cathode where it undergoes a reduction reaction as follows:

$$^1/_2\, O_2 + 2e^- \rightarrow O^{2-}$$

Equation 1-1 Cathode reaction

Equation 1-1 stands for the reduction of molecular oxygen into oxide ions at the surface of the cathode. The mobile oxide ions diffuse through the cathode and electrolyte layers into the anode in which it becomes in contact with the fuel (which corresponds to H_2 in Figure 1-1). The fuel fed into the anode undergoes the oxidation reaction introduced in Equation 1-2.

$$H_2 + O^{2-} \rightarrow H_2O + 2e^-$$

Equation 1-2 Anode reaction

The burning of fuel consumes oxide ions (O^{2-}) and generates a gradient across the electrolyte warranting further migration of these ions from the cathode into the anode. The electrons (e^-) generated in the oxidation of the fuel are fed into an external circuit for useful electrical power and innocuous water is formed as a by-product.

$$H_2 + {}^1/_2\, O_2 \rightarrow H_2O$$

Equation 1-3 Overall reaction

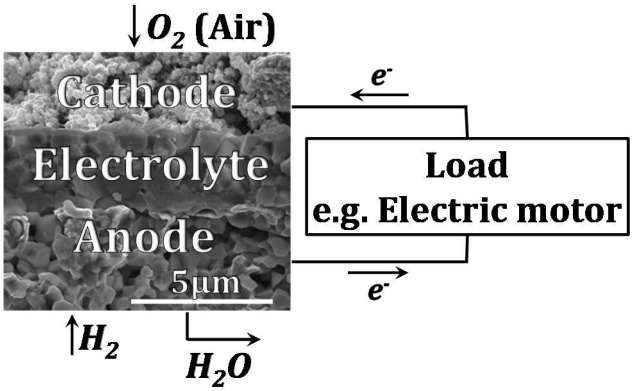

Figure 1-1 Schematic representation of a single SOFC operated with H_2. The SEM image shows the microstructure of an LSFC cathode, GDC electrolyte and a Ni-GDC anode taken from ref. 22.

Each of the cell components mentioned above must meet severe demands dictated by the cell environment in order to secure an adequate operation of the cell. These individual demands for each cell component are discussed in the Sections 0-0. The selected materials are also required to be thermal, chemically and mechanically stable at the cell operating conditions and compatible with the other components of the cell ($e.g.$ having matching thermal expansion coefficients (TECs)).

1.2.1 Anode

Since the fuel oxidation is catalysed at the anode of the cell, the material of choice for the anode must catalyse this reaction efficiently and allow for the conduction of the electrons generated in this reaction. Typically, conductivity values of 100 $S\ cm^{-1}$ are required for an efficient transport of the electrons generated[17]. The most common choice of anode materials are porous cermets[23] ($i.e.$ a composite of ceramic and metal). State-of-the-art SOFCs use Ni-YSZ due to the excellent catalytic properties of nickel metal[24]. Research in this field has also studied the development of alternative electrodes to enable the use of the readily available fuels[25] which predominantly comprise the replacement of YSZ for GDC and nickel for copper[15,24,26].

1.2.2 Cathode

Complex interactions involving high activation energies of mobile electronic, ionic and molecular species occur at the cathode, which are introduced in Equation 1-4 to Equation 1-6. The first chemical process (see Equation 1-4) involve the adsorption, dissociation and reduction of molecular oxygen taking place at the surface of the cathode in the so called triple-phase boundaries (TPBs) outlined in Figure 1-2 ($i.e.$ where the electrode, the electrolyte and the gas phase are in contact[27]). The second reaction in Equation 1-5 accounts for the diffusion of oxygen from the surface into bulk of the cathode material and lastly, the oxide ions are transferred from the cathode into the electrolyte in Equation 1-6.

$$^1/_2\, O_2(\mathrm{g}) + 2e^-(\mathrm{cathode}) \rightarrow\ O^{2-}(cathode\ surface)$$

Equation 1-4 Oxygen Reduction Reaction

$$O^{2-}(cathode\ surface) \rightarrow\ O^{2-}(cath \quad bulk)$$

Equation 1-5 Diffusion

$$O^{2-}(cathode\ bulk) \rightarrow O^{2-}(electrolyte)$$

Equation 1-6 Charge-transfer of oxygen ions across the cathode-electrolyte interface

In order to improve the performance of cathode materials, Mixed Ionic-Electronic Conductors (MIECs) materials have been investigated. Since the electrochemically active TPB region which catalyses the oxygen reduction reaction (ORR) can be extended to a finite length with MIECs.

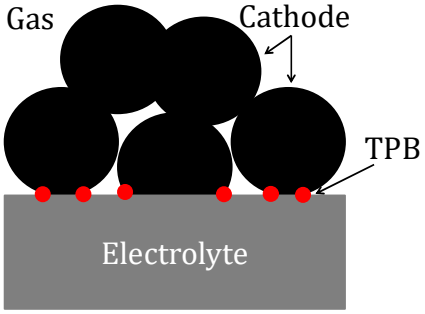

Figure 1-2 Triple Phase Boundary (TPB) region.

Modern cathode materials primarily include perovskite-type structures (see Figure 1-6 on page 10): $La_{1-x}Sr_xMnO_{3-\delta}$ (LSM)[28,29] $La_{1-x}Sr_xCo_{1-y}Fe_yO_{3-\delta}$ (LSCF)[30,31], $Ba_{0.5}Sr_{0.5}Co_{0.8}Fe_{0.2}O_{3-\delta}$ (BSCF)[32], $LaNi_{1-x}Fe_xO_{3-\delta}$ (LNF)[33], layered double perovskite such as $GdBaCo_2O_{5+\delta}$ (GBC)[34,35] and Ruddlesden– Popper type materials[36] with greatest efforts being dedicated to the study of the performance of $La_2NiO_{4+\delta}$[37,38]. Although some of these materials show high ORR activity at an intermediate 500-750 °C temperature range, the stability and compatibility issues with other electrolyte and interconnects also present in the cell prevents their utilization in IT-SOFCs[39]. Thus, despite its low oxygen ion conductivity at reduced temperatures LSM is still the most predominantly used cathode material.

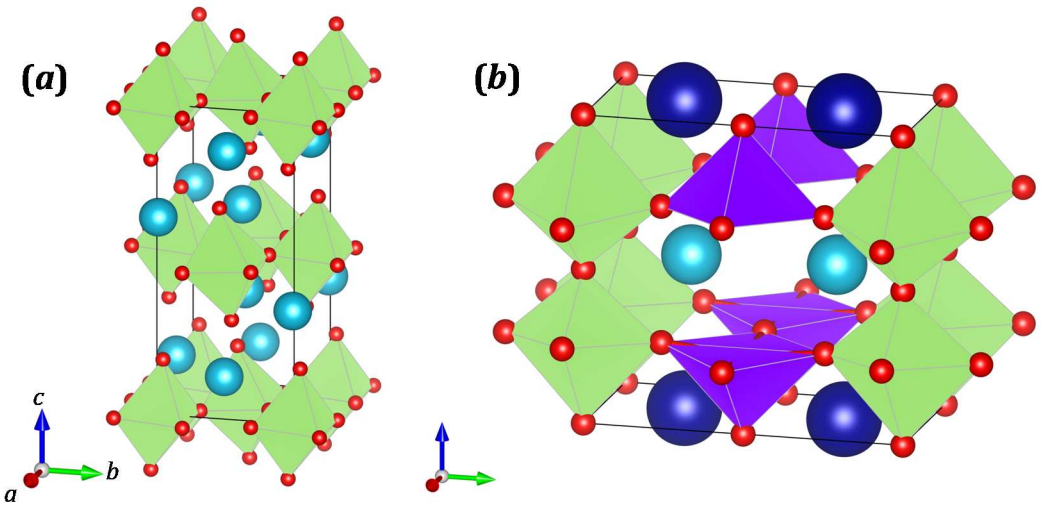

Figure 1-3 (*a*) La_2NiO_4 with a Ruddlesden-popper structure consisting of perovskite layers separated by rock salt layers with the general formula $A_{n+1}B_nO_{3n+1}$ where A = lanthanide/alkaline earth and B = transition metal. A is denoted in blue spheres, B by a green octahedra and oxygen by small red spheres. (*b*) $GdBaCo_2O_{5-\delta}$ (GBC) consisting on a double-layered perovskite structure. Gd and Ba are denoted by cyan and navy spheres respectively and Co occupies the 4 and 6-connected polyhedra in violet and green respectively.

Even in the best MIEC cathode materials reported to date, the distance that the electrode reaction extends beyond the TPB region is limited to a few microns[40]. An alternative to enhance ionic conductivity and catalytic activity for the oxygen reduction reaction (ORR)[41-43] is the catalyst infiltration in nano-architectured electrodes which results in a higher surface area of electrocatalytic cathode material. Such percolated system exhibits superior performance compared to the MIEC alone[44,45].

1.2.3 Electrolyte

Electrolyte materials are required to be dense thin layers of pure oxide ion conductors with negligible electronic conductivity[17] ($i.e.$ retain a transport number (t_O) close to unity), where the transport number is defined as:

$$t_O = \frac{\sigma_O}{\sigma_O + \sigma_e} \approx 1$$

Equation 1-7 Transport number

In Equation 1-7 the numerator 'σ_O' is the contribution of the ionic conductivity to the total conductivity and the denominator is the total conductivity which is calculated by the addition of the ionic and electronic 'σ_e' conductivities.

Assuming that the contribution of the electrolyte to the total Area Specific Resistivity (ASR) should not exceed $0.15\ \Omega\ cm^{-2}$, then for a thick film of an L thickness of 15 µm, the associated conductivity value should conduct above $> 1 \times 10^{-2}\ S \cdot cm^{-1}$ ($\sigma = L/ASR$). The best-conducting electrolyte materials studied up to date are presented later on in this chapter in section 1.4.

1.3 Next generation SOFC

As previously stated in 1.1, there is still much work to be done in the not yet matured IT-SOFC technology. A very attractive prospect which will allow spreading the use of this technology and with it revolutionize the energy future, is to accelerate the oxygen catalysis and diffusion in the cell. New alternative manufacturing routes involving the reduction of the electrolyte thickness[46], novel cell designs[47-50] and new materials are constantly being identified[4,51] as promising candidates for the next generation IT-SOFC-technology[51].

The focus of this thesis is to search for new electrolyte materials inspired by the promising interstitial ionic conduction observed in apatites and melilites. The state-of-the-art electrolytes materials are presented below to contextualize the choice of the langasite structure for doping.

1.4 Insights into electrolyte materials: state of the arts

High ionic conductivity in crystalline solids is a widely recognised phenomenon, yet rare. Fast ion migration is mostly shown at high temperatures approaching the melting point of the material. Most traditionally studied oxide electrolyte materials are aliovalently doped fluorite- (see 0) or perovskite-related (see 0) structures in which ionic transport is mediated through oxygen vacancies[52]. The conductivities of these materials along with more modern materials studied up to date (see 0) with a view to IT-SOFC applications is given in Figure 1-4. From this graph, one could see that the state-of-the-art electrolyte materials intersect with the 'Desired σ_O ' region at the higher 600-700 °C and not at the lower 500-600 °C limit.

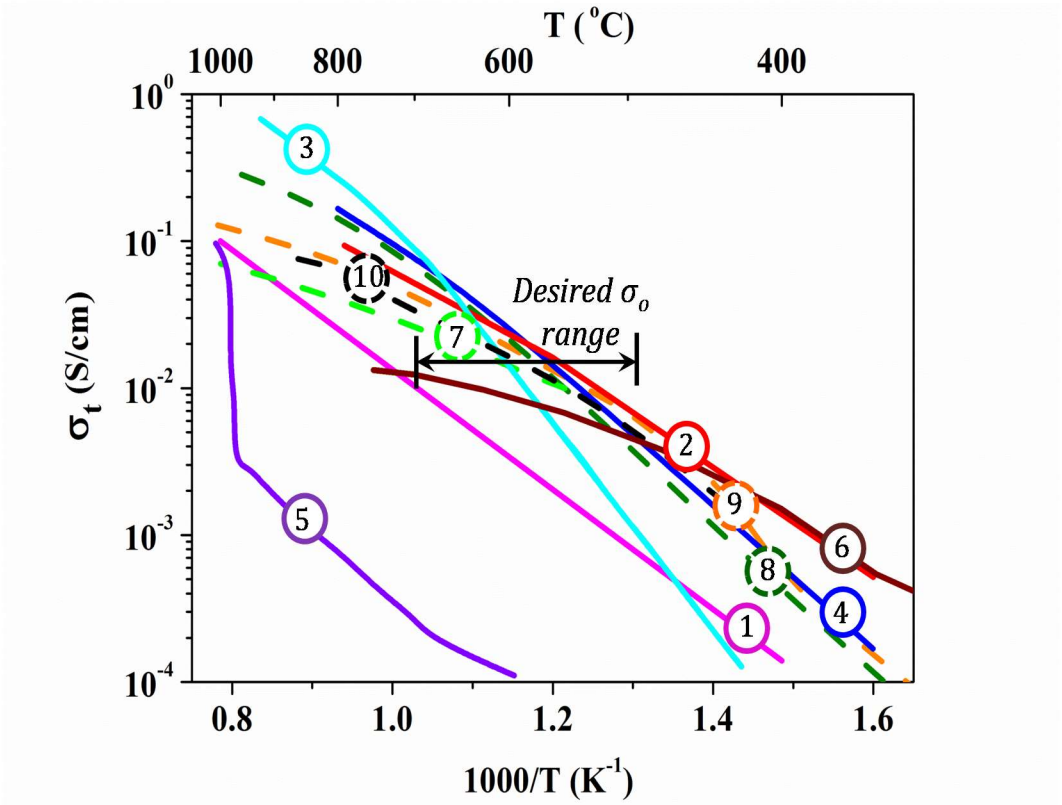

Figure 1-4 Arrhenius plot of the total conductivity of selected electrolyte materials with competitive conductivity values for their potential application in SOFC. Solid lines are used for those materials in which the oxide ion migration is mediated via vacancies and dashed lines for interstitials. For clarity the materials in the plot are labelled with a number which corresponds to the order in which they have been introduced in this chapter: (1) $Zr_{0.9}Y_{0.1}O_{1.95}$[53] (YSZ), (2) $Ce_{0.9}Gd_{0.1}O_{1.95}$[54] (GDC), (3) $Bi_{0.75}Y_{0.25}O_{1.5}$[55] (Stabilized δ-Bi_2O_3), (4) $La_{0.8}Sr_{0.2}Ga_{0.83}Mg_{0.17}O_{2.815}$[56] (LSGM), (5) $Ba_2In_2O_5$[57] (Brownmillerite), (6) $Bi_4Cu_{0.15}Ti_{0.15}V_{1.7}O_{11-\delta}$[58] (BICUTIVOX), (7) $La_{9.75}Sr_{0.25}(SiO_4)_6O_{2.895}$[59] (Si-apatite), (8) $La_{9.5}(Ge_{5.5}Al_{0.5}O_{24})O_2$[60] (Ge-apatite), (9) $La_{1.54}Sr_{0.46}Ga_3O_{7.27}$[61] (Sr-melilite) and (10) $La_{1.64}Ca_{0.36}Ga_3O_{7.32}$[62] (Ca-melilite). It should be noted that the actual conductivity values will depend on the microstructure, exact level of doping and sintering processes.

As mentioned before, in addition to good ionic conductivity values, the ideal electrolyte must meet further requirements regarding chemical and physical stability and compatibility with other components of the cell at the operating temperatures. Some of the critical issues encountered in the use of these materials for practical applications are summarized in Table 1-2.

Table 1-2 Potential oxide ion electrolytes for IT-SOFC and their associated critical issues[41,42,63].

Electrolyte	Structure type	Critical issues
$Zr_{1-x}Y_xO_{2-x/2}$ (YSZ)	Fluorite	- Poor ionic conductor at low temperature. - Incompatible with Sr-doped $LaMO_3$ (M = Mn, Co) at the cell's operating conditions.
$Ce_{1-x}M_xO_{2-\delta}$ M = Gd(GDC), Sm(SDC)	Fluorite	- Unstable at low pO_2. - Poor mechanical stability, large grain boundary resistance at lower temperature.
$Bi_{0.75}Y_{0.25}O_{1.5}$ 'δ-Bi_2O_3'	Fluorite	- Unstable at low pO_2.
$La_{1-x}Sr_xGa_yMg_{1-y}O_{3-\delta}$ (LSGM)	Perovskite	- Unstable at low pO_2. - Ga volatilization and cost - Reactive with Ni anode at elevated temperatures.
$Bi_4M_xV_{2-x}O_{11-\delta}$ (BIMEVOX)	Aurivillus	- Limited stability at variable pO_2 conditions.
$Ba_2In_2O_5$	Brownmillerite	- Unstable at low pO_2. - Poor σ_O at low temperature. - Shows a first-order phase transition accompanied by structural change. - Unstable in a CO_2 atmosphere.
$La_{9.33+x}(MO_4)_6O_2$ M = Si, Ge	Apatite	- Ge volatilization and cost. - SiO volatilization from the surface at low pO_2.
$La_{1+x}A_{1-x}Ga_3O_{7+x/2}$ A = Ca, Sr	Melilite	- Ga volatilization and cost. - Reactive with $La_2NiO_{4+\delta}$, and $La_{0.80}Sr_{0.20}MnO_{3-\delta}$.

1.4.1 Structures containing oxygen vacancies

The vacancy-driven ionic conductivity in traditionally studied electrolyte materials is largely influenced by dopant-vacancy interactions. If defect interaction takes place, the maximum value of the conductivity is not a function of the vacancy stoichiometry and will occur at a lower concentration of dopant. Thus, most research on these systems is dedicated to understand the dependence of the concentration of defects with the conductivity and type of dopants[64,65].

1.4.1.1 Fluorite related structures:

The fluorite structure (prototype CaF_2) has fluoride ions in a cubic arrangement and calcium cations inserted into half of the cubic voids (see Figure 1-5). The high ionic conduction associated with the fluorite structure, such as the fast F^- migration in PbF_2 is well-known and was first reported by Faraday over 200 years ago in 1834, where the conduction of F^- in PbF_2 takes place through excess F^- ions occupying the octahedral interstices[66]. Later in 1897, Nernst patented the first application of oxide ionic conductors for $Zr_{1-x}Y_xO_{2-x/2}$ (YSZ) in the Nernst-glower[67]. This development motivated the search of novel oxide materials with fluorite structures to meet the requirement of high oxide-ion conductivities demanded for modern applications over the past century.

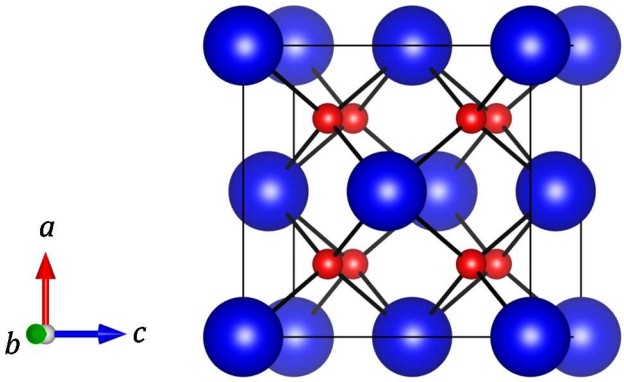

Figure 1-5 ZrO_2 fluorite structure with a cubic close-packed (ccp) array of Zr in blue and O^{2-} ions in red filling the tetrahedral voids.

Stoichiometric AO_2 oxides such as ZrO_2 (see 0) and CeO_2 (see 0) do not exhibit a transition to the conducting fluorite phase at temperatures that are of interest for technological applications. In order to induce a phase transformation at lower temperature dopants with a lower valence and similar size are accommodated into these structures, with the subsequent formation of vacancy defects. An alternative approach consists on the doping of fluorite-related M_2O_3 such as the cubic δ-Bi_2O_3 form (see 0), whose formula can also be expressed as $MO_{1.5}\square_{0.5}$ where □ denotes the presence ¼ of vacancies in the oxygen sublattice[68].

1.4.1.1.1 Stabilized zirconia $Zr_{1-x}Y_xO_{2-x/2}$ (YSZ)

Pure ZrO_2 undergoes a phase transition from monoclininc to tetragonal at 1170 °C and from tetragonal to cubic fluorite at 2370 °C, which exists up to its melting point at ~2680 °C[5]. The addition of aliovalent oxides allow for the stabilization of the cubic form at a lower temperature range which enable the use of this materials as an electrolyte[69]. The most widely used stabilized zirconia is a solid solution with yttrium: $Zr_{1-x}Y_xO_{2-x/2}$ (YSZ). Y^{3+} can be used to substitute Zr^{4+} with a higher valence resulting in the formation of oxygen vacancies. The composition with 8% mol of Y_2O_3 is found to lead to the best conductivity properties[53,70].

YSZ is the most widely used electrolyte material in operational SOFCs due its high chemical stability under the cell operating conditions and compatibility with other cell components[53]. However, the conductivity of YSZ below 850 °C is poor, thus demanding the use of high temperatures.

1.4.1.1.2 Doped Ceria $Ce_{1-x}Sm_xO_{2-\delta}$ (SDC) and $Ce_{1-x}Gd_xO_{2-\delta}$ (CGO)

Ionic conductivities of ceria-alkaline earth (*e. g*. Ca, Sr and Ba) and rare-earth (*e. g*. Gd and Sm) oxides have been investigated in relation to their structures and conductivities[71]. Amongst these strategies, the latter approach involving the substitution of Ce^{4+} cations for Gd^{3+} and Sm^{3+} gave rise to the highest conductivities inducing up to 20 % of oxygen vacancies. The most appropriate composition for use in IT-SOFCs achieving the minimum desired conductivity of 10^{-2} S·cm^{-1} at 500 °C is $Ce_{0.9}Gd_{0.1}O_{1.95}$. [72]

The ionic conductivity values reported for Sm and Gd doped ceria (SDC and CGO respectively) electrolyte materials are higher than the ones reported for YSZ at an intermediate temperature range 500-700 °C. However, the operation of SDC and CGO is affected by the partial reduction of Ce^{4+} to Ce^{3+} upon exposure to a reducing atmosphere, leading to an n-type electronic conductivity. This in turn reduces the Open Circuit Potential (OCP) making them less efficient for practical applications[72-74].

1.4.1.1.3 Stabilized δ-Bi_2O_3: Isovalently doped $Bi_{2-x}Ln_xO_3$

The cubic δ-Bi_2O_3 with a fluorite structure possesses a high ionic conductivity with a large concentration of oxygen vacancies of 25 %. Due to its high vacancy concentration, δ-Bi_2O_3 undergoes an order-disorder transition of the oxygen sublattice to a monoclinic phase below 600 °C resulting in a steep decrease in the conductivity[55].

In order to stabilize the highly conducting cubic fluorite structure several lanthanide dopants have been substituted by the isovalent Bi^{3+} cation which are reported in ref. 55,75-77. Amongst these studies, the Bi_2O_3-Y_2O_3 solid solution showed a defect fluorite-type structure stable over a wide range of temperatures[78]. The conductivity of $Bi_{0.75}Y_{0.25}O_{1.5}$ is given in Figure 1-4.

One characteristic which hinders the applicability of Bi_2O_3 in SOFC is the decomposition process to Bi metal which takes place at low oxygen partial pressures ($pO_2 \sim 10^{-13} atm$)[78].

$$Bi_2O_3 \rightarrow 2Bi\ (s) + \frac{3}{2}O_2\ (g)$$

Equation 1-8

Some studies have reported an increase in the stability of these materials at lower pO_2 values by the co-doping with Nb[79,80] and W[81,82] without inhibiting the ionic conductivity ($e.g.$ co-doped stabilized bismuth oxide with a $(Dy_2O_3)_{0.08}(WO_3)_{0.04}(Bi_2O_3)_{0.88}$ composition has an adequate conductivity value of 0.098 S·cm^{-1} at 500 °C and a thickness of 10 μm[83]).

1.4.1.2 Oxygen deficient perovskites

The ABO_3 perovskite shown in Figure 1-6 is one of the most diverse and flexible known crystal structure[84]. Moreover, perovskites can readily allocate vacancies in the oxygen sublattice, making them suitable candidates for doping.

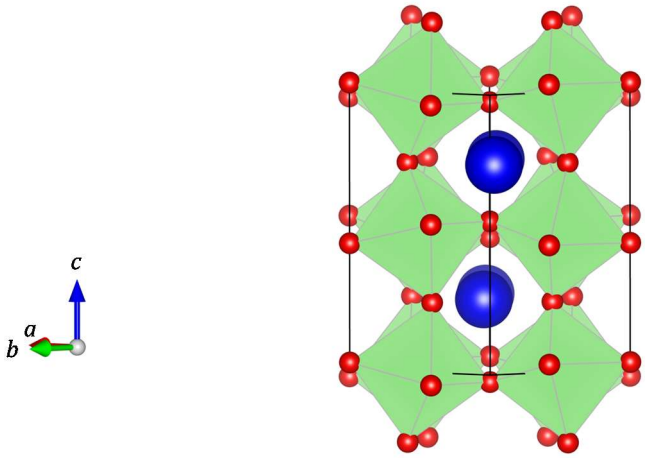

Figure 1-6 ABO_3 perovskite structure displayed by $LaGaO_3$ where A cations are denoted in blue, BO_6 octahedra in green, and oxygen atoms in red.

1.4.1.2.1 $La_{1-x}Sr_xGa_yMg_{1-y}O_{3-\delta}$ (LSGM)

The pseudocubic co-doped lanthanum gallate '$La_{1-x}Sr_xGa_yMg_{1-y}O_{3-\delta}$' (LSGM) has attracted much attention due to its remarkable ionic conduction properties with a negligible electronic contribution in the intermediate temperature range with respect to the widely used YSZ electrolytes (0.079 S·cm^{-1} at 700 °C for $La_{0.8}Sr_{0.2}Ga_{0.17}Mg_{0.83}O_{3-\delta}$[56]). The drawbacks

to the use of LSGM as an electrolyte are associated with the high cost and volatility of gallium. Moreover, LSGM is found to react with nickel which is present in most commonly used anode materials[85].

1.4.1.2.2 Brownmillerite: $Ba_2In_2O_5$

$Ba_2In_2O_5$ named after the Brownmillerite[57] (Ca_2FeAlO_5) and $Ba_3In_2MO_8$ where M = Zr[86], Hf and Ce, adopt layered perovksite-related structures in which the octahedral units alternate with tetrahedral units. $Ba_2In_2O_5$ and $Ba_3In_2MO_8$ are isostructural to $Ca_2Fe_2O_5$ and $Ca_3Fe_2TiO_8$ respectively depicted in Figure 1-7.

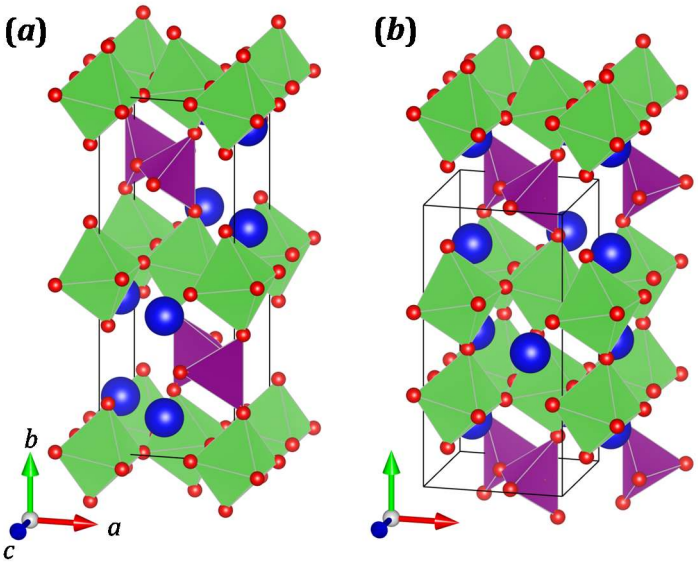

Figure 1-7 Structures of $Ca_2Fe_2O_5$ (a) and $Ca_3Fe_2TiO_8$ (b). Ca cations are denoted in blue, octahedral and tetrahedral sites occupied by Fe and Ti are depicted in green and violet respectively and oxygen atoms are given as red spheres.

With the increase in temperature, $Ba_2In_2O_5$ undergoes a phase transition from the brownmillerite structure having ordered oxygen vacancies to a disordered tetragonal phase reaching conductivity values as high as ~0.08 $S{\cdot}cm^{-1}$ at the transition temperature T_t ~930 °C.[87] Attempts to stabilise the highly conducting phase at lower temperatures involved doping at the Ba site (*e.g.* for La or Sr)[88] and the In site (*e.g.* for Ce^{4+}, Mn^{5+}, Y^{3+}, Er^{3+} or Ga^{3+})[57,89,90] or the substitution of O^{2-} anions for F^-[91]. An increase in conductivity at low temperatures with low activation energies of 0.6 eV[87] is feasible trough doping. However, the conductivity achieved in doped $BaIn_2O_5$ and $Ba_3In_2MO_8$ phases is comparable to YSZ with the added disadvantage of displaying electronic conductivity under variable redox conditions[92,93] as well as proton conductivity under water uptake at low temperatures[94,95].

1.4.1.2.3 BIMEVOX and Aurivillus phases

γ-$Bi_4V_2O_{11}$[96] is the tetragonal high temperature polymorph belonging to the Aurivillus layered-perovskite family. Its structure consists on $[Bi_2O_2]^{2+}$ layers intercalated with oxygen deficient $[VO_{3.5}\square_{0.5}]^{2-}$ slabs. At high temperatures (>570 ° C)[97] the disorder of the oxygen vacancies in the perovskite layers is responsible for an increase in the ionic conductivity. The oxide ion migration occurs within the *a-b* plane parallel to the perovskite-like layers as indicated by impedance analysis on a single crystal specimen: an increase in conductivity from 0.018 $S{\cdot}cm^{-1}$ in the direction perpendicular to the perovskite layers up to 0.63 $S{\cdot}cm^{-1}$ in the parallel direction at 700 °C was observed[98].

In an attempt to stabilise the γ-$Bi_4V_2O_{11}$ phase at lower temperatures, Abraham *et al*. design a new family of ionic conductors by the partial substitution of V for other metal ions (*e*. *g*. Cu or Ni) which they named BIMEVOX[99] (see Figure 1-8). Since Abraham's first publication in 1990 numerous attempts to dope the BIMEVOX phases were carried out involving substitutions of both Bi and V including: Ti, Cr, Fe, Ga, Zr, Sn, La, Ta[55,100,101], *etc*.

Although this family of ionic-conductors exhibit good ionic conductivity, they do not meet additional stability requirements for practical purposes. The issues associated with electronic conduction at low oxygen pressures and abnormal grain growth leading to cracking during the processing of BIMEVOX materials remains a challenge[102-104]. Amongst the several BIMEVOX systems explored up until now, the doubly substituted $Bi_4Cu_{0.15}Ti_{0.15}V_{1.7}O_{11-\delta}$ (BICUTIVOX) has attracted much attention due to its widest processing window, which allows for a successful densification of this compound with no preferred orientations[58].

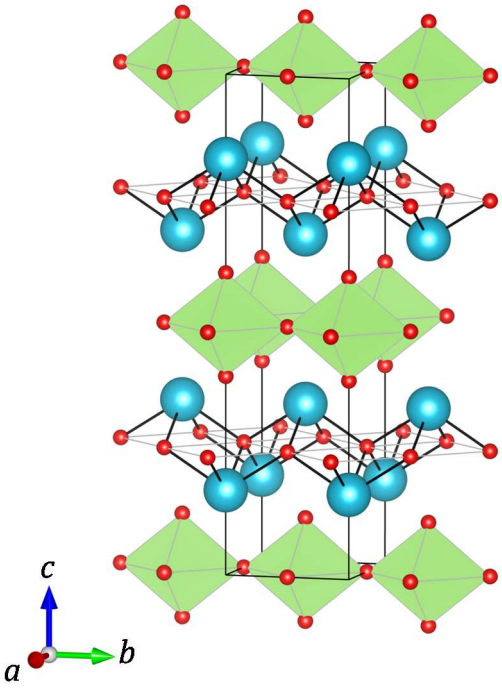

Figure 1-8 Idealized structure of $Bi_4(V_{2-x}Ni_x)O_{11-\delta}$[105] (without the splitting of the oxygen sites in the perovskite-type layer). The octahedral sites are occupied by V and Ni atoms and coordinated to six oxygen (small red spheres)/oxygen vacancies. Bi atoms are shown in blue.

1.4.2 Interstitial oxide ionic conductors

In recent years, the research in this field has shown a growing interest in targeting anisotropic flexible oxide framework structure for interstitial doping, as opposed to the more traditional approach based on the generation of oxygen vacancies by aliovalent doping of close-packed systems such as fluorite (*e*. *g*. YSZ[53], GDC[54]) and perovskite (*e*. *g*. LSGM[106]) type materials.

This highly desired lattice flexibility for fast oxide ion mobility at lower temperatures is found in rare-earth oxyapatites ($La_{9.33+x}(M^{4+}O_4)_6O_{2+x/2}$ for M = Ge or Si)[107,108] and melilites ($La_{1+x}M_xGa_3O_{7+x/2}$ for M = Sr or Ca)[61,62] based on isolated (0D) and layered (2D) tetrahedral units. Furthermore, the novel interstitial conduction pathways and high degree of

anisotropy in these systems offer the possibility of developing new conducting devices with enhanced performance.

The discovery of fast oxide ion conductivity in the apatite system with large lattice anisotropy constituted an innovative approach with respect to the previous doping studies on highly isotropic system. Moreover, the rotational flexibility of the isolated tetrahedra in Ge/Si oxyapatites is also observed in other oxide ion conductors (*e.g.* $La_{0.2}Pb_{0.8}WO_{4.1}$[109]), mixed-ionic conductors (*e.g.*$CeNbO_{4+x}$[110],), or protonic conductors (*e.g.* $La_{1-x}Sr_xNbO_{4-\delta}$[111]) with a scheelite structure. It is also worth to mention the oxygen uptake reported in cuspidines $RE_4(A_{2-x}B_xO_{7+x/2}\square_{1-x/2})O_2$ where RE^{3+} = La, Nd, Sm, Gd, A^{3+} = Al, Ga and B^{4+} = Ge, Ti[112,113]. Cuspidine's structure is based on flexible M_2O_7 dimers consisting of two interconnected tetrahedra separated by larger LnO_7 and LnO_8[114] which are able to bind the interstitial oxide. However, cuspidines have attracted less attention due to their moderate conductivities ($4.33 \times 10^{-5}\ S \cdot cm^1$ for $Gd_4Al_{0.8}Ge_{1.2}O_{7.6}\square_{0.4})O_2$ at 700 °C[113]). When speaking of interstitial-mediated oxide ion conductors we cannot fail to mention $Ca_{12}Al_{14}O_{33}$[115] (with a mayenite structure), UO_{2+x}[116,117] (fluorite) or $La_2NiO_{4+\delta}$[118,119] (with a pervoskite-related structure shown in Figure 1-3-*a*).

1.4.2.1 0D tetrahedral moieties: Apatites

Apatite materials have the general formula $A(1)_2A(2)_3(MO_4)_6X_2$ where A = Ln, Na, K, Ca, Sr Ba, Mn, Cd, Pb, ; M = Si, Ge, P, V and X =O, OH, F, Cl, Br, I[120]. Figure 1-9 shows the stacking of MO_4 tetrahedra along the *c*-direction forming three channels: one type occupied by a 9-coordinated A(1) surrounding a row of oxide ions at the centre and a third channel containing 8-coordinated (seven oxygen and one X atom) A(2) cations.

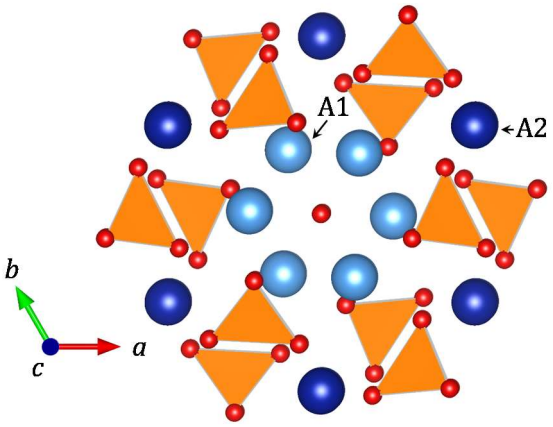

Figure 1-9 $A(1)_2A(2)_3(MO_4)_6X_2$ Apatite structure. The two large A(1) and A(2) cations are coloured in different shades of blue light and dark respectively, MO_4 polyhedra are orange and the oxygen atoms are red spheres.

Over the past years, the good conductivity properties displayed by lanthanide Si and Ge apatites with the formula $Ln_{9.33+x}$ $(Si/GeO_4)_6O_{2+3x/2}$ have attracted much attention from researchers in this field. These investigations were motivated by the low activation energies associated with the oxide interstitial migration resulting in a higher conductivity at lower temperatures (400-700 °C) compared to the formerly introduced conventional fluorite and pervoskite-based ionic conductors (see Figure 1-4). Amongst the different apatite systems explored, the conductivity was found to decrease with the decrease of the lanthanide size, with the maximum conductivity value being achieved by La-containing apatites[121,122]. Further doping strategies involve the incorporation of alkaline earth cations in $La_{8+x}A_{2-x}(Si/GeO_4)_6O_{2+x/2}$ (*e.g.* A = Sr[59,107], Ca or Ba) [59,107]. As an example, the composition of $La_{9.75}Sr_{0.25}(SiO_4)_6O_{2.875}$ shows an increase in conductivity of approximately an order of

magnitude from 5.6×10^{-3} S·cm^{-1} in $La_{10}(SiO_4)_6O_3$ to 3.2×10^{-2} S·cm^{-1} at 700 °C[59]. Additionally, eradicating the presence of cation defects hinders the diffusion of cations which could ultimately lead to chemical creep and decomposition, to be avoided in SOFC's electrolytes[123]. Other doping strategies involve the substitution on the M site by cations with lower valences: Al, Ga, Fe, Mg *etc*. [98,99, 124-127].

The interstitial oxide ions introduced by doping have been reported to be adjacent to the MO_4 tetrahedra within the periphery of the larger channels in both Si[128,129] and Ge[130,131] apatites. Although the reported oxide ion migration mechanisms are different in Si and Ge apatites, in both structures the migration of oxygen occurs predominantly along the c-direction and involve significant local structural distortions allowed by the presence of large channels and isolated tetrahedra, as determined by ^{17}O-NMR, Raman, diffraction and computational studies[108,128,129,131-133].

Although having a higher conductivity than their Si-homologues at $T > 550$ °C (due to the higher activation energies, see Figure 1-4), Ge-apatites are believe to be less suitable for practical applications as electrolytes in SOFCs due to the high volatilization and cost of GeO_2, and their tendency to glass formation[134]. Several studies related to the chemical compatibility with other cell components[125,135,136] and stability at the cell's operating conditions[137] were carried out in the preferred Si-system with promising results. The major drawbacks are attributed to the volatilization of SiO from the surface layers under reducing conditions at $T > 800$ °C.[124]

1.4.2.2 2D network: Melilites

Another structure in which the interstitial accommodation has shown remarkable conductivity values at a lower (intermediate) temperature range is the melilite. It is worth noting that the activation energy in melilites, $E_a \sim 0.4$ eV [61] is significantly lower than the typical range of $0.6 - 0.8$ eV exhibited by most oxide ion conductors.

Figure 1-10 introduces the layered structure adopted by doped $La_{1+x}A_{1-x}Ga_3O_{7+x/2}$ for A = Ca[62] or Sr[61]. The constituents corner-sharing tetrahedra configured an infinite 2D-network Ga_3O_7 alternating with $(La/A)_2$ layers along the c-axis

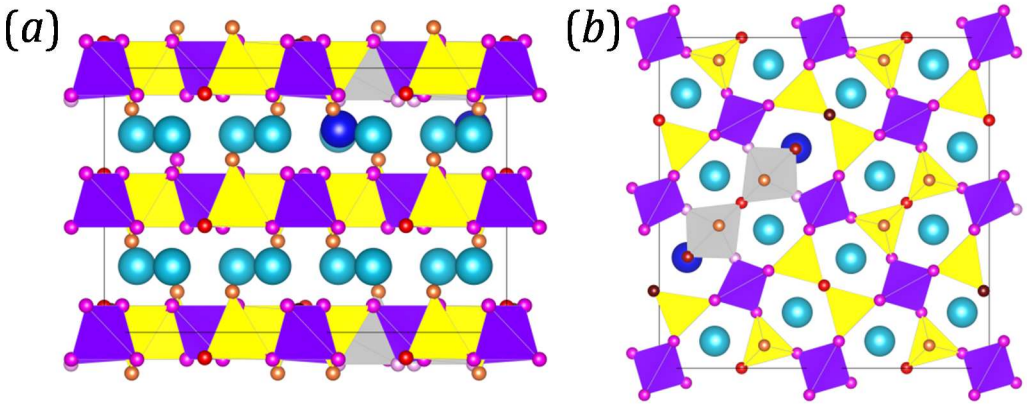

Figure 1-10 $La_{1.54}Sr_{0.46}Ga_3O_{7.27}$ melilite structure viewed along the *c* (*a*) and *a*-axes (*b*) depicted with the same colour code used for langasite throughout the main text of this thesis to allow a direct comparison between the two layered structures: cyan for the large A cations, violet and yellow for the 4-connected and 3-connected tetrahedra respectively and grey for the 5-coordinated site binding the interstitial oxide. A cations which are displaced from their original position due to the presence of interstitial oxide ions are coloured in a darker shade of blue. Different shades of red are used to distinguish the oxygen sites: O1 is red, $(O1)_{int}$ is mahogany, O2 is orange, O3 is magenta, $(O3)_{int}$ is pale pink and O4 is maroon which are further discussed in page 117. The black solid lines delimit a 2 × 2 × 2 supercell.

Upon doping, melilites incorporate extra oxygen within the tetrahedral layer between the La/A cations lying in the pentagonal channels. The interstitial anion is found to bind Ga2 containing one apical oxygen (see Figure 1-10). In ref. 61 , it was suggested that the oxide-ion conduction occurs through a cooperative-type mechanism involving a concerted knock-on motion of interstitial and lattice oxygen. Facile rotation of GaO_5 units facilitates the migration of oxygen interstitial to adjacent pentagonal rings[138], with the conduction of oxygen occurring predominantly within the layers along the *a*-*b* plane[139-141].

Further doping strategies carried out in these systems involve the substitution of La for other lanthanides (*e*. *g*. Pr, Nd, Sm, Eu, Ga, Dy, Yb and Y) where a decrease in conductivity was observed with the smaller Ln size[142,143]. The role of the contraction on the A-cationic size with the conductivity was further evidenced in $La_{1-x}Ce_xSrGa_3O_{7+\delta}$ $(0 \leq x \leq 1)$, where the oxidation of Ce^{3+} to the smaller Ce^{4+} localizes and constrains the mobility of the interstitials decreasing the conductivity[144]. It is worth pointing out the intrinsic flexibility of the melilite structure to accommodate both interstitial and oxide vacancies. $Sr_{1.6}Na_{0.4}MgSi_2O_{6.8}$ with 2.86 % of oxygen vacancies shows an acceptable conductivity of $6 \times 10^{-3}\ S \cdot cm^{-1}$ at 700 °C (~4 orders of magnitude higher than oxygen-stoichiometric $Sr_2MgSi_2O_7$) [145].

Reactivity tests were performed between melilites and promising IT-SOFCs cathode materials: $La_2NiO_{4+\delta}$, $La_{0.80}Sr_{0.20}MnO_{3-\delta}$, and $La_{0.8}Sr_{0.2}Fe_{0.8}Cu_{0.2}O_{3-\delta}$. This study showed that while significant reactivity was observed with $La_2NiO_{4+\delta}$, and $La_{0.80}Sr_{0.20}MnO_{3-\delta}$, no significant amount of secondary phases were formed with $La_{0.8}Sr_{0.2}Fe_{0.8}Cu_{0.2}O_{3-\delta}$ up to 1300 °C. This is an encouraging result for the future application of melilites in IT-SOFC [146].

Unlike isolated tetrahedra, crystal structures based on extended interconnected polyhedra such as melilites are very common in nature, and the fast oxide ion migration shown by $La_{1+x}Sr_{1+x}Ga_3O_{7+x/2}$ opens up the possibility of targeting a wide range of materials for doping.

1.5 Synthesis by intelligent targeting

The conductivities exhibited in the intermediate temperature range by these latterly explored oxide ion conductor families is competitive with, and in some cases even higher than those of the most commonly used electrolyte materials (see Figure 1-4). These results motivate further research in order to expand the understanding of the structural requirements that allow for a fast oxide-ion migration. This section concentrates on identifying the key structural features which enable the accommodation of extra oxygen in apatites and melilites. The gaining of expert chemical insight is then followed by the identification of new target structures and their synthesis.

- One crucial feature is the presence of channels containing large cations (*e*. *g*. La, Sr) with variable coordination number, as the interstitial oxide ions introduced by doping are located within the vicinity of these channels.

- The presence of large cations provides the isolated/layers of MO_4 with a large separation. This separation equals to ~5.3 Å melilites and is even larger ~7.2 Å in apatites.

- The presence of tetrahedra containing non-bridging oxygen seems to facilitate the interstitial accommodation (*e*. *g*. in melilites tetrahedra containing a non-oxygen are able to bind the interstitials and sustain their mobility).

1.5.1 Langasite structure

We identified in langasites the key crystal features allowing the accommodation of interstitial oxygens in apatites and melilites introduced in 1.5. In the past, langasites have attracted attention due to their piezoelectric, non-linear optical[147,148], magnetic[149], multiferroic[150], ferroelectric and dielectric properties; allowing for several substitutions to modify their electromechanical properties. More recently the protonic conductivity of the Sr-doped $La_{3-x}Sr_xGa_5SiO_{14-x/2}$ has been reported by Svendsen *et al*. in ref. 151. The work presented in this thesis focuses on the oxide ion conductivity of the aliovalently doped $La_3Ga_{5-x}Ge_{1+x}O_{14+x/2}$ and constitutes the first oxide ionic conductivity studies undertaken in this family of materials.

There are four types of cation sites in langasites (see Figure 1-11) which crystallize in a trigonal unit cell (space group *P*321) with the formula $A_3BC_3D_2O_{14}$. A and B notations represent a decahedral (twisted Thomson cube) site, and an octahedral site. C and D represent 4 and 3-connected tetrahedral sites respectively, with the size of D being smaller than that of C. In langasites, large A cations are found to lie within the 6-membered channels running parallel to the *c*-axis. Analogously to melilites (see Figure 1-10), the 2D-network of tetrahedra intercalates with layers of large A cations. Although in contrast to melilites, the B octahedra interconnect the C tetrahedra on the top and bottom layers providing langasite's framework with a 3D connectivity. The large A site provides a ~5.1 Å separation between the layer of tetrahedra in $La_3Ga_5GeO_{14}$ matching the $d_{A\text{-}A}$ ~5.3 Å separation in $LaSrGa_3O_7$, which allows for the accommodation of the interstitial oxide ion.

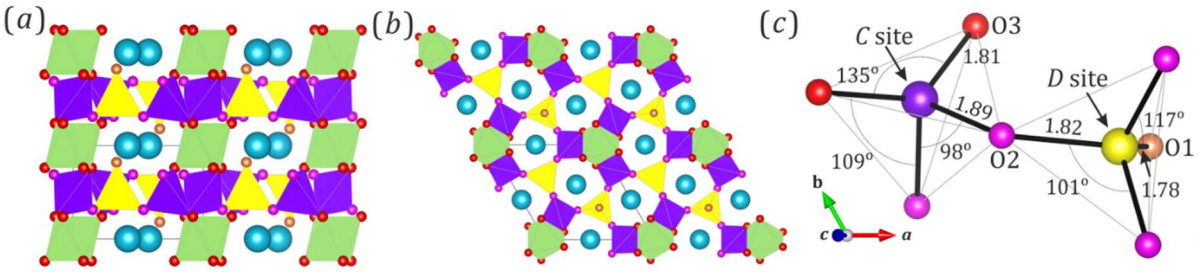

Figure 1-11 View of the NPD refined $La_3Ga_5GeO_{14}$ structure (see page 87) along (a)[100] and (b) [001] directions with the space group $P321$ (No. 150). The distinct $A_3BC_3D_2O_{14}$ sites have been plotted in different colours: blue is used for the A site where La lies and green for the octahedral B site. The 4-connected tetrahedral C site is plotted in violet and the 3-connected tetrahedral D site in yellow. The connectivity between the C and D sites tilted 15° along the [100] direction for perspective is shown in (c). The three oxygen crystallographic sites are plotted in shades of red: orange for the apical oxygen O1, magenta for O2 interconnecting the two tetrahedral sites C and D and red for O3 bridging C and B.

Lattice deformation in langasites could arise due to the presence of 3-connected tetrahedra (plotted in yellow in Figure 1-11), since it is the non-saturated tetrahedra in melilites which are able to bond the interstitial oxygen as determined by powder neutron diffraction (NPD) techniques[61].

Langasite's mixed framework allows the accommodation of a large number of cations with different valences, ranging from A(I) to A(III), B(II) to B(VI) and T(II) to T(IV) for both tetrahedral sites C and D. A table with all the compositions found in the literature with a langasite structure is given in Appendix 1. Moreover, some members of the langasite family of materials have been reported to show displacive transformations from the trigonal $P321$ structure to produce an ordered structure (in space group $A2$) by the loss of the threefold rotation axis, as reported for $La_3SbZn_3Ge_2O_{14}$[152] whose structure is shown in Figure 1-12-a. A considerable displacement of the oxygen atoms of up to 1 Å was observed in the $A2$ polymorph whereas the cation sites were locked in place and La changed its coordination number from 8 to 7. An analogous reversible $P321 \rightleftarrows A2$ transition occurring under a pressure of ~12 GPa was also observed in $La_3Nb_{0.5}Ga_{5.5}O_{14}$ and $La_3Ta_{0.5}Ga_{5.5}O_{14}$[153]. Moreover, langasites can be considered as members of a wider $M_{5-p}T_{4+p}O_{14}$ structural family[154] in which the different trigonal $P321$ and monoclinic $I2/a$ structure types are related *via* a reconstructive transformation involving the replacement of a the tetrahedral C site in $P321$ by an octahedron in $I2/a$. The monoclinic $I2/a$ type of $Pb_3CuGe_5O_{14}$ is shown in Figure 1-12. The projection along the c-axis (Figure 1-12b) reveals the presence of strongly folded vierer chains of tetrahedra occupied by germanium which also occupies the octahedra. Cu occupies the former tetrahedral C site and forms an elongated Jahn-Teller octahedron coloured in a darker shade of green. Such polymorphic transitions and ability to host a large variety of cations allude to a certain degree of flexibility of the langasite structure, making the langasite a very enticing target for doping.

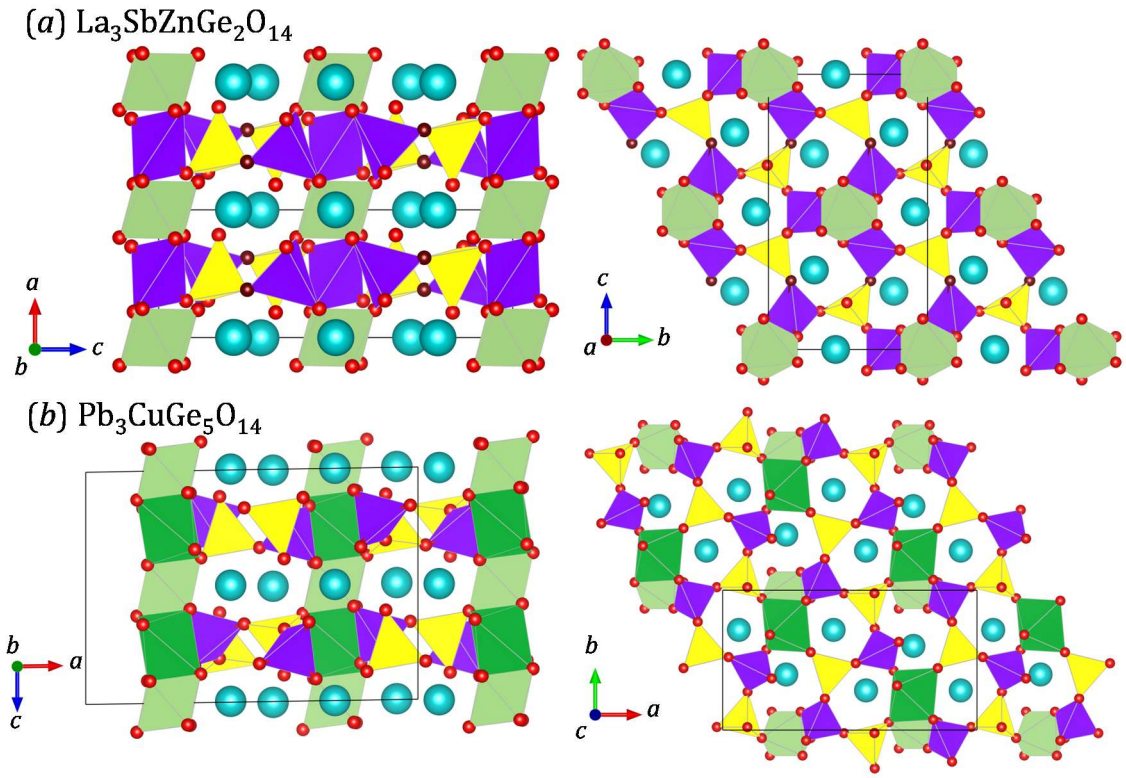

Figure 1-12 (*a*) $La_3SbZnGe_2O_{14}$ projected along *b* (left) and *a*-axes (right). (*b*) $Pb_3CuGe_5O_{14}$ projected along the *b* (left) and *c*-axes (right). Large La and Pb cations are denoted by cyan spheres, 3 and 4-connected tetrahedral sites are depicted in yellow and violet respectively and octahedral sites in green. In (*a*) the oxygen sites that move 1 Å away from its original position in langasites are coloured in mahogany. In (*b*) the former C site, now coordinated to six oxygen atoms is occupied by copper and this octahedron is coloured in a darker shade of green to differentiate it with the other octahedral site in the structure.

2 EXPERIMENTAL TECHNIQUES

The experimental chapter aims to provide detailed information on the distinct methods followed by the author for the preparation of new ceramic materials as well as those techniques utilized for their compositional, structural characterization and performance for their potential use as electrolytes for solid oxide fuel cells. Subsections within this chapter are arrayed by an overview of the given technique, data analysis and instrumentation.

2.1 Material synthesis and preparation

2.1.1 The traditional solid-state reaction method

The traditional solid-state reaction method consists of mixing stoichiometric amounts of the starting reagents and grinding in an agate mortar until a well-mixed fine powder is obtained. Afterwards, the samples are annealed in alumina crucibles at high temperatures (typically greater than 900 °C in oxides) in suitable furnaces[155]. Alternatively, stabilized zirconia crucibles and protective platinum foil can be used when samples show evidence of reaction with the alumina crucible.

This widely used synthetic route for solid polycrystalline materials is based on the migration of mobile ions across an interface generated by the contact in between reactants undergoing a heating treatment. In the thermally activated reaction mixture the lattice energy of reactants is overcome and bonds are broken and formed leading to the formation of a product layer which will in turn separate the reactants. The continuous diffusion of ions would ultimately lead to the formation of a final product[156].

Numerous process can be carried out to improve the reaction rates (*i. e.* achieve a more efficient cation diffusion). Such as the uniaxial pressing of powders into pellets prior to the annealing at elevated temperatures, which decreases the inter-particle void space to a great extent increasing the reaction points between particles. A higher surface area available for reaction (*i. e.* smaller reactant particle size) will also increase the reaction rate. During the synthetic work carried out in this thesis, mechanical milling was used for this purpose; stoichiometric mixtures of the starting materials are placed in zirconia containers with zirconia balls and alcohol which will act as dispersing agent (either ethanol or propan-2-ol were used). The introduction of a liquid media into the milling process constitutes a crucial step to achieve the smallest particle size attainable by this

process. Otherwise, once the milled particles reach a size of approximately 20 μm, surfaces forces will start to interact causing the powder particulates to stick together[157]. The amount of powder milled was typically a third of the volume of solvent. The reactants were milled in air in a Planetary Micro Mill Pulverisette 7 classic line by using a rotating disc speed of 350 rpm with reversed rotation every 15 minutes over 45 cycles. Figure 2-1 shows the particle size before (a and c) and after (b and d) undergoing the planetary ball milling under these conditions.

When several annealing cycles at high temperatures were required to obtain phase purity either manual or mechanical re-grinding was performed in between heating cycles. As the solid-state reaction progresses, the product layer at the interface thickens, decreasing the reaction rate ($i.e.$ making it more difficult for the remaining particles to react). Intermediate re-grinding will therefore increase the number of contact points speeding up the reaction.

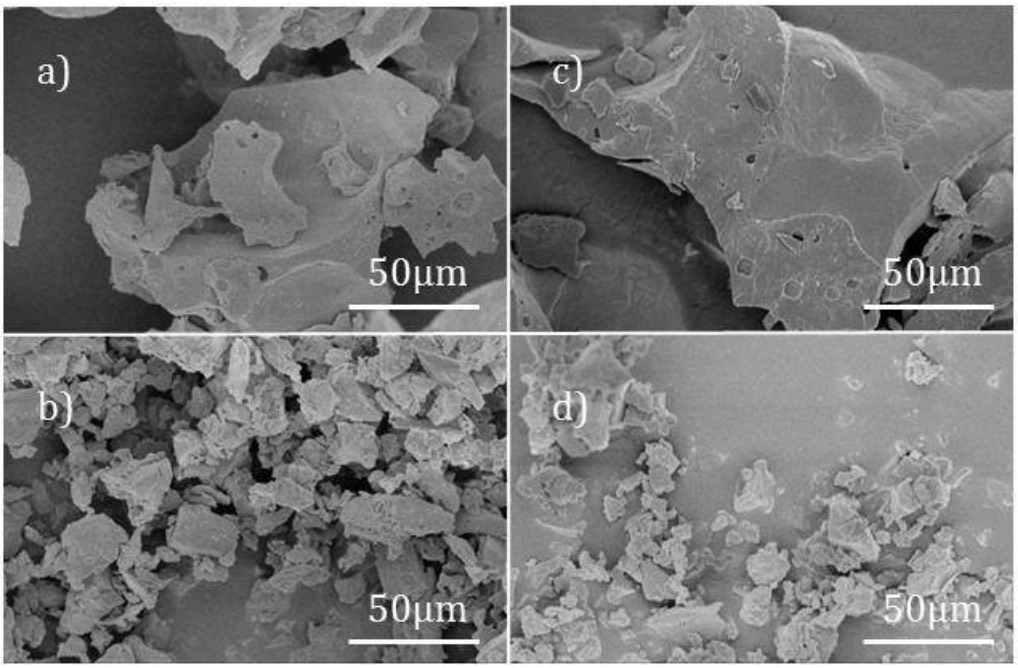

Figure 2-1 SEM images of the particle size obtained after manually grinding a $La_3Ga_4Ge_2O_{14.5}$ 60 % dense pellet (a and c) and the same powders after mechanical milling (b and d).

In systems containing Ge/Ga volatilization was prevented by the use of the volatile reactant in excess or the covering of a pellet with sacrificial powder. Surrounding a pressed pellet with sacrificial powder of the same composition reduces the loss of the more volatile component. To further ensure the attainment of highly accurate elemental ratios in the final product the surfaces of the sintered pellet were ground with sand paper to avoid concentration gradients throughout the thickness of the pellet.

An adequate selection and processing of the starting materials is key in order to achieve the desired stoichiometry in the final product of the reaction. Therefore, hygroscopic reactants such as rare earth oxides were stored at 950 °C prior to weighing so as to prevent the hydroxide formation when exposed to air moisture at room temperature. Furthermore, to avoid the use of moisture sensitive alkaline oxides, carbonates were used instead. Reaction mixtures containing carbonates were fired for 5-6 hours at 900 °C as loose powders in order to enable decomposition and removal of carbonates from the precursor mixture.

2.1.2 The Pechini method

This solution-based synthetic method for the preparation of ceramics at low temperature receives its name after Pechini P. Maggio, who in 1967, patented a novel method for the synthesis of barium titanate *via* an intermediate resin solution.[158] The Pechini method commences with an aqueous solution of the cations of interest. The metal cations are then chelated by an organic complexing agent solution, such as citric acid (CA, $C_6H_8O_7 \cdot 2H_2O$).

After the chelation of cations in solution with the carboxylic acid, a polyhydroxy alcohol such as ethylene glycol (EG, $C_2H_4(OH)_2$) is added to the activated mixture which is heated up to 100-130 °C to promote the polyester formation reaction. During this stage of polyesterification reaction also known as gelation, the viscosity of the solution increases drastically as a consequence of the polymer chain augmentation and the evaporation of the solvent, ultimately resulting in the formation of a gel. The continuous growth of the polymer is supported by the presence of at least two functional groups (-OH and -COOH) in these monomers which impinge on one another linking and forming a continuous network.[159,160]

When all the solvent has been evaporated and the polymerization process is completed the cations are trapped in a relatively rigid polymer network preserving the initial homogeneity of the solution. It is this mixing of reagents on an atomic level which brings the possibility of increasing the reaction rate and decreasing the final synthetic temperature. The obtained resin is thermally decomposed at 600 °C in order to remove all the organic matter from the mixture of reactants prior to the final sintering step. The strong foaming of the reaction mixture at this intermediate calcination step prevents the segregation of phases.

After the organic precursors have been oxidized, one is left with a highly homogeneous mixture of an intermediate phase compound with the proper stoichiometry of the metal ions with very fine grains (typically 20 to 50 nm[161]). The obtained product is then calcined at the synthetic temperature for synthesis completion. A comparison between the two synthetic methods: Solid state reaction method and Pechini is given in the next page in Table 2-1[162].

Table 2-1 Comparison between the Solid-state and Pechini synthetic methods. The doping limit and densification accounts for the $La_3Ga_{5-x}Ge_{1+x}O_{14x/2}$ system which is the focus of study in this thesis.

	Traditional solid-state reaction method	Pechini method
Typical T required	- Depends on the system. By the thumb-rule one could said that the T will be at least 2/3 of the T_m. - Powders can be pelletized to push the grains together	- Usually decreased by ~400° with respect to solid-state reaction method.
Product Obtained	- Thermodynamically stable compounds are obtained. - The high T required by this technique might cause the evaporation of a volatile reactant. Requires the addition in excess of the given volatile reactant or the use of sacrificial powder to prevent the formation of the undesired product.	- Synthesis of metastable compounds which cannot be prepared by solid-state reaction
Typical particle size and homogeneity	- The manual mixing of the starting reagents in the pestle and mortar gives micrometer (μm) particle sizes and Poor chemical homogeneity leading sometimes to the formation of secondary phases. - Particle size could be decreased below 100 nm by means of ball-milling.	- Typically 20-50 nm - The precursors are mixed at an atomic level
Reactivity of the precursors mixture	- Requires a complete disruption of the structure (*i. e.* breaking/forming many bonds). The driving force being the difference between the free energies of formation (ΔG_{for}) of the products and reactans.	- Intermediate compound (frequently amorphous) with the proper stoichiometry of the metal ions.
Doping limit (x) in $La_3Ga_{5-x}Ge_{1+x}O_{14+x/2}$	- 0.3	- 1.5
Densification	- > 90 % dense pellets can be easily achieved at 1300 °C	- Pellets are not dense at the synthetic T - Pellet densification is expensive: HIP, SPS.

2.2 Dense pellet preparation

Average density and uniformity of the microstructure can have a crucial impact on the ultimate physical properties of a given material under study. Moreover, the preparation of pellets with a high density, desirably greater than 90 % of the crystallographic density, is a pre-requisite for the electrochemical performance evaluation of the new materials synthesized for the duration of the work presented here. The average density of ceramics accounts for their degree of compaction which can be calculated as the fraction of theoretical density,

$$\phi = 1 - P$$

Equation 2-1

Where the term ϕ accounts for the volume fraction of the solid and P is the void fraction. The pore volume within the sintered samples was accurately determined by the Archimedean method which consists of submerging a sintered pellet in a liquid of known density such as distilled water. When doing so, the pellet will undergo an apparent loss of weight which is equal to the weight of the displaced water and its volume can be precisely calculated as:

$$\rho = \frac{m_1}{m_3 - m_2}\rho_l$$

Equation 2-2

where ρ is the calculated density, m_1 is the mass of the dry specimen, m_2 is the apparent mass of the immersed specimen, $m_3$is the mass of soaked specimen and ρ_l is the density of the liquid.

The more traditional method for densification based on the sintering of ceramics by prolonged heating at a temperature close to the melting point was carried out when the nature of the material will allow this simple approach. Under other conditions, more newly developed sintering techniques such as spark plasma or hot isostatic sintering were undertaken as discussed below.

2.2.1 Conventional Sintering

Sintering is the process in which powdered form samples are heated close to their melting point, entailing a great increase in the density of the material. In order for this process to be favourable, a decrease in the total energy of the system ΔG_T must occur[162]. During sintering, the high energy surfaces at the solid-air interface of the powder particles are replaced by the low energy grain boundary solid-solid interface in the densified material resulting in a lessening of the free energy associated to the surfaces of the grains that can be then expressed as,

$$\Delta G_s = \gamma_s(Final\ surface\ area - Initial\ surface\ area)$$

Equation 2-3

where γ_S is the specific surface energy. The driving force (DF) for the closure of an isolated spherical pore during the sintering process and can be expressed in terms of the pressure P, the aforementioned γ_S and the radius of the curvature of the pore as:

$$DF \propto P = \frac{2\gamma_S}{r}$$

Equation 2-4

The solid-state sintering process described here is categorized in three different stages: initial, middle and final stages. During the sintering process the different pathways for the transport of material can occur either at the surface of a grain adjacent to a pore, grain boundary (interface between two grains) or lattice (bulk of the grain). Due to the fact that these diffusion processes are thermally activated each mechanism will be dominant in different stages of the process depending on their activation energies, E_a.

- Initial stage

At the initial stage, the solid powders constitute an assembly of grains with very high porosity. As the temperature increases, the surface of the grains becomes smooth and diffusion of the material takes place in order to fill the pores resulting in the formation of necks (points of contact) between the grains. In this process, the gas trapped in the pores gives rise to an internal pressure that opposes the driving force for the shrinkage. It could be easily deduced from Equation 2-4, that the driving force for the removal of small pores is greater than that for larger pores. Larger pores remain towards the end of the diffusion process whereas the small porosity is decreased by up to12 %.

- Middle stage

Grain boundary diffusion, with a higher E_a, dominates over surface diffusion at higher temperatures. Diffusion on the grain boundaries brings the centres of the grains together resulting in the densification of the ceramic body. Surface and grain boundary mechanism of diffusion substantially decrease the porosity of the ceramic body, achieving a final density greater than 90 % at the end of the intermediate stage of sintering.

- Final stage

In the final stage of sintering, a further increase of the temperature will once again change the dominant mechanism for sintering from grain boundary to lattice diffusion. This stage is characterized by the dwindling of the remaining isolated pores and grain growth, achieving full densification.

For most conventional ceramics, the increase in density and grain size is proportional to the sintering time. However, when volatile elements are present adverse effects such as compositional changes and the formation of secondary phases must be considered. To counter adverse volatilization related problems during sintering a double crucible set up was used, where the outermost crucible contains sacrificial powder with identical composition.

One alternative approach aimed at shortening the heating time at high temperatures is the so called reactive sintering. In this method, the ceramic body is composed of the unreacted precursors that will undergo a solid-state reaction forming the desired new phase during sintering. The reaction occurring between the grains causes an additional stress in the green body increasing the density of the final product. Sometimes, a part of the ceramic material

melts and provides a liquid phase during sintering. This liquid phase constitutes a medium for faster flow of material to fill the pores.

Other methods carried out to enhance densification during sintering are the cold isostatic pressing of the sample prior to sintering and the use of binders introduced in 2.2.1.1 and 2.2.1.2.

2.2.1.1 Cold Isostatic Pressing (CIP)

Cold isostatic pressing is a powerful tool for powder compaction that uses a hydraulic fluid to apply a hydrostatic pressure achieving a greater degree of compaction of the green body. Thus, CIP represents an advantage from the previously mentioned uniaxial pressing in 2.1.1. A greater compaction translates into a higher contact area and which allows the theoretical density to be approached in a faster manner[163].

In the work presented here, a CIP with 200 MPa pressure was used. Samples are typically milled beforehand, so as to achieve a small starting particle size, pelletized and then sealed in waterproof bags and lowered into a hydraulic fluid.

2.2.1.2 Binders

Binders can play a crucial role in the final bulk density and strength of the sintered bodies. Thermoplastic compounds are the most widely used binders, including two of the most common commercial polymer binders of vinyl nature used in this work: polyvinyl butyral (BUTVAR) and polyvinyl alcohol PVA (see Figure 2-2). The C-C linkage and –OH groups in their molecular structure provide them with great adhesion properties. These binders have a strong affinity to adsorption on oxide particles dispersed on water (on the PVA case) or ethanol (when using BUTVAR)[164,165].

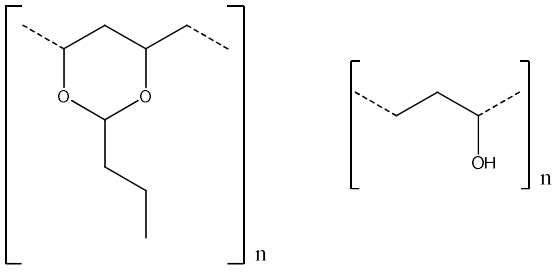

Polyvinyl Butyral (BUTVAR) Polyvinyl Alcohol (PVA)

Figure 2-2 Idealized chemical structure of polyvinyl butyral and polyvinyl alcohol.

The thermal debinding of such thermoplastic materials accounts for a controlled removal of the binder upon heating, prior to the final sintering which ultimately produces a dense ceramic. The debinding treatment is essential to avoid undesired uncontrolled binder decomposition. Big volumes of gas at high pressures could result in the cracking of the ceramic.[166] First, the liquid must be removed by evaporation at ~150-200 °C in stage 1 and then the binder must be removed by thermal decomposition at temperatures between ~300-700 °C in stage 2[163].

(1) Stage 1: Drying (120-200 °C)

Initially the powders are mixed with a binder consisting of a solution of the polymeric agent (typically 15 wt% binder). The solvent is then removed by drying the mixture at ~120-200 °C, which leads to a rearrangement of the particles to achieve a denser packing[167] (*i. e.* the polymer gives a compressive stress holding the particles together).

(2) Stage 2: Binder burnout (300-700 °C)

During the binder burnout, the polymer undergoes several decompositions at temperatures covering a range of 200-450 °C, depending on the polymer's molecular weight. High-molecular-weight polymers will degrade along many possible pathways into low-molecular-weight segments which can remain in the ceramic up to temperatures higher than 600 °C. The binder burnout temperature for PVA and BUTVAR used in this work was found to be ~450 °C[164]. The flow of these volatile residues leads to stress due to changes in the temperature and pressure profiles and enhances the final density of the ceramic.

2.2.2 Hot Isostatic Pressing

Hot isostatic pressing (HIP-ing) involves the simultaneous application of a high pressure with an inert gas (therefore isostatic) and elevated temperature. The combination of pressure and temperature can achieve a particular density at a lower temperature than the required for sintering alone, typically greater than $0.7T_m$[168,169].

In a hot isostatic press configuration (see Figure 2-3) there are no dies as the pressure arises from atoms of gas colliding with the can where the powder material is embedded. As densification occurs, the powder shrinks and the external can shrinks with it to the same extent in all directions. The motion of the gas atoms at high velocities of ~900 m·s^{-1} can generate an applied pressure to a system as high as 300 MPa.

When pressure is applied in addition to heat, the densification mechanisms are modified from those in 2.2.1. The HIP densification mechanism introduces a new term into Equation 2-4 to account for the applied pressure 'P_{appl}'[170].

$$P_{eff}^2 = \frac{2\gamma_s}{r} + P_{appl}$$

Equation 2-5

In HIP the applied external pressure completely swamps the surface-energy force for pore closure for a pore of greater than 40 nm of diameter (for $\gamma_s = 1\,J \cdot m^2$ and an external pressure of 100 MPa) causing any gas in a pore to dissolve in the matrix. Moreover, the gas diffuses to the surface rather than to other pores. Only when a pore is reduced to a diameter of 40 nm (for the given conditions of $\gamma_s = 1\,J \cdot m^2$ and $P_{appl} = 100\,MPa$) the driving force due to surface energy ($2\gamma_s/r$) becomes comparable to that due to the externally applied pressure (P_{appl}). Thus, relatively high temperatures ($\geq 0.7\,T_m$) are required to raise the diffusivities in the material sufficiently for pore closure.

It should be noted that prior to the pressurization treatment it is desirable to avoid any trapped gas. This is overcome by the application of vacuum to the encapsulated powders. The HIP experiments presented in this thesis were carried out by Michael Gaultois at the University of Santa Barbara (CA, USA).

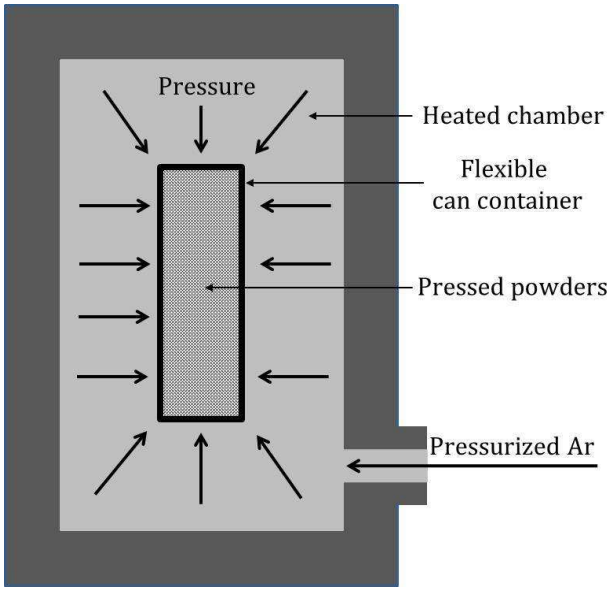

Figure 2-3 Schematic view of a Hot Isostatic Pressing (HIP) chamber.

2.2.3 Spark Plasma Sintering

Spark plasma sintering is a fast sintering method which allows for the densification of materials at intermediate temperatures (800-1200 °C – a few hundred degrees lower than in conventional sintering processes, $\sim 0.7T_m$)[169]. Full densification can be achieved in just a few minutes including heating and cooling times. Such a short sintering time is achieved by the simultaneous application of a uniaxial pressure and a direct current. These features make SPS sintering a valuable technique for the compaction of powdered samples with thermal instability[171], composites[172,173] and nano-sized powders without significant grain growth[174-176], materials synthesis[177] and batteries assembly[178,179] just to name a few of the many applications that SPS finds in the development of advanced functional materials[180].

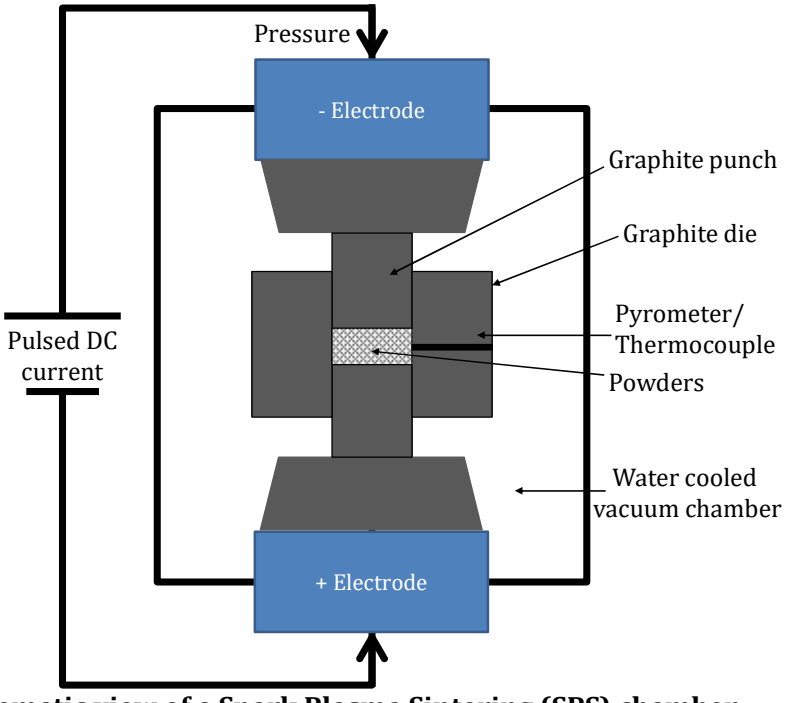

Figure 2-4 Schematic view of a Spark Plasma Sintering (SPS) chamber.

In Figure 2-4, showing a schematic representation of the SPS chamber, the powdered sample lies within the two plungers of a graphite die. A pulsed DC current is applied to the electrically conductive graphite die acting as a heating element at the same time as it is exerting a uniaxial pressure to the sample of up to 100 MPa. SPS processes allow for very fast heating rates as high as $1000\,°\ min^{-1}$ [180]. The temperature is measured with a thermocouple inserted into the die for temperatures below 700 °C. When $T \geq 700\,°C$, the temperature is recorded by an optical pyrometer focused on the surface of the die.

In SPS, the heating of the materials occurs due to both processes: the contact with the graphite die and the self-heating of the sample accomplished by the application of a pulsed DC current. As a consequence of the applied DC current there is an increased plasticity at the grain boundaries by Joule's effect. The electric field promotes the motion of charged species that in turn give rise to grain sliding and compaction with the aid of an applied pressure. The use of a pulsed (on-off) DC current as opposed to a static electric field is essential in order to avoid a permanent charge separation in the glassy phase. The pulsed current allows for a discharge of the accumulated charges at particles boundaries. Although the generation of a plasma is controversial and questioned by numerous authors[181], it is generally accepted that the pulsed current does influence the reaction patterns of the cooperative mechanisms involved in sintering and promotes the plastic deformation at the particles surface[182]. An evidence for this is that while it is true that SPS is a more effective sintering method for those electrically conductive materials where a higher local heat generation is possible, SPS has also proved success in the sintering of insulating ceramics such as Al_2O_3[183].

Densification in SPS occurs *via* a localized rise in temperature at a contact point between particles. The processes involved in sintering are localized at the particles surface, which allows full densification without inter-particle reaction and grain growth.

In this work a Sumitomo Coal SPS-1050 SPS apparatus was used. This system is able to exert a maximum load of 100 kN and produce a pulsed current as high as 5 kA for an applied voltage of 10 V. Rapid pulses of 3 ms in length were used with a pattern of 12:2 on and off pulses. Experiments were carried out under vacuum conditions and 2.5-6 g of fine powders were pressed in a 20 mm Outside Diameter (OD) and 40 mm tall graphite die. The SPS apparatus was operated by me with the training provided by Dr Amit Rana at the Mercury Centre (Sheffield, UK).

The theoretical maximum pressure applicable in SPS is limited by the compressive strength of the die. Most commonly used dies in SPS sintering are made of graphite with a compressive strength of up to 150 MPa[169]. Experimentally, the maximum loading pressure admitted in a SPS set up using a high-density graphite die is 80-140 MPa[184].

2.2.3.1 Spark plasma sintering with a WC die

A double acting die described in ref. 185 allowed us to apply higher pressures - up to 1 GPa on a Ø = 5 mm sample. This device is composed of an external graphite die, inside of which there are two protective discs of WC connecting it to an internal smaller 12 mm tall die. The body of the smaller die is made of graphite and the plungers are made of SiC. By means of this double-acting die the full densification (>98 %) was achieved in YSZ and SDC at only 850 and 750 °C respectively[185].

The experiments at a higher pressure were carried out by Dr Jinfeng Zhao at University of California, Davis (USA) also in a Sumitomo Coal SPS-1050 SPS apparatus using the same pulse pattern specified in 2.2.3.

2.3 Materials Characterisation

2.3.1 Structural Analysis: Powder Diffraction

Powder diffraction is a powerful tool for the analysis of crystalline materials. It is a non-destructive technique used for multiple purposes such as phase identification, quantitative analysis of multi-component samples and the determination of grain size, strain and preferred orientations. Moreover, in certain instances powder diffraction allows for full characterization of crystal structures similarly to the one obtained by a single crystal experiment with the added benefit that powder diffraction can be extended to a wider spectrum of samples including those which are difficult or impossible to obtain as single crystals.

Diffraction occurs when a crystal is oriented towards an incoming beam of electromagnetic waves of suitable wavelengths such that the waves interfere constructively between ordered layers of atoms. The elastically scattered radiation can be mathematically defined by Bragg's law.

$$n\lambda = 2d_{hkl}\, sin\theta$$

Equation 2-6 Bragg's law

where n is an integer number, λ is the wavelength of the incident electromagnetic wave, d is the spacing between parallel planes of atoms denoted by the hkl indices and θ is the Bragg angle.

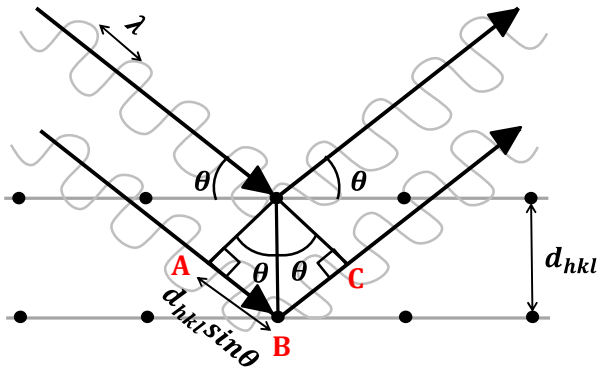

Figure 2-5 Schematic representation of Bragg's law.

Figure 2-5 depicts Bragg's law for two contiguous rows of atoms where the incident radiation with wavelength λ is 'reflected' in phase interfering constructively. Bragg's law states that constructive interferences from successive planes will occur when the path difference ($\overline{AB} + \overline{BC}$ in Figure 2-5) equals to an integer of the incident wavelengths.

Typical diffraction experiments consist of irradiating a sample at a fixed λ. The randomly oriented polycrystallites will simultaneously diffract the beam giving rise to cones of diffracted intensity around the beam axis (Scherrer cones) collected in a detector. The diffraction patterns are produced by scanning across a narrow strip, where the scattering angle is calculated from the angle between the beam axis and the ring. The compression of 3D data into a 1D scan can lead to the loss of information due to peak overlap. This loss of information can be minimized by high resolution diffraction producing sharp diffracted peaks.

In order for diffraction to occur it is necessary to irradiate the sample with X-rays, thermalized neutrons or electrons whose wavelength corresponds to the same order of or smaller than the interatomic distances (typically ~1 Å). Figure 2-6 depicts the penetration of beams of neutrons, X-rays and electrons in matter. Neutrons and electrons have a wavelength defined by the Broglie relationship and can therefore be diffracted. As depicted in Figure 2-6 electrons and X-rays beam interact with the electrons in the materials and do not penetrate deeply in the sample, as opposed to the uncharged neutrons. The interaction between neutrons and matter can take place in the nuclei and through magnetic dipole-dipole interactions.

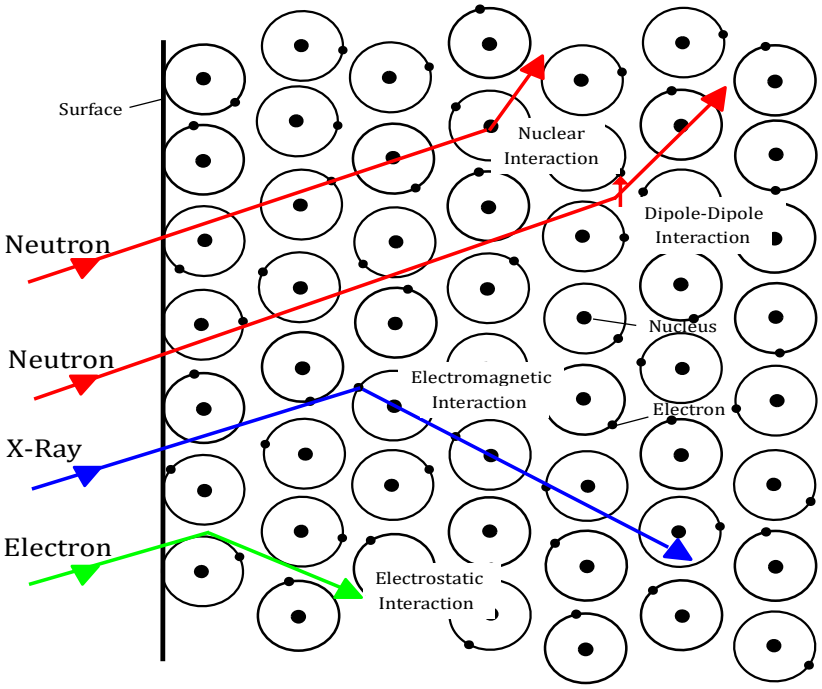

Figure 2-6 Schematic view of the different Scattering interactions mechanisms of electrons, X-rays and neutrons.

In this thesis, combined X-ray and neutron diffraction techniques were used for the characterization of the materials studied. A more detailed description of these techniques is given in the following subsections.

2.3.1.1 Powder X-ray Diffraction

A diffraction pattern (Fourier transform of the crystal structure) consists of a set of discrete reflections each of which is a wave defined by an amplitude and a relative phase. The sum of vectors is known as the structure factor '$F(hkl)$'.

$$F(hkl) = \sum_{j=1}^{N} f(\theta)'_j \, e^{[2\pi i \, (hx_j + ky_j + lz_j)]}$$

Equation 2-7

$f(\theta)'$ is the scattering factor a of the jth atom in the unit cell with coordinates hx_j , ky_j and lz_j. The integers h, k and l are the Miller indices and N is the number of atoms in the unit cell.

In order to account for time averaged temperature dependent movement of atoms about their mean equilibrium, the scattering factor, $f(\theta)'$ in Equation 2-7 is expressed as a function the thermal vibrations parameters which are denoted by either 'B' or 'U' with units of Å^2.

$$f'(\theta) = f(\theta)\exp\left(-\frac{Bsin^2\theta}{\lambda^2}\right) = f(\theta)\exp\left(-\frac{8\pi Usin^2\theta}{\lambda^2}\right)$$

Equation 2-8

Where $f(\theta)$ is the scattering factor for a stationary atom and $f'(\theta)$ refers to the vibrating atom. The exponential term in Equation 2-8 $-\frac{Bsin^2\theta}{\lambda^2}$ could also be defined anisotropically as an ellipsoid and becomes:

$$-2\pi^2(U^{11}h^2a^{*2} + U^{22}k^2b^{*2} + U^{33}l^2c^{*2} + U^{12}hka^*b^* + U^{13}hla^*c^* + U^{23}klb^*c^*)$$

Equation 2-9

U^{ij} parameters are known as Anisotropic Displacement Parameters or ADPs. The strong correlation of these parameters with the temperature allows for the discrimination of dynamic and static disorder, since the more temperature dependant dynamic disorder will be significantly reduced at lower temperatures.

The value of $f(\theta)$ is maximised at θ = 0° since forward scattered X-ray amplitudes always result in constructive interference. At larger angles $f(\theta)$ falls off smoothly and monotonically to zero. This fact explains the general appearances of X-ray diffraction patterns where the intensity values decay with increasing 2θ. The value of maximum $f(\theta)$ is proportional to the atomic number of the atom (Z) corrected for valence charge. For this reason, the scattering power of light atoms such as oxygen (Z=8) is weaker than that of heavy atoms such as tungsten (Z = 74).

From diffraction experiments only the amplitudes $|F(hkl)|$ of the reflections are obtained and not their phases, known as the '$phase\ problem$' which can be overcome by analytical methods[186]. The recorded intensity is defined by the square of the amplitude of the scattering factor with additional corrections: the Lorentz polarisation correction (Lp), absorption corrections (Abs) and the scale factor (s)[187]:

$$I_{hkl} = s\,|F(hkl)|^2\,Lp\,Abs$$

Equation 2-10

The intensities of the peaks in a diffraction pattern contain information about atomic coordinates and displacement parameters, just as in a single-crystal diffraction experiment. This makes possible the extraction of structural information by refinement methods such as the Rietveld method briefly discussed in 2.3.1.3.1.3.

2.3.1.1.1 Laboratory X-ray Diffraction (XRD) sources

In this work, two diffractometers were used:

- a Panalytical X'Pert Pro diffractometer with a Co source using a monochromator selecting $K\alpha_1$ radiation of λ = 1.7890 Å in a Bragg Brentano (reflection) geometry operated at 40 kV and 40 mA.

- a Bruker D8 Advance diffractometer equipped with a monochromatic Cu $K\alpha_1$ (λ = 1.5406 Å) source, which can be operated in either Debye-Scherrer (transmission) or Bragg-Brentano geometries (see Figure 2-7).

Since the elements present in the materials analysed in this work do not significantly fluoresce in the K_α X-rays produced by either Cu or Co targets, the two diffractometers above were both used for routine analysis.

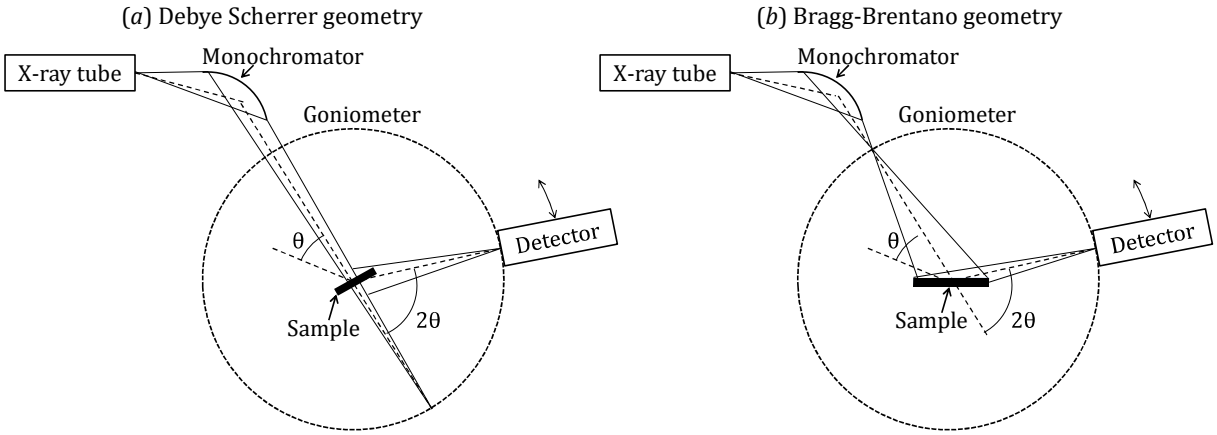

Figure 2-7 Schematic representation of diffractometers in (a) Debye-Scherrer and (b) Bragg-Brentano geometries where a monochromator located before the sample stage separates $K_{\alpha 1}$ and $K_{\alpha 2}$. The goniometer used to position the sample at different orientations is represented by a dotted line and the movement of the rotation of the detector by 2θ is denoted by a double ended arrow.

In reflection geometry, powdered samples were prepared by careful grinding of the sample with acetone, which was afterwards pipetted into a zero background sample holder (Si wafer cut on an odd plane). After acetone evaporation, a smooth surface of fine sized material is obtained. A smooth surface is imperative in order to avoid artificially strong peaks at high 2θ values, and changes in the peak positions due to surface roughness or absorption effects (see Figure 2-8). The preparation of samples running in transmission geometry was carried out by sprinkling the finely ground powders on to a Scotch tape.

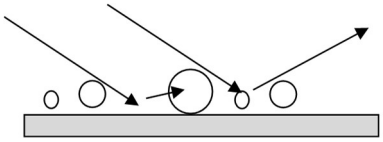

Figure 2-8 Schematic diagram showing the origin of surface roughness/porosity effect, where some diffracted beams are absorbed by the material[188].

The data collection was varied depending on the purposes of the experiment. A typical quick data collection of 30 min at a 20-60° 2θ range was used for phase identification and analysis of the reaction progress. When required, higher-quality scans were recorded for several hours (4-12 h) for Rietveld refinement purposes at a wider 10-100° 2θ range.

2.3.1.1.2 Synchrotron source

Synchrotron sources receive a useful flux of several orders of magnitude greater than a typical laboratory instrument. Furthermore, *via* a selection of short wavelength data to higher 2θ values can be obtained, allowing for a higher resolution.

In synchtrotron radiation sources, the electrons generated in an electron gun are accelerated into dedicated machines in ultrahigh vacuum: first into a linear accelerator (Linac) that leads into a booster and finally into the large storage ring (see Figure 2-9). In the synchrotron at Diamond the storage rings consists of a ~560 m long 48-sided polygon[189]. Diamond uses a 'double bend' magnet configuration in which two bending magnets are placed in each of 24 straight sections in order to guide the electrons. The energy of a moving electron is given by $= m_e c^2/\sqrt{1 - v^2/c^2}$, hence in this 3 GeV[190] storage ring, the electrons are travelling at a speed of 0.9999999855c.

Synchrotron radiation is emitted when charged particles travelling at relativistic speeds change velocity when following a curved trajectory at a bending magnet (undulator or wiggler[191]). This emitted light is then funnelled into the experimental stations or beamlines.

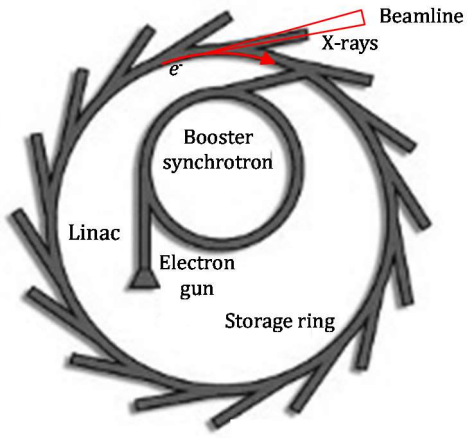

Figure 2-9. Schematic ilustration of a synchrotron taken from ref. 189. The tangential fan of radiation emitted from a bending magnet is represented in red.

I11 is the beamline used for the Synchrotron X-ray Diffraction (SXRD) data collection in Chapter 5 (see page 146). I11 operates in a Debye-Scherrer geometry, the X-ray beam is monochromated by a liquid nitrogen cooled Si(111) double crystal over the 5-30 keV range. A multianalyzing Si crystal assembly (MAC) high resolution detector system was used. The MAC detector allows for the simultaneous capture of multiple diffraction patterns which are afterwards merged into a single array with a 0.001° step size [190,192].

In Chapter 3, SXRD data at ambient conditions was collected on $La_3Ga_5SiO_{14}$ and $La_3Ga_5TiO_{14}$ in BL01C2 powder diffraction end station at the NSRRC (Taiwan). BL01C2 is a Debye-Scherrer type diffractometer that uses X-ray energies within the range 8-35 keV delivered from a wavelength shift magnet. A 2D MAR345 imaging plate detector was used and the data was converted to 1D profile by GSAS-II software[193].

2.3.1.2 Neutron Powder diffraction

Neutrons also have a wave-particle dual nature and it is this characteristic which is its use as a crystallographic probe. The wavelength, velocity and energy are related by de Broglie equation:

$$\lambda = \frac{h}{m_n v} = \frac{2}{\sqrt{2m_n E}} = \frac{2}{\sqrt{2m_n k_B T}} = 2dsin\theta$$

Equation 2-11

where λ is the wavelength in Å , E is the energy of the neutron in meV, h is the Planck's constant, m_n is the neutron mass (1.675×10^{-27} kg), k_B is Boltzmann's constant and T is the temperature in K . Based on their wavelengths neutrons can be classified in three categories listed in Table 2-2. Thermal neutrons whose wavelength are of the same order of atomic radii ($\sim 1 - 2$ Å) are most commonly used for diffraction studies.

Table 2-2 Classification of neutrons according to their energy, temperature and wavelength.

	Energy (meV)	Temperature (K)	Wavelength (Å)
Cold	0.1-10	1-120	30-4
Thermal	5-100	60-1000	4-1
Hot	100-500	1000-6000	1-0.04

Neutrons are non-charged particles with a magnetic moment ($s \pm 1/2$) and can be scattered by the nuclear force as well as by unpaired electrons in magnetic atoms. Thermal neutrons diffract at point-like nucleus, since the dimensions over which the nuclear forces operate are at a range of 10^{-15} m and neutron wavelengths are $\sim 10^5$ times larger. As a result the neutron scattering cross sections σ_{tot} is independent of the diffraction angle and the intensity of the peaks in the diffraction patterns does not decay with increasing 2θ values. The total neutron scattering cross section σ_{tot} is calculated from of b as:

$$\sigma_{tot} = 4\pi\overline{b^2}$$

Equation 2-12

where b is the scattering length and is given in units of barn; 1 barn = 10^{-28} m^2. The scattering length is influenced by complex neutron-nucleus and spin state interactions, and it can be coherent or incoherent. Due to the difficulties to reliably describe b in terms of fundamental constants, these are determined experimentally for each isotope and tabulated[194]. Interestingly, unlike X-rays, neutrons do not interact with atoms in a way that is correlated with their atomic number. This is of great value to identify light atoms such as protons or oxygen atoms in the presence of heavy atoms as well as in isotopic-labelling techniques, but could have some drawbacks in the study of vanadium compounds or for a mixture of positive and negative scatterers on a crystallographic site.

Neutrons are generated at large neutron scattering-facilities that can be classified in two types depending on the way in which neutrons are produced: reactor and spallation sources. The ISIS facilities used for data collection in this thesis are of the second type.

At ISIS, protons are produced by accelerators and stored in rings. The beams of accelerated protons are afterwards diverted into a water-cooled tungsten target causing the 'spallation' of neutrons and fragmentation of the tungsten nuclei into smaller atoms. The moderated neutrons are then directed to the different experimental beamlines.

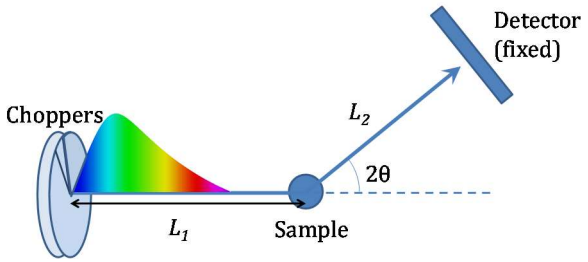

Figure 2-10 Schematic array of a TOF diffractometer. An array of choppers generates a pulsed polychromatic beam that travels a flight path denoted by L_1 to reach the

sample. The diffracted neutron beam then reaches the detector at a fixed position at L_2.

Figure 2-10 depicts a powder diffractometer at a spallation source which is fed with a pulsed beam of neutrons. Neutron pulses of suitable energies are achieved by blocking unwanted neutrons with rotating disk devices called choppers. The applied method of determining the wavelength λ of the scattered neutrons is to measure their time of flight (TOF) over a known flight path, L, from the source to the sample (L_1) and later over the scattering path to detector at a fixed 2θ position (L_2).

$$\nu = \frac{(L_1 + L_2)}{TOF}$$

Equation 2-13

Relating Equation 2-13 with the Broglie equation (see Equation 2-11), TOF can be related to the d-spacing as follows,

$$TOF = \frac{m_n\,(L_1 + L_2)\,2dsin\theta}{h}$$

Equation 2-14

Besides the limited accessibility of neutrons exclusive to large facilities, available neutron beams have very low intensities ($\sim 10^4\ neutrons\ s^{-1}mm^{-2}$) compared to synchrotron sources ($\sim 10^8\ phonons\ s^{-1}mm^{-2}$). The low flux of neutrons coupled to their weak interaction with matter extend the duration of neutron diffraction experiments to several hours.

In the TOF arrangement the resolution ($\Delta d/d$) of a TOF-diffractomter is given by

$$\Delta d/ \quad = \sqrt{\Delta\theta^2 cot^2\theta + (\Delta t/t)^2 + (\Delta L/L)^2}$$

Equation 2-15

Where the terms $\Delta\theta$, Δt and ΔL account for uncertainties for the scattering angle, time of flight and path length respectively. It can be concluded from Equation 2-15 that the highest resolution is given at high θ (back-scattering), short pulse durations and long paths.

2.3.1.2.1 High Resolution Powder Diffractometer, HRPD

The uncertainty in the scattering angle $\Delta\theta$ introduced in Equation 2-15 can be minimized by an increase in the length of the flight path from the sample to the detectors, L_2. However, this measure has the counter-effect of reducing the solid angle ($\Delta\Omega_i$) reached at the detector: $\Delta\Omega_i \cong 2\pi R_i \Delta R_i$ where R_i and ΔR_i are the length and width of the annuli respectively. Since the increase in L_2 is compromised it is usually fixed to 1-2 m whereas L_1~10 m for most diffractometers. However, the High Resolution Powder Diffractometer (HRPD) has a very long path L_1 of about 100 m which provides it with a $\Delta d/d$ ~5 × 10^{-4} at the backscattering and ~2 × 10^{-3} at the 90° bank, which measures peaks with d-spacings up to ~3.2 Å. The 30° bank extends to larger d-spacing albeit at lower resolution. See Figure 2-11 for a schematic view of the detectors array. The detectors make use of methane that absorbs neutrons to produce detectable ionic radiation.

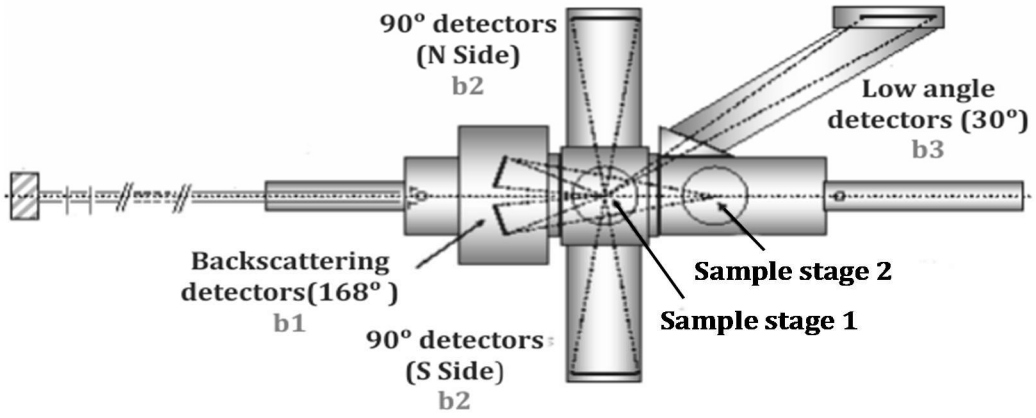

Figure 2-11 Schematic plan view of the HRPD detector configuration taken from the HRPD user manual[195]. In the work carried out in this thesis sample stage 1 was used.

In the NPD experiments introduced in Chapter 4 and Chapter 5, large amounts of finely ground powders (4-6 g) were introduced in Ø = 11 mm vanadium cans.

A major advantage of neutron diffraction is their ability to penetrate large sample environment chambers needed for variable temperature and pressure experiment. In this thesis variable temperature neutron diffraction studies (VT-NPD) were carried out from 9 up to 873 K.

The low temperatures were achieved with a close-cycled refrigerator (CCR) that works on the basis of a controlled cyclic compression and expansion of high pressure helium gas which allows for temperatures as low as 4 K. CCRs have the additional advantage, with respect to helium cryostat, to be mounted on the instrument's vacuum system reducing parasitic background by cutting down the extra-shielding.

Standard furnaces able to operate up to 1000 °C were used for high temperature experiments. The sample is surrounded by a large vanadium heating element under high vacuum, which in turn is surrounded by heat shields made of vanadium to again, minimise the parasitic background.

2.3.1.2.2 GEneral Materials diffractometer, GEM

The General Materials Diffractometer (GEM) is a high intensity instrument designed to have extremely good detector coverage by employing multiple detectors over a wide 2θ range shown in Figure 2-12. These features make GEM of great use for the structural study of a wide range of materials[196]

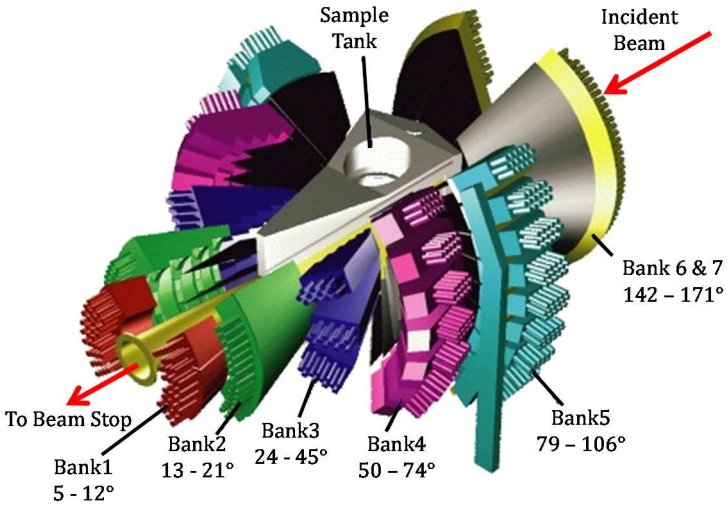

Figure 2-12 Schematic diagram of the GEM detector configuration taken from ref.196. The bank 5X not indicated in the figure is an extension of bank 5 situated adjacent to it.

The length of the incident flight path of GEM is ~17 m. All the detectors in GEM are ZnS/^{6}Li scintillator detectors with a total area of 7.270 m^{2}. The absorption of a neutron in a detector results in a flash of light that is transmitted *via* fibre optic cables to photomultiplier tubes (PMTs). The parameters corresponding to the eight detector banks on GEM are given in Table 2-3[197].

Table 2-3 Parameters of the GEM detector array[197]

Bank	2θ(°)	$L_2(m)$	$\Omega(srad)$	$\Delta d/d$
1	5.32-12.67	2.4	0.056	4.7×10^{-2}
2	13.44-21.59	1.5	0.093	2.4×10^{-2}
3	24.67-45.61	1.1-1.9	0.478	1.7×10^{-2}
4	50.07-74.71	1.0-1.4	0.988	7.9×10^{-3}
5	79.17-106.60	1.4	1.135	5.1×10^{-3}
5X	106.2-114.19	1.4	0.378	5×10^{-3}
6	142.50-149.72	1.5-1.7	0.280	3.4×10^{-3}
7	149.98-171.40	1.0-1.4	0.443	3.5×10^{-3}

The sample preparation for those materials measured in GEM was identical to that described previously in 2.3.1.2.1 for HRPD. The data was collected in banks 1-6, where bank 5 corresponded to the combination of banks 5 and 5X and bank 6 to 6 and 7 add up together.

2.3.1.3 PXRD Data Analysis

As a first approach for the analysis of newly synthesized phases and when tracking the reaction progress, experimental diffraction patterns were assigned to calculated patterns of known phases compiled in the International Centre for Diffraction Data (ICDD) Powder Diffraction File 2 (PDF2) database[198]. HighScore[199] search/match software sequentially identifies and filters the possible phases present based on the peaks observed in the diffraction pattern and inputted compositional information. Alternatively, diffraction patterns were simulated in TOPAS[200] from candidate structural models and compared to the experimental pattern.

2.3.1.3.1.1 Indexing

The main goal of the indexing process is to determine the unit cell and space group from a list of observed peak positions. This is done by the assignment of the appropriate Miller indices to each peak observed in the diffraction pattern. When indexing a pure sample, the indexed unit cell should account for all the observed reflections.

In the work presented here, the powder-pattern indexing was performed in TOPAS[200,201]. This automated indexing process relies on a computer algorithm testing a large amount of unit cells against the observed peak list. The relationship between peak positions (d-spacing) and unit cell is given by the basic indexing equation M_{hkl} relating reciprocal cell parameters ($A - F$) and indices ($h - l$):

$$M_{hkl} = \frac{4sin^2\theta}{\lambda^2} = \frac{1}{d^2} = Ah^2 + Bk^2 + Cl^2 + Dkl + Ehl + Fkh$$

Equation 2-16

The software uses a trial and error auto-indexing algorithm and provides the user with many plausible cells. The various possibilities are ranked by their indexing figure of merit 'M_{20}'[202]. The goodness of the match between the calculated positions and the experimental values is calculated by the average difference of the experimental and matched Q values '$\bar{\varepsilon}$', where Q $(= 1/d^2)$ up to the 20th observed peak.

$$M_{20} = \frac{Q_{20}}{2\bar{\varepsilon}N_{20}}, where\ \bar{\varepsilon} = \langle|Q_{exp} - Q_{calc}|\rangle$$

Equation 2-17

The term N_{20} refers to the number of calculated lines up to the 20th observed peak, $\bar{\varepsilon}$ denotes the goodness of the match between the calculated positions and the experimental values calculated by the averaged difference between the experimental (Q_{exp}) and matched (Q_{calc}) Q values up to the 20th observed peak, where Q $(= 1/d^2)$. Due to the possible presence of unobserved peaks by systematic absences M_{20} values between 20 and 30 and normally a good indication of finding the correct space group.

2.3.1.3.1.2 Pawley Fitting

The Pawley method[203] offers the possibility to refine the intensity values expected for every Bragg peak, without inputting any crystal structure information. This method provide superior zero shift value, background function, peak profile function and unit cell parameters with little effort and computational time.

The Pawley refined unit cell parameters and background can afterwards be inputted into a Rietveld refinement to use as a starting point. Moreover, the goodness-of-fit parameters obtained by Rietveld can be compared to the ones derived from a Pawley fitting (perfect model) in order to judge the goodness of the final model obtained by Rietveld.

2.3.1.3.1.3 Rietveld Refinement

In 1969, H.M. Rietveld[204] proposed the idea to calculate the entire powder pattern using a variety of refinable parameters and to improve a selection of these parameters by minimizing the weighted sum of the squared differences between the calcualted ($y_{calc,i}$) and observed models ($y_{obs,i}$), 'S_y':

$$S_y = \sum_i w_i (y_{obs,i} - y_{calc,i})^2$$

Equation 2-18 Cost function

where the weight 'w_i' is taken to be the inverse of the quadratic form of the variance σ in the determination of $y_{obs,i}$.

$$w_i = \frac{1}{\sigma^2(y_{obs,i})} \approx \frac{1}{N}$$

Equation 2-19

The weight can also be expressed as a function of the number of observed counts N, since the standard deviation can be approximated by $\sigma = \sqrt{N}$ for large N values. In Equation 2-18, the model function '$y_{calc,i}$' is parameterized by both crystal structure and experiment:

- for a constant wavelength experiment

$$y_{calc,i} = y_b + s \sum_{hk} |F(hkl)|^2 \, Lp \, Abs \, \phi \, (2\theta_i - 2\theta_{hkl}) \, \Delta(2\theta_i)$$

Equation 2-20

- or for a TOF instrument:

$$y_{calc,i} = y_b + s \sum_{hkl} |F(hkl)|^2 \, Lp \, Abs \, \phi \, (2t_i - 2t_{hk}) \Delta(t\theta_i)$$

Equation 2-21

Note that in Equation 2-20 and Equation 2-21 's' accounts for the scale factor and should not be mistaken for S_y in Equation 2-18, y_b refers to background function which was fit with a Chebyshev polynomial function in the refinements presented in chapters 3-5. The terms $\Delta(2\theta_i)$ and $\Delta(t_i)$ refer to the angular and time acceptance of the detectors at a given $2\theta_i$ angle for CW or t_i in TOF experiments. Due to a combination of instrumental factors and sample broadening the intensity of the peaks do not appear at a given $2\theta_i$ or $2t_i$ location, but distributed around this value. This distribution is denoted by $\phi\ (2\theta_i - 2\theta_{hkl})$ and $\phi\ (2t_i - 2t_{hkl})$ in Equation 2-20 and Equation 2-21 respectively and it is known as the profile or peak shape function. In this thesis, a pseudo-Voigt function ($pV(x)$) is refined to model the experimental peak profiles due to its good results[205]. This profile function is a combination of Gaussian $G(x)$ and Lorentzian $L(x)$ functions.

$$pV(x) = (1 - \eta)G(x) + \eta L(x)$$

Equation 2-22

Where the η shape or mixing parameters can range from $\eta = 0$ (Gaussian) to $\eta = 1$ (Lorentzian) and even $\eta > 1$. The mixing parameter is in turn a function of three refinable parameters: $lora$, $lorb$ and $lorc$ so that $\eta = lora + lorbtan\theta + lorc/cos\theta$.[206] For the refinement of TOF data from spallation neutron sources more complex pseudo-Voigt peak shape functions were used, which take into account the time dependence of the neutron intensity (pulse shape)[207]. In the pseudo-Voigt function the Full Width at Half Maxima (FWHM) of the diffracted peaks increases smoothly with 2θ making this an isotropic function. However, in high resolution powder diffraction an increase in the peak width may occur in proportion to the diffraction order due to microstrain within the sample of study. In 1999 Stephens[208] developed a model for multi-dimensional distribution of lattice metric in which each crystallite is treated as having its own multi-dimensional distribution. Each

reflection can then be expressed in terms of moments of this distribution. For a given set of planes with Miller indices hkl, the interplanar d-spacing can be expressed by Equation 2-16. In the Stephens model each grain is imagined to have its own set of $A - F$ parameters. Even though the average of the $A - F$ parameters has to obey the symmetry conditions imposed by the lattice which may require the mean of some of the parameters to be zero, there may be a distribution about zero that accounts for random strains of the sample. This finally leads to a dependence of the strain broadening with the so-called 'S_{HKL}' terms that account for the symmetry restrictions. S_{HKL} is related to the variance of M_{hkl} as:

$$\sigma^2(M_{hk}) = \sum_{HKL} S_{HKL} h^H k^K l^L$$

Equation 2-23

where H, K and L signify the components of the strain tensor and are defined for $H + K + L = 4$.

A Rietveld refinement is usually carried out by turning on the variables to be refined in a stepwise manner. Attempts to refine all of the parameters at once as a first approach are unlikely to succeed[209]. Moreover, the Rietveld method (or any iterative method for that matter) demands a sufficiently good initial model to use as the starting point of the refinement. Thus, the starting values for the lattice parameters should be close to the true values in order to ensure sufficient overlap between the predicted and observed peaks. It should then be possible to 'turn on' the scale factors and background function, which is followed by refinement of atomic positions, displacement parameters, site occupancies, preferred orientations (if needed) and so on.

An examination of the graphic output of the refinement at the intermediate stages is necessary in order to track the progress of the refinement. The identification of mismatches between the calculated and observed patterns by visual inspection are an indication of what parameters should be further refined/corrected in the subsequent stages. Table 2-4 lists the factors influencing distinct features of the calculated Rietveld function.

Table 2-4 Factors contributing to distinct features of the calculated Rietveld function[187,188,209].

Feature	Contribution from	
	Sample:	Experiment:
Background	Amorphous material Compton Scattering Local structure Lattice dynamics Fluorescence	Sample holder Detector noise
Profile Shape	Micro-strain Crystallite size	Monochromation Axial divergence In plane divergence Slit width
Peak Intensity	Atomic positions Temperature factors Occupancy Preferred orientations Absorption Surface roughness Sample transparency Powder average Atomic scattering factors	Polarization Beam intensity Detector type
Peak positions	Lattice parameters Space group Macro-strain	Wavelength Sample displacement Zero shift

Additional information on the progress of a refinement can be obtained by the comparison of the fitting errors for the different models and the same data[210]. The weighted R-factor (R_{wp}) is a commonly quoted measure of fit. R_{wp} is defined as the square root of the cost function (or weighted sum of square residuals) divided by the weighted intensities $\sum_i w_i (y_{obs,i})^2$.

$$R_{wp} = \sqrt{\frac{\sum_i w_i (y_{obs,i} - y_{calc,i})^2}{\sum_i w_i (y_{obs,i})^2}}$$

Equation 2-24 Weighted profile *R*-factor

Another useful error parameter is the expected R-factor (R_{exp}) which is the "best possible R_{wp}" calculated by the assumption that the numerator in Equation 2-24 takes its expected value, which equals to the $N - P + C$ degrees of freedom for the refinement ($i.e.$ the number of data points less the number of varied parameters).

$$R_{exp} = \sqrt{\frac{N - P + C}{\sum_i w_i (y_{obs,i})^2}}$$

Equation 2-25 Expected *R*-factor

The ratio of the two aforementioned R-values known as goodness-of-fit denoted as S or χ and commonly quoted as χ^2 value in the literature.

$$\chi^2 = \frac{\sum_i w_i (y_{obs,i} - y_{calc,i})^2}{N - P + C} = \left(\frac{R_{wp}}{R_{exp}}\right)^2$$

Equation 2-26

χ^2 defined in Equation 2-26 can be thought as the ratio between the sum of square residuals to its ideal value, χ^2 should therefore never drop below one. Although desirable, χ^2 values do not always approach unity since high intensity datasets tend to provide larger χ^2 values (due to the higherR_{wp}). There are no absolute χ^2 values to use as a guideline. A better approach is to use the R_{wp} obtained for a structure-free Pawley fit as an indication for the validation of the final model[210].

The final review of the refinement is a crucial process which includes: the attainment of a good visual fit between the calculated and observed model with a near-flat residual line ($y_{obs,i} - y_{calc,i}$), to check that the last parameters introduced in the refinement did not introduce significant differences to the visual fit of the data as well as to seek for the presence of unexpected correlation between parameters. Lastly and most importantly, the refined parameters must be chemically and physically sensible.

One should also check for the possibility of whether the refinement happens to fall in local minimum. The Rietveld method is based on gradient search using derivatives of S_y (see Equation 2-18). Once the system has settled within a local minimum, traditional refinements with parameters shifts based on gradients fail because the gradients are zero at a local minima. The litmus test to check for global/local convergence of the refinement is to input variations on the starting model to seek whether the same solution is obtained. Lastly, the final models were collated with complementary techniques such as Fourier maps[211] (or difference Fourier maps) to check for un-modelled scattering intensity, and Bond Valence Sum (BVS) calculations[212] to test the chemical plausibility of the refined structure.

2.3.1.3.1.4 Maximum Entropy Method (MEM)

The Maximum Entropy Method (MEM) allow for the extraction of information from an incomplete data set ($e.g.$ missing structure factor phase or overlapping peaks)[213]. When the entropy of a system is maximized, every pixel of the density map will have the same probability and the information thereof extracted will be demanded by the data and not an artefact of the method. The goal of MEM is to find the density that maximizes the entropy 'S'.[214]

$$S = -\sum_{i=1}^{N_{pix}} \rho_i log\left(\frac{\rho_i}{\bar{\rho}}\right)$$

Equation 2-27

where N_{pix} accounts for the data points throughout the unit cell , ρ_i is the density at the ith point and $\bar{\rho}$ is the mean density of the cell.

MEM is commonly used as a complementary method for deriving the most probable charge-density distribution and a fast approach to visualize the type of disorder. MEM is often complimented with other techniques such as charge flipping[215] or Rietveld[216,217] and it has been successfully applied to the investigation of disordered structures and the determination of diffusion pathways in ionic conductors which are difficult to solve by Rietveld alone[218-220]. The MEM analysis presented in this thesis was performed by Dr Michael Pitcher with JANA 2006[221].

2.3.2 Electron Microscopy

Electron microscopy (EM) constitutes a powerful tool for structural and elemental characterization of materials. The use of electrons for sample illumination, allows for a high magnification power of up to 1,500,000x, whereas optical microscopes have a magnification below 2000x. Electron as well as optical microscopes can be divided into three sections: The illumination system, the specimen stage and the imaging system[222].

In EM, the illumination system is comprised by an electron gun (which typically consists of a tungsten filament or LaB_6) bombarding electrons that are focused onto the specimen by the condenser lenses. The condenser lenses are magnetic and electric fields able to condense and disperse the negatively charged electrons. Thus, condenser lenses act in an analogous way to glass lenses in optical microscopes. Additionally, the intensity of the beam reaching the sample can be varied by the condenser aperture, a small hole in a metal located below the condenser lenses.

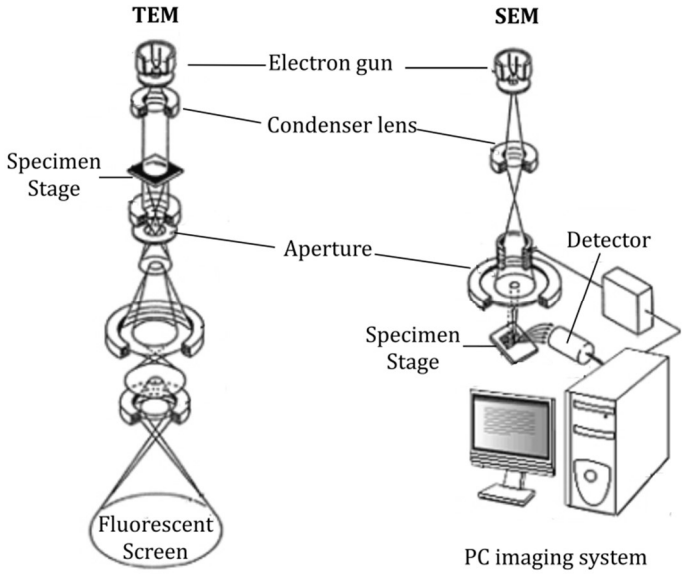

Figure 2-13 Comparative schematic view of a Transmission Electron Microscope (TEM) on the left side of the image and a Scanning Electron Microscope (SEM) on the right. The image was taken from JEOL handbook[223].

Figure 2-13 gives a comparative schematic view of two electron microscopes: a transmission electron microscope (TEM) and a Scanning Electron Microscope (SEM). Both instruments have different features and resolution power that will be further explained in the following subsections.

2.3.2.1 The Transmission Electron Microscope

In Transmission Electron Microscopy, the electrons ejected from the heated electron gun into a vacuum are accelerated by a high potential. Ruska *et al*. [224] expressed the wavelength of accelerated electrons (ignoring relativistic effects) as,

$$\lambda = \frac{h}{\sqrt{2meV_{acc}}}$$

Equation 2-28

where h refers to the Planck's constant ($h = 6.626 \times 10^{-34}\, J \cdot s$), m and e are the mass and charge of the electrons and V_{acc} is the acceleration voltage for the electrons. By means of an applied accelerating potential the electrons wavelength shrinks to short wavelengths ($e.g.$ λ~5 pm at 50 kV) able to penetrate a thin specimen (up to ~200 nm of thickness) and form a transmission electron diffraction pattern or an image with a low spatial resolution when the TEM microscope is working in diffraction or imaging modes respectively.

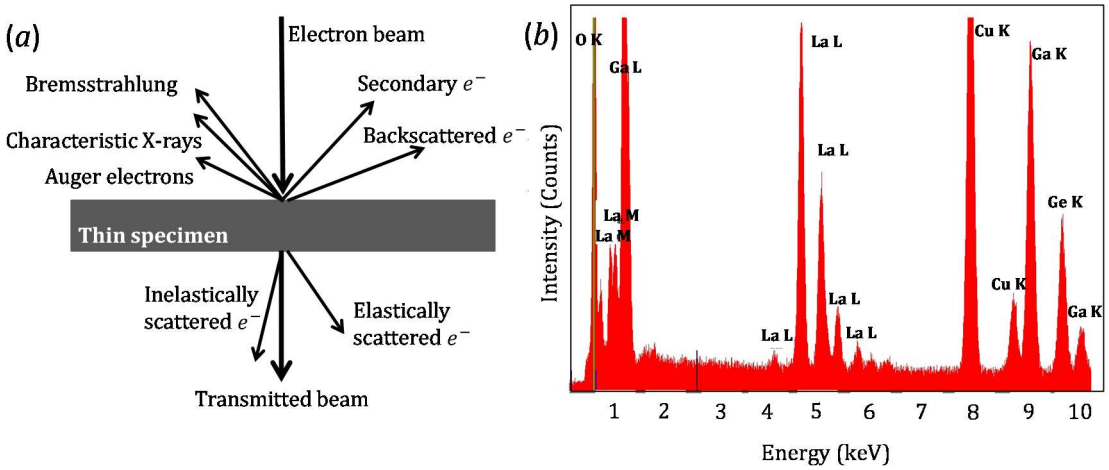

Figure 2-14 (a) Signals originated from high energy electron bombardment of a thin specimen. (b) EDX spectrum of $La_3Ga_4Ge_2O_{14.5}$, the X-ray energy in keV is given in the x-axis and the number of counts in the y-axis.

Additionally, an X-ray detector can be incorporated into TEM microscopes allowing for a quantitative analysis of the elements present within nano-sized crystallites by Energy Dispersive X-ray Spectroscopy (EDX). When an atom absorbs a quantized amount of energy, an inner-shell electron is scattered inelastically leaving an electron vacancy. Characteristic X-rays occur as a consequence of de-excitation processes in which an electron from an outer shell higher in energy fills an electron vacancy in an inner shell. During this process a phonon whose energy is characteristic of the atomic number Z of the atom is released. The emitted photons are recorded by the detector and an X-ray emission spectrum is produced. The EDX spectrum in Figure 2-14-b shows a continuum of energy,E_0, or bremsstrahlung which accounts for electrons that are accelerated towards the nucleus emitting photons with a broad range of energy and characteristic peaks of the of elements analysed. The number of X-ray photons contributing to the characteristic peak of an element A 'N_A'is given by:

$$N_A = n_A t \sigma_A \omega_A N_e$$

Equation 2-29

where n_A is the number of A atoms, t is the thickness of the sample, σ_A ionization cross section factor which depends on the type of inner shell (K, L, $etc.$), ω_A is the X-ray fluorescence factor and N_e is the number of electrons passing through the sample.

During the quantification analysis, the background is subtracted from the spectrum and additional corrections which account for absorption from a finite depth in the sample or fluorescence by other X-rays generated in the sample are applied. Additional peaks

attributed to Cu or Fe in the immediate vicinity of the sample are often visible in the recorded spectrum (see Cu K peak in Figure 2-14) are not considered in the quantification. The elements are quantified with respect to a standard whose exact composition is known beforehand. The instrument calibration was carried out by measuring the peak-intensity ratio (N_A/N_B) of a standard containing two elements A and B in a known ratio n_A/n_B. [225]

$$\frac{n_A}{n_B} = \frac{\sigma_B \omega_B}{\sigma_A \omega_A} \frac{N_A}{N_B}$$

Equation 2-30

In this thesis, the TEM work was carried out using a JEOL 2000FXII operating with a W electron source at 200 keV, and a JEOL 3010HR with a LaB_6 electron source run at 200 keV. These microscopes were operated by me with the training provided by Dr Simon Romani.

2.3.2.2 The Scanning Electron Microscope

The Scanning Electron Microscope (SEM) is formed by an electron-optical column which operates in a similar manner to the TEM column (see Figure 2-13). However, in contrast to TEM, in SEM the images are formed by scanning the surface of a bulk specimen. The primary incoming electrons are focused into an electron probe that is scanned across the bulk specimen in two perpendicular directions. A 2D image is form by collecting secondary electrons released from the solid from each point on the specimen.

SEM is a valuable technique that can provide information regarding the topography of the solid or powders under study as well as elemental analysis. In the work carried out in this thesis SEM constituted a valuable tool for a better understanding of the pellets morphology at a micron scale. A Hitachi S-4800 scanning electron microscope was used operated by Dr Marco Zanella.

2.3.3 Electrochemical Characterisation: Impedance and Modulus Spectroscopy of polycrystalline solid electrolytes

Electrochemical impedance describes the response of a circuit to an alternating current or voltage as a function of frequency. It constitutes a very powerful technique for the evaluation of the electrochemical phenomena involved in a wide range of studies such as corrosion[226], evaluation of coatings[227], electrodeposition[228] and fuel-cell diagnosis[52,229,230]. This section is referred to the study of the conductivity in solid polycrystalline samples.

The impedance (Z) can be expressed as a function of the current (I) and voltage (E) as,

$$E\ [\mathrm{V}] = \frac{I\ [\mathrm{A}]}{Z\ [\Omega]}$$

Equation 2-31

This expression is analogous to the more simplistic Ohm's law ($E = I/R$) which holds only in DC theory for an ideal resistor R, when $f = 0\ Hz$. However, impedance is a more complex phenomenon that not only takes into account the differences in amplitude of two voltage and current waveforms $E(t)$ and $I(t)$ but also their shift in time or phase. Thus, the impedance function can also be expressed as a complex number, where the aforementioned resistance R is the real component and the reactance X is the phase shifted imaginary

component which is in turn constituted by the capacitive reactance X_C and the inductive reactance X_L.

$$Z_{total} = Z' + jZ'' = R\,[\Omega] + jX[\Omega] = R + j(X_C + X_L)$$

Equation 2-32

where j is the imaginary number and indicates an anticlockwise rotation by $\pi/2$ relative to the real part of the impedance, Z'. The Euler's formula $\exp(j\phi) = cos\phi + jsin\phi$ allows us to relate the real and imaginary components of the impedance in the Argand plane which is commonly referred to as the complex impedance plane.

Typically, an AC impedance experiment consists of the application of an AC potential signal $E(t)$ with a frequency, $\nu \equiv \omega/2\pi$ into a system. As a consequence of the applied voltage, a current $I(t)$ shifted by θ with respect to $E(t)$ is generated and measured.

$$Z_{total} = \frac{E(t)}{I(t)} = \frac{E_0 \sin(\omega t)}{I_0 \sin(\omega t + \theta)}$$

Equation 2-33

In Equation 2-33, E_0 and I_0 are the amplitudes of the applied and measured signals respectively. When a small voltage is applied into the system whose amplitude 'E_0' is less than the thermal voltage, $V_T = kT/q$, where k is the Boltzmann constant, T is the absolute temperature and q is the charge of the mobile species responsible for the conductivity, the impedance Z is time independent and the system is electrically linear. In this scenario, the measured signal can be transformed from the time domain into the equivalent frequency domain by a Fourier transform.

2.3.3.1 Nyquist plot: Electrical Circuit elements

In samples of a polycrystalline nature such as the ones studied in this work, the perturbation of the lattice near the grain boundaries influences the transport processes giving rise to a differentiation on the responses observed by different regions within a sample. The different regions are usually characterized by a resistance and capacitance placed in parallel which is known as an 'RC element', whereas the use of inductors is rarely considered and there is controversy to find a physicochemical meaning to this phenomenon.

Table 2-5 Circuit element symbol and impedance equivalent

Circuit Element		Impedance
Resistor		$Z = R$
Capacitor	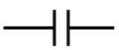	$Z = Xc\,[\Omega] = -1/j\omega[\mathrm{Hz}]C[F]$
Inductor	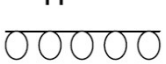	$Z = XL = j\omega L$

Each 'RC elements' associated with an arc in the complex impedance is characterized by a "time constant" or "relaxation time" τ given by:

$$\tau\,[s] = R[\Omega]C[F]$$

Equation 2-34

The relaxation time τ in Equation 2-34, relates to the relaxation frequency ω by $\omega\tau = 1$. The value of the capacitance is commonly calculated from the highest angular frequency

ω_{MAX} value of the imaginary impedance Z" at the top of a semicircle in the complex impedance plot in Figure 2-15.

$$\omega_{MAX}\,[Hz]R[\Omega]C[F] = 1$$

Equation 2-35

For a 'parallel *RC*' above a certain frequency the impedance of the capacitor becomes much smaller than that of R, effectively removing the resistor from the circuit at the lowest frequencies (rightmost of the Nyquist plot).Thus, R values can be read from the intercept with the Z' axis. From Equation 2-35 it is derived that for a full semicircle to be observed in the complex impedance plane $\omega_{max}\tau \gg 1$ must be satisfied. A common approach that allows bringing the bulk arc within the range of frequencies measured is to lower the temperature thus increasing τ.

The impedance of polycrystalline materials can be treated as layers of different thicknesses which are inverse proportionally related to the capacitance ($i.e.$ low capacitances are assigned to thick layers of bulk material and high capacitances to thinner layers such as grain boundaries, electrodes, $etc.$). Typical ranges of capacitance values associated to different phenomena have been reported by Irvine *et al*. in ref.231. Thus, the calculation of geometry corrected capacitance values, allows correlating an arc observed in the Nyquist plot to a specific region of the sample.

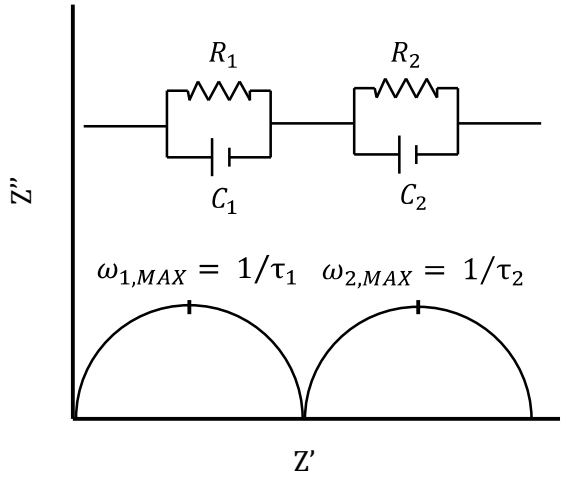

Figure 2-15 Idealized Impedance spectrum showing two clearly defined time constants τ_1 and τ_2 . The corresponding simple equivalent circuit comprising two *RC* elements 1 and 2 in series is represented on top of the arcs.

Different RC elements with well-separated time constants τ differing from one another by orders of magnitude will give rise to well-resolved semicircles in the Nyquist plot. However, polycrystalline samples usually show deviation from a perfect semicircle in the impedance plane and appeared instead as a single elongated arc[232]. These deviations could be due to numerous factors such as the closeness of the time constant between two processes, sample inhomogeneity or presence of defects. There are numerous models to fit these elongated semicircles into RC circuits. Complex Nonlinear Least Squares Fitting (NLLSF) programmes are used to fit a series of overlapped arcs observed in the complex impedance plane to equivalent circuit models which are not based in physical evidences[233,234].

2.3.3.2 Combined Impedance and Modulus Spectroscopy

In the work carried out in this thesis when complex plots for the impedance were dominated by the most resistive component the data was analysed by the combination of impedance and modulus formalism. This approach allowed us to separate the bulk component from the grain boundary contributions.

In the plot of the imaginary component of the modulus M'' and impedance Z'' vs the frequency the Debye peaks account for:

$$\mathrm{M}'' = \frac{\mathrm{C}_0}{\mathrm{C}}\left(\frac{\omega\mathrm{RC}}{1+(\omega\mathrm{RC})^2}\right)$$

Equation 2-36

$$Z'' = R\left(\frac{\omega RC}{1+(\omega RC)^2}\right)$$

Equation 2-37

where C_0 is the capacitance of a free cell given by $\mathrm{C}_0 = \varepsilon_0\mathrm{A}/\mathrm{l}$ (where $\varepsilon_0 = 8.854\ 10^{-4}\ F \cdot cm^{-1}$ is the permittivity of free space and 'A' and 'l' are the area and length of the pellet), C is the capacitance of the material, ω is the angular frequency, $\omega = 2\pi\mathrm{f}$ where f is the applied frequency in Hz. At the peak maxima where $\omega_{\mathrm{max}}\mathrm{RC} = 1$ it holds that:

$$\mathrm{M}'' = \frac{\mathrm{C}_0}{2\mathrm{C}}$$

Equation 2-38

$$\mathrm{Z}'' = \frac{\mathrm{R}}{2}$$

Equation 2-39

Based on Equation 2-38 the peak maxima at the M'' spectra is proportional to $1/C$ and the modulus plot will therefore be dominated by the thicker layers of the samples with smaller capacitances. On the other hand, at the peak maxima Z'' is proportional to the resistance R and the Z'' plot will be dominated by the most resistive component. It is then possible to differentiate the distinct components to the impedance in a polycrystalline sample by the combined use of the M'' and Z'' plots.

The relaxation time introduced in Equation 2-34 can alternatively be expressed as a function of the fundamental parameters conductivity (σ) and permittivity (ε) as $\tau = (\varepsilon_0\varepsilon'/\sigma)$. Thus, the conductivity can be expressed as a function of the frequency at the maxima of the Debye peaks in the M'' plot as:

$$\sigma = 2\pi\mathrm{f}_{\mathrm{max}}\varepsilon_0\varepsilon$$

Equation 2-40

Permittivity values frequently range from 20 to 40, and they do not show a large variation with temperature. Therefore, the position of the peaks in M'' plots is mostly correlated to the changes in conductivity.

Porosity corrections were applied to the as-measured permittivity values ε'. The Heidinger approximation[235] introduced in Equation 2-41 accounts for the porosity P correction to the measured dielectric constant ε'.

$$\varepsilon' = \varepsilon\left(1 - \frac{3P(\varepsilon - 1}{2\varepsilon + 1}\right)$$

Equation 2-41

The Heidinger model successfully describes the dependence of ε with porosity *P* values up to 0.4[236,237]. Permittivity approaches to its intrinsic value at high frequencies. Experimentally it was observed that the measured values of the permittivity were constant at $10^{-2} \times 10^{6}$ Hz. The intrinsic permittivity ε' used in our calculations were measured at room temperature under dry conditions at ~10^{5} Hz, close to the limit frequency of 2 MHz delimited by the Agilent E4980 LCR meter capacity.

2.3.3.3 The experiment

2.3.3.3.1 Sample preparation

In order to relate the calculated resistance to the conductivity of the sample the dimensions of the sample need to be considered. For a given sample of a length l and a surface area A, the conductivity σ is given by:

$$\sigma\ [S \cdot cm^{-1}] = \frac{l[cm]}{R[\Omega]A\ [cm^2]}$$

Equation 2-42

High density pellets with parallel faces with uniform 1-2 mm thickness were prepared. Commercially available noble metal pastes were painted on the sides of these dense pellets to perform as electrodes. Given the range of temperatures (350-950 °C) studied in this thesis gold was used as this metal performs well at such high temperatures. Furthermore, this material was found to be chemically inert avoiding undesired processes in the system such as the charge-transfer and polarisation at the electrode-electrolyte interface. Gold wires are attached *via* the noble metal paste and wrapped around platinum wires in the measurement rig.

Two impedance analysers were used for the work carried out in this thesis: an Agilent E4980 LCR meter over the 20 Hz - 2 MHz frequency range using 300 mV perturbation voltage and a Solartron 1255B Frequency response analyser coupled to a Solartron 1287 electrochemical interface and a 1296 Dielectric + FRA equipment over the 100 mHz - 1 MHz frequency range, also using a 300 mV perturbation voltage.

2.3.3.3.2 Variable pO_2

The study of the pO_2-dependence with the conductivity allows us to confirm that the oxide ions are responsible for the conductivity and the electronic contribution to the conductivity is negligible ($i.e.\ \sigma_{ionic} \gg \sigma_{electronic}$)[238].

In this work, samples were evaluated as a function of pO_2 at a constant temperature. These experiments were carried out in a tube furnace where the oxygen partial pressure is controlled by mixing Ar, O_2, CO and CO_2 in different ratios. Ar/O_2 (for high pO_2 range) and CO/CO_2 (for low pO_2 range). This CO_2/CO equilibrium allows for changes in pO_2 as:

$$CO + \frac{1}{2}\ O_2 \rightleftarrows\ CO_2$$

Equation 2-43

For which:

$$\Delta G° = -RT \ln\left(\frac{pCO_2}{pCO\sqrt{pO_2}}\right)$$

Equation 2-44

Where $\Delta G°$ represents the standard Gibbs energy changes, R is the gas constant and T is the temperature in K. The isolation of pO_2 in the above equation leads to the final expression of pO_2 as a function of the CO/CO_2 ratio which is monitored by a 617 programmable electrometer, $\Delta G°$ and T:

$$pO_2 = \left(\frac{pCO_2}{pCO}\right)^2 \frac{1}{e^{-2\Delta G°/RT}}$$

Equation 2-45

where

$$\Delta G°[J] = -282{,}400 + 86.81T$$

Equation 2-46

The sample was allowed to equilibrate (sometimes for several hours) between each set of measurements before proceeding with the reading of a value. It should be noted that a higher dwelling time was required to stabilize the sample at lower oxygen partial pressures. Moreover, reversibility tests were performed after the measurements at the lowest pO_2studied.

The measured conductivities were plotted as a function of pO_2 where the ionic conductivity can be identified as the pO_2-independent conductivity. Ionic conductivity is defined as:

$$\sigma_{ionic} = Zq_i \frac{\mu_0}{T} e^{-E_a/kT}$$

Equation 2-47

where Z is the amount of charge carried by the ionic species with a charge q, concentration C_i and ionic mobility μ, and E_a is the activation energy for the ionic migration. The activation energy can be extracted from the temperature dependence with the conductivity in the Arrhenius plot. If $\log\sigma_{ionic}T$ is plotted as function of $1/T$, E_a can be calculated equating the slope of the plot to $-E_a/(kl\,n(10))$.

3 EXPLORATION OF SYNTHETIC ROUTES TO INTERSTITIAL OXIDE IN $La_3Ga_5MO_{14}$ LANGASITES M=Si, Ge, Ti, Sn, Hf AND Zr

This chapter introduces the synthetic work comprising the doping of $La_3Ga_5MO_{14}$ where M = Si, Ti, Ge, Zr, Sn and Hf with a langasite structure. Different doping approaches were carried out all consisting of substituting a host cation by one of similar size and a higher valence so as to incorporate interstitial oxide ions. Various dopants were selected for substituting La, Ga and M host cations on the different sites: Ce^{4+} for La^{3+} on the A site Nb^{5+}, Ta^{5+}, Mo^{6+} and W^{6+} were used as dopants in the B octahedral site and lastly the substitution of M^{4+} for Ga^{3+} on the B, C and D sites was attempted. Conductivity measurements were carried out on those $La_3Ga_5MO_{14}$-based systems incorporating extra oxygen. $La_3Ga_{5-x}Ge_{1+x}O_{14+x/2}$ was identified as the most promising candidate system showing the greatest improvement in conductivity ($\sim 4 \times 10^{-3}$ S·cm^{-1} for $x = 0.3$ at 700 °C) with respect to the parent $La_3Ga_5O_{14}$ material ($\sim 1 \times 10^{-5}$·S cm^{-1} at 700 °C). Moreover, $La_3Ga_{5-x}Ge_{1+x}O_{14+x/2}$ has shown a remarkable flexibility for the accommodation of extra oxygen evidenced by the incorporation of 5.36 % of extra oxygen in $La_3Ga_{3.5}Ge_{2.5}O_{14.75}$. Such an extent of the solid solution was achieved by the careful tuning of the reaction conditions *via* Pechini's route.

All the syntheses and analyses presented in this chapter are my original work, with the exception of the synthesis and conductivity measurements in $La_{3-x}Ce_{1+x}Ga_5SiO_{14+x/2}$ that were carried out by Dr Maria Tsiamtsouri.

3.1 Target materials

In sections 3.3.2.1-3.3.2.3 the exploratory work carried out on each doping mechanism is individually discussed. The doping strategies involve the substitution of a host lattice cation by a dopant with a higher valence and a similar size to that of the host cation (see Table 3-1).

Table 3-1 Coordination, charge and ionic radius of the host (M) and dopant (M') cations on sections 0-0.

Section	System	Site	Coordination	Host		Dopant	
				Charge	Ionic radius (Å)	Charge	Ionic radius (Å)
3.3.2.1	$La_{3-x}Ce_xGa_5MO_{14+x/2}$	A	VIII	La^{3+}	1.032	Ce^{4+}	0.97
3.3.2.2	$La_3Ga_5M_{1-x}M'^{5+}_xO_{14+x/2}$ and $La_3Ga_5M_{1-x}M'^{6+}_xO_{14+x}$	B	VI	Ge^{4+}	0.39	Nb^{5+}	0.64
						Ta^{5+}	0.64
						Mo^{6+}	0.59
						W^{6+}	0.6
3.3.2.3	$La_3Ga_{5-x}M'_{1+x}MO_{14+x/2}$	B/D	VI/IV	Ga^{3+}	0.62/0.47	Si^{4+}	0.54/0.4
						Ge^{4+}	0.53/0.39
						Ti^{4+}	0.605/0.42
						Zr^{4+}	0.72/0.59
						Sn^{4+}	0.75/0.55
						Hf^{4+}	0.58/0.71

Ionic radii are taken from ref. 239.

3.2 Experimental Methods

3.2.1 Synthesis

The exploratory synthesis of doped $La_3Ga_5MO_{14}$ were carried out by the traditional solid-state reaction method involving the mixing of stoichiometric amounts of the binary oxides used as starting materials as follows: lanthanum (III) oxide (Alfa Aesar, Reacton 99.99 %), cerium (IV) oxide (Alfa Aesar, 99.9 %), niobium (V) oxide (Sigma Aldrich, 99.99 %), tantalum (V) oxide (Sigma Aldrich, 99.99 %), molybdenum (VI) oxide, tungsten (VI) oxide, gallium (III), oxide (Alfa Aesar, 99.99 %), silicon (IV) oxide (Alfa Aesar, 99.9 %), germanium (IV) oxide (Sigma Aldrich, 99.99 %), titanium (IV) oxide Alfa Aesar, 99.9 %), zirconium (IV) oxide (Sigma Aldrich, 99 %), tin (IV) oxide (Alfa Aesar, 99.9 %) and hafnium (IV) oxide (Alfa Aesar, 99 %).

The aforementioned precursors were thoroughly combined by manual grinding in an agate mortar until a well-mixed fine powder was obtained. Afterwards, the samples were annealed in alumina crucibles at high temperatures ranging from 1200 to 1400 °C in suitable furnaces. The heating programmes typically involved heating and cooling cycles at a rate of 3 ° min^{-1} and dwell times of 12 hours. Repeated cycles of grinding and calcination were avoided due to Ga (and Ge) volatility concerns in these systems. Alternative ways to achieve phase purity such as the decrease in particle size by means of mechanical milling of the precursor or an alternative solution based Pechini approach were carried out for promising systems: $La_3Ga_{5-x}Ge_{1+x}O_{14+x/2}$, $La_3Ga_{5-x}Ti_xSiO_{14+x/2}$, $La_3Ga_{5-x}Ti_xGeO_{14+x/2}$ and $La_3Ga_{5-x}Sn_xTiO_{14+x/2}$ introduced in sections 3.3.2.3.1.1-3.3.2.3.1.4. The mechanical milling sets consisted of combining 3-6 g of powdered material with eight ø = 10 mm sized balls of

zirconia in a ø = 40 mm zirconia pot at the rotation speed of 350 rpm for 15 cycles operating with direction reversal and a 10 min pause time after each 15 min cycle.

Additionally, $La_{3-x}Ce_xGa_5GeO_{14+x/2}$, $La_3Ga_5Ge_{1-x}Ta_xO_{14+x/2}$, $La_3Ga_5Ge_{1-x}M'^{6+}{}_xO_{14+x}$ where M'^{6+} = Mo and W, $La_3Ga_{5-x}Ti_xGeO_{14+x/2}$ and $La_3Ga_{5-x}Ge_{1+x}O_{14+x/2}$ were further explored by the Pechini method. This alternative reaction route comprised the mixing in an aqueous media of stoichiometric amounts of lanthanum (III) nitrate (Alfa Aesar, 99.99 %), a pre-made solution of ammonium cerium (IV) nitrate (Sigma Aldrich, ACS ≥ 98.5 %) whose exact cerium (IV) concentration was evaluated beforehand by means of ICP elemental analysis, gallium (III) (Alfa Aesar Puratronic 99.999 %) nitrate, ammonium molybdate (Alfa Aesar, 99.99 %), ammonium (para)tungstate hydrate (Sigma-Aldrich, 99.99 %) and both a commercial Ta-oxalate solution (H.C. Strack) and a solution made from tantalum (V) chloride (Alfa Aesar, 99.8 %) following the procedure reported in ref.240 were used as precursors of tantalum, a commercial solution of titanium (IV) bis(ammonium lactacto) dihydroxide (Sigma-Aldrich) and germanium (IV) oxide (Sigma-Aldrich ≥ 99.99 %). The reactant solution was later combined with equimolar quantities of citric acid as a chelating agent and ethylene glycol. The solution was left to polymerize for 15 hours at 175 °C in a hot plate until dry. The resulting gel was afterwards calcined at 600 °C for 60 hours and the amorphous mixture of reactants were thereafter separated into different batches, pressed into pellets and fired at the various synthetic temperatures explored for 12 hours.

The actual compositions of the synthesized samples were determined by Energy Dispersive X-ray analysis (EDX) in a JEOL FX2000 and a JEOL 3010 Transmission Electron Microscopes (TEM) operated at 200 kV.

3.2.2 XRD, SXRD and NPD

The X-ray powder diffraction patterns were collected in a PANalytical X'pert Pro diffractometer with a Co-source ($K_{\alpha1,Co} = 1.7890$ Å) and in a Bruker D8 Discovery diffractometer with a Cu-source ($K_{\alpha1,Cu} = 1.5406$ Å). Synchrotron X-ray powder diffraction data (SXRD) was collected in $La_3Ga_5TiO_{14}$ and $La_3Ga_5SiO_{14}$ specimens at the BL01C2 beamline at the NSRRC (Taiwan) at a wavelength of 0.56357 Å over a 2θ range from 3.5 to 42° at 297 K. High resolution powder neutron diffraction data was collected in $La_3Ga_5GeO_{14}$ in HRPD at ISIS (UK) also at room temperature. Rietveld refinement and Pawley fittings of the synthesized phases were performed with TOPAS[200].

3.2.3 Conductivity determination

Dense pellets of the following compositions were prepared for AC impedance measurements: $La_{2.5}Ce_{0.5}Ga_5SiO_{14.25}$, $La_3Ga_{4.7}Ge_{1.3}O_{14.15}$, $La_3Ga_{4.7}Ti_{0.3}SiO_{14.15}$ and $La_3Ga_{4.8}Sn_{0.3}Ti_{0.9}O_{14.1}$. As well as the parent materials: $La_3Ga_5GeO_{14}$, $La_3Ga_5SiO_{14}$ and $La_3Ga_5TiO_{14}$. The sintering protocol involved CIPing the pre-reacted powders at 200 MPa followed by a prolonged 12 hours sintering at 1250-1350 °C and slow cooling to room temperature at a rate of 1 ° min^{-1}. This procedure yield ceramic discs with ρ ≥ 90 % of their theoretical density. The pellets were painted with gold paste acting as electrodes and then cured in a furnace at 600 °C for 3 hours.

AC impedance Spectroscopy analyses were performed in air under ambient pressure in a Solartron 1255B Frequency Response Analyser coupled to a Solartron 1296 dielectric interface at a temperature range 600-1000 °C from 0.01 Hz to 1 MHz while applying a perturbation voltage of 300 mV.

3.3 Results and Discussion

3.3.1 Cation Distribution of $La_3Ga_5M^{4+}O_{14}$ (M = Si, Ti, Ge, Zr, Sn, and Hf

The site preference as a function of the M^{4+} cationic size in $La_3Ga_5M^{4+}O_{14}$ where M^{4+} = Si, Ti, Ge, Zr, Sn and Hf is reported by Takeda *et al*. in ref.241 , as determined by a site-multiplicity Rietveld refinement of powder X-ray diffraction data on $La_3Ga_5MO_{14}$ polycrystalline samples synthesized by the solid-state reaction method at high temperatures. Herein, a study of $La_3Ga_5MO_{14}$ with M = Si, Ti and Ge is presented, analogous to the one in ref.241. $La_3Ga_5MO_{14}$ compositions with M = Sn, Hf and Zr did not form phase pure samples and a small amount of pyrochlore phase $La_2M_2O_7$ (~1-3 % in mass) was observed. The coexistence of langasite as a main phase with a $La_2M_2O_7$ impurity in M = Sn, Hf and Zr samples was also observed in ref.241. Due to the difficulties in achieving phase pure $La_3Ga_5MO_{14}$ with M = Sn, Hf and Zr, only the Rietveld refined PXRD data for $La_3Ga_5MO_{14}$ with M =,Si, Ge and Ti are presented here. The data for $La_3Ga_5MO_{14}$ with M = Sn, Hf and Zr in Figure 3-2 is taken from ref. 241.

Synchrotron data of $La_3Ga_5GaSiO_{14}$ and $La_3Ga_5TiO_{14}$ was refined in a $P321$ space group using the models from ref.241 as the starting point of the refinements. Symmetry allowed atomic positions, lattice parameters, zero shift and scale factors were refined initially. Due to the fact that refined U_{ij} cation thermal parameters were spherical they were reverted to B_{eq}. The total occupancies of the B, C and D sites were enforced to add up to 1 and the relative occupancies of M^{4+}/Ga on these sites were refined.

The peak profile was refined with a pseudo-Voigt function giving a good fit of the peaks (see Figure 3-1). The background was refined with a Chebysev function using twelve polynomials which adds up to 39 variables refined in each data set. The refined compositions in the final model were $La_3Ga_{5.07(2)}Ti_{0.93(2)}O_{14}$ and $La_3Ga_{5.02(1)}Si_{0.98(1)}O_{14}$ which are in good agreement with their nominal composition. The fitting errors and visual fit of the refinements are introduced in Table 3-2 and Figure 3-1. Additionally a table with the refined atomic positions is given in Appendix 2. The refinement of the $La_3Ga_5GeO_{14}$ NPD data is introduced in detail in chapter 4 along with $La_3Ga_4Ge_2O_{14.5}$ and $La_3Ga_{3.5}Ge_{2.5}O_{14.75}$ doped compositions. Therefore the refinement steps in $La_3Ga_5GeO_{14}$ are omitted in this section to avoid repetition.

Table 3-2 Fitting errors of the Rietveld refined $La_3Ga_5MO_{14}$ with M = Si and Ti SXRD data.

	$La_3Ga_5SiO_{14}$	**$La_3Ga_5TiO_{14}$**
R_{wp}	6.102	6.926
$S = R_{wp}/R_{exp}$	1.477	1.183

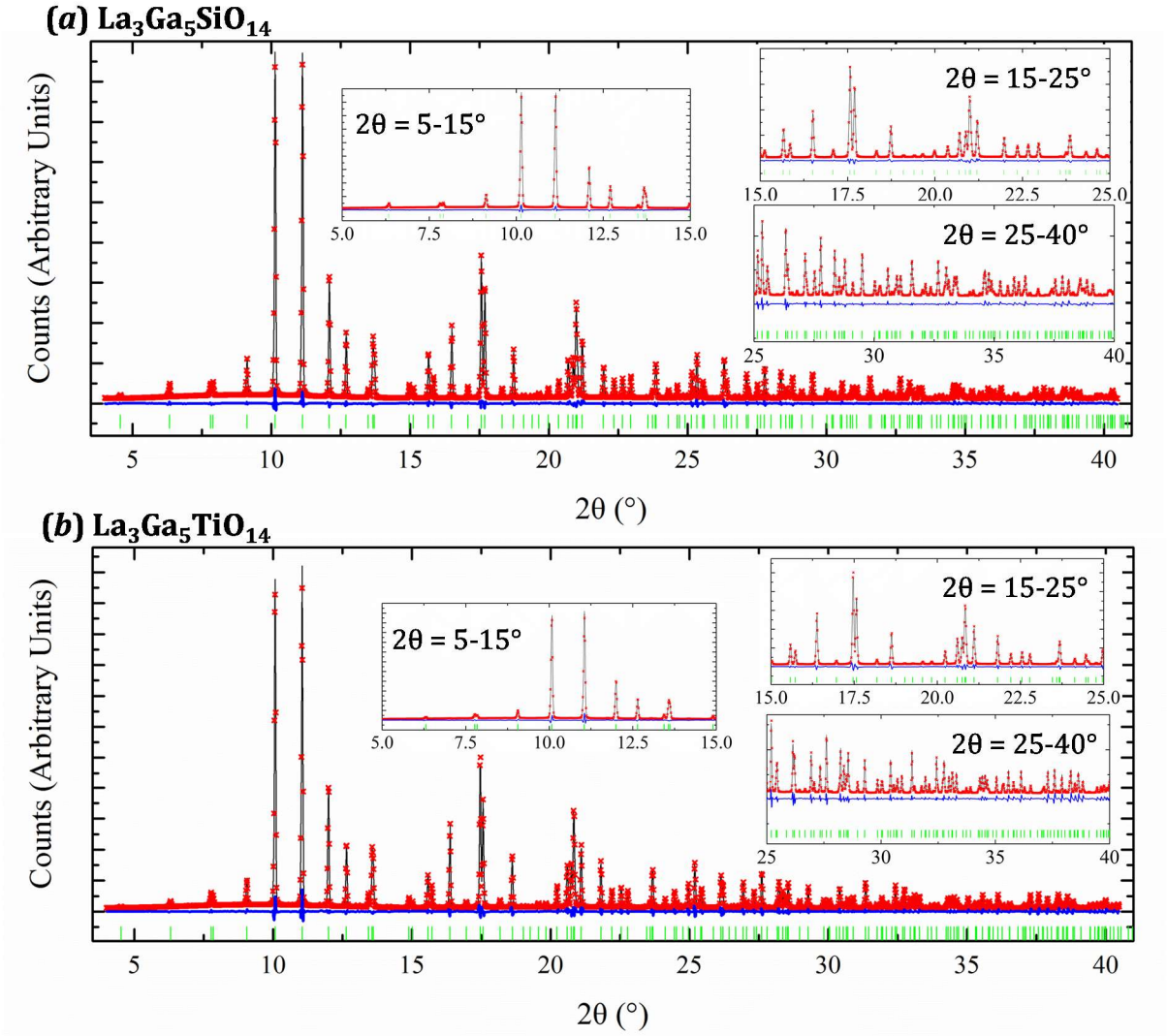

Figure 3-1 SXRD refinement of $La_3Ga_5SiO_{14}$ (*a*) and $La_3Ga_5TiO_{14}$ (*b*). The red crosses indicate the observed data, the black solid line the calculated model, the blue horizontal line the difference between the two and the vertical green lines the position of the Bragg peaks.

The analysis of the refined atomic parameters as a function of the M^{4+} cation size (see Appendix 2 for the refined atomic parameters in $La_3Ga_5MO_{14}$ M = Si and Ti and page 88 for $La_3Ga_5GeO_{14}$) revealed that smaller cations such as Si and Ge (ionic radii for 4-coordinated Si^{4+} and Ge^{4+} are 0.26 Å and 0.39 Å respectively[239]) were found to have a disordered structure with a mixture of Ga and Si/Ge on the smaller tetrahedral D site. Since Ga^{3+} and Ge^{4+} have the same number of electrons, they are indistinguishable by X-ray diffraction techniques and the proposed cation site distribution in $La_3Ga_5GeO_{14}$ was made based on calculated bond valence sums (BVS). Amongst the calculated BVS for B, C and D sites the highest $BVS_{Ge} = 3.4$ corresponded to the smaller tetrahedral D (2d) site and its occupancy was therefore fixed to ½ of Ga and Ge. The site occupancy for Ga and Ge in $La_3Ga_5GeO_{14}$ will be further discussed later on in this thesis in Chapter 4. Larger Ti^{4+} shows a disordered structure with Ti partly occupying the octahedral B and tetrahedral C sites, which is in good agreement with ref.241. The even larger Sn, Hf and Zr cations were found to occupy solely the octahedral B site, thus constituting ordered structures[242].

A summary table with the site preferences, and structural distortions calculated from the SXRD $La_3Ga_5SiO_{14}$ and $La_3Ga_5TiO_{14}$ data and the NPD refined $La_3Ga_5GeO_{14}$ model was constructed in Table 3-3.

Table 3-3 Summary of the refined lattice constants, site preferences and structural distortion of $La_3Ga_5MO_{14}$ with M = Si, Ge and Ti for comparison with the values reported by Takeda *et al*.

M^{4+}	**Si**	**Ge**	**Ti**
Ionic radii[239] (Å) r^{IV} / r^{VI},*	0.26/0.4	0.39/0.53	0.42/0.605
a (Å)	8.17733(3)	8.20886(2)	8.23718(4)
c (Å)	5.09799(3)	5.10535(2)	5.11713(4)
V (Å^3)	295.225(3)	297.935(2)	300.687(4)
Density (g/cm^3)	5.725(5)	5.909(3)	5.735(8)
Site preference:			
B(1a)	Ga	Ga	0.31(3)Ga+0.69(3)Ti
C(3f)	Ga	Ga	0.92(2)Ga+0.08(2)Ti
D(2d)	0.51(1)Ga+0.49(1) Si	0.5Ga+0.5 Ge	Ga
Mean ($\overline{\boldsymbol{M-O}}$) distances (Å):			
$(\overline{A-O})$, D_8	2.610	2.598	2.603
$(\overline{B-O})$, D_6	1.996	1.992	1.991
$(\overline{C-O})$, D_4	1.854	1.845	1.862
$(\overline{D-O})$, D_4,	1.706	1.804	1.809
Distortion, Δ (magnified by 10^4):			
A site	56	51	53
C	20	14	2.9
D	6.3	1.1	4.2

* r^{IV} and r^{VI} for Ga^{3+} are 0.47 and 0.62 Å respectively[239].

The distortion 'Δ'[243] introduced in Table 3-3 is a dimensionless parameter which accounts for the mean relative deviation to the average bond lengths and is calculated as:

$$\Delta = \frac{1}{N}\sum_{i=1}^{N}\left(\frac{R_i - \bar{R}}{\bar{R}}\right)^2$$

Equation 3-1

where N is the coordination number of the given site, R_i account for the individual $M-O$ lengths and $\bar{R}$ is the mean $\overline{M-O}$ value in Å. Note that distortions for the octahedral B site are not given in Table 3-1 as they equal to zero since all the $M-O$ distances in the coordination sphere of B are identical.

To further evaluate the dependence of the $M-O$ distances in $La_3Ga_5MO_{14}$ as a function of the M cation size the calculated and reported values in ref. 242 were plotted against the effective M^{4+} radii in Figure 3-2. This graph shows a good agreement between these two sets of values.

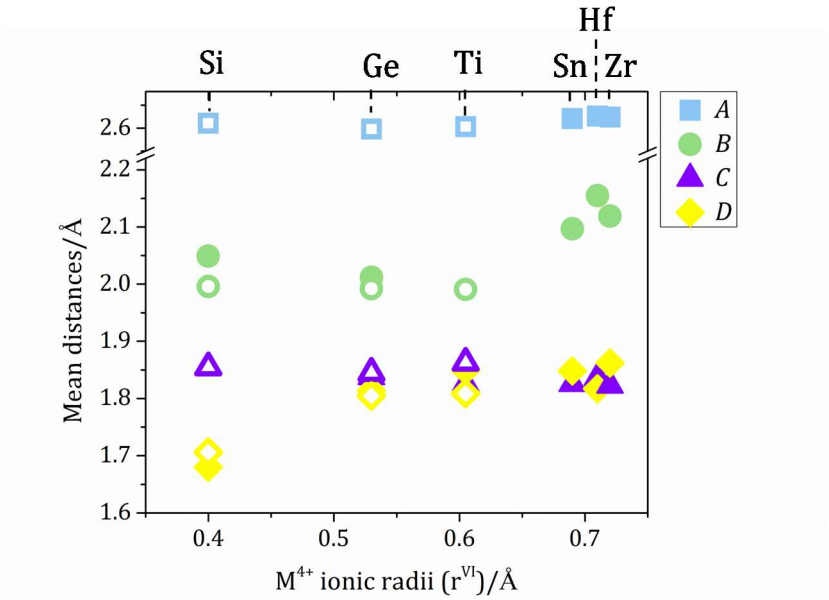

Figure 3-2 Dependence of the mean $\overline{M-O}$ distances with the cation size in $La_3Ga_5MO_{14}$ by Takeda *et al.* (filled-symbols) and in this study (open symbols). The reported and calculated $\overline{A-O}$ and $\overline{C-O}$ distances in $La_3Ga_5MO_{14}$ with M^{4+} Si-Ti are overlapping with each other.

From the inspection of Figure 3-2 it can be concluded that the size of the M cation in $La_3Ga_5MO_{14}$ affects the octahedral B and tetrahedral D sites showing a greater variation in their relative distances with respect to $La_3Ga_5SiO_{14}$ of 15 and 12 % respectively. The effect of the M cations in the mean distances is more tenuous in the tetrahedral C site and the 8-coordinated A site with a ~1 and 2 % variation respectively.

3.3.2 Synthetic Outcomes

3.3.2.1 A-site doping: $La_{3-x}Ce_{1+x}Ga_5MO_{14+x/2}$

The substitution of Ce^{4+} for La^{3+} on the A site in $La_{3-x}Ce_{1+x}Ga_5MO_{14+x/2}$ was attempted in systems for which M^{4+} = Si, Ge, Ti and Sn. The reaction mixtures for several x values (0.1, 0.25 and 0.5) were prepared by the solid-state reaction method and separated into different batches that were calcined at different temperatures given in Table 3-4. Repeated cycles involving calcination and intermediate grinding of the reaction mixture were carried until reaction completion was achieved, as determined by XRD. The outcomes obtained at each temperature studied are also given in Table 3-4.

No incorporation of cerium (IV) was observed in $La_{3-x}Ce_{1+x}Ga_5MO_{14+x/2}$ with M = Ge, Ti and Sn. The PXRD patterns of these systems show the formation of the parent $La_3Ga_5MO_{14}$ langasite and unreacted cerium (IV) oxide.

For M = Si^{4+}, the incorporation of cerium into the A site was found succesful for $0 \leq x \leq 0.5$. The synthetic conditions leading to the succesful doping of cerium involved three calcination cycles with intermediate grinding. The sintering temperatures at each calcination cycle were increased from 1200 °C in fifty degrees steps up to 1300 °C in the final cycle that yield phase purity.

Table 3-4 Synthetic conditions and phases obtained for $La_{3-x}Ce_{1+x}Ga_5MO_{14+x/2}$ with M = Si, Ge, Ti and Sn.

	Nominal compositions (x = 0.1, 0.25 and 0.5)	Synthetic Temperature (°C)	Phases formed
Disordered	$La_{3-x}Ce_xGa_5SiO_{14+x/2}$	1200-1300	$La_{3-x}Ce_xGa_5SiGeO_{14+\delta}$ up to x=0.5, CeO_2, SiO_2 and $LaGaO_3$
	$La_{3-x}Ce_xGa_5GeO_{14+x/2}$	800-1200	$La_3Ga_5TiO_{14}$ + CeO_2 ($Fm\bar{3}m$) + $LaGaO_3$
	$La_{3-x}Ce_xGa_5TiO_{14+x/2}$	1300-1400 (T_m~1400)	$La_3Ga_5TiO_{14}$ + CeO_2 ($Fm\bar{3}m$) + TiO_2 ($C2/m$)
Ordered	$La_{3-x}Ce_xGa_5SnO_{14+x/2}$	1300-1400	$La_3Ga_5SnO_{14}$ + CeO_2 ($Fm\bar{3}m$) + $La_2Sn_2O_7$

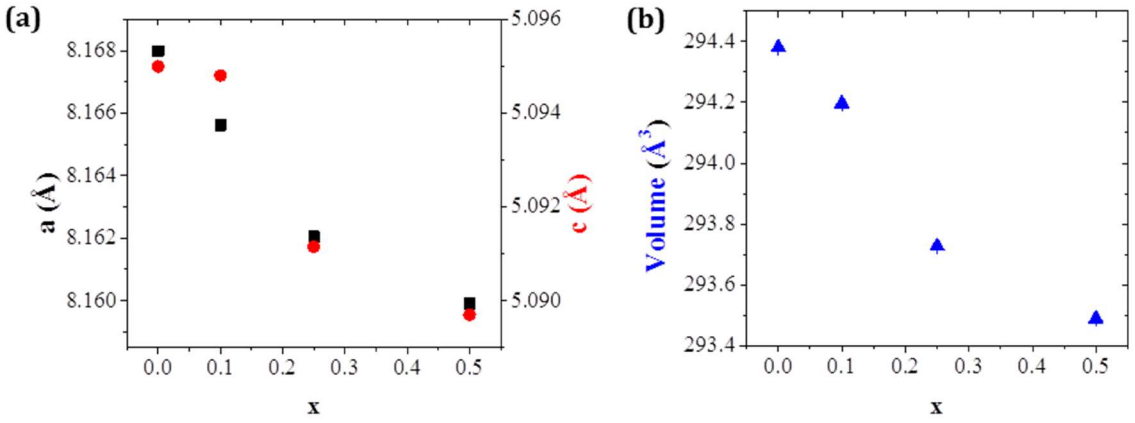

Figure 3-3 Evolution of the *a* and *c* lattice parameters (*a*) and cell volume (*b*) as a function of '*x*' in $La_{3-x}Ce_xGa_5SiO_{14+\delta}$. *a* lattice parameter is represented as red circles and black squares are used for *c* in (*a*). In (*c*), blue triangles are used to designate cells' volumes. The errors of each value as 1 × e.s.d are frequently lying behind the symbols.

Upon doping, a slight decrease in the cell volume of ~0.9 Å^3 was observed from 294.380(6) Å^3 in $La_3Ga_5SiO_{14}$ to 293.49(1) Å^3 in $La_{2.5}Ce_{0.5}Ga_5SiO_{14+\delta}$. Such a subtle change in the volume suggests a change in the oxidation state of the dopant incorporated from Ce^{4+} to Ce^{3+} with a larger ionic radii (the ionic radii for these cations are: $r_{Ce^{4+},VIII}$ = 0.97 Å and $r_{Ce^{3+},VIII}$ = 1.143 Å)[239]. Comparable results were observed in isovalent substitutions of La^{3+} by Nd^{3+} is discussed later on in this thesis in section 5.2.1.1 (see page 124). The substitution of 17 % of La^{3+} by Nd^{3+} in $La_{2.5}Nd_{0.5}Ga_4Ge_2O_{14.5}$ entails a decrease of ~1.9 Å^3 of the volume of the cell from 297.35(7) in $La_3Ga_4Ge_2O_{14.5}$ to 295.50(3) Å^3 (with $r_{Nd^{3+},VIII}$ = 1.109 Å,[239] having a similar ionic radii to that of Ce^{3+}, VIII)[239].

3.3.2.2 B-site doping: $La_3Ga_5M_{1-x}(Nb/Ta)_xO_{14+x/2}$ and $La_3Ga_5M_{1-x}(Mo/W)_xO_{14+x}$

The syntheses carried out in this section 3.3.2.2 aimed at the introduction of extra interstitial oxide ions in $La_3Ga_5GeO_{14}$ by the substitution of Ge^{4+} for Ta^{5+}, Mo^{6+} and W^{6+}. These syntheses were approached by Pechini in order to avoid the formation of $LaNbO_4$ and $LaTaO_4$ impurities, which are favoured by high temperatures (~1300 °C) demanded by the solid-state reaction method. The Pechini method was found to lower the temperature for the formation of the langasite phase, which was now observed at 800 °C. However, M^{5+} and M^{6+} impurity containing phases were present in the product of the reaction with still no

evidence of dopant incorporation into the langasite structure (*i.e.* there was no change in the lattice parameters of the main langasite phase after repeated firings as determined by Pawley fitting of the XRD data).

Table 3-5 Synthetic conditions and phases obtained for the B site doping approaches attempted in $La_3Ga_5GeO_{14}$.

Nominal compositions studied (x = 0.1, 0.25 and 0.5)		Synthetic Temperature (°C)	Phases formed
$La_3Ga_5Ge_{1-x}M'^{5+}_xO_{14+x/2}$	M' = Ta^{5+}	800-1300	$La_3Ga_5GeO_{14}$ + $La_3Ga_{5.5}Ta_{0.5}O_{14}$
	M' = Nb^{5+}	1200-1300	$La_3Ga_5GeO_{14}$ + $La_3Ga_{5.5}Nb_{0.5}O_{14}$
$La_3Ga_5Ge_{1-x}M'^{6+}_xO_{14+x}$	M' = Mo^{6+}	800-1300	$La_3Ga_5GeO_{14}$ + $La_2Mo_2O_9$
	M' = W^{6+}	800-1300	$La_3Ga_5GO_{14}$ + La_2GeO_4 + Ga_2O_3 + WO_3

3.3.2.3 B, C, D-sites doping $La_3Ga_{5-x}M'^{4+}_xMO_{14+x/2}$

The synthetic exploration of $La_3Ga_{5-x}M'^{4+}_xMO_{14+x/2}$ constitutes the most extensive approach undertaken with a total of 27 different compositions analysed. These studies reveal that a modest amount of interstitial oxide ions can be introduced in langasites where M cations have a smaller size comparable to that of Ga (*i.e.* Si, Ge and Ti). The outcomes of several explorations carried out by the solid-state reaction method at high temperatures ranging from 1250-1350 °C are summarized in Table 3-6 where each $La_3Ga_{5-x}M'^{4+}_xMO_{14+x/2}$ is categorized as '×', '*i*' or '✓' whose meaning is explained below.

Table 3-6 Chart showing the outcome of the preliminary exploratory synthesis for $La_3Ga_{5-x}M'^{4+}_xMO_{14+x/2}$ where '×' = $La_3Ga_5MO_{14}$ + impurities, '*i*' = $La_3Ga_5M_{1-x}M'_xO_{14}$ + impurities and '✓' = $La_3Ga_{5-x}M'_xMO_{14+x/2}$.

		Host $La_3Ga_5MO_{14}$ langasites targeted for doping					
		Disordered			Ordered		
	M'⁴⁺\M⁴⁺	Si	Ge	Ti	Sn	Hf	Zr
Dopant M'⁴⁺	Si	×	i	i	i	i	i
	Ge	i	✓	i	i	i	i
	Ti	✓	✓	×	i	i	i
	Sn	i	×	✓			
	Hf	i	i	i			
	Zr	i	i	i			

In Table 3-6, the red crosses '×' account for systems in which the host $La_3Ga_5MO_{14}$ langasite did not show a change in the lattice parameters after tests involving various temperatures and several annealing cycles with intermediate re-grinding of the powders. These resulted in a mixture of the parent $La_3Ga_5MO_{14}$ langasites and other impurity phases identified by PXRD. The '×' systems are as follows: $La_3Ga_{5-x}Si_{1+x}O_{14+x/2}$, $La_3Ga_{5-x}Ti_{1+x}O_{14+x/2}$, $La_3Ga_{5-x}Sn_xGeO_{14+x/2}$. This unsuccessful group of attempted compositions constitutes the smallest group in number amongst the three categories that the exploratory synthesis outcomes were classified in. For most of the systems studied, there was indeed a change in the lattice parameters of the host langasite targeted for doping whether it was the case that the M'^{4+} dopant was incorporated into the host structure by the substitution of Ga^{3+} as desired or by the substitution of the isovalent host M^{4+} cation.

The '*i*' symbol account for this later group in which instead of the formation of langasite phases incorporating extra oxygen with the given formula $La_3Ga_{5-x}M'^{4+}{}_xMO_{14+x/2}$ a series of $La_3Ga_5M_{1-x}M'_xO_{14}$ compositions were obtained. In $La_3Ga_5M_{1-x}M'_xO_{14}$, the M'^{4+} dopant is substituting the isovalent M^{4+} cation instead of Ga^{3+} and no extra oxygen is incorporated into the structure as a result. The synthetic conditions and phases formed in this '*i*' category are listed in Table 3-7.

Table 3-7 Summary of the outcome and synthetic conditions attempted for various systems with $La_3Ga_{5-x}M'_xMO_{14+x/2}$ targeted nominal compositions resulting in the formation of $La_3Ga_5M_{1-x}M'_xO_{14}$: '*i*'

	Synthetic Nominal Composition (where x = 0 – 0.75)	Synthetic Conditions (°C)	Phases formed
Disorderred $La_3Ga_5MO_{14}$ langasites where M = Si, Ge or Ti	$La_3Ga_{5-x}Si_xGeO_{14+x/2}$	1000 - 1350	$La_3Ga_5Ge_{1-x}Si_xO_{14}$ + $LaGa_{0.75}Ge_{0.93}O_{4.485}$
	$La_3Ga_{5-x}Si_xTiO_{14+x/2}$	1200-1300	$La3Ga5Ti_{1-x}Si_xO_{14}$ + $La_2Ti_2O_7$
	$La_3Ga_{5-x}Ge_xSiO_{14+x/2}$	1200-1350	$La_3Ga_5Si_{1-x}Ge_xO_{14}$ + $La_2Si_2O_7$+ SiO_2
	$La_3Ga_{5-x}Ge_xTiO_{14+x/2}$	1200-1350	$La_3Ga_5Ti_{1-x}Ge_xO_{14}$ + $La_2Ti_{2-x}Ge_xO_7$
	$La_3Ga_{5-x}Sn_xSiO_{14+x/2}$	1200-1350	$La_3Ga_5Si_{1-x}Sn_xO_{14}$ +SiO_2
	$La_3Ga_{5-x}M'_xMO_{14+x/2}$ for M'=Hf or Zr and M = Si, Ge or Ti	1000-1350	$La_3Ga_5M_{1-x}M'_xO_{14}$ + $La_2M'_{2-x}M_xO_7$
Ordered $La_3Ga_5MO_{14}$ where M = Sn, Hf or Zr	$La_3Ga_{5-x}M'_xMO_{14+x/2}$ for M' = Si, Ge or Ti and M = Sn, Hf or Zr	1000-1350	$La_3Ga_5M_{1-x}M'_xO_{14}$ + $La_2M_{2-x}M'_xO_7$
	$La_3Ga_{5-x}M_{1+x}O_{14+x/2}$ For M = Sn, Hf or Zr	These compositions were not attempted*	

* $La_2M_2O_7$was present as a minority impurity phase for the parent $La_3Ga_5MO_{14}$where M = Sn, Hf or Zr (see page 54).

Amongst the 20 nominal $La_3Ga_{5-x}M'_xMO_{14+X/2}$ compositions studied falling within the '*i*' category, the formation of a minority pyrochlore impurity phase was observed for all the systems studied with the exception of two: $La_3Ga_{5-x}Si_xGeO_{14+x/2}$ and $La_3Ga_{5-x}Sn_xSiO_{14+x/2}$:

- In the synthetic exploration of $La_3Ga_{5-x}Si_xGeO_{14+x/2}$, $LaGa_{0.75}Ge_{0.93}O_{4.485}$ was identified as the more predominant impurity. $LaGa_{0.75}Ge_{0.93}O_{4.485}$ is an unreported phase which is further discussed later on in this chapter in page 76.

- A SiO_2 impurity was present for all $La_3Ga_{5-x}Sn_xSiO_{14+x/2,}$ with x = 0.1, 0.2, 0.4, 0.5 and 0.6 compositions studied. This impurity became more predominant as the amount of dopant 'x' increased. This indicates that Sn^{4+} is substituting Si^{4+} and not Ga^{3+}.

The remaining doping strategies listed in Table 3-7 lead to the formation of $La_2M_2O_7$ impurities where M = Si, Ti, Sn, Hf and Zr. Moreover, a change in the lattice parameters of the $La_2M_2O_7$ impurity was observed attributed to the formation of a $La_2M'_{2-x}M_xO_7$ solid solution. As an example, the Rietveld refinement of the outcomes of the exploratory syntheses in $La_3Ga_{5-x}Ti_xSnO_{14+x/2}$ are given in Figure 3-4. The PXRD patterns were collected after the 3rd heating cycle at 1300 °C, when the reaction completion was achieved. The fitting parameters of the refinements and the trend in the lattice parameter recorded for the majority langasite phase is shown in Table 3-8 and Figure 3-5 respectively. The Rietveld refinement were carried out by the refinement of the background, peak shape, lattice parameters for the pyrochlore and langasite phases and scale factor for each phase. The atomic positions and thermal parameters were not refined as these were only short scans (~30 min) aimed at determining the langasite and impurity phase ratio as well as testing the potential interstitial oxide accommodation by seeking trends in the lattice parameters as a function of 'x', which in this case as in the other systems within the 'i' category was found unsuccessful.

The initial mixture of reaction with $La_3Ga_{5-x}Ti_xSnO_{14+X/2}$ nominal composition was found to form $La_3GaSn_{1-x}Ti_xO_{14}$ langasite and $La_2Ti_{2-x}Sn_xO_7$ pyrochlore phases predominantly, amongst other impurity phases. There is a continuous change in a and c lattice parameters of the majority langasite phase for x up to 0.5 (see Figure 3-5). For x = 0.8, a plateau of the lattice parameters was observed. This sample was analysed by EDX elemental analysis in the TEM (see Figure 3-6-*c*). The averaged composition for the langasite and pyrochlore phases were established as: $La_{2.98(7)}Ga_{4.8(1)}Ti_{0.43(6)}Sn_{0.78(3)}O_{14.11(3)}$ and $La_{1.94(5)}Ga_{0.06(3)}Ti_{1.85(4)}Sn_{0.15(2)}O_{7.00(1)}$ respectively.

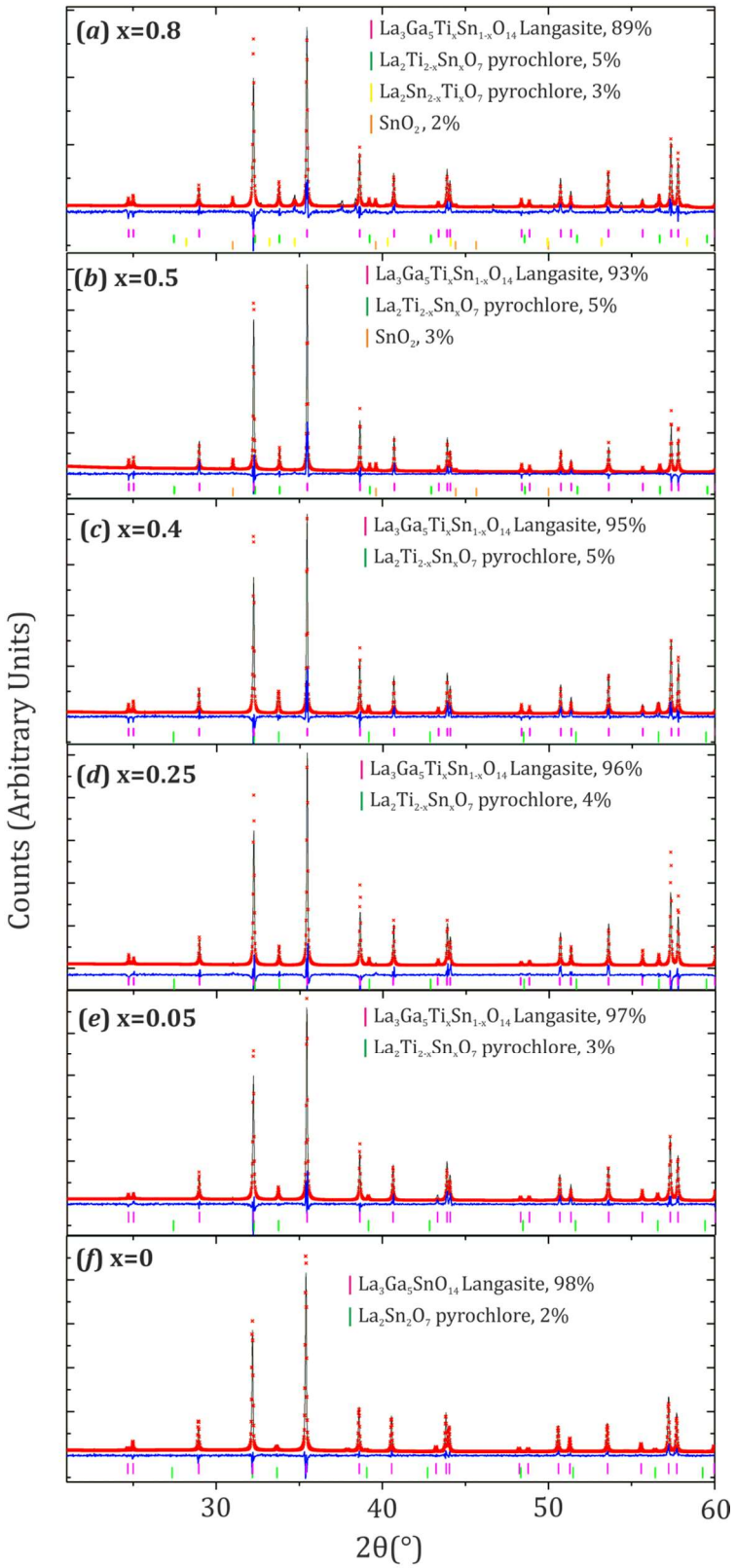

Figure 3-4 Rietveld refined $La_3Ga_{5-x}Ti_xSnO_{14+x/2}$ with the nominal compositions: (a) $x = 0.8$, (b) $x = 0.5$, (c) $x = 0.4$, (d) $x = 0.25$, (e) $x = 0.05$ and (f) $x = 0$ in space group $P321$. The vertical lines are indicating the Bragg positions of the peaks accounting for the phases identified as follows: magenta for langasite, green and yellow for pyrochlore phases, and orange for SnO_2. The calculated percentages in mass for each phase are also given in the graphs.

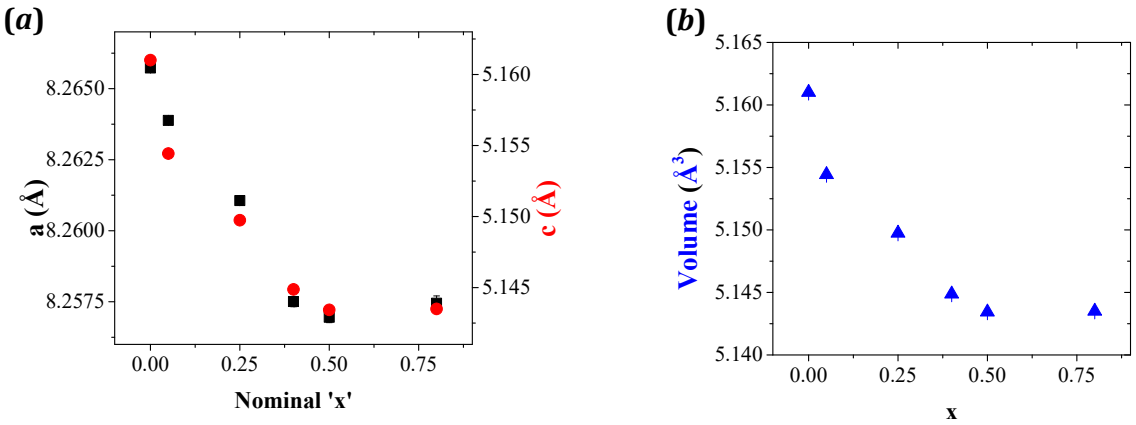

Figure 3-5 Evolution of the *a* and *c* lattice parameters in (*a*) and cell volume (*c*) in the samples with the $La_3Ga_{5-x}Ti_xSnO_{14+x/2}$ nominal compositions synthesized by the solid-state reaction method at 1300 °C for the samples with $x = 0.8, 0.5, 0.4, 0.25, 0.05$ and 0.

Table 3-8 Fitting parameters of the Rietveld refined $La_3Ga_{5-x}Ti_xSnO_{14+x/2}$ data

x	0	0.05	0.25	0.4	0.5	0.8
R_{wp}	11.2	11.28	19.31	16.19	16.02	16.42
$S = R_{wp}/R_{exp}$	1.32	1.34	2.24	1.77	1.86	1.79

The EDX analyses of three *'i'* systems with nominal compositions: $La_3Ga_{4.7}Si_{0.3}ZrO_{14.15}$, $La_3Ga_{4.5}Zr_{0.5}SiO_{14.25}$ and $La_3Ga_{4.2}Ti_{0.8}SnO_{14.4}$ are reported in Figure 3-6 (*a-c* respectively). The compositional mappings were done based on the analysis of approximately ten crystallites in each sample. The results of the EDX elemental analysis are in good agreement with the conclusions obtained from the PXRD data analysis. Although there was a change in the composition of the main langasite phase demonstrated by a change in the lattice parameters, the presence of M^{4+}-rich impurities suggests that the M'^{4+} dopant was substituting the isovalent host cation and not Ga^{3+}, with no extra oxygen being incorporated.

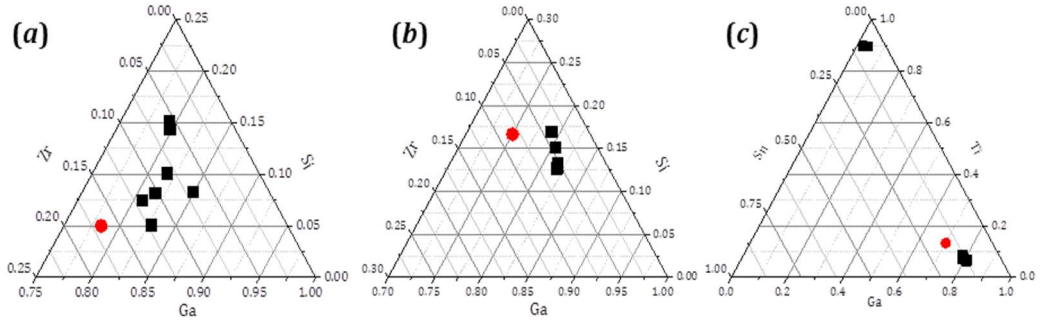

Figure 3-6 EDX of (*a*) $La_3Ga_{4.7}Si_{0.3}ZrO_{14.15}$, (*b*) $La_3Ga_{4.5}Zr_{0.5}SiO_{14.25}$ and (*c*) $La_3Ga_{4.2}Ti_{0.8}SnO_{14.4}$ targeted nominal compositions plotted as a red circle. Mixture of precursors with stoichiometric nominal compositions *a-c* were annealed at 1300°C for three heating cycles with two intermediate grinding steps. The analysed compositions are plotted in black filled squares in the graph. The averaged measured compositions are (*a*) $La_{3.02(7)}Ga_{4.87(9)}Si_{0.6(2)}Zr_{0.5(2)}O_{14.05(6)}$, (*b*) $La_{2.94(7)}Ga_{4.89(8)}Si_{0.9(1)}Zr_{0.29(4)}O_{14.08(4)}$ and two clusters were identified in (c) with the averaged compositions of $La_{2.98(7)}Ga_{4.8(1)}Ti_{0.43(6)}Sn_{0.78(3)}O_{14.11(3)}$ and $La_{1.94(5)}Ga_{0.06(3)}Ti_{1.85(4)}Sn_{0.15(2)}O_{7.00(1)}$ corresponding to the langasite and pyrochlore phases respectively.

To account for the volatilization of Ga in these systems as a plausible cause for the change in stoichiometry of the mixture of reactants that could ultimately result in the formation of undesired impurity phases, an extra step was added to the heating programme. This extra step involved dwelling at 800-900 °C for 4-8 hours before reaching the final temperature of 1000-1350 °C. This synthetic strategy also resulted in the formation of the phases enumerated in Table 3-7 and the volatilization of Ga_2O_3 was discarded as the cause of impurity formation.

3.3.2.3.1 Successfully doped $La_3Ga_{5-x}M'^{4+}{}_xMO_{14+x/2}$

The successfully doped $La_3Ga_{5-x}M'^{4+}{}_xMO_{14+x/2}$ systems incorporating extra oxide ions denoted by a green tick mark '✔' were introduced in Table 3-6. $La_3Ga_{5-x}Ge_{1+x}O_{14+x/2}$, $La_3Ga_{5-x}Ti_xSiO_{14+x/2}$, $La_3Ga_{5-x}Ti_xGeO_{14+x/2}$ and $La_3Ga_{5-x}Sn_xTiO_{14+x/2}$ synthesized under the conditions specified in Table 3-9 are able to incorporate a modest amount of around ~0.7-2.1 % of interstitial oxide ions. Henceforth, the study of each successfully doped composition is presented in more detail; ternary phase diagrams with the actual compositions determined by EDX and the observed trends in lattice parameters are given.

Table 3-9 Synthesized $La_3Ga_{5-x}M'^{4+}{}_xMO_{14+x/2}$ compositions introducing extra oxygen

Section	Nominal Composition	Optimal synthetic temperature T_{opt} (°C)	Doping limit $x_{max}/\%_{O_{int}}$	Impurities formed when $T > T_{opt}$ or $x > x_{max}$
3.3.2.3.1.1	$La_3Ga_{5-x}Ge_{1+x}O_{14+x/2}$	1300	0.3 / 1.07	$LaGa_{0.87}Ge_{0.93}O_{4.7}$
3.3.2.3.1.2	$La_3Ga_{5-x}Ti_xSiO_{14+x/2}$	1300	0.3 / 1.07	SiO_2
3.3.2.3.1.3	$La_3Ga_{5-x}Ti_xGeO_{14+x/2}$	750	0.6 / 2.14	$LaGa_{0.87}Ge_{0.93}O_{4.7}$
3.3.2.3.1.4	$La_3Ga_{5-x}Sn_xTiO_{14+x/2}$	1250	0.2 / 0.71	$La_2Ti_{2-x}Sn_xO_7$

3.3.2.3.1.1 $La_3Ga_{5-x}Ge_{1+x}O_{14+x/2}$

The extent of the solid-solution achieved by the solid-state reaction method at 1300 °C in $La_3Ga_{5-x}Ge_{1+x}O_{14+x/2}$ expanded to x values up to 0.3 (see Table 3-9). The firing of nominal compositions with $x > 0.3$ resulted in the formation of $La_3Ga_{4.7}Ge_{1.3}O_{14.15}$ and a minority $LaGa_{0.87}Ge_{0.93}O_{4.7}$ impurity phase. The characterization of this impurity and the demonstration of the incorporation of extra oxygen in $La_3Ga_{5-x}Ge_{1+x}O_{14+x/2}$ by means of EDX elemental analysis is presented in section 3.3.4 entitled '3.3.4 Synthesis optimization: Obtaining phase pure $La3Ga3.5Ge2.5O14.75$ *via* Pechini.'.

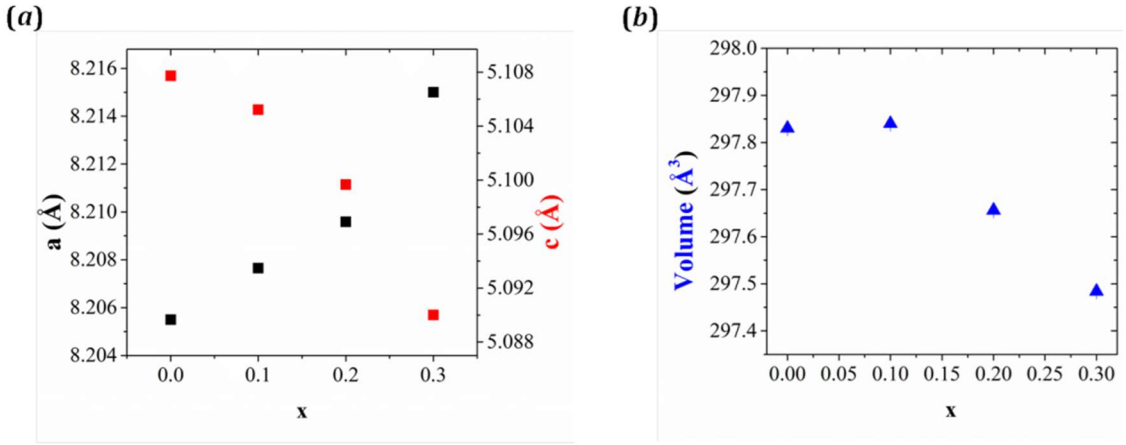

Figure 3-7 $La_3Ga_{5-x}Ge_{1+x}O_{14+x/2}$ (*a*) Change in the *a* and *c* lattice parameters denoted by black and red squares respectively and (*b*) change in the cell volume by blue triangles as function of *x* determined by Pawley fitting.

3.3.2.3.1.2 $La_3Ga_{5-x}Ti_xSiO_{14+x/2}$

Doped $La_3Ga_{5-x}Ti_xSiO_{14+x/2}$ nominal compositions where x = 0, 0.25, 0.5 and 0.75 were synthesized by the solid-state reaction method. A linear trend in the lattice parameter as a function of x was observed, a and c lattice parameters increase and decrease respectively with the increase in the nominal x values up to 0.5 (see Figure 3-8). $La_3Ga_{4.25}Ti_{0.75}SiO_{14.375}$ (x = 0.75) nominal composition studied was found to form a SiO_2 impurity and a main langasite phase matching the lattice parameters caculated for $La_3Ga_{4.5}Ti_{0.5}SiO_{14.25}$ (x = 0.5). Therefore, the doping limit in $La_3Ga_{5-x}Ti_xSiO_{14+x/2}$ was set as x = 0.5.

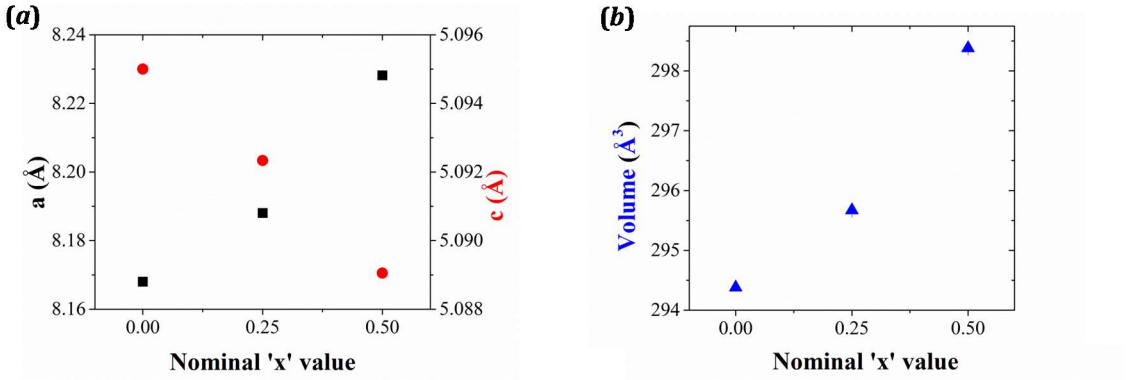

Figure 3-8 Change in lattice parameters for $La_3Ga_{5-x}Ti_xSiO_{14+x/2}$ with x = 0, 0.25 and 0.5 determined by Pawley fitting. In (*a*) *a* lattice parameters are represented in black squares, *c* in red circles and in (*b*) the cell volume is represented in blue triangles.

Once the doping limit in $La_3Ga_{5-x}Ti_xSiO_{14+x/2}$ was established for x ~0.5, a 94 % dense $La_3Ga_{4.5}Ti_{0.5}SiO_{14.25}$ (x = 0.5) pellet was prepared and its conductivity measured. The conductivity results for successfully synthesized '✓' $La_3Ga_{5-x}M'^{4+}_xMO_{14+x/2}$ compositions are discussed later on in this chapter in section 3.3.3 entitled '3.3.3 Screening of the Conductivity'. The actual composition of $La_3Ga_{4.5}Ti_{0.5}SiO_{14.25}$, whose conductivity was studied by means of AC impedance in 3.3.3.2, was determined by EDX analysis in the TEM. The compositions of ten crystallites are plotted in a ternary phase diagram shown in Figure 3-9.

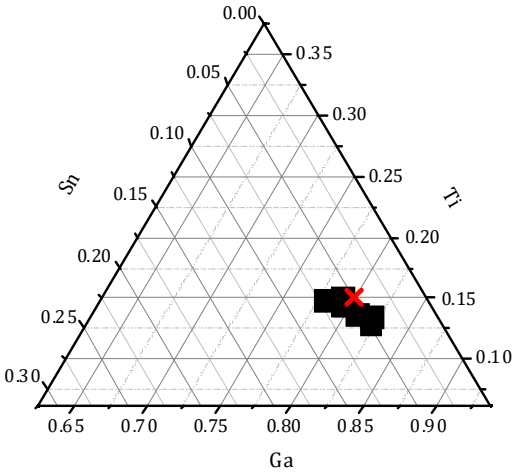

Figure 3-9 Ternary phase diagram showing the EDX compositional mapping of the samples with a $La_3Ga_{4.5}Ti_{0.5}SiO_{14.25}$ nominal composition. The cluster of compositions studied represented by black filled squares gave an average value of $La_{2.95(4)}Ga_{4.72(6)}Ti_{0.277(7)}Si_{0.99(1)}O_{14.27(3)}$ that was approximated to $La_3Ga_{4.7}Ti_{0.3}SiO_{14.15}$ in which the sum of cations adds up to 9, for the sake of simplicity in the later discussion in 0. The composition of $La_3Ga_{4.7}Ti_{0.3}SiO_{14.15}$ is denoted in the phase diagram by a red cross.

3.3.2.3.1.3 $La_3Ga_{5-x}Ti_xGeO_{14+x/2}$

The syntheses of $La_3Ga_{5-x}Ti_xGeO_{14+x/2}$ members was first addressed by the solid-state reaction method showing promising results. A trend in the Pawley fit calculated lattice parameters was observed for 'x' values as high as 0.8. However, other impurity phases such as $La_2Ti_2O_7$ and $LaGa_{0.87(3)}Ge_{0.93(3)}O_{4.7(1)}$ were identified in the PXRD patterns. Due to the fact that mechanical milling of the precursors and intermediate mixtures of reactants did not get rid of the presence of impurities neither was able to decrease the temperature for the synthesis of $La_3Ga_{5-x}Ti_xGeO_{14+x/2}$, the Pechini method was carried out as an alternative route. The final temperature of the synthesis by Pechini was set to 750 °C and dwell for 12 hours. An increase in the synthetic temperature to 800 °C was precluded by the formation of a $LaGa_{0.87}Ge_{0.93}O_{4.7}$ impurity. Phase pure $La_3Ga_{5-x}Ti_xGeO_{14+x/2}$ samples with x = 0.25, 0.5, 0.75 and 1 were synthesized at 750 °C and the trend in the lattice parameters calculated by Pawley is given in Figure 3-10. We then proceeded to determine the actual composition of the highest doped $La_3Ga_4TiGeO_{14.5}$ (x = 1) by EDX. The ternary phase diagram for the compositional mapping of the EDX data collected in over 10 crystallites and its PXRD pattern are shown in Figure 3-11 *a* and *b* respectively.

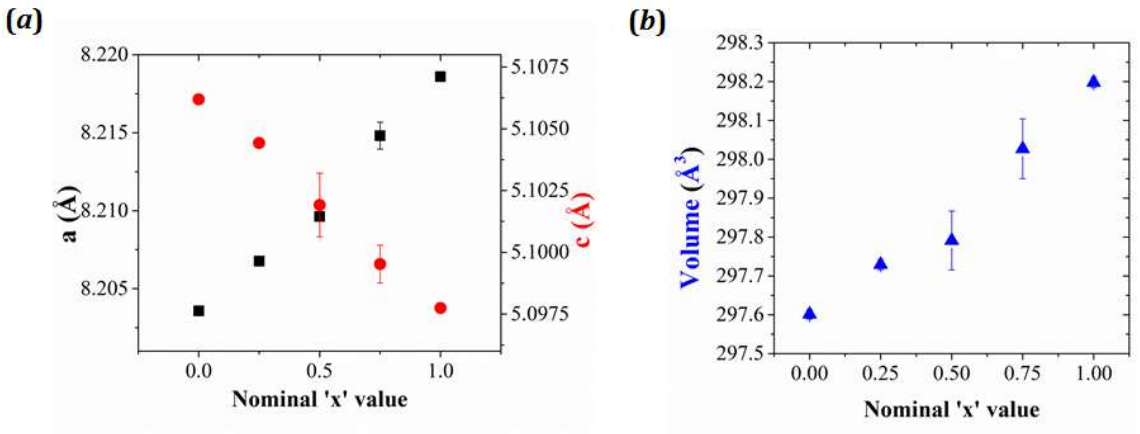

Figure 3-10 Vergard's law for $La_3Ga_{5-x}Ti_xGeO_{14+x/2}$ where x = 0, 0.25 and 0.5. In (a) the a lattice parameters are represented in black squares and c in red circles. In (b) the volume is represented in blue triangles.

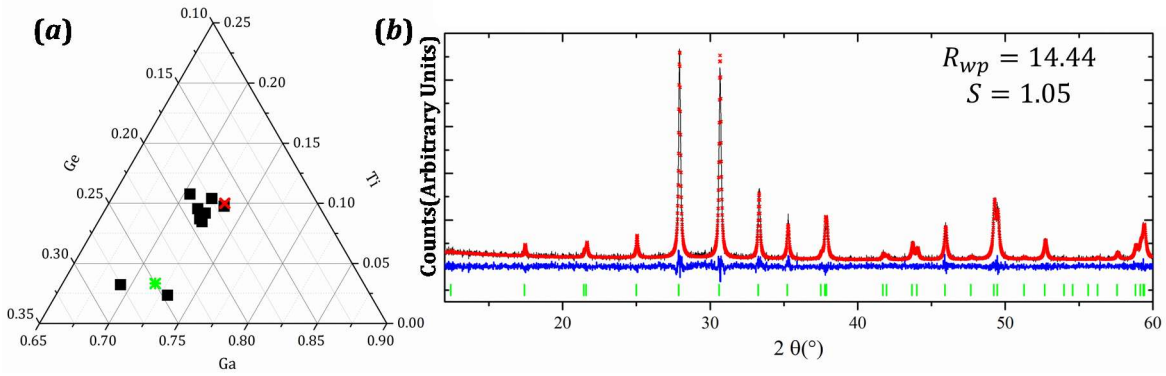

Figure 3-11 (a) Compositional EDX mapping and (b) Rietveld refined PXRD data of the sample with nominal composition $La_3Ga_4TiGeO_{14.5}$ synthesized by Pechini at 750 °C. In (a), the collected data is represented by black squares, whereas the averaged measured values of the two clusters round up to nine cations are denoted by a red cross ($La_3Ga_{4.4}Ti_{0.6}GeO_{14.3}$) and a green asterisk ($La_3Ga_{4.3}Ti_{0.2}Ge_{1.5}O_{14.35}$).

The mapping of the EDX data evidence the higher compositional inhomogeneity shown by $La_3Ga_{5-x}Ti_xGeO_{14+x/2}$ when compared to the other compositions studied in this section. The Ti-richer compositional cluster in Figure 3-11(a) is formed by eight crystallites analysed whose compositions averaged to $La_{3.03(6)}Ga_{4.30(7)}Ti_{0.57(5)}Ge_{1.09(5)}O_{14.33(3)}$. Two out of ten crystallites analysed show a deviation from the majority cluster towards Ge-richer compositions. The averaged composition of this two deviated data points is $La_{3.0(1)}Ga_{4.3(1)}Ti_{0.17(3)}Ge_{1.6(1)}O_{14.44(7)}$ which was rounded up to $La_3Ga_{4.3}Ti_{0.2}Ge_{1.5}O_{14.35}$ represented by a green asterisk in Figure 3-11-a.

Although $La_3Ga_{4.4}Ti_{0.6}GeO_{14.3}$ could in principle be a good candidate for interstitial oxide ion conduction incorporating an acceptable 2.14 % of O_{int} , the high compositional inhomogeneity observed by EDX and the low temperatures (below 750 °C) that this system was restricted to are major disadvantages. Due to these difficulties encountered on the processing of $La_3Ga_{5-x}Ti_xGeO_{14+/2}$ its study was discontinued and no conductivity data is reported on these systems.

3.3.2.3.1.4 $La_3Ga_{5-x}Sn_xTiO_{14+x/2}$

The $La_3Ga_{4.8}Sn_{0.2}TiO_{14.1}$ and $La_3Ga_{4.5}Sn_{0.5}TiO_{14.25}$ nominal compositions were synthesized by the solid-state reaction method at 1250 °C. PXRD patterns of these samples were recorded and elemental analysis was performed by EDX mapping as shown in Figure 3-12.

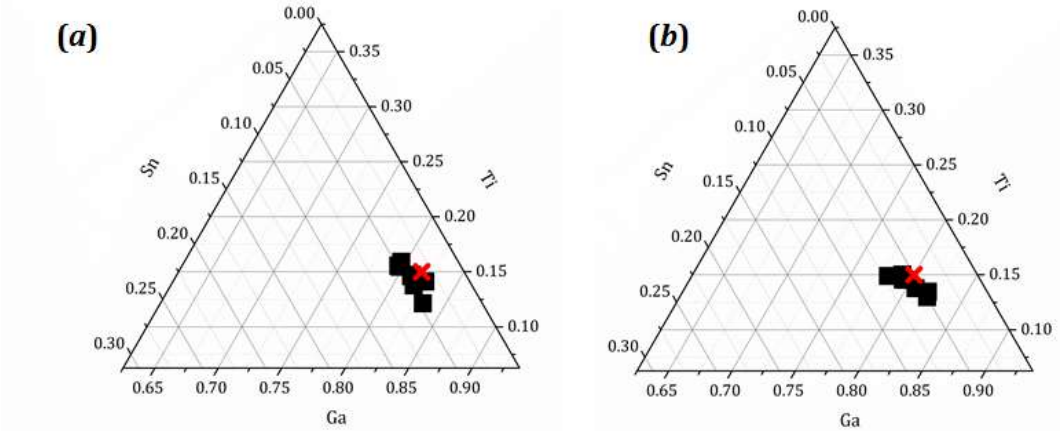

Figure 3-12 EDX compositional study of $La_3Ga_{4.8}Sn_{0.2}TiO_{14.1}$ (*a*) and $La_3Ga_{4.5}Sn_{0.5}TiO_{14.25}$ (*b*) nominal compositions. The data collected is represented in black filled squares and the red crosses denote the averaged compositions rounded up to nine cations: $La_3Ga_{4.9}Sn_{0.2}Ti_{0.9}O_{14.05}$ and $La_3Ga_{4.8}Sn_{0.3}Ti_{0.9}O_{14.1}$ in (*a*) and (*b*) respectively.

The sample with a nominal composition of $La_3Ga_{4.8}Sn_{0.2}TiO_{14.1}$ (x = 0.2) gave an actual composition of $La_{2.97(7)}Ga_{4.9(1)}Sn_{0.27(3)}Ti_{0.88(7)}O_{14.07(4)}$ and $La_3Ga_{4.5}Sn_{0.5}TiO_{14.5}$ (x = 0.5) gave an actual composition of $La_{2.94(5)}Ga_{4.8(1)}Ti_{0.88(9)}Sn_{0.36(6)}O_{14.12(6)}$. Once again the M'^{4+} dopant was found to replace the host isovalent M^{4+}. The presence of a $La_2M_2O_7$ minority phase was identified in the PXRD pattern. However, in $La_3Ga_{5-x}Sn_xTiO_{14+x/2}$ unlike in those systems studied lying within the '*i*' category $\sim {}^{2}/_{3}$ of the Sn^{4+} introduced into the main langasite phase are substituting Ga^{3+}, thus introducing ~1.1 % of extra oxygen in $La_3Ga_{4.8}Sn_{0.3}Ti_{0.9}O_{14.1}$.

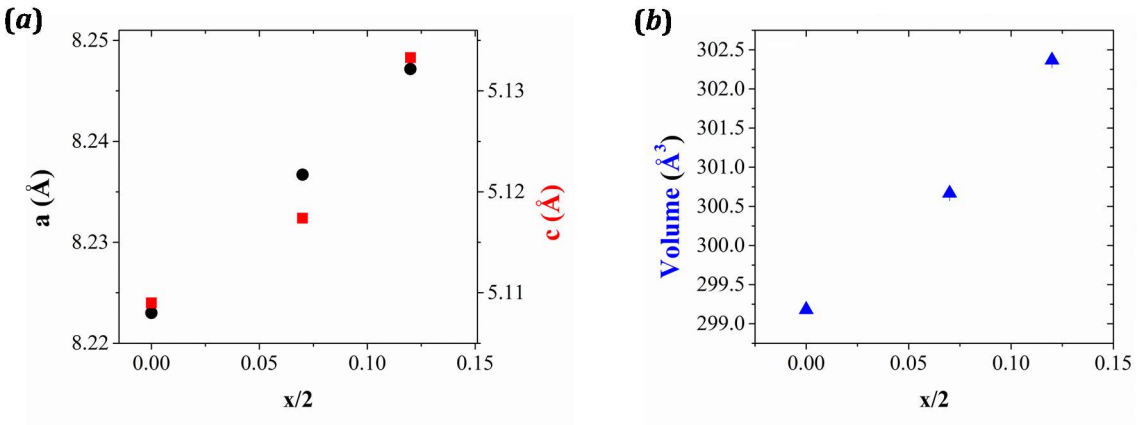

Figure 3-13 Trend in *a* (black circles) and *c* (red squares) lattice parameters (*a*) and cell volume (blue triangles) (*b*) in $La_3Ga_{5-x}Sn_xTiO_{14+x/2}$ as a function of the amount of interstitial oxide ions incorporated estimated by EDX (see Figure 3-12).

In Figure 3-13 above, the trend in the *a* and *c* lattice parameters (*a*) and cell volume (*b*) are plotted vs the amount of extra oxygen incorporated ($\sim x/2$). The amount of extra oxygen incorporated accounts for the actual ratio of cations determined by EDX, which followed a

linear trend with a and c lattice parameters increasing with the increase in $x/2$ and an overall increase in the volume of the cell by ~3.5 Å^3.

3.3.3 Screening of the Conductivity

Since the doping studies of $La_3Ga_5MO_{14}$ are motivated by their potential application as electrolyte materials in solid-oxide fuel cells, conductivity measurements of doped langasites were performed. These tests served us to identify promising candidate materials.

3.3.3.1 $La_{2.5}Ce_{0.5}Ga_5SiO_{14+\delta}$

To evaluate the effect of the cerium doping on the conductivity in $La_{2.5}Ce_{0.5}Ga_5SiO_{14+\delta}$, AC impedance spectroscopy were performed in 93 and 90 % dense ceramic discs of $La_{2.5}Ce_{0.5}Ga_5SiO_{14+\delta}$ and $La_3Ga_5SiO_{14}$ respectively. The total conductivity was extracted from the complex impedance plot. The intercept of the recorded asymmetric semi-circular arc corresponded to the total resistivity ($R_{bulk} + R_{grain\ boundary}$) of these system. The assignments of the conductivity were done based on the calculated corrected capacitance values of the order of ~10^{-11} F (see Figure 3-14-*a* and *b* for the complex impedance plots of x = 0.5 and 0). The measured values for total conductivity of $La_3Ga_5SiO_{14}$ are in good agreement to those reported in ref.151.

Only a modest increase in conductivity was observed in $La_{2.5}Ce_{0.5}Ga_5SiO_{14+\delta}$ when compared to the parent phase from 0.31×10^{-4} to 1.39×10^{-4} S·cm^{-1} at 700 °C. The small increase in conductivity could be motivated by the partial reduction of Ce^{4+} to Ce^{3+} during the course of the synthesis as suggested in 0.

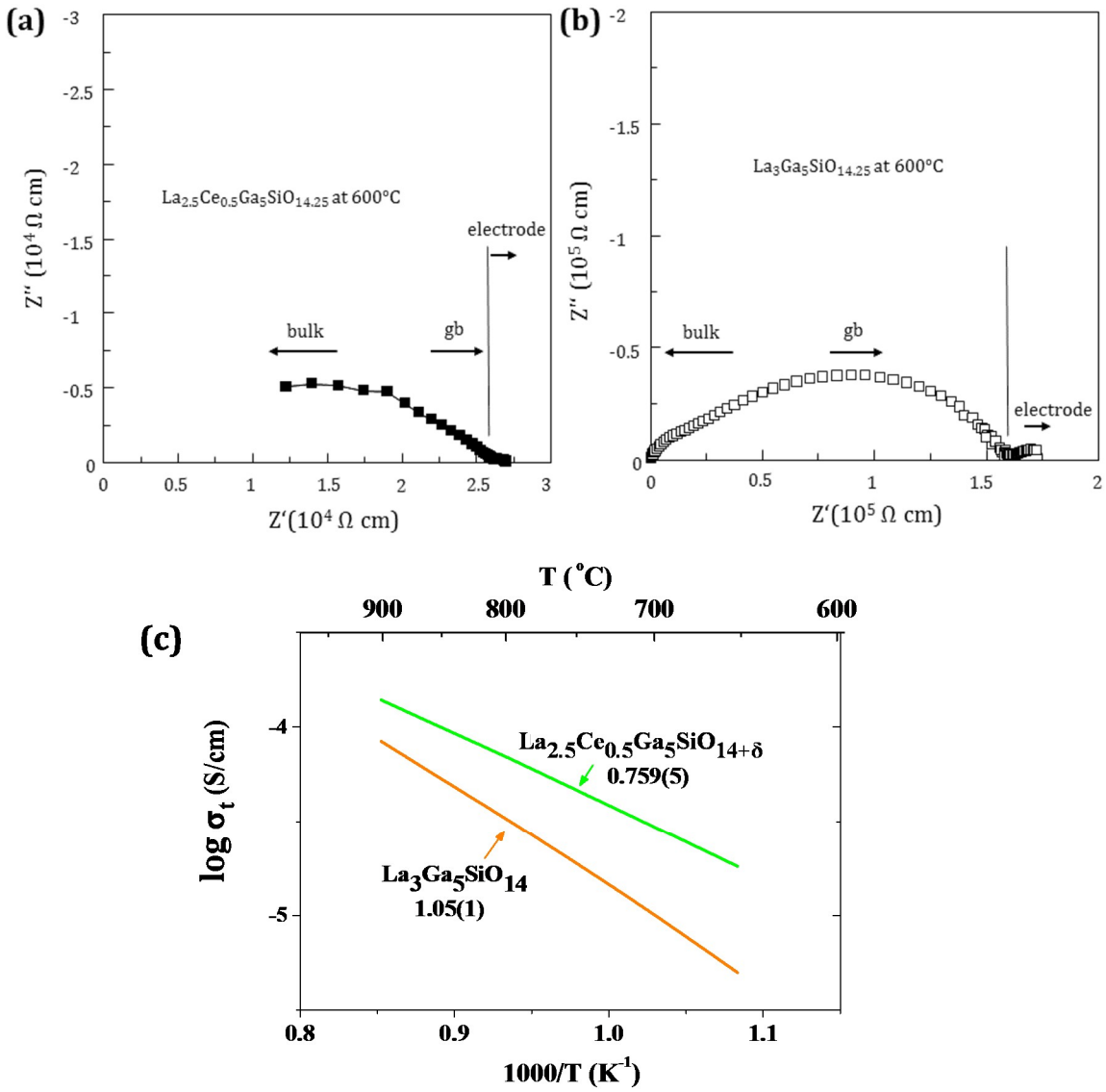

Figure 3-14. (*a*) Complex impedance plots of $La_{2.5}Ce_{0.5}Ga_5SiO_{14+\delta}$ and (*b*) $La_3Ga_5SiO_{14}$ at 600 °C where the assignment of bulk, grain boundary (gb) and electrode responses were made with regards of their measured capacitances' scales of 10^{-11} F·cm^{-1}. The Arrhenius plots of the conductivity of $La_{2.5}Ce_{0.5}Ga_5SiO_{14+\delta}$ in green and $La_3Ga_5SiO_{14}$ in orange are shown in (*c*), where the activation energies in eV are also given.

To ensure that the $La_{2.5}Ce_{0.5}Ga_5SiO_{14+\delta}$ pellet survived the conditions applied to the system in the AC impedance experiment, the pellets were ground and PXRD patterns of the powders were measured (see Figure 3-15). The Pawley fit refined lattice parameter in a *P*321 space group are as follows: a = 8.19614(4) Å, c = 4.91601(3) Å and 285.997(3) Å^3, with the errors assigned to refined lattice parameters values being 1 × e.s.d, which compares to the before-measurement values reported in Figure 3-3. The post-measurement PXRD patterns revealed no presence of extra peaks that would indicate the decomposition of the pellet during the measurement.

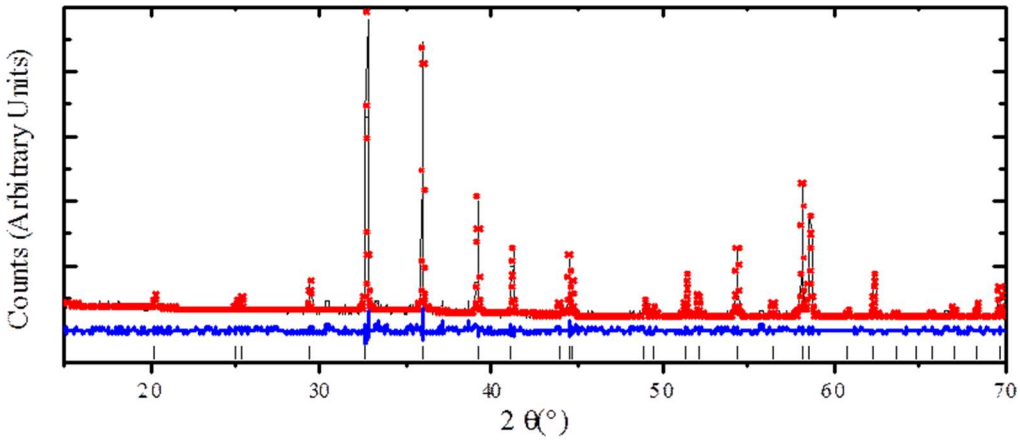

Figure 3-15 Pawley fit for $La_{2.5}Ce_{0.5}Ga_5SiO_{14+\delta}$ after impedance. The black solid line denotes the experimental data, red crosses designate the fit to the data, the blue line the fit between both, and the vertical lines are indicating the Bragg positions of the peaks. The refined fitting parameters are as follows: R_{wp} = 7.94, R_{exp} = 5.41 and S = 1.47. The PXRD pattern was recorded in PANanlytical X'pert Pro diffractometer equipped with a Co source ($K_{\alpha 1,Co} = 1.7890$ Å).

3.3.3.2 $La_3Ga_{5-x}M'^{4+}{}_xMO_{14+x/2}$

A total of six dense pellets ($\rho \geq 90$ %) were prepared. Those with the aforementioned '✓' compositions incorporating extra oxygen: $La_3Ga_{4.7}Ge_{1.3}O_{14.15}$, $La_3Ga_{4.7}Ti_{1.3}SiO_{14.15}$ and $La_3Ga_{4.8}Sn_{0.3}Ti_{0.9}O_{14.1}$ and the parent materials: $La_3Ga_5GeO_{14}$, $La_3Ga_5SiO_{14}$ and $La_3Ga_5TiO_{14}$. The sintering temperatures and final densities achieved for each $La_3Ga_{5-x}M'_xMO_{14+x/2}$ system studied are given in Table 3-10.

Table 3-10 Sintering conditions and final densities of the $La_3Ga_{5-x}M'_xMO_{14+x/2}$ specimens studied.

System	Temperature T_{opt} (°C)	Density (%)
$La_3Ga_{4.7}Ge_{1.3}O_{14.15}$	1300	93
$La_3Ga_5GeO_{14}$	1275	92
$La_3Ga_{4.7}Ti_{1.3}SiO_{14.15}$	1300	94
$La_3Ga_5SiO_{14}$	1250	90
$La_3Ga_{4.8}Sn_{0.3}Ti_{0.9}O_{14.1}$	1300	97
$La_3Ga_5TiO_{14}$	1300	97

The total conductivity values were extracted from the intercept of the arcs present in the complex impedance plane (see Figure 3-16). The type of response (bulk, grain boundary or electrode) was assigned based on the geometry-corrected capacitance values[231].

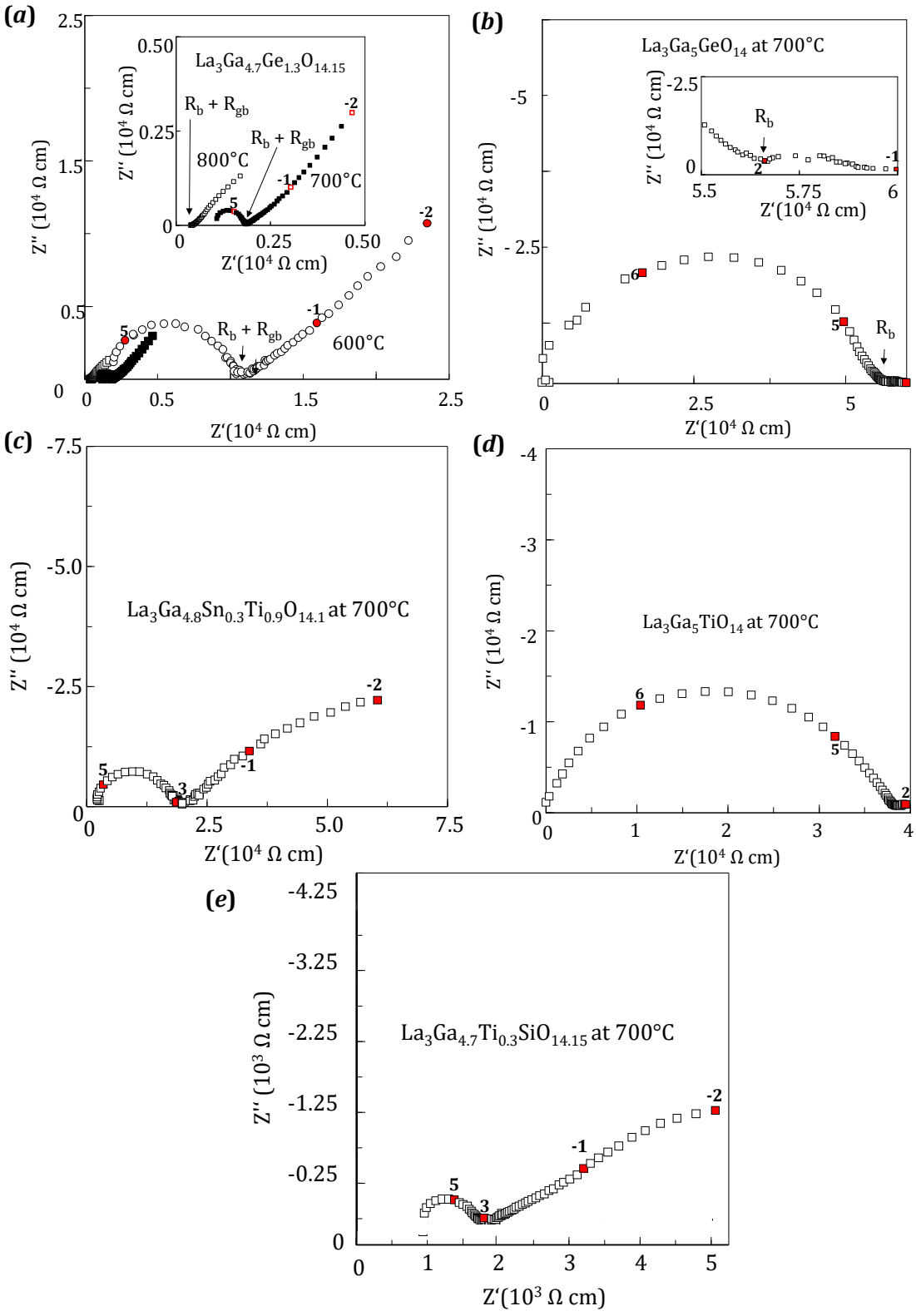

Figure 3-16 Complex impedance plots for (*a*) $La_3Ga_{4.7}Ge_{1.3}O_{14.15}$ at 600, 700 and 800 °C showing the Warburg arc characteristic of oxide-ion conductors, (*b*) for the insulating $La_3Ga_5GeO_{14}$ parent material at 700 °C. Figures (*c-e*) show the complex impedance plots for $La_3Ga_{4.8}Sn_{0.3}Ti_{0.9}O_{14.1}$, $La_3Ga_5TiO_{14}$ and $La_3Ga_{4.7}Ti_{0.3}SiO_{14.15}$ at 700 °C. Refer to section 3.1 for the complex impedance plot of $La_3Ga_5SiO_{14}$. The bold numbers denote the logarithm of the frequency of the adjacent points highlighted in red.

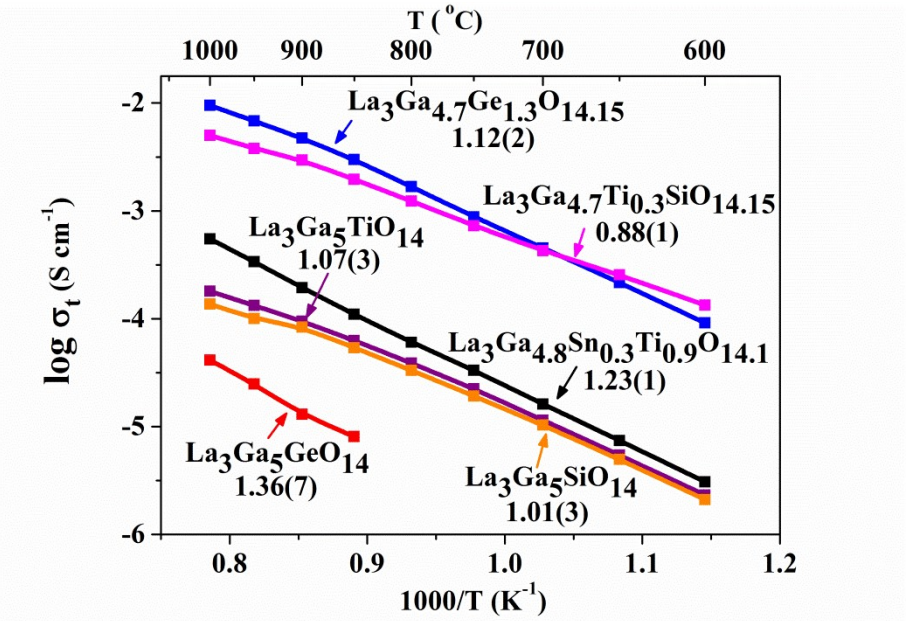

Figure 3-17 Arrhenius plot of the total conductivity of doped $La_3Ga_{4.7}Ge_{1.3}O_{14.15}$, $La_3Ga_{4.7}Ti_{0.3}SiO_{14.15}$ and $La_3Ga_{4.8}Ti_{0.9}Sn_{0.3}O_{14.15}$ and parent $La_3Ga_5GeO_{14}$, $La_3Ga_5SiO_{14}$ and $La_3Ga_5TiO_{14}$ langasites. Activation energies in eV for every composition measured are specified near their compositions' labels in the graph.

Figure 3-17 shows an increase in the total conductivity for all the doped compositions studied when compared to their respective un-doped materials. The greatest improvement in conductivity of two orders of magnitude is shown by $La_3Ga_{4.7}Ge_{1.3}O_{14.15}$ (~ 4.54×10^{-4} S·cm^{-1} at 700 °C) with respect to the un-doped Ge-langasite ($La_3Ga_5GeO_{14}$, ~8.76×10^{-7} S·cm^{-1}). The second best improvement is observed for $La_3Ga_{4.7}Ti_{0.3}SiO_{14.15}$ having increased from 1.03×10^{-5} S·cm^{-1} in $La_3Ga_5SiO_{14}$ up to 4.54×10^{-4} S·cm^{-1} at 700 °C. Lastly, there was only a modest increase in the total conductivity by 40 %, of less than one order of magnitude from 1.15×10^{-5} to 1.61×10^{-5} S·cm^{-1} in $La_3Ga_{4.8}Sn_{0.3}Ti_{0.9}O_{14.1}$ (see Table 3-11 for the comparative list of the measured total conductivity at 700 °C).

Table 3-11 Comparison of the total conductivity of $La_3Ga_{5-x}M'^{4+}{}_xMO_{14+x/2}$ doped systems

Actual (EDX) composition	$\%O_{int}$	Doped σ_t at 700 °C (S·cm^{-1})	Parent σ_t at 700 °C (S·cm^{-1})
$La_3Ga_{4.7}Ge_{1.3}O_{14.15}$	1.07	4.54×10^{-4}	8.76×10^{-7} *
$La_3Ga_{4.7}Ti_{0.3}SiO_{14.15}$	1.07	4.54×10^{-4}	1.03×10^{-5}
$La_3Ga_{4.8}Sn_{0.3}Ti_{0.9}O_{14.1}$	0.71	1.61×10^{-5}	1.15×10^{-5}

* Extrapolated value

In addition to the increase in conductivity observed in doped langasites, the Warburg electrode response characteristic of oxide ionic conductivity was also present in the complex impedance plots of doped compositions (see Figure 3-16 *a*, *c* and *e*). In Figure 3-16- *a* the arcs at 600, 700 and 800 °C are represented for $La_3Ga_{4.7}Ge_{1.3}O_{14.15}$ and demonstrates how the Warburg electrode response becomes more dominant with the increase in temperature until it is found to collapse into a single semi-circular arc at 800 °C.

The total resistivity values are then extracted from the intercept of the arc with the x-axis corresponding to the real part of the impedance, Z'.

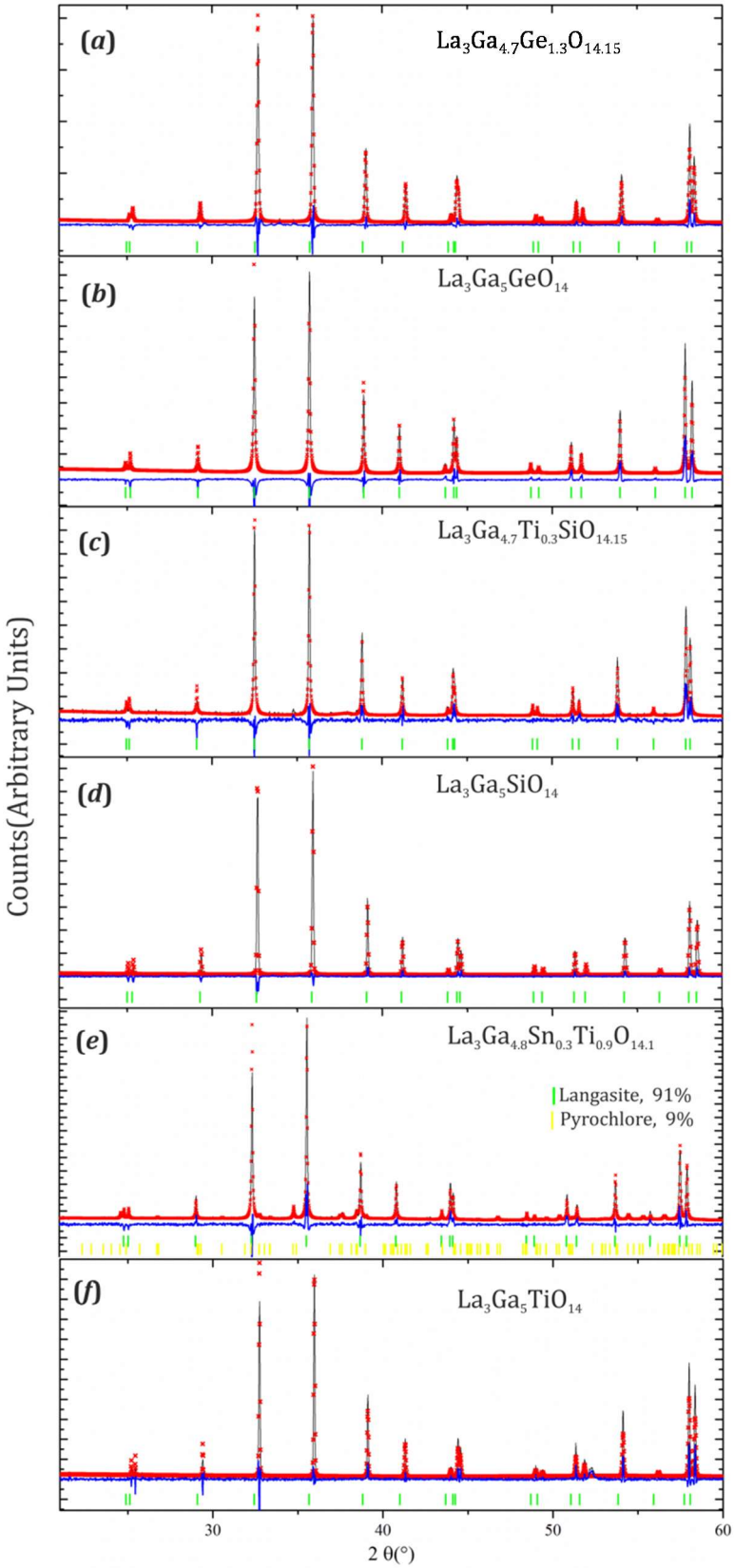

Figure 3-18 Post measurement XRD Rietveld refinements of (*a*) $La_3Ga_{4.7}Ge_{1.3}O_{14.15}$, (*b*) $La_3Ga_5GeO_{14}$, (*c*) $La_3Ga_{4.7}Ti_{0.3}SiO_{14.15}$, (*d*) $La_3Ga_5SiO_{14}$, (*e*) $La_3Ga_{4.8}Sn_{0.3}Ti_{0.9}O_{14.1}$ and (*f*) $La_3Ga_5TiO_{14}$.

After AC impedance experiments were performed, the pellets were polished in order to remove the gold electrodes, ground and the post-measurement PXRD patterns were recorded to check the stability of the samples under the experimental conditions. The post measurement PXRDs given in Figure 3-18 revealed no presence of additional phases or change in composition of the main langasite phase after conductivity measurements were carried out. It should be noted that the 9 % of pyrochlore phase observed in Figure 3-18 for $La_3Ga_{4.8}Sn_{0.3}Ti_{0.9}O_{14.1}$ was present in the sample before the AC impedance measurements were performed.

Table 3-12 Fitting and lattice parameters of the post-measurement Rietveld refined $La_3Ga_{5-x}M'_xMO_{14+x/2}$ and $La_3Ga_5MO_{14}$ XRDs. Before-measurement lattice parameters can be consulted in Figure 3-7, Figure 3-8 and Figure 3-13.

	$La_3Ga_5GeO_{14}$	$La_3Ga_{4.7}Ge_{1.3}O_{14.15}$	$La_3Ga_5SiO_{14}$	$La_3Ga_{4.6}SiTi_{0.4}O_{14.2}$	$La_3Ga_5TiO_{14}$	$La_3Ga_{4.8}Ti_{0.9}Sn_{0.3}O_{14.15}$
Post-Measurement						
R_{wp}	15.79	12.81	13.24	20.32	21.7	16.12
S	2.01	1.88	1.70	1.76	1.57	1.78
a (Å)	8.2045(1)	8.2150(1)	8.1695(6)	8.2269(3)	8.2270(1)	8.2488(2)
c (Å)	5.1068(1)	5.0836(8)	5.0918(6)	5.0880(2)	5.1084(8)	5.1338(2)
V(Å^3)	297.71(1)	297.105(9)	294.306(6)	298.23(3)	299.430(9)	302.52(2)

Based on the promising conductivity results displayed by $La_3Ga_{4.7}Ge_{1.3}O_{14.15}$ our efforts were directed solely onto this system having the greatest potential amongst all explored compositions.

3.3.4 Synthesis optimization: Obtaining phase pure $La_3Ga_{3.5}Ge_{2.5}O_{14.75}$ *via* Pechini.

Once $La_3Ga_{5-x}Ge_{1+x}O_{14+x/2}$ was identified as the most promising candidate, the syntheses of $La_3Ga_{5-x}Ge_{1+x}O_{14+x/2}$ was approached by Pechini as an alternative route to the solid-state reaction method. In hopes to expand the extent of the solid solution to values $x > 0.3$, with $x = 0.3$ being the doping limit encountered by the solid-state reaction method.

The formation of a langasite phase by Pechini was first observed at 700 °C (see Figure 3-19). This result constitutes a remarkable decrease of 500 °C in the synthetic temperature from 1200 °C in the solid-state reaction method. The synthetic temperature was optimized (T_{opt}) for every composition studied as the decomposition temperature (T_{decomp}) in $La_3Ga_{5-x}Ge_{1+x}O_{14+x/2}$ is found to vary with the dopant content 'x', being lower for the materials with a higher content in Ge.

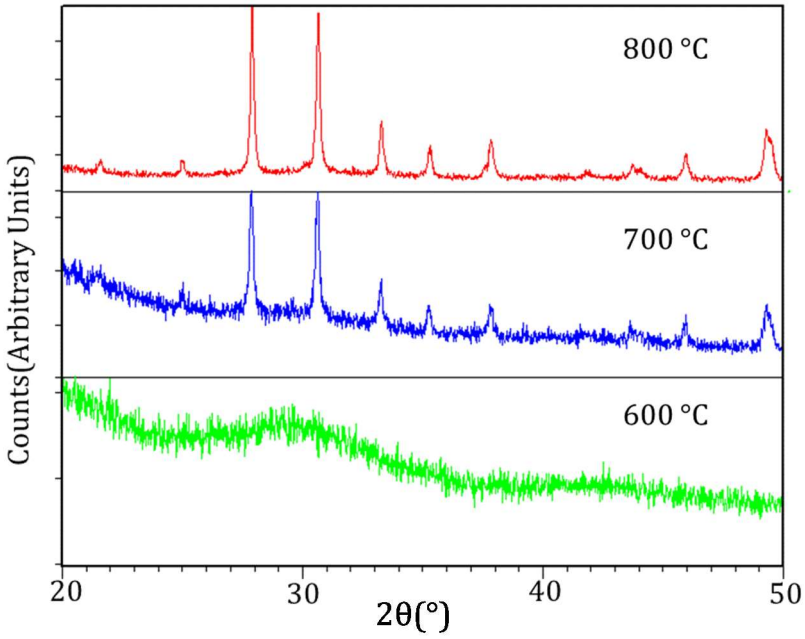

Figure 3-19 Investigation of the synthetic temperature conditions of $La_3Ga_{4.5}Ge_{1.5}O_{14.25}$ Pechini precursors after a 60 hours sintering at 600 °C (green), 12 hours sintering at 700 °C (blue) and 12 hours sintering at 800 °C (red). The PXRD patterns were collected on a PANalytical X'pert Pro diffractometer with a Co-source ($K_{\alpha 1,Co} = 1.7890$ Å).

Figure 3-20 shows the decomposition temperature of $La_3Ga_{5-x}Ge_{1+x}O_{14+x/2}$ vs the amount of dopant 'x' incorporated for the range of compositions $0.4 \leq x \leq 1.5$. Decomposition temperatures were determined by the analysis of the PXRD patters after dwelling for 12 hours at each temperature studied. Figure 3-20 shows an asymptotic decrease in the decomposition temperature in $La_3Ga_{5-x}Ge_{1+x}O_{14+x/2}$ with the increase in 'x'. On the other hand, $0 \leq x \leq 0.3$ compositions were stable at high temperatures ~1300 °C close to their melting point at ~1350 °C, and they are not represented in Figure 3-20. The higher stability of $0 \leq x \leq 0.3$ doped compositions made them accessible by the traditional solid-state reaction method as previously reported in 0.

The synthetic temperature of samples with $x > 0.3$ was subsequently lowered by 50 °C below T_{decomp} reported in Figure 3-19 in the newly developed Pechini route. $La_3Ga_{5-x}Ge_{1+x}O_{14+x/2}$ compositions with $x > 0.3$ were phase pure after a single firing of the mixture of reactants and dwell for 12 hours at a temperature T_{opt} below T_{decomp}, so that $T_{opt} = T_{decomp} - 50$ °C.

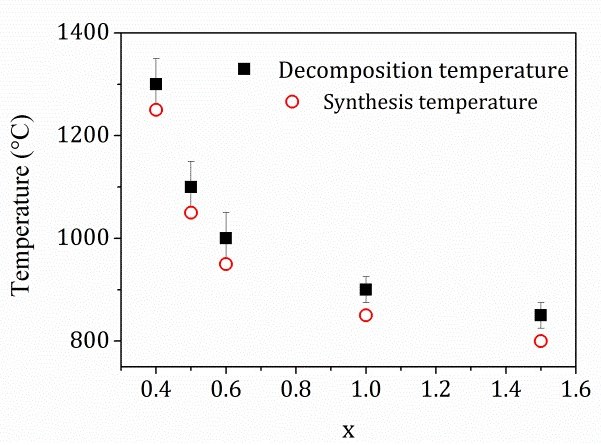

Figure 3-20 Decomposition temperature variation with x in $La_3Ga_{5-x}Ge_{1+x}O_{14+x/2}$ for x = 0.4, 0.5, 0.6 1 and 1.5.

The evolution in a and c lattice parameters and the overall volume of the cell as a function of the dopant content 'x' is shown in figure (Figure 3-21) within a $0 \leq x \leq 1.5$ solid solution range. Within this range of compositions, there is an increase in the a lattice parameter, decrease of c and an overall lessening of the volume of the cell by ~0.5 $Å^3$ which supports the substitution of Ga^{3+} by Ge^{4+} with a smaller ionic radii[239]. The cell parameters determined within the $0 \leq x \leq 0.3$ range of compositions are in good agreement with those values presented in 0 synthesized by the traditional solid-sate reaction method.

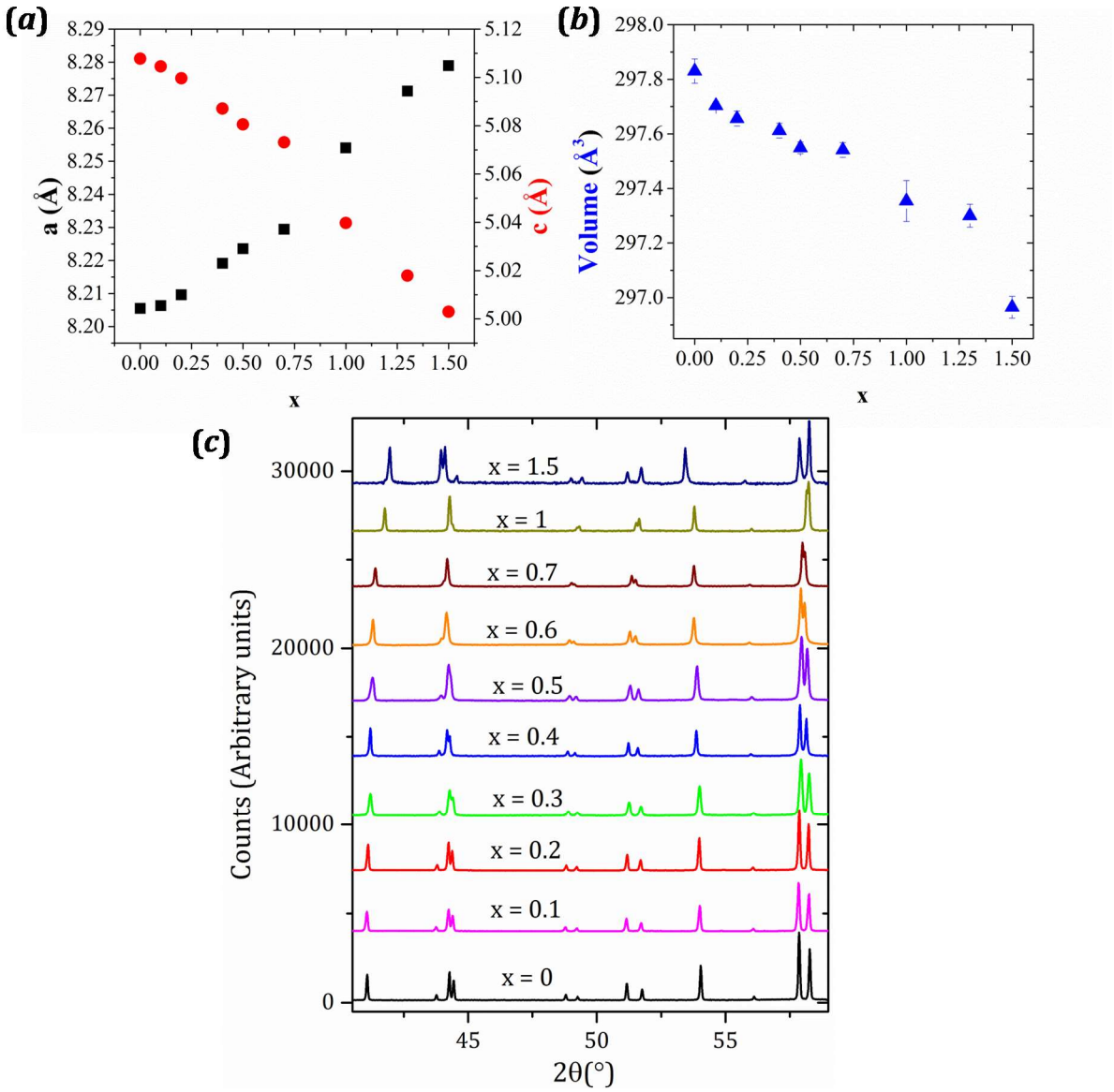

Figure 3-21 (*a*) Observed trend in the refined *a* and *c* lattice parameters for $La_3Ga_{5-x}Ge_{1+x}O_{14+x/2}$ vs '*x*', denoted by black squares and red circles respectively. (*b*) Change of the cell volume. (c) XRD patterns of $La_3Ga_{5-x}Ge_{1+x}O_{14x/2}$ samples synthesized by Pechini measured in PANanalytical ($K_{\alpha 1,Co} = 1.7890$ Å), this plot evidence a shift in the Bragg peaks with the change in compositions with no presence of peaks attributed to impurity phases.

Attempts to produce $La_3Ga_{5-x}Ge_{1+x}O_{14+x/2}$ samples for $x > 1.5$, or increasing the annealing temperature above the T_{decomp} resulted in the formation of a minority impurity phase with the composition $LaGa_{0.87(3)}Ge_{0.98(3)}O_{4.7(1)}$ determined by elemental Energy Dispersive X-ray (EDX) analysis in the TEM (see page 81). Phase indexing of this unreported phase was hindered due to the low intensity peaks of this minority phase and the strong overlapping with those peaks of the main langasite phase. Due to a lack of success to form $LaGa_{0.87(3)}Ge_{0.98(3)}O_{4.7(1)}$ in a greater proportion no further characterization of the impurity was carried out and only the composition of this phase is reported in this study.

Figure 3-22 shows the XRD patterns measured on two samples that were originated from the same initial mixture of precursor with a $La_3Ga_{4.4}Ge_{1.6}O_{14.3}$ (x = 0.6) nominal composition

prepared by Pechini. After an intermediate firing at 600 °C, the initial batch of reactants was split in two and annealed for 12 hours below and above T_{decomp} = 1100 °C at 1000 °C and 1300 °C. The PXRD pattern of $La_3Ga_{4.4}Ge_{1.6}O_{14.3}$ (x = 0.6) sintered at 1000 °C revealed the formation of a single phase langasite with no presence of unassigned peaks (see Figure 3-22). On the contrary, the same x = 0.6 precursor powder annealed above T_{decomp} at 1300 °C resulted in the formation of a lower-doped langasite majority phase and impurities. The phases related peaks are denoted by asterisks in Figure 3-22. The EDX analysis of this later impurity-rich sample ultimately allowed for the identification of $LaGa_{0.87(3)}Ge_{0.98(3)}O_{4.7(1)}$ as the composition of the more predominant impurity phase (see Figure 3-23-a). The majority langasite phase in this sample show a large compositional inhomogeneity averaged to $La_{3.0(2)}Ga_{4.5(5)}Ge_{1.5(4)}O_{4.2(2)}$. In Figure 3-23-$a$ the composition of the 'oxygen saturated langasite' $La_3GaGe_5O_{16}$ (denoted by a green triangle) is plotted along with the spotted phases (denoted by black squares) to account for the fact that the $LaGa_{0.87(3)}Ge_{0.93(3)}O_{4.7(1)}$ impurity, which is not reported in the literature, is located in an equidistant point to both $La_3GaGe_5O_{16}$ and $La_3GaGe_5O_{14}$ compositions.

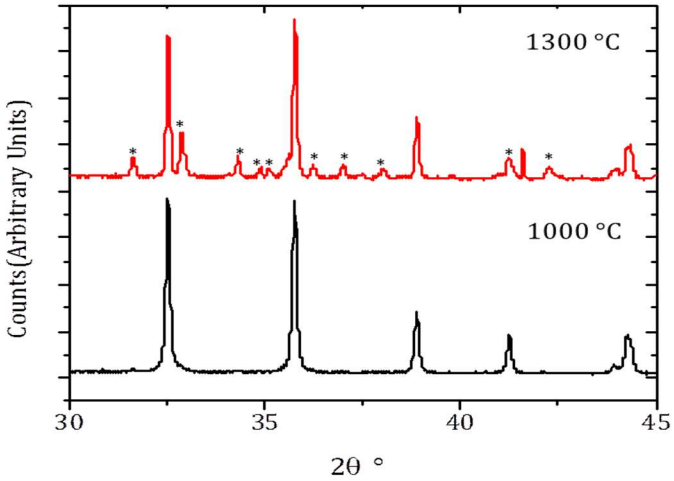

Figure 3-22 PXRD patterns of two samples with the $La_3Ga_{4.4}Ge_{1.6}O_{14.3}$ nominal compositions synthesized by Pechini and annealed at 1300 °C for 12 hours above its T_{decomp} (red) and below at 1000 °C (black). The asterisks denote extra peaks attributed to impurity phases.

The ternary phase diagram in Figure 3-23-b shows a more homogeneous cluster matching the nominal composition of x = 0.5 in a sample synthesized by Pechini at 1000 °C for 12 hours and SPS-sintered at 1100 °C for 5 min at 50 MPa. The conductivity of this sample is discussed in section 4.2.2 entitled 'Evaluation of the conductivity by AC impedance'. Plots $c-d$ show the EDX analysis of samples with x = 0, 1 and 1.5 nominal compositions (denoted by a red cross) prepared *via* Pechini and sintered at 1200, 850 and 800 °C respectively. The averaged analysed compositions in $c-d$ are as follows: $La_{3.02(6)}Ga_{4.55(5)}Ge_{1.43(4)}O_{14.21(2)}$, $La_{2.93(4)}Ga_{4.05(3)}Ge_{2.01(4)}O_{14.51(2)}$ and $La_{3.04(7)}Ga_{3.50(6)}Ge_{2.47(6)}O_{14.73(3)}$ respectively. These samples were characterized by NPD and NMR and these experiments are further discussed in Chapter 4.

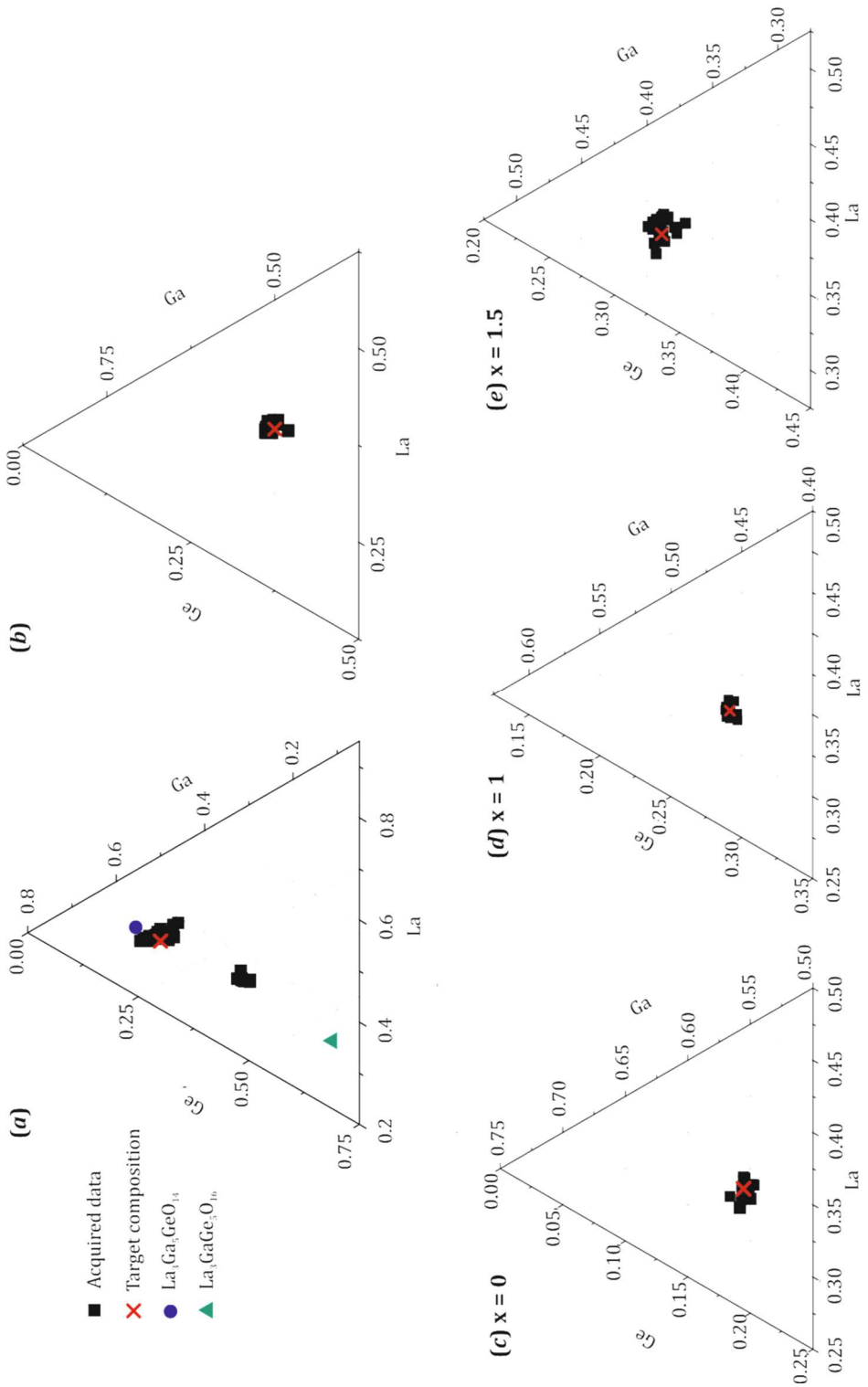

Figure 3-23 EDX analysis of langasites synthesized by Pechini: (a) sample with a $x = 0.6$ nominal composition annealed at 1300 °C for 12 hours, (b) $La_3Ga_{4.5}Ge_{1.5}O_{14.25}$ annealed at 1000 °C for 12 hours and SPS-sintered at 1100 °C for 5 min at 50 MPa and ($c-d$) x = 0, 1 and 1.5 nominal compositions sintered at 1200, 850 and 800 °C respectively. Nominal compositions are denoted by red crosses and the spotted phases by black squares. In (a) the 'oxygen saturated $La_3GaGe_5O_{16}$ langasite' is denoted by a green triangle and $La_3Ga_5GeO_{14}$ by a blue circle.

Table 3-13 Summary table of the actual EDX averaged compositions analysed

Nominal Targeted Compositions	Actual (EDX) Compositions
(a) $La_3Ga_{4.4}Ge_{1.6}O_{14.3}$	$La_{3.0(2)}Ga_{4.5(5)}Ge_{1.5(4)}O_{14.2(2)}$ + $LaGa_{0.87(3)}Ge_{0.93(3)}O_{4.7(1)}$
(b) $La_3Ga_{4.5}Ge_{1.5}O_{14.25}$	$La_{3.02(6)}Ga_{4.55(5)}Ge_{1.43(4)}O_{14.21(2)}$
(c) $La_3Ga_5GeO_{14}$	$La_{2.99(7)}Ga_{4.98(5)}Ge_{1.03(6)}O_{14.01(3)}$
(d) $La_3Ga_4Ge_2O_{14.5}$	$La_{2.93(4)}Ga_{4.05(3)}Ge_{2.01(4)}O_{14.51(2)}$
(e) $La_3Ga_{3.5}Ge_{2.5}O_{14.75}$	$La_{3.04(7)}Ga_{3.50(6)}Ge_{2.47(6)}O_{14.73(3)}$

In order to properly asses the introduction of extra oxygen into the langasite an extensive analysis of the elemental compositions of the doped synthesized phases was carried out by Energy Energy dispersive X-Ray analysis (EDX) in the transmission electron microscope (TEM). Dozens of particles for each doped compositions ($a - d$) were analysed and the data is mapped in the ternary phase diagrams introduced in Figure 3-23. For the convenience of the reader, a summary table correlating both nominal and EDX averaged compositions is given (see Table 3-13). Samples $b - e$ were annealed below its decomposition temperature (see Figure 3-20) and the EDX and target compositions are in good agreement with the biggest deviation of the EDX composition from the nominal composition is of a negligible ~0.2 %. The elemental analysis in the TEM for $La_3Ga_{5-x}Ge_{1+x}O_{14+x/2}$ compositions presented here thus demonstrates the successfully substitution of Ga for Ge at the desired ratio by the Pechini method.

3.4 Summary and Conclusion

During the whole of this chapter the synthetic exploration work carried out on over thirty doping approaches involving $La_3Ga_5MO_{14}$ with a langasite structure where M could be Si, Ge, Ti, Sn, Hf and Zr were presented. Amongst the compositions explored by the solid-state reaction method: $La_{2.5}Ce_{0.5}Ga_5GeO_{14.25}$, $La_3Ga_{4.7}Ge_{1.3}O_{14.15}$, $La_3Ga_{4.6}SiTi_{0.4}O_{14.2}$ and $La_3Ga_{4.8}Sn_{0.3}Ti_{0.9}O_{14.1}$ were able to accommodate a modest amount of interstitial oxides (0.71-1.79 %). A preliminary screening of their conductivity identified $La_3Ga_{5-x}Ge_{1+x}O_{14+x/2}$ as the most promising candidate showing an increase in conductivity of over two orders of magnitude from ~8.76×10^{-7} S·cm^{-} in $La_3Ga_5GeO_{14}$ to ~4.54×10^{-4} S·cm^{-1} in $La_3Ga_{4.7}Ge_{1.3}O_{14.15}$ (x = 0.3) at 700 °C.

The next logical step once the search for a good candidate was narrowed to $La_3Ga_{5-x}Ge_{1+x}O_{14+x/2}$ was to endeavour to approach the synthesis of these materials by an alternative route to solid-state reaction method in hopes to expand the solid solution regime and consequently the conductivity. The Pechini method lowered the formation of $La_3Ga_{5-x}Ge_{1+x}O_{14+x/2}$ by 500 °C from the solid-state reaction method. This allowed to times by five the amount of dopant incorporated into the structure 'x' from 0.3 ($\%_{O_{int}}$~1.07) in the solid-state reaction method up to x = 1.5 ($\%_{O_{int}}$~5.36). Such $\%_{O_{int}}$achieved by Pecihini is higher than the reported values in doped apatites and melilites structures (3.86 and 5.57 % respectively). This result demonstrates an outstanding flexibility shown by the $La_3Ga_5GeO_{14}$ langasite structure for the accommodation of interstitial oxide ions.

4 INTERSTITIAL OXIDE ION CONDUCTION IN THE ALIOVALENTLY DOPED $La_3Ga_{5-x}Ge_{1+x}O_{14+x/2}$ MEDIATED *via* A $(Ga/Ge)_2O_8$ UNIT

This chapter describes the structural and conductivity characterization of doped $La_3Ga_{5-x}Ge_{1+x}O_{14+x/2}$ compositions. The determination of the location of the extra oxygen introduced by doping and the induced local deformation was possible by the combined use of Solid-State ^{17}O and ^{71}Ga Nuclear Magnetic Resonance (NMR) techniques, high-resolution Neutron Powder Diffraction (NPD) and Density Functional Theory (DFT) calculations. The conductivity was determined by means of AC impedance spectroscopy and the mobility of the extra oxygen is also discussed in this chapter.

4.1 Experimental Methods

4.1.1 XRD and NPD

Powder neutron diffraction data was collected in the High Resolution Powder Diffraction instrument (HRPD) in ISIS, UK. The $La_3Ga_{3.5}Ge_{2.5}O_{14.75}$ data presented in this thesis was collected at 9, 297, 473, 673 and 873 K, $La_3Ga_4Ge_2O_{14.5}$ at 11 and 297 K and $La_3Ga_5GeO_{14}$ at 297 K. A closed-cycle refrigerator was used for the collection of data at 9 and 11 K

whereas an in situ furnace was employed for higher temperatures. Structural Rietveld refinement was performed with TOPAS refinement software[200].

X-ray powder diffraction patterns were collected in a PANalytical X'pert Pro diffractometer with a Co-source ($K_{\alpha 1,Co} = 1.7890$ Å) to corroborate the phase purity of the samples studied after undergoing sintering and conductivity experiments. The Rietveld refinement and Pawley fittings of the PANalytical data were also performed with TOPAS[200].

4.1.2 DFT calculations

Periodic plane-wave DFT calculations were performed using the VASP[244] and Castep[245] packages. Initial structural relaxations with VASP were run in a 2 × 2 × 2 supercell of the parent $La_3Ga_5GeO_{14}$ cell, with a 2 × 2 × 3 k-point grid. Cell parameters and atomic positions were optimized until all atomic forces were below 0.01 eV/Å, using the PBE functional[246], projector augmented-wave potentials[247], and a plane-wave cut-off energy of 600 eV. Calculation of NMR parameters was carried out using GIPAW[248-250] as implemented in Castep, after structures had been re-optimized with the same functional and cut-offs as those used with VASP, and using pseudo-potentials automatically generated on-the-fly by Castep. The DFT calculations were performed by Dr Matthew Dyer.

4.1.3 Solid-State NMR Spectroscopy

The NMR data acquisition and analysis presented in this thesis was carried out by Dr Frederic Blanc.

4.1.3.1 ^{17}O NMR

Oxygen ^{17}O isotope enrichment was performed in as prepared $La_3Ga_{5-x}Ge_{1+x}O_{14+x/2}$ samples with x = 0, 0.5, 1 and 1.5 following the post synthesis oxygen exchange protocol in ref. 251 consisting of heating the samples in a sealed Pyrex tube under 60 % ^{17}O enriched O_2 gas (Isotec) at 750 °C for 24 hours using a heating-cooling rate of 5 ° min^{-1}.

^{17}O NMR experiments were carried out on 9.4 T Bruker Advance III 400 MHz spectrometer using a Bruker triple resonance 4 mm HXY (in double resonance mode) tuned to X = ^{17}O at $\nu_0 = 54.25\ MHz$ and spinning the samples at a MAS rate of $\nu_r = 14\ kHz$, and on a 20 T Bruker Advance II 850 MHz spectrometer using a Bruker triple resonance 3.2 mm HXY (in double resonance mode) tuned to X = ^{17}O at $\nu_0 = 115.28\ MHz$ and spinning the samples at a MAS rate of $\nu_r = 22\ kHz$. Rotor synchronized Hahn echo experiments were carried out with one rotor period using a pulse length π/2 = 1 μs at a rf field amplitude of $\nu_1 = 83\ kHz$ and a recycle delay of 1 s. Two-dimensional triple-quantum MAS experiments[252,253] were performed at 9.4 T using a z-filter pulse sequence.[254] Hard and soft pulses were performed at rf field amplitudes of 83 kHz and 10 kHz, respectively. The experimental ^{17}O isotropic chemical shifts $\delta_{iso,cs}$ were obtained from the 3QMAS z-filter data. The ^{17}O quadrupolar coupling constant C_Q and asymmetry parameters η_Q[255], are obtained from fitting the ridge line shapes and checked to be in agreement with the P_Q obtained independently from the δ_2 and δ_1 positions[256].

4.1.3.2 ^{71}Ga NMR

^{71}Ga NMR experiments were performed on a 20 T Bruker Advance II 850 MHz spectrometer using a Bruker triple resonance 1.3 mm HXY (in double resonance mode) for fast MAS experiments at $\nu_r = 65\ kHz$ and a Bruker triple resonance 3.2 mm HXY (in double resonance mode) for static experiments tuned to X = ^{71}Ga at $\nu_0 = 259.3\ MHz$. One-

dimensional MAS NMR spectra were recorded using a rotor-synchronized (1 period) Hahn echo sequence with selective pulses ($\pi/2$ pulse length of 4 μs) at a radio-frequency (rf) field amplitude of $\nu_1 = 16\ kHz$. A double-frequency sweep (DFS)[257] pulse of 2 ms from 800 to 200 kHz at a rf field amplitude of 15 kHz giving an optimum signal enhancement of 2 was used for all MAS experiments. One-dimensional static NMR spectra were obtained with QCPMG acquisition with 3000 echos and 204 points per echo. A recycle delay of 2 s, sufficient to obtain quantitative data, was used for all ^{71}Ga experiments.

The ^{71}Ga and ^{17}O chemical shifts were externally referenced to a 1M solution of $Ga(NO_3)_3$ in water and to water respectively, all at 0.0 ppm. NMR data were processed and simulated using the Bruker Topspin package.

4.1.4 Sintering of doped $La_3Ga_{5-x}Ge_{1+x}O_{14+x/2}$

Dense specimens for impedance measurements with > 80 % of the theoretical density were prepared by annealing at 1275 °C for 24 hours for $La_3Ga_{5-x}Ge_{1+x}O_{14+x/2}$ with $0 \leq x \leq 0.2$. For the intermediate $0.3 \leq x \leq 0.7$ region, dense pellets were prepared by Spark Plasma Sintering (SPS) using a 200 ° min^{-1} heating rate, at 1000-1100 °C hold for 4-5 min with an applied pressure of 50 MPa. All SPS-sintered samples were mechanically milled prior to their sintering. Powders were combined with eight ø = 10 mm sized balls of zirconia in a ø = 40 mm zirconia pot at a rotation speed of 350 rpm for 15 cycles operating with direction reversal and a 10 min pause time after each 15 min cycle. 2.5-6 g of fine milled powders were pressed in a 20 mm Outside Diameter (OD) and 40 mm tall graphite die. Alternatively, the SPS sintering of highly doped $La_3Ga_{5-x}Ge_{1+x}O_{14+x/2}$ compositions with x = 1 and 1.5 was carried out in a double acting WC die[185] at a pressure of 550 MPa which allowed to decrease the sintering temperature down to the synthetic temperatures of 850 and 800 °C for x = 1 and 1.5 respectively. The sintering temperatures were dwelled for 5 min and a heating and cooling rate of 200° min^{-1} was used. In this smaller double acting die with a 5 mm OD and 12 mm length, the amount of powder was reduced to 1.5 g. All SPS experiments were conducted under vacuum in a Sumitomo Coal SPS-1050 SPS apparatus able to exert a maximum load of 100 kN and produce a pulsed current as high as 5 kA for an applied voltage of 10 V. Rapid pulses of 3 ms in length were used with a pattern of 12:2 on and off pulses. After undergoing SPS-sintering, the graphite contaminated specimens were heated at 700 °C for 60 hours under flowing oxygen. The complete removal of graphite was verified by CHN analysis.

Two compositions $La_3Ga_4Ge_2O_{14.5}$ (x = 1) and $La_3Ga_{3.5}Ge_{2.5}O_{14.75}$ (x = 1.5) were sintered by Hot Isostatic Pressing (HIP). These powders were encapsulated in ⌀ = 8 mm and 10 mm long Ag cans under vacuum. Sealed Ag cans were HIPed in an ASEA QIH-3 hot isostatic press using a molybdenum furnace and ultra-high purity argon. The HIP cycle consisted of the application of a pressure of 300 MPa for eight hours with simultaneous heating of the samples at their synthetic temperatures: 850 °C for $La_3Ga_4Ge_2O_{14.5}$ and 800 °C for $La_3Ga_{3.5}Ge_{2.5}O_{14.75}$. HIP experiments were carried out by Michael Gaultois.

4.1.5 Conductivity

The electrical properties of the materials studied here have been determined by means of AC Impedance spectroscopy using an Agilent E4980 LCR meter over the 20 Hz - 2 MHz frequency range using 300 mV perturbation voltage and a Solartron 1255B Frequency response analyzer coupled to a Solartron 1287 electrochemical interface and a 1296 Dielectric + FRA equipment over the 100 mHz - 1 MHz frequency range, using the same perturbation voltage of 300 mV. The measurements were carried out using compressed dry air at an interval of temperatures ranging from 350 to 1000 °C. Gold wires were attached

with gold paste to perform as electrodes after undergoing a heating treatment at ~625 °C for 5 hours. The $La_3Ga_{4.5}Ge_{1.5}O_{14.25}$ pO_2-dependence with the conductivity at 10^{-15} - 1 atm pO_2 was evaluated at 400, 500, 600 and 800 °C by a controlled mixing of Ar, O_2, CO and CO_2 in different ratios. The partial oxygen pressure was monitored by an YSZ potentiometric sensor and equilibration of the samples with the gas environment was ensured at each data point collected by the dwelling of gases for several hours.

HIP-sintered $La_3Ga_4Ge_2O_{14.5}$ (x = 1) and SPS sintered $La_3Ga_{4.65}Ge_{1.35}O_{14.175}$ (x = 0.35), $La_3Ga_{4.5}Ge_{1.5}O_{14.25}$ (x = 0.5), $La_3Ga_{4.45}Ge_{1.55}O_{14.275}$ (x = 0.55) and $La_3Ga_{4.3}Ge_{1.7}O_{14.35}$ (x = 0.7) were coated with a thin layer of gold and analysed by Scanning Electron Microscopy (SEM) in a Hitachi S-4800.

The possibility of proton conduction was investigated in $La_3Ga_5GeO_{14}$ by Thermal Gravimetric Analysis (TGA) in a TA Instruments Q600 thermal analyser. ~100 mg of powders were heated up to 1000 °C in an alumina crucible at a rate of 3° min^{-1} with a gas flow rate of 50 ml/min (compressed air, BOC). The instrument was calibrated using ZrO_2 as the standard material.

4.2 Results and discussion

4.2.1 Structural characterization

Although challenging, as diffraction is a technique that works for long range order and interstitials are disordered sites with a low occupancy, NPD has proven very valuable to probe the location of interstitial oxides[61,119,129,130,144]. In this thesis, high-resolution NPD studies of $La_3Ga_5GeO_{14}$ (x = 0), $La_3Ga_4Ge_2O_{14.5}$ (x = 1) and $La_3Ga_{3.5}Ge_{2.5}O_{14.75}$ (x = 1.5) were undertaken in order to locate the interstitial oxygen and induced local deformation on the neighbouring sites. Moreover, for the doped compositions $La_3Ga_4Ge_2O_{14.5}$ (x = 1) and $La_3Ga_{3.5}Ge_{2.5}O_{14.75}$ (x = 1.5) the data was acquired at very low temperatures of 11 and 9 K respectively so as to get minimal complication from the thermal displacement of the atoms. Additionally, data at the higher temperatures of 200, 400 and 600 °C was collected for $La_3Ga_{3.5}Ge_{2.5}O_{14.75}$ (x = 1.5), which allowed us to corroborate the consistency of the proposed model throughout a wider temperature frame, also closer to the operating conditions of a SOFC.

The presence of additional oxygen is manifest in the nuclear scattering density map of $La_3Ga_{3.5}Ge_{2.5}O_{14.75}$ (shown in Figure 4-1) by the presence of unassigned scattering density in the vicinity of the 6-membered tunnels displaced towards the C and D tetrahedral sites. Figure 4-1 depicts highly disordered scattering density attributed to various new oxygen sites rather than a well-defined sole interstitial site. Further extra scattering density around other atomic sites is attributable to positional disorder associated with the local structural relaxation required to accommodate the oxygen excess.

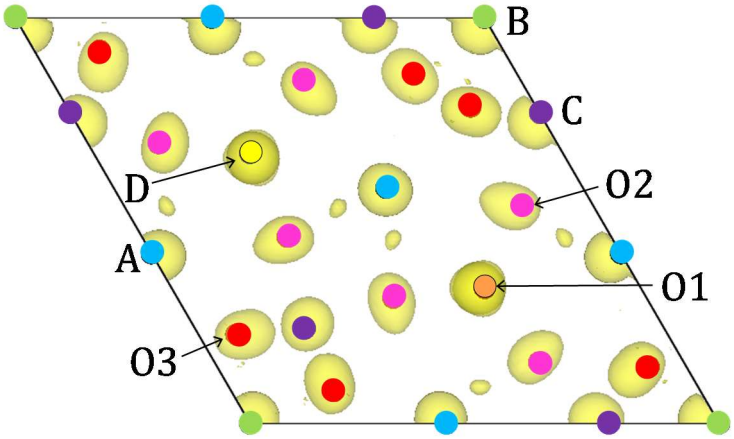

Figure 4-1 Crystallographic identification of interstitial oxide sites in $La_3Ga_{3.5}Ge_{2.5}O_{14.75}$ (x = 1.5) at 9 K. The atoms in $La_3Ga_5GeO_{14}$ (x = 0) are overlaid onto the Maximum Entropy Map (MEM) of the unit cell viewed along [001]. The A site occupied by La is given in cyan, B in green, C in violet and D in yellow. The three framework oxygen sites are O3 in red, O2 in magenta and O1 in orange. The yellow surfaces represent regions of positive scattering density calculated by MEM. Note that there are some positions which do not correspond to the sites in the parent phase, which are due to interstitial oxide ions.

4.2.1.1 DFT model

To overcome the challenging task of refining the atomic coordinates of disordered low occupancy oxide positions inducing local strain, a DFT averaged model approach was carried out. This approach provides us with a suitable model to use as a starting point for the refinement. $2 \times 2 \times 2$ supercells with the $La_3Ga_4Ge_2O_{14.5}$ (x = 1) composition were constructed, with additional oxide ions placed at locations of high nuclear scattering density, and their geometries relaxed with density functional theory (DFT). The lowest energy $2 \times 2 \times 2$ DFT calculated supercell (Figure 4-2 $a-c$) was collapsed into a $1 \times 1 \times 1$ $P321$ cell to use as a starting point in the Rietveld refinement of the HRPD data. In the $2 \times 2 \times 2$ supercell shown in Figure 4-2 $a-c$, the extra oxygen is found in the 6-membered channels, coordinated to both C and D sites forming an edge-sharing M_2O_8 unit.

The predicted energetically favourable location of the extra oxygen incorporated by doping within M_2O_8 (coloured in grey in Figure 4-2 $a-c$) is found in an existing material with the formula: $La_3GaGe_5O_{16}$[258] (Figure 4-2 d and e), which we refer to as the oxygen saturated langasite. Along the a-axis (Figure 4-2-d), the oxygen saturated langasite ($La_3GaGe_5O_{16}$) with a $P\bar{1}$ space group can be seen as the stacking of large La cations and octahedra with alternating layers of 4 and 3-connected tetrahedra (plotted in yellow and violet respectively) and two pseudo square based pyramid Ge polyhedra sharing one edge (Ge_2O_8, in grey). The bond lengths and angles of this Ge_2O_8 unit present in $La_3GaGe_5O_{16}$ are given in Appendix 5. The view along the b-direction in Figure 4-2-e reveals the presence of two types of channels: a 6-membered channel analogous to that of langasites containing one La and a 'collapsed' channel with 2 La sites (the new A' sites are coloured in a darker shade of blue for distinction). The collapsed channels are formed as a consequence of the displacement of the 3-connected D tetrahedral site across the channel to form a Ge_2O_8 unit with a former tetrahedral D site. As a consequence of the displacement of these tetrahedra, the two former 4-connected C sites bridged by this D site are now 3-connected (hence coloured in yellow). The formula of $La_3GaGe_5O_{16}$ can be expressed as $AA'_2BCD_2E_2O_{16}$ where A' and E account for the newly arisen A and five-coordinated sites respectively.

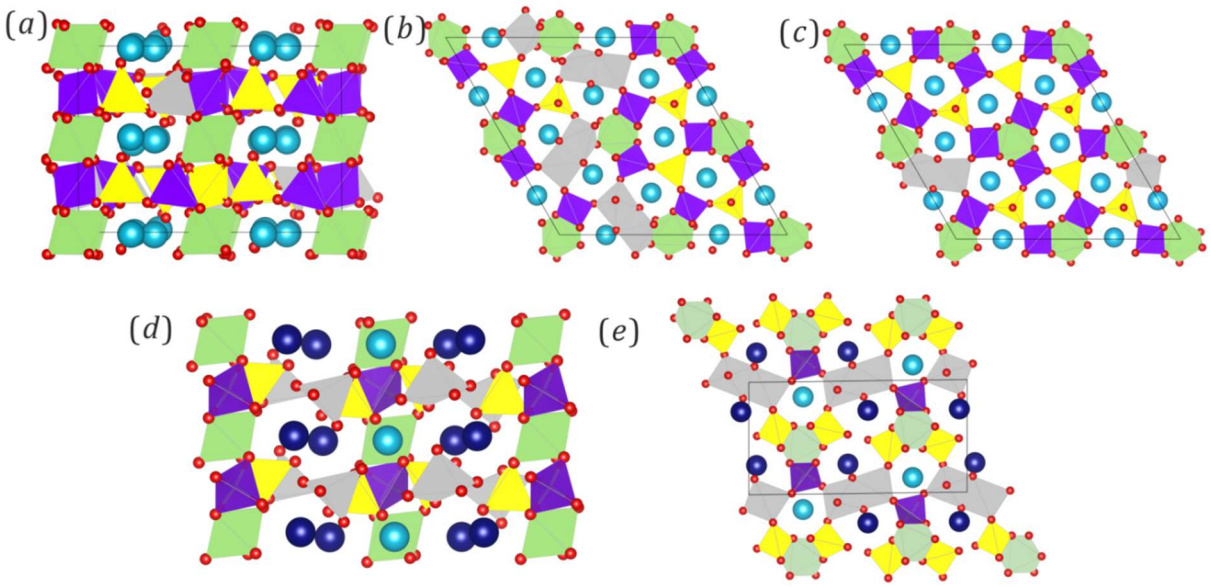

Figure 4-2 View of the $La_3Ga_4Ge_2O_{14.5}$ $2 \times 2 \times 2$ DFT calculated supercell along [100] (a). The $2 \times 2 \times 1$ top (b) and bottom (c) layers of interconnected polyhedra are plotted separately along the [001] direction to avoid the overlapping of the 5-coordinated (grey) sites with the 2d and 3f sites. The 'oxygen saturated langasite' with the formula $La_3GaGe_5O_{16}$ and space group $P\bar{1}$ (No. 2) is shown along [100] in (d) and along the [010] direction in (e). The La cations lying in the merged channels are denoted in navy for distinction.

Overall, to account for the formation of the Ge_2O_8 pairs the collapsed $P321$ introduces three new oxygen crystallographic sites namely O4-O6 (See Figure 4-5 introduced later on in this chapter when the refined model is presented in 4.2.1.2). All bond lengths and distances involved in the four Ge_2O_8 local environments predicted in the $2 \times 2 \times 2$ $La_3Ga_4Ge_2O_{14.5}$ supercell as well as the averaged Ge_2O_8 environment in the collapsed $P321$ cell used as the starting point of the refinement are given in the Appendix 5.

4.2.1.2 Locating the O_{int} by high-resolution NPD

This section deals with the validation of the DFT averaged-model as the most suitable starting model for the refinement of high-resolution NPD diffraction data of doped langasites. A summary of the step-by step refinement strategy followed for the attainment of the final model is presented.

The possibility of the lowering of the symmetry of the cell upon doping was tested by performing a Pawley fitting of the NPD data in the space groups $P321$ and $P1$. The goodness of fit for these fittings are compared in Table 4-1. Although there was a great improvement in the graphical fits as $P1$ added many Bragg reflections, the goodness of fits are worse, as $P1$ also decreased R_{exp} significantly, while decreasing R_{wp} not as much and $P321$ was retained for Rietveld refinement. For all compositions at all the temperatures studied, the best fit of the data was obtained for a $P321$ space group and no symmetry changes were observed in the aforementioned temperature range from 9 to 873 K (see Table 4-1 for fitting errors and Appendix 3 for a graphic representation of the Pawley fits).

Table 4-1Comparison of the R_{wp}, R_{exp} and S parameters for the Pawley fitting of $La_3Ga_5GeO_{14}$, $La_3Ga_4Ge_2O_{14.5}$ and $La_3Ga_{3.5}Ge_{2.5}O_{14.75}$ at the temperatures specified in $P321$ and $P1$ space groups.

Composition	Temperature (K)	HPRD d-spacing	$P321$		$P1$	
			R_{wp} / R_{exp}	S	R_{wp} / R_{exp}	S
$La_3Ga_5GeO_{14}$	297	0.8-2.6 (b1) 0.8-3.7 (b2) 2.6-7.9 (b3)	2.032 / 1.786	1.138	1.751 / 1.412	1.240
$La_3Ga_4Ge_2O_{14.5}$	11	0.6-2.6 (b1) 0.8-3.9(b2) 2.5-8.7(b3)	1.837 / 0.961	1.911	1.571 / 0.760	2.067
	297	0.6-2.6 (b1) 0.8-3.9(b2) 2.5-8.7(b3)	2.435 / 1.771	1.375	2.038 / 1.399	1.457
$La_3Ga_{3.5}Ge_{2.5}O_{14.75}$	9	0.5-2.2 (b1) 0.7-3.3 (b2) 1.1-8.7 (b3)	1.363 / 0.670	2.034	1.020 / 0.338	3.019
	297	0.5-2.2 (b1) 0.7-3.3 (b2) 1.1-8.7 (b3)	1.854 / 1.014	1.829	1.271 / 0.673	1.889
	473	0.5-2.2 (b1) 0.7-3.3 (b2) 1.1-8.7 (b3)	1.293 / 0.709	1.824	1.294 / 0.469	2.761
	673	0.5-2.2 (b1) 0.7-3.3 (b2) 1.1-8.7 (b3)	1.553 / 0.919	1.690	1.467 / 0.825	1.778
	873	0.5-2.2 (b1) 0.7-3.3 (b2) 1.1-8.7 (b3)	1.230 / 0.815	1.509	1.715 / 0.729	2.352

To test the veracity of the DFT averaged model approach, the evolution of the goodness of fit '*S*'or chi 'χ' fitting parameters at different stages of the Rietveld refinement were tracked and summarized in Table 4-2, where the comparison between the Pawley fit and the refinement of the neutron data using the parent model as a starting point are also given. The Pawley fitting of the data into a *P*321 space group set the 'best possible' fitting parameters which allowed us to assess the goodness of the refined models.

The Rietveld refinements of two possible models were initially attempted: the parent $La_3Ga_5GeO_{14}$ model and the collapsed DFT averaged *P*321 cell were used as shown in Figure 4-4. The two approaches to the refinement lead to different outcomes for the parent $La_3Ga_5GeO_{14}$ and doped $La_3Ga_4Ge_2O_{14.5}$ and $La_3Ga_{3.5}Ge_{2.5}O_{14.75}$ langasites. The attempt to refine the undoped $La_3Ga_5GeO_{14}$ with the averaged DFT cell as a starting point failed as it revealed no presence of extra oxygen sites represented in the predicted model (as expected), leading to nonphysical occupancies and thermal parameters of these sites. Thus the refinement of the undoped $La_3Ga_5GeO_{14}$ langasite was stopped at the parent model stage.

When using the parent $La_3Ga_5GeO_{14}$ langasite as the initial model for the Rietveld refinement of $La_3Ga_4Ge_2O_{14.5}$ and $La_3Ga_{3.5}Ge_{2.5}O_{14.75}$ NPD data, the framework structure of non-electroneutral $La_3Ga_4Ge_2O_{14}$ and $La_3Ga_{3.5}Ge_{2.5}O_{14}$ compositions were refined at first leading to a poor visual fit of the data (see Figure 4-3-a). The refinement of the framework

structure was followed by the inclusion of extra oxygen into a general position to account for the presence of the interstitial. This extra oxygen was located in the middle of the 6-membered rings within the layer of tetrahedra where the interstitial oxygen lies in the melilite structure. When refined, the atomic positions for the new oxygen site moved away from the centre of the channel into the vicinity of C and D tetrahedral sites. Attempts to split the neighbouring sites (C, D, La, and O1-O3) to pinpoint the local relaxation around the interstitial failed to describe a local environment with suitable O-O distances ($d_{O2-O_{int}}$ = 1.2 Å). It was therefore concluded that the inclusion of a single interstitial site was not sufficient to probe the relaxation of the local environment in doped langasites.

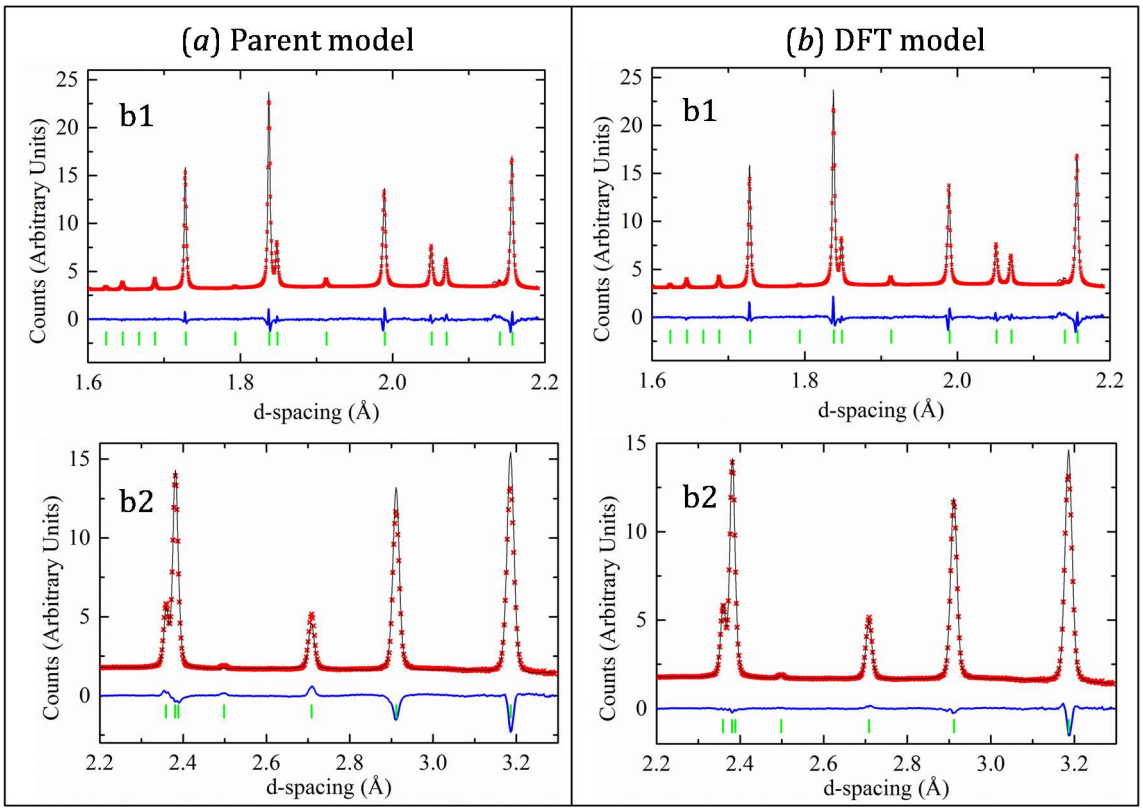

Figure 4-3 NPD Rietveld refinement of $La_3Ge_{3.5}Ge_{2.5}O_{14.75}$ at 9 K using two different approaches: (a) parent model ($R_{wp} = 2.487, R_{exp} = 0.726$ and $S = 3.425$) and (b) the initial refinement *via* a DFT model ($R_{wp} = 2.003, R_{exp} = 0.726$ and $S = 2.757$). Top figures account for the backscattering bank (b1) and the bottom figures for the detector at 90° (b2).

An initial Rietveld refinement *via* an averaged DFT model lowered the goodness by ~10 % from 2.249 to 2.052 in $La_3Ga_4Ge_2O_{14.5}$ (x = 1) at 11 K and by a higher ~20-30 % from 3.425 to 2.757 in $La_3Ga_{3.5}Ge_{2.5}O_{14.75}$ 9 K with respect to the former parent model (see Table 4-2). Due to this improvement on the goodness of fit obtained by the DFT averaged model and the fact that the calculated position of the extra oxygen sites also matched the extra intensity observed in the nuclear scattering map shown in Figure 4-1, this model was retained for further refinement.

Figure 4-3 accounts for the Rietveld refinement of $La_3Ga_{3.5}Ge_{2.5}O_{14.75}$ (x = 1.5) at 9 K using these two approaches. Two different d-spacing ranges are shown in the banks with the highest resolution 1.6-2.2 Å in bank 1 and 2.2-3.2 Å in bank 2. This figure demonstrates bigger mismatches between the calculated and observed peaks for the parent model approach in comparison with the DFT model approach.

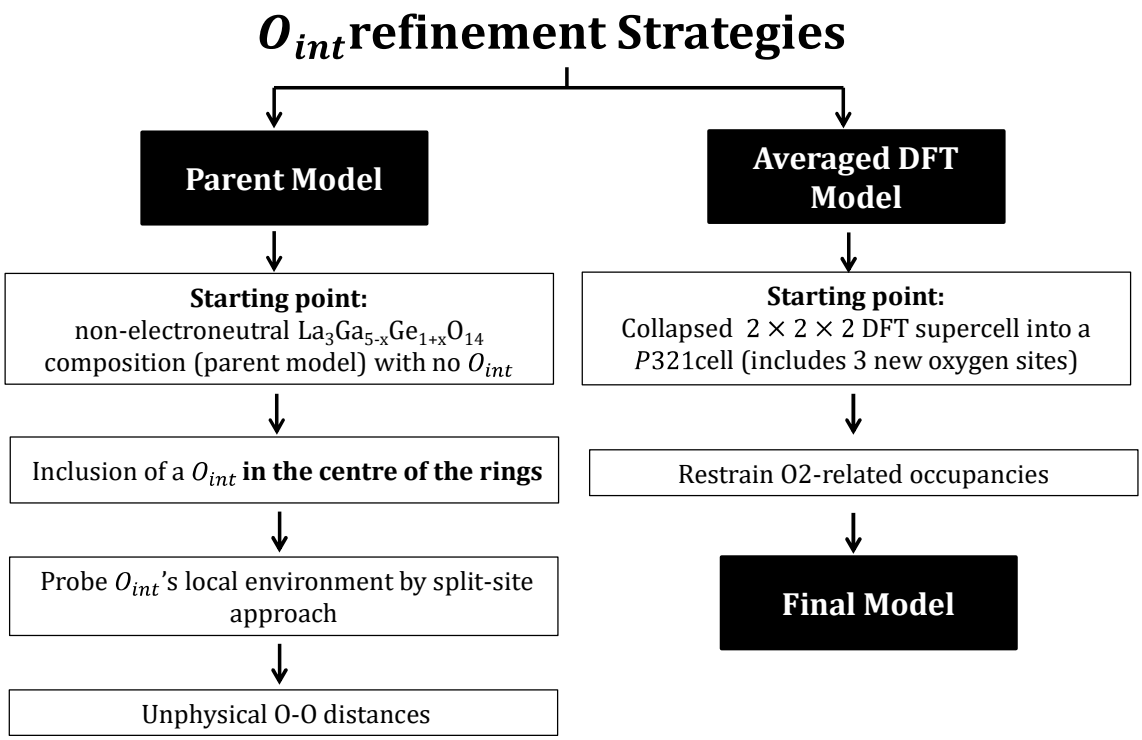

Figure 4-4 Flow-chart showing the refinement steps of the two different refinement strategies undertaken in this work.

Table 4-2 Evolution of *S* values chart for the refinement of the different $La_3Ga_{5-x}Ge_{1+x}O_{14+x/2}$ compositions studied at various temperatures ranging from 9 to 873 K.

	$S_{La_3Ga_5GeO_{14}}$	$S_{La_3Ga_4Ge_2O_{14.5}}$		$S_{La_3Ga_{3.5}Ge_{2.5}O_{14.75}}$				
	297 K	11 K	297 K	9 K	297 K	473 K	679 K	873 K
Pawley fit	1.138	1.911	1.375	2.034	1.829	1.824	1.497	1.509
↓	↓	↓			↓			
Parent model	1.493	2.249	1.736	3.425	3.077	2.625	1.794	1.976
↓		↓			↓			
Original DFT Averaged model		2.052	1.622	2.757	2.460	2.209	1.643	1.614
↓								
occO5 = 3occO6		2.034	1.543	2.544	2.221	1.972	1.444	1.554
↓								
Restrain O2-related occupancies		2.029	1.538	2.527	2.201	1.949	1.429	1.532
↓								
Final model		2.021	1.524	2.516	2.187	1.936	1.421	1.485

A polyhedral representation of the final model for $La_3Ga_{3.5}Ge_{2.5}O_{14.75}$ at 9 K is given in Figure 4-5, which introduces six Ge_2O_8 environments found in a $La_3Ga_{3.5}Ge_{2.5}O_{14.75}$ $2 \times 2 \times 2$ supercell. Additionally, a $2 \times 2 \times 1$ section of the $La_3Ga_{3.5}Ge_{2.5}O_{14.75}$ supercell along the c-axis is given in (b) in order to avoid the overlapping of different types of polyhedral along this direction. In Figure 4-5 the six oxygen sites (framework O1-O3 sites and new O4-O6 sites) are plotted in different shades of red for distinction. The sites named O4 and O6 are the two edge sharing oxygen sites in Ge_2O_8. In the later discussion of the refined model we referred to O6 as the incorporated extra oxygen as it is located closer to the La site in the centre of the channel (See view of the refined $La_3Ga_{3.5}Ge_{2.5}O_{14.75}$ model at 9 K along the a-axis in Figure 4-5-b where O6 is depicted in maroon). O4 located at the opposite end of the edge in Ge_2O_8, is referred as 'displaced O2'. O4 accounts for the displacement of O2 bridging the C and D sites adjacent to O6 over 1 Å apart from its original position, away from the interstitial site. From the DFT model an expected ratio of 1:1 between O6 and O4 at the Ge_2O_8's edge is expected. The preliminary refinement of the DFT model showed a good agreement to the expected 1:1 ratio between O4 and O6 sites. Moreover, the refined occupancies for these sites were also in good agreement with the expected values of 1/8 in $La_3Ga_{3.5}Ge_{2.5}O_{14.75}$ and 1/12 in $La_3Ga_4Ge_2O_{14.5}$.

In the original DFT model, the incorporation of O6 into a Ge_2O_8 pair entails the relaxation of one O2 oxygen per Ge_2O_8 binding the tetrahedral C site into the new crystallographic site O5 (plotted in pale pink in Figure 4-2). O5 moves away from the interstitial which opens up

the O5-D-O6 angle to ~80°. The preliminary refinement showed a much higher occupancy of O5 than originally suggested by the DFT model, indicating that a greater number of O2 framework sites were relaxed in order to accommodate the Ge_2O_8 unit. This number was round to three times the predicted value ($i.e.$ occO5 = 3occO6) as suggested from the refined value. Presumably, two O5 bind the D (yellow) metal centre and the third O5 site binds the C metal centre (in violet) as pointed out by the original DFT model. The goodness of fit between the two models with occO5 = occO6 (original DFT model) and occO5 = 3occO6 were compared to clarify whether further split of the O2 site was actually needed. Besides the different occupancies of O5, there were no significant differences between the two models showing few structural changes in terms of bond lengths and angles between the refined and calculated Ge_2O_8 unit. The refinement of the occO5 = 3occO6 model show better goodness of fit and was therefore retained for further refinement ($e.g.$ there is an improvement in S from 2.757 to 2.545 for the 9 K data set of $La_3Ga_{3.5}Ge_{2.5}O_{14.75}$, see Table 4-2).

The next step of the refinement involved the constraint of the fractional occupancies of O2, O4, O5 and O6 to their expected ratios ($i.e.$ O2 = 1-4occO6, occO5 = 3occO6 and occO4 = occO6). The occupancies of O1 and O3 gave values close to unity in the initial refinement and were fixed to 1. Additional constraints regarding the occupancies of Ga and Ge were also introduced so as to match the sum of Ga and Ge on each site to add up to 1 ($i.e.$ for a given x site the occupation of Gex was constrained to be equal to 1-Gax). Moreover, the total Ge content was constrained in the refinement so as to match the calculated oxygen content in order to attain charge neutrality in the refined composition. Once constraints were applied all the thermal parameters were described anisotropically (ADPs) with the exception of the O2-related sites: O4, O5 and O6, whose thermal parameters B_{eq} were constrained as identical.

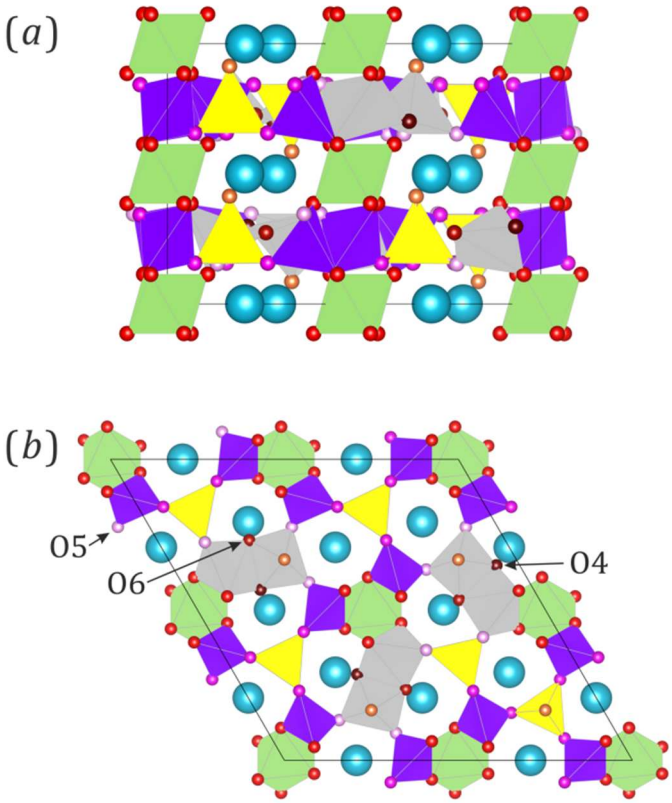

Figure 4-5 Polyhedral representation of the $2 \times 2 \times 2$ Rietveld refined $La_3Ga_{3.5}Ge_{2.5}O_{14.75}$ structure using HRPD bank 1 (168°) and 2 (90°) data collected at 9 K. The $2 \times 2 \times 2$ along [100] in (a) was split in two $2 \times 2 \times 1$ top (b) and bottom (c) layers. The same colour scheme as Figure 4-2 (see page 88) and Figure 1-11 (see page 17) is used as well as 3 different shades of red for the new oxygen sites: mahogany for the displaced O2 (O4) site, pale pink for the split O2 site (O5) and maroon for the incorporated extra oxygen (O6).

The final step of the refinement involved the removal of O2-related occupancy constraints that were set for O2 and O4-O6. This was followed by the refinement of anisotropic thermal parameters for O2 and O5 which have high enough occupancies (~0.5 and 0.35 respectively vs an occupancy of ~0.115 for O4 and O6 for $La_3Ga_{3.5}Ge_{2.5}O_{14.75}$) to have meaningful ADPs.

In the combined bank 1-3 HRPD Rietveld refined model of $La_3Ga_{3.5}Ge_{2.5}O_{14.75}$ at 9 K shown in Figure 4-5, the refined oxygen occupancies match the expected values pointing at the success of the DFT averaged model which predicted the presence of extra oxygen mediated *via* a Ge_2O_8 unit. This oxygen ratio is also maintained for the $La_3Ga_4Ge_2O_{14.5}$ composition studied and other temperatures evaluated introduced later on in this chapter in 4.2.1.4. A summary of the refined total oxygen content in the final models is introduced in Table 4-3. The total oxygen content is slightly over estimated in $La_3Ga_{3.5}Ge_{2.5}O_{14.75}$, although close to the expected value of O_{TOTAL} ~14.75. Final structural parameters and fit of the calculated final model to the actual data are given in Appendix 4.

Table 4-3 Refined oxygen occupancies in the final models

	Temperature (K)	O2	O4	O5	O6	O_{TOTAL}
$La_3Ga_5GeO_{14}$	297	0.982(3)				13.89(3)
$La_3Ga_4Ge_2O_{14.5}$	11	0.660(4)	0.083(1)	0.261(4)	0.089(2)	14.56(7)
	297	0.646(2)	0.085(1)	0.262(2)	0.084(2)	14.46(4)
$La_3Ga_{3.5}Ge_{2.5}O_{1414.75}$	9	0.666(3)	0.120(2)	0.247(4)	0.123(1)	14.94(6)
	297	0.570(3)	0.110(3)	0.351(4)	0.121(2)	14.90(7)
	473	0.618(3)	0.118(2)	0.294(2)	0.122(1)	14.91(5)
	673	0.624(3)	0.114(2)	0.286(2)	0.123(1)	14.89(5)
	873	0.499(3)	0.115(2)	0.410(2)	0.123(1)	14.89(5)

In all the refinements, the background was fitted in a Chebyshev function. In the refinement of the $La_3Ga_{3.5}Ge_{2.5}O_{14.75}$ 9-673 K data-set with a lower d-spacing (see Table 4-1) the peaks shape were fitted using an expanded pseudo-Voigt function to account for Stephens' model[208] for microstrain broadening for time-of-flight data in a trigonal geometry for bank 1 and 2 and a pseudo-Voigt function for bank 3 with a lower resolution. The 873 K data set, the highest temperature that $La_3Ga_{3.5}Ge_{2.5}O_{14.75}$ was analysed at, is an exception and the Stephen's model for a triclinic geometry was used instead. At the high temperature of 873 K, lowering the Stephens' corrections geometry to triclinic improved the goodness of fit by ~12 % from 1.695 to the final value of 1.485. $Difa$ were refined for b1-b3 in the combined refinement whereas $Difc$ constants were refined for the lower resolution banks at 90°(b2) and 30°(b3)[259].

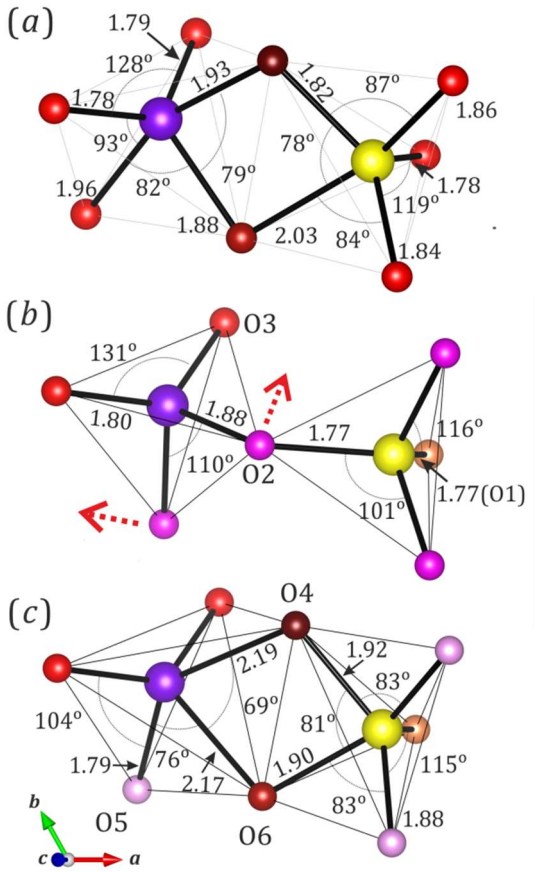

Figure 4-6 Local environments around the interstitial oxygen in the DFT calculated supercell (*a*), and in the refined structure (*b* and *c*). (*a*) is showing one of the four $(Ga/Ge)_2O_8$ pairs present in the $2 \times 2 \times 2$ DFT supercell. The bond angles and interatomic distances are very similar amongst the four different pairs resembling a square-based pyramid geometry, therefore only one is shown in the main text for simplicity (See Appendix 5 for all DFT predicted $(Ga/Ge)_2O_8$ dimers). In (*b*) the interstitial oxygen is not present and O2 (magenta) is bridging the C (violet) and D (yellow) sites. In the refined $(Ga/Ge)_2O_8$ unit (*c*) three new oxygen sites are displayed: two O2 framework oxygens, O5 (pale pink) and O4 (mahogany) have been relaxed away from the interstitial oxygen O6 (maroon) and the direction of their movement is indicated with red dashed arrows.

In doped langasites, the incorporation of the interstitial in the 6-membered channels provokes a rearrangement of the O2 oxygen sites. Bond lengths and angles involved in the refined $(Ga/Ge)_2O_8$ units are given in Appendix 5. The separation between the edge sharing O4 and O6 oxygen sites equals to 2.5 Å in the refined $La_3Ga_{3.5}Ge_{2.5}O_{14.75}$ model at 9 K (see Figure 4-6), while the same distance in the DFT averaged model equals to 2.44 Å and in $La_3GaGe_5O_{16}$ the edge sharing oxygen sites are separated by 2.45 Å. O5-C-O6 and O4-C-O6 angles narrower than 80° (see Figure 4-6), are also present in the DFT supercell. These angles could be increased to more sensible values closer to 80° by approaching the atom in C to O6. To test this hypothesis, a splitting of the C site was carried out which worsen the goodness of fit '*S*' by 14 %. Even though there is a clear elongation of the refined ADPs for the C site towards O6 (see Figure 4-8), a distinct split C site (or the splitting of any cation site for that matter) did not improve the fit and was therefore not considered in the final refinement.

4.2.1.3 Bond Valence Sum (BVS)

The determination of the Ga/Ge distribution along the B, C and D sites by NPD techniques is hampered by the close coherent scattering length values of these two atoms (7.288 barn for Ga and 8.185 barn for Ge[260]). Moreover, Ga^{3+} and Ge^{4+} cations have the same number of electrons which makes them indistinguishable by means of X-ray diffraction. Although ^{71}Ga static NMR data revealed the presence of Ga in all three B, C and D sites the determination of an accurate relative ratio of Ga on each site was impeded due to the large broadening of the peak ascribed to the 3f site, see 4.2.1.5.2 for further details on the ^{71}Ga NMR.

Due to the fact that a clear location of the Ga and Ge atoms is obstructed by means of both diffraction and NMR techniques the bond valence sum (BVS) of the B, C and D cation sites were evaluated as an alternative approach that would allow us to assess the preferential location of Ga and Ge in B-D sites in doped langasites. The BVS for these sites were calculated for $La_3Ga_5GeO_{14}$ (x = 0), $La_3Ga_4Ge_2O_{14.5}$ (x = 1) and $La_3Ga_{3.5}Ge_{2.5}O_{14.75}$ (x = 1.5) at 297 K. The calculated BVS are plotted as a function of the dopant content 'x' in Figure 4-7, assuming each site is fully occupied by Ga in (a) and by Ge in (b). The octahedral B and smaller tetrahedral D sites showed a linear increase of the BVS with the doping level, while the tetrahedral C site remained constant from x = 0 to 1.5.

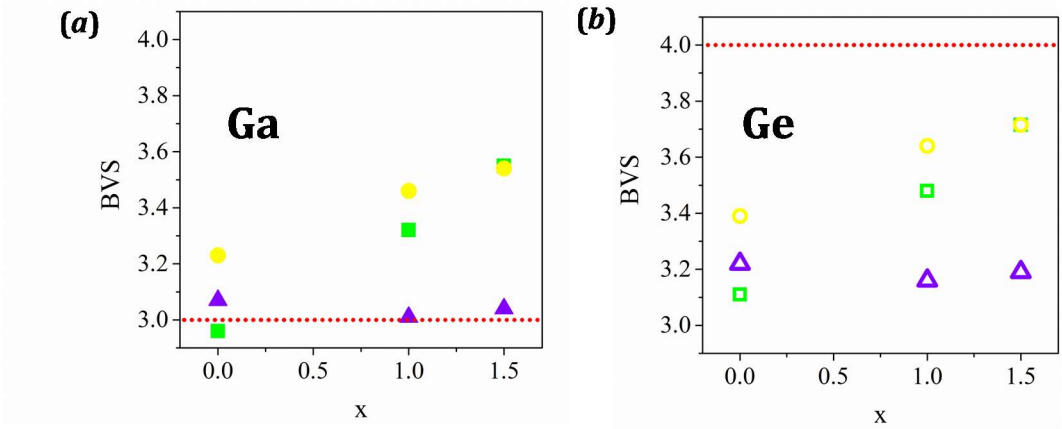

Figure 4-7 Calculated Bond valence sum of the three distinct B, C and D cation sites in $A_3BC_3D_2O_{14}$ for the NPD refined $La_3Ga_{5-x}Ge_{1+x}O_{14+x/2}$ models where x = 0, 1 and 1.5 at 297K. The symbols were coloured using the same scheme as in the polyhedral representations: green circles were used for B, violet triangles for C and yellow diamonds for D. In (a) the filled symbols account for Ga and in (b) the open symbols account for Ge. The ideal BVS of 3 and 4 for Ga and Ge are represented by a red dotted line in (a) and (b) respectively.

From the BVS representation of B, C and D sites for x = 0, 1 and 1.5 $La_3Ga_{5-x}Ge_{1+x}O_{14+x/2}$ langasites it is derived that upon doping, Ge would preferably substitute Ga in the octahedral B and smaller tetrahedral D site having an apical oxygen (O1) making the Ge_2O_8 more likely to be a $(Ga/Ge)_2O_8$ unit with Ga and Ge preferably occupying the tetrahedral C and D sites respectively. This can also be justified in terms of an electrostatic argument. The most stable conformation of Ga and Ge cations with different charges is to be alternated as B(Ge)-C(Ga)-D(Ge) rather than positioned adjacent to an atom with the same charge.

Table 4-4 Calculated BVS values for local (M_2O_7 and M_2O_8) and averaged environments for the A sites occupied by La, and B, C and D sites occupied by Ga and Ge.

Temperature (K)			297	11	297	9	297	473	673	873
x			0	1	1	1.5	1.5	1.5	1.5	1.5
La			2.88	2.95	2.85	2.99	2.86	3.09	2.83	2.77
B (1a)	Ga	Average	2.96	3.32	3.32	3.56	3.55	3.53	3.50	3.48
	Ge	Average	3.11	3.49	3.48	3.74	3.72	3.70	3.67	3.66
C (3f)	Ga	M_2O_7	3.07	3.00	2.99	2.98	3.04	3.04	3.01	2.91
		M_2O_8		3.00	3.25	3.08	3.03	3.04	3.01	2.78
		Average		3.00	3.01	2.99	3.04	3.04	3.01	2.89
	Ge	M_2O_7	3.22	3.15	3.14	3.13	3.19	3.03	3.16	3.06
		M_2O_8		3.15	3.42	3.23	3.18	3.19	3.16	2.92
		Average		3.15	3.16	3.14	3.19	3.05	3.16	3.04
D (2d)	Ga	M_2O_7	3.23	3.38	3.46	3.53	3.53	3.51	3.53	3.74
		M_2O_8		3.62	3.53	3.45	3.64	3.56	3.53	3.52
		Average		3.40	3.46	3.52	3.54	3.52	3.53	3.71
	Ge	M_2O_7	3.39	3.55	3.64	3.71	3.70	3.69	3.53	3.93
		M_2O_8		3.80	3.70	3.62	3.82	3.74	3.53	3.70
		Average		3.57	3.64	3.70	3.71	3.70	3.53	3.90

Furthermore, the bond valence for all the cations in x = 0, 1 and 1.5 refined models at temperatures ranging from 9-873 K were calculated and are presented in Table 4-4. For the tetrahedral C and D sites the BVS of the two plausible M_2O_7 and M_2O_8 local environments are given. The difference in the BVS between these two local environments is typically small: between 2-5 % for the D site and practically non-existent for the C site.

Overall, the good agreement between the calculated BVS of the cations and their oxidation states is a good indication of the veracity of the proposed model. Moreover, the range of the averaged calculated BVS for the oxygen sites is also reasonable ranging from 1.7 for O6 to 2.1 for O1.

4.2.1.4 VT NPD studies of $La_3Ga_{3.5}Ge_{2.5}O_{14.75}$

This section presents the variable temperature high resolution neutron powder diffraction studies of $La_3Ga_{3.5}Ge_{2.5}O_{14.75}$ at 9, 297, 473, 673 and 873 K in HRPD. The refined models in this temperature region are examined to seek for trends and consistency of the proposed model.

Figure 4-8 shows the asymmetric unit cell of the refined models for $La_3Ga_{3.5}Ge_{2.5}O_{14.75}$ at 9, 297, 473, 673 and 873 K. As previously stated in 4.2.1.2 all atoms, excluding O4 and O6 oxygen sites were refined anisotropically. O4 and O6 thermal parameters were kept isotropic due to their low occupancies ~1/8. While, most cations' ADPs are spherical, with the exception of the atom in the C site which is elongated towards O6 as earlier mentioned in 4.2.1.2 . Oxygen ADPs (O1-O3 and O5) are elongated along the ab plane. This elongation is analogous to the one observed in melilites where the oxide ion conduction occurred along

the 2D plane of interconnected tetrahedra[61,62,143,144]. The evaluation of the shape of the oxygen's ADPs in Figure 4-8 shows how this feature remains constant throughout the interval of temperatures studied while an increase in their size is also noticeable.

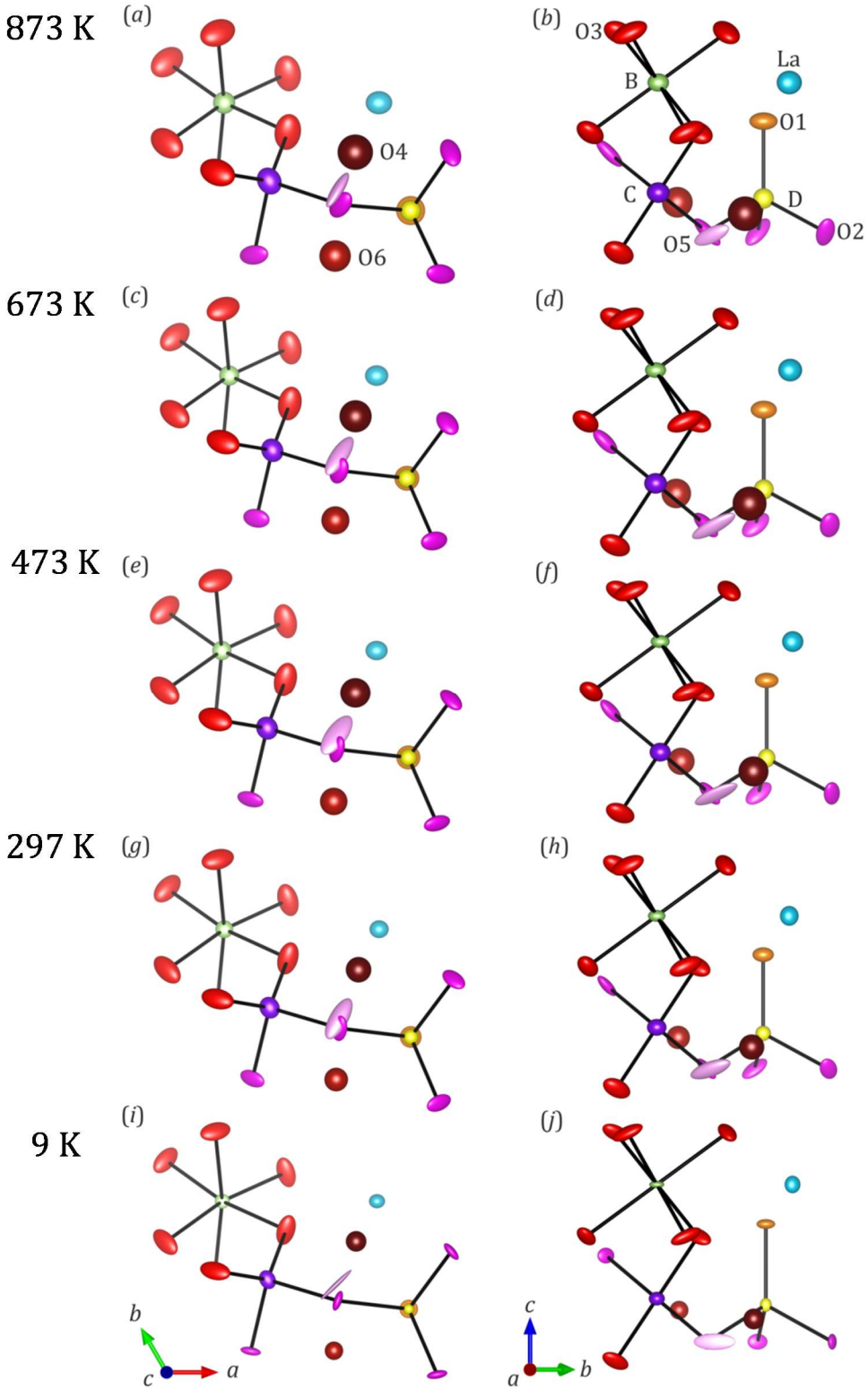

Figure 4-8 (*a* - *j*) Plot of the asymmetric unit cell of the refined models for $La_3Ga_{3.5}Ge_{2.5}O_{14.75}$ at various temperatures 9-873 K specified in the figure. Anisotropic thermal parameters are given with a 50 % probability. Oxygen ADPs (excluding O4 and O6 oxygen sites that were refined isotropically) are elongated along the *a*-*b* plane (analogously to melilites where the oxide ion conduction occurred along the 2D plane of interconnected tetrahedra[140]).

With increasing temperature, an isotropic expansion of the cell is observed (see figure Figure 4-9 *a* and *b*). To further evaluate the variation in the thermal parameters with the increase in temperature, the anisotropic thermal parameters were converted to B_{eq} and plot as a function of temperature in Figure 4-9-*c*. Overall, there is an expected increase in the thermal parameters for all atoms accompanying the cell volume expansion with temperature. The higher value of the thermal parameters of the new oxygen sites O4-O6 can be correlated to the local structure disorder induced by the presence of excess oxide ions[129] in the langasite structure.

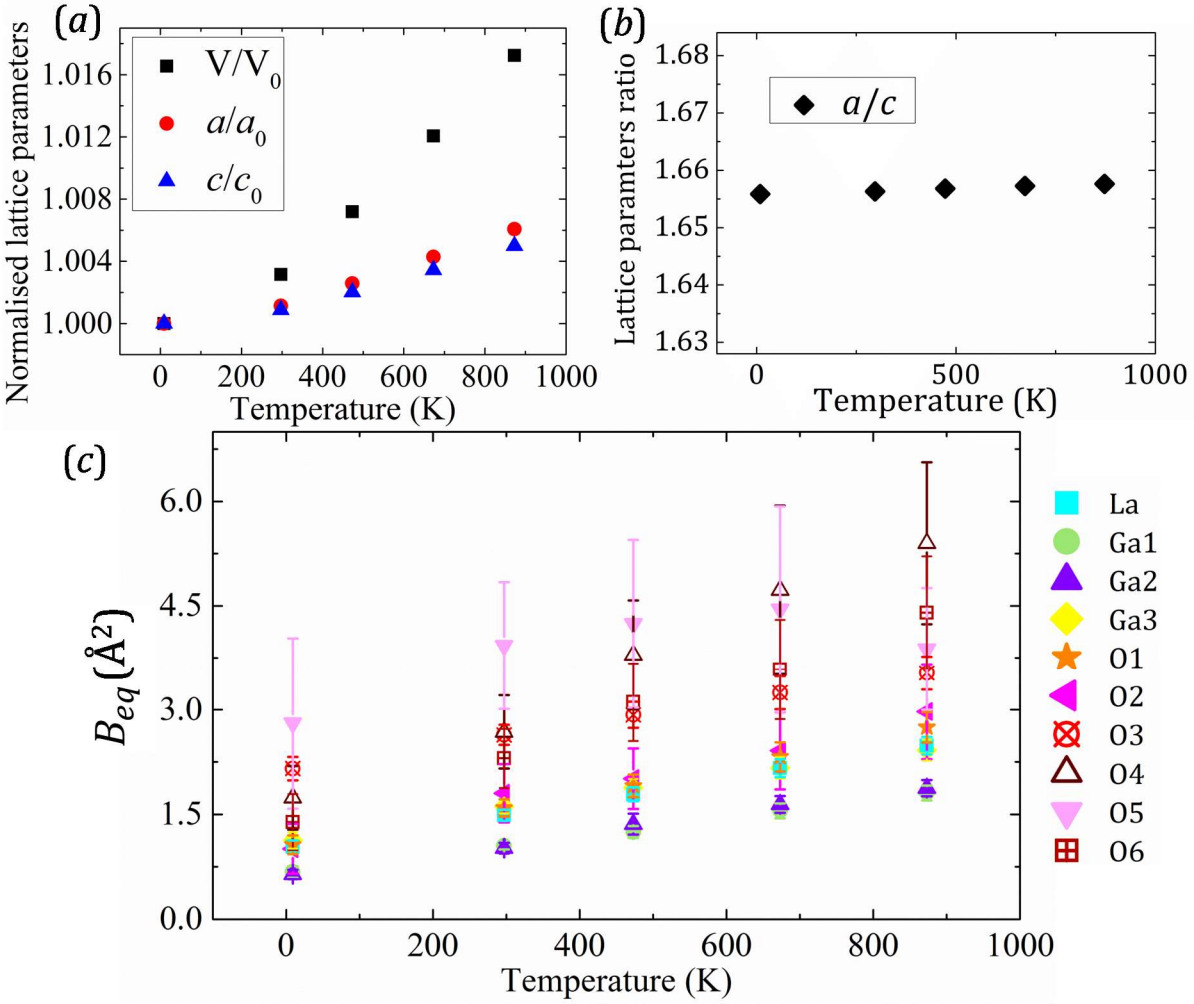

Figure 4-9 (*a*) Variation of the normalized lattice parameters with temperature. (*b*) a/c lattice parameter ratio showing isotropic expansion of the cell with the increase in temperature. (*c*) Variation of the B_{eq} with temperature for the different atomic sites. The errors plotted account for 3 × e.s.d.

4.2.1.5 NMR

Diffraction is a technique which informs us about long-range averaged structures and it is therefore limited when it comes to interpreting local structural distortion particularly at low concentration. *Au contraire*, solid-state Nuclear Magnetic Resonance (NMR) is a powerful tool able to reveal chemical environments on the atomic scale. Previous studies have successfully probed the local defect environment in other electrolyte materials such as LSGM[261] and apatites[131,262].

Herein, we introduce ^{71}Ga and ^{17}O NMR spectroscopy data which in combination with Density Functional Theory (DFT) and total energy and GIPAW NMR calculations[251,263] has

allowed us to understand the structural defects on $La_3Ga_{5-x}Ge_{1+x}O_{14+x/2}$ with $0 \leq x \leq 1.5$. The NMR analysis presented here was carried out by Dr Frederic Blanc who made use of the DFT model calculated by Dr Matthew Dyer for the GIPAW NMR calculations.

Table 4-5 Experimental and calculated ^{17}O, ^{71}Ga and ^{73}Ge NMR Parameters for $La_3Ga_5GeO_{14}$ and $La_3Ga_4Ge_2O_{14.5}$.[a]

Site	Environment	Coordination	$\delta_{iso,cs}$ / ppm[b]	C_Q / MHz	η_Q
O	O1	Ga^{IV}-O	**175(10)**	**4.5(0.4)**	**0.5(0.2)**
			180.7[c]	4.3	0.0
			192.1[d] (σ_{sd} = 22.2)	4.1 (σ_{sd} = 0.2)	0.1
		Ge^{IV}-O	**122(20)**	**3.9(0.3)**	**0.6(0.2)**
			153.9[c]	5.7	0.0
			164.5[d] (σ_{sd} =17.2)	5.7 (σ_{sd} = 0.3)	0.1 (σ_{sd} = 0.1)
	O2	Ga^{IV}-O-M^{IV} (M = Ga, Ge)	135(10)	3.5(0.4)	0.1(0.2)
		Ga^{IV}-O-Ga^{IV}	138.8[c]	3.0	0.9
			143.9[d] (σ_{sd} = 10.5)	3.4 (σ_{sd} = 0.4)	0.8 (σ_{sd} = 0.2)
		Ga^{IV}-O-Ge^{IV}	140.0[c]	5.0	0.4
			145.6[d] (σ_{sd} = 22.5)	5.0 (σ_{sd} = 0.4)	0.6 (σ_{sd} = 0.2)
	O3	Ga^{IV}-O-Ga^{VI}	**199(10)**	**3.8(0.2)**	**0.4(0.2)**
			204.7[c] (σ_{sd} = 0.3)	4.0 (σ_{sd} = 0.3)	0.7 (σ_{sd} = 0.1)
			195.3[d] (σ_{sd} = 15.5_	4.2 (σ_{sd} = 0.6)	0.7 (σ_{sd} = 0.2)
		Ga^{IV}-O-Ga^{V}	135.6[d] (σ_{sd} = 15.4)	2.6 (σ_{sd} = 0.3)	0.4 (σ_{sd} = 0.2)
		Ga^{IV}-O-Ge^{V}	189.0[d] (σ_{sd} = 15.3)	6.3 (σ_{sd} = 0.3)	0.4 (σ_{sd} = 0.1)
		Ge^{VI}-O-Ga^{V}	212.4[d] (σ_{sd} = 19.5)	5.1 (σ_{sd} = 0.3)	0.7 (σ_{sd} = 0.1)
		Ge^{VI}-O-Ga^{IV}	209.6[d] (σ_{sd} = 12.8)	4.9 (σ_{sd} = 0.6)	0.8 (σ_{sd} = 0.2)
	O_{int}	Interstitial	**270(10)**	**3.0(0.2)**	**0.4(0.2)**
			271.6[d] (σ_{sd} = 11.6)	2.7 (σ_{sd} = 0.3)	0.5 (σ_{sd} = 0.1)
Ga	C(3f)	Td	-[e]	-[e]	-[e]
			140.7[c]	25.3	0.8
			135.6[d] (σ_{sd} = 18.8)	26.5 (σ_{sd} = 5.4)	0.5 (σ_{sd} = 0.2)
		V	-[e]	-[e]	-[e]
			109.5[d] (σ_{sd} = 10.2)	23.3 (σ_{sd} = 5.7)	0.5 (σ_{sd} = 0.2)
	D(2a)	Td	250(10)	16(1)	-[e]
			276.5[c]	13.9	0.0
			263.9[d] (σ_{sd} = 11.1)	13.2 (σ_{sd} = 4.2)	0.2 (σ_{sd} = 0.1)
		V	140(10)	13(2)	-[e]

			177.3[d] (σ_{sd} = 4.5)	10.0 (σ_{sd} = 2.6)	0.6 (σ_{sd} = 0.4)
	B(1a)	Oh	15(10) 32.2[c] (σ_{sd} = 2.0) 44.5[d] (σ_{sd} = 7.9)	6(1) 5.0 (σ_{sd} = 1.7) 8.1 (σ_{sd} = 4.8)	-[e] 0.0 0.5 (σ_{sd} = 0.3)
Ge	D(2a)	Td	210.9[c] (σ_{sd} = 0.8) 164.8[d] (σ_{sd} = 3.2)	15.5 16.6 (σ_{sd} = 5.7)	0.0 0.5 (σ_{sd} = 0.2)
		V	55.2[d] (σ_{sd} = 12.5)	18.2 (σ_{sd} = 3.6)	0.6 (σ_{sd} = 0.2)
	B(1a)	Oh	-101.5[d] (σ_{sd} = 3.2)	16.6 (σ_{sd} = 5.7)	0.6 (σ_{sd} = 0.1)

[a] Experimental and calculated values are given in bold and plain text, respectively. ^{17}O and ^{71}Ga experimental values were obtained from the 2D 3QMAS and 1D MAS spectra, respectively (see experimental section for further details). Experimental ^{73}Ge NMR spectra were not obtained due to its low sensitivity. The calculated ^{17}O, ^{71}Ga and ^{73}Ge isotropic shielding σ were converted into isotropic chemical shifts δ following an expression of the form $\delta = \sigma_{ref} + m\sigma$ with (σ_{ref}, m) = (223.70 ppm, -0.888) for ^{17}O,[264] = (1502.63 ppm, -0.867) for ^{71}Ga,[131] = (1424.24 ppm, -1) for ^{73}Ge.[265] Standard deviations σ of the calculated data are given in the table (unless the values are less than 0.1). [b] The isotropic chemical shift δ is reported, except for ^{71}Ga where only the experimental shift δ is given (obtained from 1D MAS spectra) and is compared to the ^{71}Ga calculated isotropic chemical shift δ. This is a fair assumption since the ^{71}Ga quadrupolar induced shift (determined as $\delta_{,Q} = - P_Q^2/40\nu_0(^{71}Ga)^2$ with P_Q and $\nu_0(^{71}Ga)$ the quadrupolar product and the ^{71}Ga Larmor frequency), from which δ is shifted from δ is found lower than 0.1 ppm at 20 T. [c] Calculated for the $La_{24}Ga_{40}Ge_8O_{112}$ supercell corresponding to the $La_3Ga_5GeO_{14}$ langasite structure. [d] Calculated for $La_{24}Ga_{32}Ge_{16}O_{116}$ supercell corresponding to the $La_3Ga_3Ge_2O_{16}$ langasite structure. [e] This ^{71}Ga NMR signal is not observed experimentally under the conditions (20 T and MAS frequency of 65 kHz) used here (see Figure S5). [f] Not determined experimentally.

4.2.1.5.1 ^{17}O NMR

The ^{17}O MAS NMR spectra (^{17}O spin I = 5/2) of ^{17}O enriched $La_3Ga_5GeO_{14}$ obtained at a magnetic field of 9.4 and 20 T are shown in Figure 4-10-*a*. These spectra are characterized by a broadening of the NMR lines due to the presence of a second-order quadrupolar interaction, which is not averaged out to zero by MAS, but which can be removed by two-dimensional (2D) triple-quantum magic angle spinning (3QMAS) experiments[252,254], given in Figure 4-10-*c*. The 2D spectra were fitted with four signals at isotropic chemical shift $\delta_{iso,cs}$ of 199, 175, 135 and 122 ppm and used to accurately reproduced the 1D ^{17}O MAS NMR spectra of $La_3Ga_5O_{14}$ at each field in Figure 4-10-*a*. The fitting parameters for spectral assignment were determined by NMR DFT GIPAW calculations and are given in Table 4-5. GIPAW simulated spectra are highlighted in red in Figure 4-10 and reproduce well the experimental data giving confidence in the accuracy of these calculated parameters[261,263,266].

Two main signals of similar intensity resonance bands are observed in the ^{17}O MAS NMR spectra at $\delta_{iso,cs}$ = 199 and 135 ppm. These bands are assigned to the equally populated O3 oxygen bridging between tetrahedral C and octahedral B sites, and the O2 oxygen bridging between the two tetrahedral sites C and D. Noticed that the GIPAW calculations discriminate two O2 arising from a bridging oxygen between two coordinated C and D sites hosting Ga or Ge cations due to the ordering within the 2×2×2 DFT supercell used in the calculations.

However such distinction is not possible experimentally due to disorder. The third resonance band is observed experimentally at $\delta_{iso,cs} = 175\ \delta_{iso,cs} = 122\ pm$ and computed at 153.9 ppm. The differences between the experimental and calculated $\delta_{iso,cs}$ were attributed to the large errors in the determination of the experimental parameters for O1 since this signal is obscured by that of O2[264].

The ^{17}O MAS NMR spectra of ^{17}O enriched $La_3Ga_{5-x}Ge_{1+x}O_{14+x/2}$ (with $0 \leq x \leq 1.5$) obtained at a 20 T are depicted in Figure 4-10-*b* . Doped compositions have a relatively similar line shape to that of $La_3Ga_5GeO_{14}$ with an additional downfield resonance centred at 270 ppm (see Table 4-5), not present in $La_3Ga_5GeO_{14}$ is observed in $La_3Ga_{5-x}Ge_{1+x}O_{14+x/2}$ (with $0.5 \leq x \leq 1.5$), whose intensity becomes greater with increasing Ge concentration. This signal evokes an observed shift at ~280 ppm assigned to a GeO_5 unit in $La_8CaYGe_6O_{26.5}$ and $La_8Y_2Ge_2O_{27}$ apatites [131]. We have similarly calculated the ^{17}O GIPAW NMR parameters of $La_3Ga_4Ge_2O_{14.5}$, from a DFT supercell, and used the full set of calculations for signal assignment of the experimental spectra and identify the O resonances giving rise to the additional resonance predicted at 281.7 ppm (Table 4-5). The estimation of the experimental quadrupolar coupling constant $C_{Q,exp}$ ~3 MHz and asymmetry parameter $\eta_{Q,exp}$ ~0.4 are also supported by the determination of the calculated quadrupolar coupling constant $C_{Q,cal}$ = 3.5 MHz and asymmetry parameter $\eta_{Q,cal}$ = 0.7 for this interstitial oxygen.

Although quantification of NMR signal intensities of quadrupolar nuclei such as ^{17}O must be interpreted with caution,[267] the relative content of interstitial oxygen as determined by integration of the ^{17}O MAS NMR signal of $La_3Ga_{3.5}Ge_{2.5}O_{14.75}$ yields a value of 6 ± 2 %, in agreement with the accommodation of over 5 % of extra oxygen.

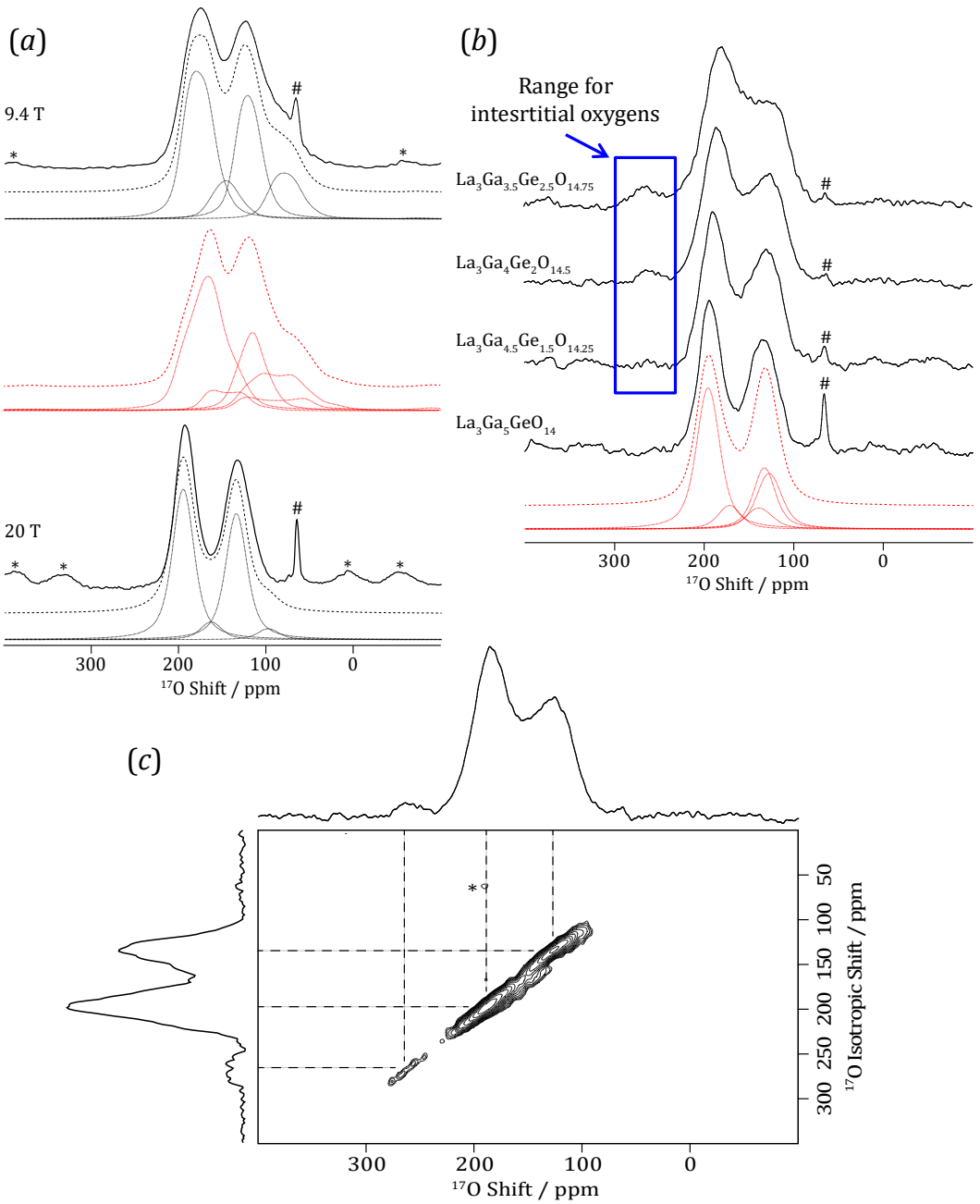

Figure 4-10 (*a*) ^{17}O MAS NMR spectra of ^{17}O enriched $La_3Ga_5GeO_{14}$ obtained at 9.4 and 20 T (full lines). The one-dimensional simulated spectrum (dashed lines) and deconvoluted spectra (dotted lines) obtained from two-dimensional sheared ^{17}O triple-quantum (3Q) MAS NMR (black) and the GIPAW NMR calculations (red) are given below the experimental data at 9.4 T in (*a*) and at 20 T in (*b*). In (*b*) ^{17}O MAS NMR spectra of $La_3Ga_{5-x}Ge_{1+x}O_{14+x/2}$ with $0 \leq x \leq 1.5$ obtained at a magnetic field of 20 *T* is given and the region where the peak associated to the interstitial oxygen is observed is highlighted in the spectra. (*c*) Two-dimensional sheared ^{17}O triple quantum (3Q) MAS NMR spectrum of ^{17}O enriched $La_3Ga_4Ge_2O_{14.5}$. Left: isotropic projection of the 2D 3Q MAS spectrum. Top: ^{17}O MAS NMR spectrum. The symbols # and * denotes absorbed H_2O and spinning side bands respectively.

4.2.1.5.2 ^{71}Ga NMR

In this study increase in coordination number of Ga coupled to the introduction of interstitial oxides is probed by ^{71}Ga NMR[261,265]. ^{71}Ga (spin I = 3/2) is the isotope of choice in these experiments due to its higher sensitivity with respect to ^{69}Ga (spin I = 3/2) yielding sharper NMR lines (due to its smaller quadrupolar moment Q of -10.7 10^{-30} m^2 vs -17.1 10^{-30}). Figure 4-11 introduces the ^{71}Ga MAS NMR spectra of $La_3Ga_{5-x}Ge_{1+x}O_{14+x/2}$ with $0 \leq x \leq 1.5$ obtained at 20 T and under very fast MAS at 65 kHz.

The ^{71}Ga spectrum of $LaGa_5GeO_{14}$ presents one signal at 15 ppm corresponding to the central transition of the 6-coordinated Ga site as well as a broad signal (with a full width at half maximum of approximately 45 kHz) centred at around 240 ppm and corresponding to Ga in tetrahedral geometry, the increase in shift with decreasing coordination number being typical of ^{71}Ga (and other nuclei)[261,264,268,269]. Two tetrahedral Ga sites C and D are present in $LaGa_5GeO_{14}$ and site-averaged GIPAW NMR calculations reveal that both sites have large quadrupolar coupling constants C_Q with values of 25.3 and 13.9 MHz, respectively (Table 4-5). While the 13.9 MHz value obtained for the D site is on the upper limit of C_Q values usually obtained for Ga in tetrahedral geometry[261,264], the much larger value of 25.3 MHz (and η_Q = 0.8) obtained for a tetrahedral Ga site are unusual and reflects the highly distorted calculated Ga geometry of this C site with 2 short Ga-O distances (of 1.838 and 1.845 Å) and 2 elongated Ga-O bonds (of 1.895 and 1.992 Å). The predicted calculated MAS linewidth of the C site is approximately 600 kHz at 20 T and is therefore significantly larger than the 65 kHz MAS frequency used in Figure 4-11 yielding a broad and complex MAS lineshape and preventing its observation even under the MAS and high field condition used here.

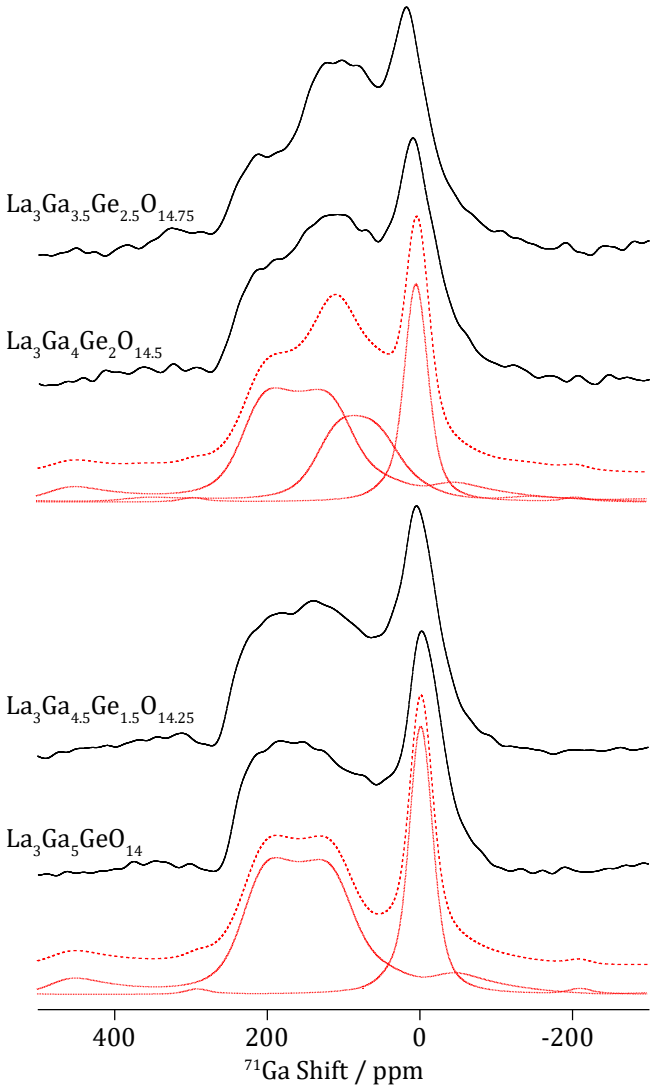

Figure 4-11 ^{71}Ga MAS NMR spectra of $La_3Ga_{5-x}Ge_{1+x}O_{14+x/2}$ (with $0 \leq x \leq 1.5$) obtained at 20 T and under MAS rates of 65 kHz. The spectra were recorded with a 2 ms DFS enhancement pulse[257]. The one-dimensional simulated spectrum (dashed lines) and deconvoluted spectra (dotted lines) were obtained from best fit simulations (see Table 4-5) and depicted in red to distinguish them from the experimental data denoted by solid black lines.

The ^{71}Ga MAS NMR spectra of $La_3Ga_{5-x}Ge_{1+x}O_{14+x/2}$ $0.5 \leq x \leq 1.5$ reveal a third resonance in addition to the previously observed 2 resonances at 15 and 240 ppm in $La_3Ga_5GeO_{14}$. This third resonance increases in intensity with Ge content and appears at a shift around 140 ppm intermediate between the resonances 15 and 240 ppm which account for 6 and 4 fold symmetries, respectively. Both shift and quadrupolar constant (C_Q ~13 MHz) values of the new ^{71}Ga resonance indicate the presence of a 5-coordinated Ga site. Similar NMR parameters were reported for Ga in trigonal bipyramidal geometry in $LaGaGe_2O_7$ (δ = 89.6 ppm, C_Q = 11.6 MHz)[269], and calculated Ga in squared pyramidal geometry in Sr- and Mg-doped $LaGaO_3$ (δ = 150 ppm, C_Q = 10.1 MHz)[261]. The site-averaged GIPAW NMR calculations on $La_3Ga_4Ge_2O_{14.5}$ predict a 5 fold coordinated squared pyramidal Ga D site appearing at a shift of 177.3 ppm with C_Q of 10 MHz (Table 4-5), in fair agreement with the experimental data. The calculations also predict a very large C_Q (> 23 MHz) for a 5-coordinated Ga C site which is not resolved or observed in the ^{71}Ga MAS NMR spectra at 20 T as discussed above. These ^{71}Ga NMR results highlight a change of coordination number

of Ga atoms needed to accommodate the extra oxygen incorporated and indicates the presence of 5-coordinated Ga.

Ge also has an NMR active nucleus, ^{73}Ge, with a spin 9/2, that was not considered in this study due to its very low sensitivity arising from a combination of low gyromagnetic ratio, large quadrupolar moment and low natural abundance[265]. Despite this, the computed ^{73}Ge NMR parameters for both $La_3Ga_5GeO_{14}$ and $La_3Ga_4Ge_2O_{14.5}$ are introduced in Table 4-5 since ^{73}Ge shift is also sensitive to the Ge coordination number[265,270]. Similarly, the study of La by NMR was also discarded here due to the very large C_Q[261] values in the 45.4 – 59.9 MHz and 24.6 – 80.2 MHz range for decahedral La.

4.2.2 Evaluation of the conductivity by AC impedance

4.2.2.1 Sample preparation: Conventional, SPS and HIP Sintering

The asymptotic decrease in the decomposition temperature with the increase in dopant content in $La_3Ga_{5-x}Ge_{1+x}O_{14+x/2}$ for $x > 0.3$ (see section 3.3.4 in page 75) hampers the preparation of specimens with acceptable densities for conductivity determination purposes.

At a first instance these difficulties were addressed by the addition of binders (BUTVAR and PVA 3-15 wt%) and decrease in particle size of the powdered precursors by mechanical milling followed by CIP-ing in samples with a nominal composition of $La_3Ga_{4.5}Ge_{1.5}O_{14.25}$ (x = 0.5) and a decomposition temperature of 1100 °C. The addition of binders and mechanical milling typically allow decreasing the temperature for the full densification of a ceramic body by 50-100 °C. These techniques were not sufficient to achieve full densification of $La_3Ga_{4.5}Ge_{1.5}O_{14.25}$. Alternatively, the fast-sintering techniques Hot Isotactic Pressing (HIP) and Spark Plasma Sintering (SPS) were carried out for $La_3Ga_{5-x}Ge_{1+x}O_{14+x/2}$ with $x > 0.3$ due to the dramatic decrease in the decomposition temperature several hundred of degrees apart from the melting point T_m~1350 °C.

- Hot Isostatic Pressing

The density of HIP-ed $La_3Ga_4Ge_2O_{14.5}$ (x = 1) and $La_3Ga_{3.5}Ge_{2.5}O_{14.75}$ (x = 1.5) materials calculated with the Archimedes balance and the volume obtained from Rietveld was found to be 73 % for $La_3Ga_4Ge_2O_{14.5}$ (x = 1) HIP-ed at 850 °C, and a lower 50 % density was determined in $La_3Ga_{3.5}Ge_{2.5}O_{14.75}$ (x = 1.5) sintered at 800 °C. The low density obtained in $La_3Ga_{3.5}Ge_{2.5}O_{14.75}$ (x = 1.5) is not suitable for AC impedance measurement purposes. On the other hand, a 73 % density obtained for $La_3Ga_4Ge_2O_{14.5}$ (x = 1) is adequate for the determination of the bulk conductivity in a 350-525 °C range following the procedure in 2.3.3.2. The morphology of the 73 % dense $La_3Ga_4Ge_2O_{14.5}$ (x = 1) sample was investigated in the Scanning Electron Microscope (SEM), see Figure 4-12.

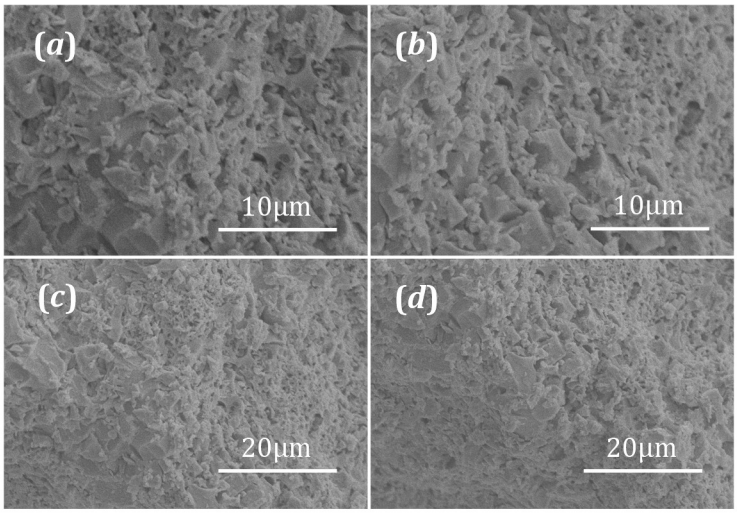

Figure 4-12 SEM images HIP-sintered $La_3Ga_4Ge_2O_{14.5}$ with a density of 73 %. The sintering conditions involved heating the sample at 850 °C for 8 hours while simultaneously applying a pressure of 300 MPa.

The SEM images of Au-coated $La_3Ga_4Ge_2O_{14.5}$ (x = 1)presented in Figure 4-12 were taken in the cross section of a broken side. They revealed a loose microstructure, although some well-developed ~2-4 μm grains are visible, generally there is poor connectivity between the grains due to a high porosity.

PXRD patterns of the HIP-ed specimens were collected to investigate the possibility of the samples undergoing undesired reactions during the sintering process leading to the formation of impurities. The comparison between the PXRD patterns before and after HIP for both $La_3Ga_4Ge_2O_{14.5}$ (x = 1) and $La_3Ga_{3.5}Ge_{2.5}O_{14.75}$ (x = 1.5) are presented in Figure 4-13. An incipient formation of a $LaGaGeO_5$ impurity denoted by black filled squares in Figure 4-13 was observed in the samples after HIP. Even though these materials were stable at the experimental temperatures (under air and ambient pressure), the low O_2 partial pressures and the high pressure of 300 MPa applied during the HIP appeared to change the equilibrium of the reaction. Moreover, an increase in the cell volume from 296.79(2) to 299.23(5) $Å^3$ in $La_3Ga_{3.5}Ge_{2.5}O_{14.75}$ (x = 1.5) after undergoing HIP process determined by the Pawley fitting of the PXRD patterns in Figure 4-13 (see Table 4-6), indicates a change in composition of the majority langasites phase with the loss of Ge. In $La_3Ga_4Ge_2O_{14.5}$ (x = 1), the Pawley fitting of the data demonstrates no change in the lattice parameters before and after HIP, which suggests that there is no change in composition.

Due to the reactivity of doped langasites under the sintering conditions specified above and the high cost associated to this technique as well as to the silver cans in which the samples were embedded, an alternative method involving the Spark Plasma Sintering (SPS) of powdered langasite specimens was attempted. Since in SPS the high pressure conditions are only held briefly over a period of a few minutes, the formation of impurities was thought to be avoided by this technique.

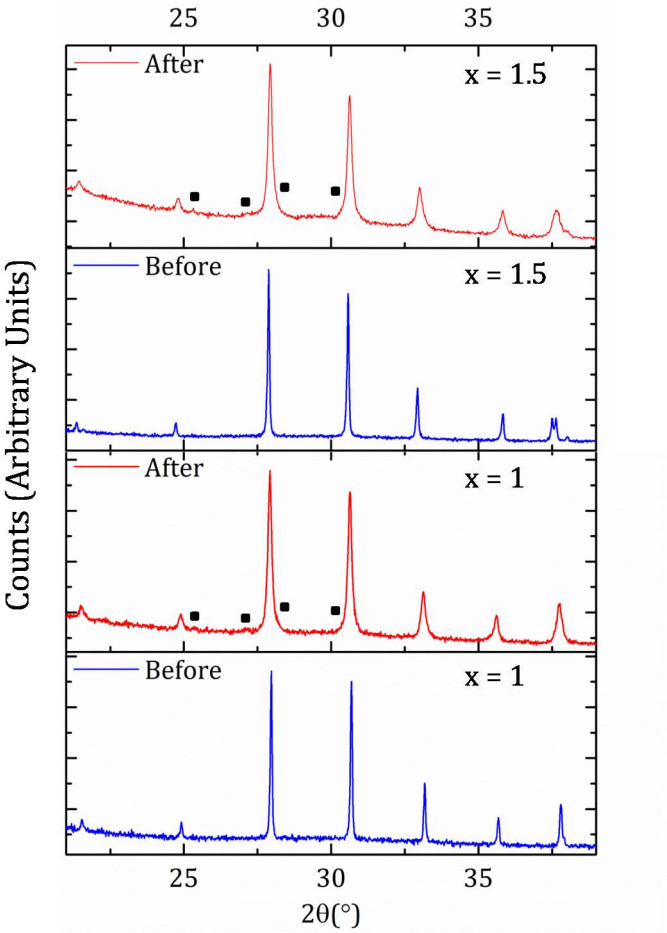

Figure 4-13 XRD patterns of $La_3Ga_{3.5}Ge_{2.5}O_{14.75}$ (x = 1.5) and $La_3Ga_4Ge_2O_{14.5}$ (x = 1) before and after undergoing HIP sintering. The filled squares denote the presence of a $LaGaGeO_5$ impurity. The PXRD patterns were collected in a Bruker diffractometer with a Cu source ($K_{\alpha 1,Cu}$ = 1.5406 Å).

Table 4-6 Fitting parameters and refined lattice parameters for the Pawley fitting of the samples in Figure 4-13.

Nominal Compositions	R_{wp}	S	a (Å)	c (Å)	V (Å³)
$La_3Ga_{3.5}Ge_{2.5}O_{14.75}$					
Before HIP	7.28	1.19	8.2813(2)	4.9971(2)	296.79(2)
After HIP	6.18	2.53	8.2611(6)	5.0629(1)	299.23(5)
$La_3Ga_4Ge_2O_{14.5}$					
Before HIP	6.78	1.20	8.2521(1)	5.0372(1)	297.07(1)
After HIP	5.35	1.13	8.2512(2)	5.0380(3)	297.05(2)

- SPS sintering

$0.3 \leq x \leq 0.7$ compositions were sintered *via* SPS at temperatures ranging from 1050-1000 °C for dwelling periods ranging from 4 to 10 min (see Table 4-7 for further details). The grain morphology and microstructure of sintered pellets with x = 0.35, 0.5, 0.55 and 0.7 was investigated in the Scanning Electron Microscope (SEM). The fractured surface SEM images given in Figure 4-14 show good connectivity between particles and small porosity, only some intra-granular pores with $\emptyset < 1\ \mu m$ are visible for $La_3Ga_{4.5}Ge_{1.5}O_{14.25}$ (x = 0.5).

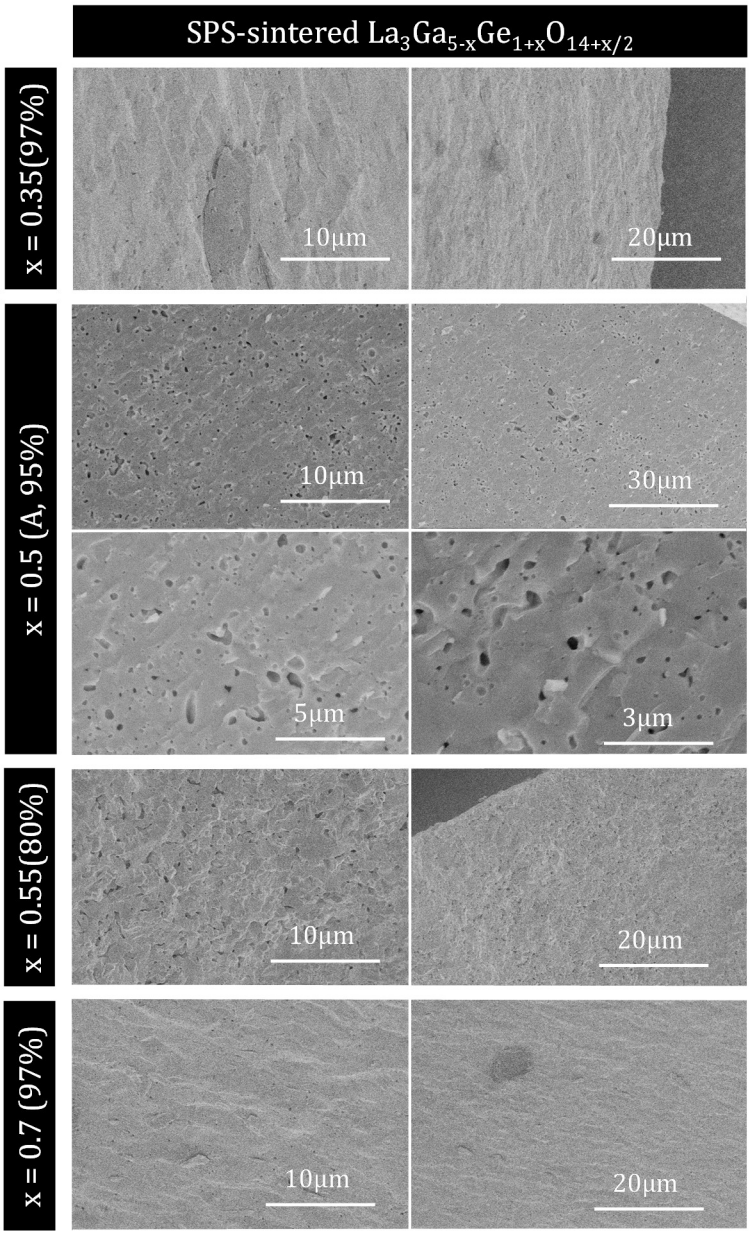

Figure 4-14 SEM images of the cross section of Au-coated SPS - sintered $La_3Ga_{5-x}Ge_{1+x}O_{14+x/2}$ pellets with x = 0.35, 0.5, 0.55 and 0.7. Their relative density is given between brackets next to the dopant content 'x'.

Attempts to sinter $La_3Ga_4Ge_2O_{14.5}$ (x = 1) and $La_3Ga_{3.5}Ge_{2.5}O_{14.75}$ (x = 1.5) with the lowest decomposition temperatures of 900 and 850 °C respectively in a graphite die at a pressure of 50 MPa were unsuccessful. A $LaGaGeO_5$ impurity was formed after heating these compositions above T_{decomp} at 1000 °C for only 1 min. In order to lower the sintering

temperature so as to match the synthetic temperatures of 850 and 800 °C the applied pressure was increased from 50 to 550 MPa by the use a of a double acting die in which a small ⌀ = 5 mm graphite die with WC plungers is embedded in a bigger ⌀ = 20 mm die. Presumably, the lower conductivity subsequently measured for these materials could also be hindering the synthesis at routine SPS-sintering pressure values of ~50 MPa.

The synthetic routes followed for the preparation of dense pellets whose conductivity was afterwards measured by AC impedance are listed in Table 4-7. Compositions within the $0 \leq x \leq 0.2$ ranges were annealed by prolonged firings of 24 hours at 1275 °C. Ge-richer $0.3 \leq x \leq 1.5$ compositions were annealed by Spark Plasma Sintering at lower temperatures ranging from 1150-800 °C. The densities (ρ), activation energy values (Ea_{bulk}) calculated from Figure 4-17 and Heidinger corrected permittivity values (ε_H) are also presented in this table.

Table 4-7 Sintering conditions for the $La_3Ga_{5-x}Ge_{1+x}O_{14+x/2}$ pellets measured by AC impedance

x	ρ (%)	ε_H	Ea_{bulk} (eV)	Sintering Conditions • Conventional Sintering			
				Temperature (°C)		Dwell (h)	
0	80	33.7	1.19	1275		24	
0.1	86	27.4	1.12	1275		24	
0.2	94	34.8	1.19	1275		24	
x	ρ (%)	ε_H	Ea_{bulk} (eV)	• SPS Sintering T(°C)	Dwell(min)	Ramp rate (° min^{-1})	Pressure (MPa)
0.3 (A)	95	43.4	1.09	1150	10	200	50
0.3 (B)	97	35.8	1.16	1150	10	200	50
0.35	97	28.2	1.20	1150	10	200	50
0.4	97	36.9	1.20	1150	10	200	50
0.45	97	38.8	1.21	1150	10	200	50
0.5(A)	95	41.3	1.20	1100	10	200	50
0.5 (B)	97	39.2	1.12	1100	10	200	50
0.55	80	39.4	1.24	1050	5	200	50
0.6	87	46.5	1.24	1050	5	200	50
0.7	97	26.3	1.25	1050	5	200	50
1	73	37.3	1.35	850	5	200	550
1.5	72	33.2	1.41	800	5	200	550

4.2.2.2 Total and bulk conductivity

The Arrhenius plot of the total and bulk conductivity of $La_3Ga_{5-x}Ge_{1+x}O_{14+x/2}$ for $0 \leq x \leq 0.5$ measured in air is shown in Figure 4-15 at 350-900 °C. The bulk conductivity at 350-500 °C (filled symbols) was calculated with the Heidinger[235] corrected permittivity and f_{max} at the M'' vs frequency plot (see 2.3.3.2). The total conductivity values at 500-950 °C (open symbols) were extracted from the intercept of the arcs in the complex impedance plane and the assignment of the type of response was done on the basis of the corrected capacitance values[231] (see 2.3.3.1).

Figure 4-15-*c* shows an increase in the total conductivity by two orders of magnitude in doped $La_3Ga_{4.5}Ge_{1.5}O_{14.25}$ (x = 0.5) and $La_3Ga_{4.7}Ge_{1.3}O_{14.15}$ (x = 0.3) langasites (~4 × 10^{-3} S·cm^{-1} at 700 °C) with respect to the un-doped parent material ($La_3Ga_5GeO_{14}$,

$\sim 1 \times 10^{-5}$ S·cm^{-1}). In addition to this, the Warburg electrode response was observed in the complex impedance plots for doped langasites. Figure 4-15-*a* shows the evolution of the complex impedance plots for $La_3Ga_{4.7}Ge_{1.3}O_{14.15}$ (x = 0.3) as a function of temperature. As the temperature increases the pellet response moves above the observable frequency range. Therefore, at 800 °C and higher temperatures the total conductivity is extracted from the intercept. This characteristic feature of ionic conductors is not exhibited by the insulating $La_3Ga_5GeO_{14}$ parent phase (see Figure 4-15-*c*).

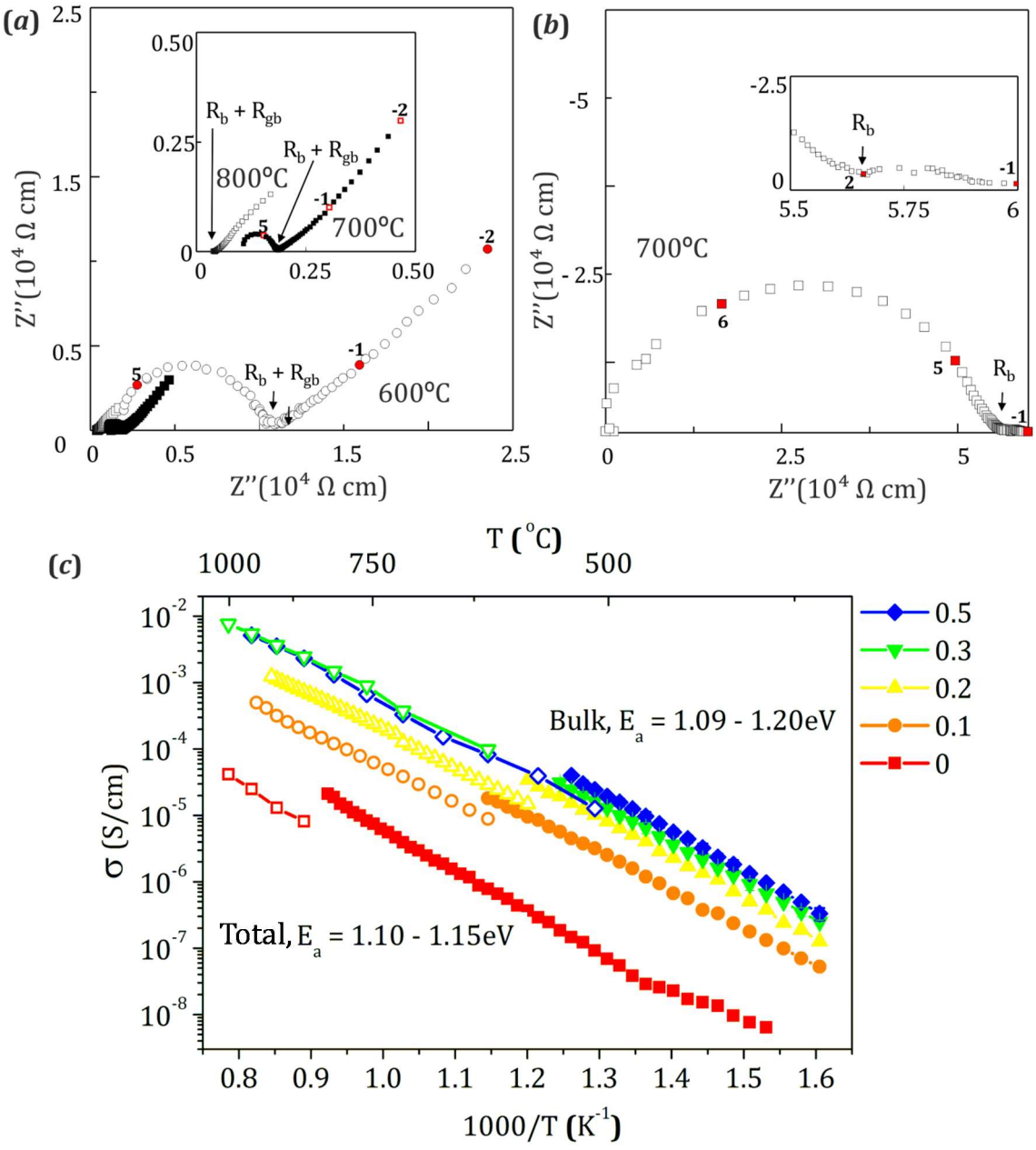

Figure 4-15(*a*) Complex impedance plots for $La_3Ga_{4.7}Ge_{1.3}O_{14.15}$ (x = 0.3) at 600, 700 and 800 °C showing the Warburg arc characteristic of oxide-ion conductors. (*b*) Complex impedance plot for the insulating $La_3Ga_5GeO_{14}$ (x = 0) parent material at 700 °C. In both figures *a* and *b*, the numbers in bold denote the logarithm of the frequency at the adjacent point highlighted in red. (*c*) Arrhenius plots of the total conductivity (empty symbols) and bulk (filled symbols) of $La_3Ga_{5-x}Ge_{1+x}O_{14+x/2}$ for x = 0, 0.1, 0.3 and 0.5 $La_3Ga_{5-x}Ge_{1+x}O_{14+x/2}$.

For the compositions studied, the total conductivity at temperatures above 525 °C is dictated by the grain boundary which was found constant for samples with $x \geq 0.3$ (see overlapping of the conductivity values for $x = 0.3$ and 0.5 in Figure 4-15-*c*). Thus, in order to properly asses the change in conductivity in $La_3Ga_{5-x}Ge_{1+x}O_{14x+/2}$ as a function of the amount of dopant 'x' incorporated we looked at the bulk conductivity at a lower temperature range of 350-525 °C. At such range, the M'' vs frequency plot given in Figure

4-16 allows us to discriminate the bulk and grain boundary contribution to the total conductivity[230,271,272] under the conditions measured up to 2 MHz.

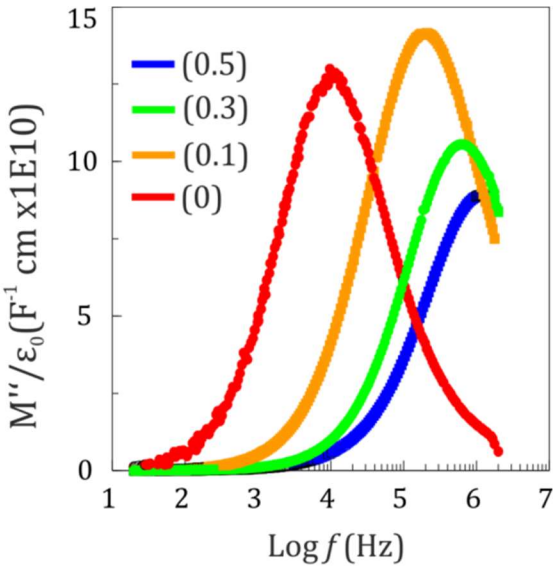

Figure 4-16 Shift in the peak maxima in the *M''* plot for $La_3Ga_{5-x}Ge_{1+x}O_{14+x/2}$ with x = 0, 0.1, 0.3 and 0.5 towards higher frequency values with the increase of x.

The dielectric constants of $La_3Ga_{5-x}Ge_{1+x}O_{14+x/2}$ with $0 \leq x \leq 1.5$ were measured at room temperature on dry specimens. The calculated value for the parent $La_3Ga_5GeO_{14}$ material is $\varepsilon_{H\,x=0} = 34$ close to the reported value of $\varepsilon_{La3Ga5SiO14} = 27$ for the Si analogue (with the permittivity of $La_3Ga_5GeO_{14}$ being higher than that of $La_3Ga_5SiO_{14}$ due to the higher polarizability of Ge)[273].

The maximum conductivity was measured for 0.4, 0.45 and 0.5 compositions showing overlapping conductivity values (Figure 4-17-a). In addition, the errors associated with reproducibility of samples were calculated in two specimens with x = 0.3 and x = 0.5. The estimated deviations are approximately 20 % of the observed conductivity and the error bars often lie behind the symbol in Figure 4-17.

The activation energy values Ea_{bulk} for all samples were calculated from the slope of the linear fit of the Arrhenius plot of the conductivity as described in 2.3.3.3.2. Due to the high number of data points acquired at a narrow interval of temperature the calculated errors of the linear fit were small (typically associated to the third or fourth decimal places) and not meaningful. Therefore, the calculated activation energies were round to two decimal places in the list that is presented in Table 4-7.

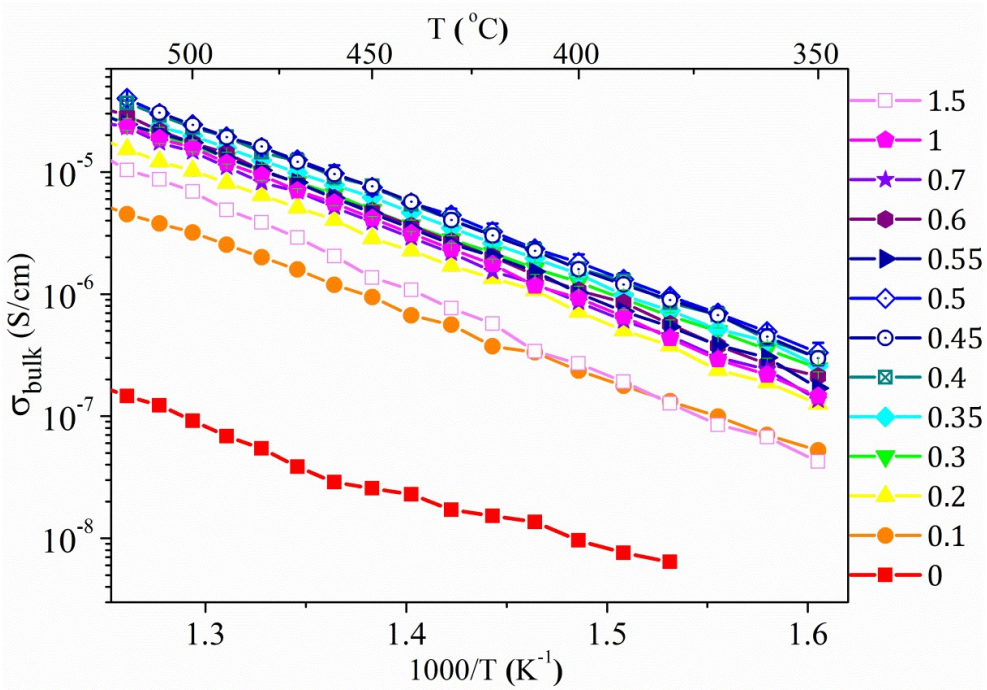

Figure 4-17 Change in the bulk conductivity for $La_3Ga_{5-x}Ge_{1+x}O_{14+x/2}$ with $0 \leq x \leq 1.5$.

4.2.2.3 pO_2 dependence of the conductivity

In order to characterize the defects responsible for the increase in the conductivity, $La_3Ga_{4.5}Ge_{1.5}O_{14.25}$ (x = 0.5) lying within the $0.35 \leq x \leq 0.5$ range of compositions with the highest conductivity was evaluated as a function of different oxygen partial pressures by the oxygen concentration cell method. Its conductivity was found constant at pO_2 values ranging from 1 to 10^{-15} atm as demonstrated in Figure 4-18. This is evidence of the ionic conducting nature of $La_3Ga_{5-x}Ge_{1+x}O_{14+x/2}$ with negligible electronic conductivity.

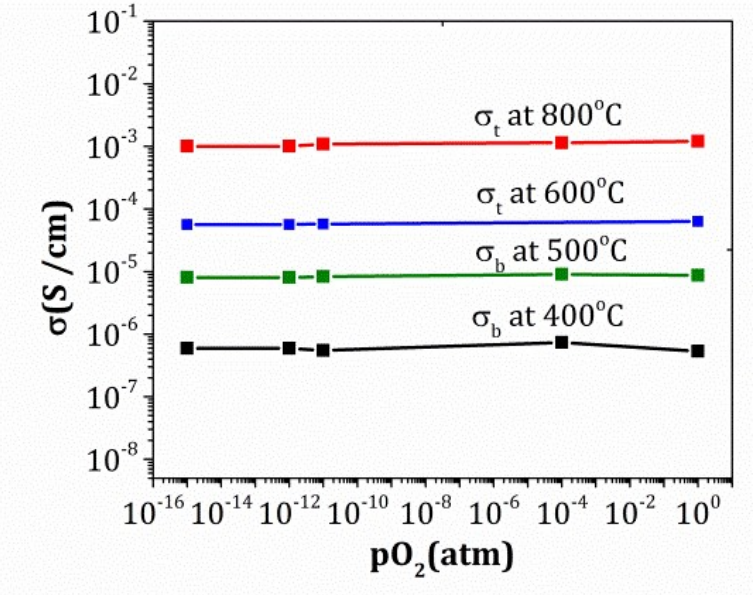

Figure 4-18 pO_2 dependence of total (σ_t)/bulk (σ_b) conductivity of $La_3Ga_{4.5}Ge_{1.5}O_{14.25}$ (x = 0.5).

4.2.2.4 Test for proton conduction

Conductivity experiments in a dry and wet atmosphere were carried out for the parent and most conductive $La_3Ga_{4.5}Ge_{1.5}O_{14.25}$ (x = 0.5) langasite to investigate whether there is evidence for proton conduction in these materials. The analyses were carried out by flowing dry compressed air from a cylinder through the set up directly (dry conditions) and intercalating a bubbler containing water (wet conditions). Figure 4-19-a shows that for both compositions studied, the calculated bulk conductivity is identical under wet and dry atmospheres suggesting that there is no proton conduction. Additionally, Thermal Gravimetric Analysis (TGA) was performed in $La_3Ga_5GeO_{14}$ showing no evidence of water incorporation on the sample (see Figure 4-19-b).

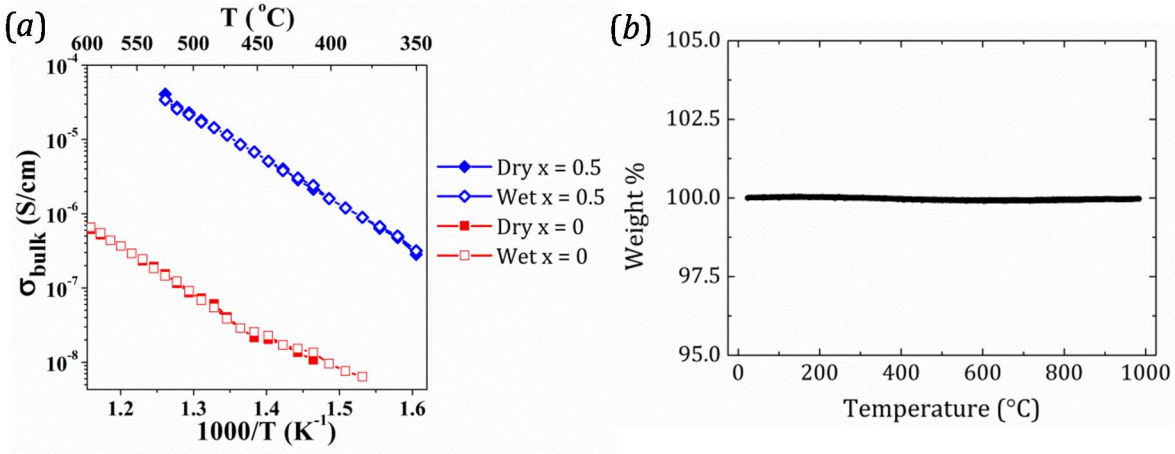

Figure 4-19 (a) Bulk conductivity of $x = 0$ (red squares) and 0.5 (blue diamonds) $La_3Ga_{5-x}Ge_{1+x}O_{14+x/2}$ in a dry and wet air atmospheres in filled and open symbols respectively. (b) TGA data of $La_3Ga_5GeO_{14}$ showing no change on mass upon heating up to 1000 °C.

4.2.3 Comparison with melilites

4.2.3.1 Structural comparison

The relaxation and cooperative distortions occurring in this family of materials are markedly different to those for the 0D isolated tetrahedra-based structure of the apatite and even for the 2D tetrahedral network of the melilite with a higher structural resemblance to langasites. Figure 4-20 is showing the structural relaxation around the interstitial and the bulk structure in two adjacent channels for the melilite (a) and langasite (b) structures. Similarly to the langasite, the interstitial oxygen O4 in the melilite is found within the Ga1-Ga2 tetrahedra layer between the La/Sr cations lying in the pentagonal channels. However, unlike to the langasite, the interstitial oxygen (O4) is found to bind solely to one tetrahedral Ga2 site containing one apical oxygen named O2 (see Figure 4-20-a). The bulk $Ga2O_4$ tetrahedra is shown in yellow in Figure 4-20-c, where Ga2 is bonded to O1, bridging Ga2 to a contiguous Ga2 site, and two O3, which are in turn bonded to neighbouring Ga1 sites. In the presence of the interstitial oxygen (O4), depicted in Figure 4-20-d, Ga2 is displaced towards the triangular O3-O2-O3 face of the original tetrahedron to $(Ga2)_{int}$ approaching the oxygen interstitial with a ~1.81 Å distance. Further relaxation within $(Ga2)_{int}O_5$ occurs as the two O3 sites move to the relaxed $(O3)_{int}$ (see Figure 4-20-c) position to make, with O2, three coplanar oxides around $(Ga2)_{int}$ resulting in a distorted trigonal bipyramid-like configuration. O4 is electrostatically stabilized by the rearrangement of La/Sr to $(La/Sr)_{int}$,

lying 0.45 Å closer to the interstitial defect. In contrast, the O1 which is not directly bound to $(Ga2)_{int}$ moves further away from O4 to $(O1)_{int}$[61].

The cooperative displacement that takes place as a consequence of the interstitial accommodation is dissimilar in melilites and langasites, regardless of the structural resemblance between the two. In the refined langasite model, a flattened shape of the atomic displacement parameters (ADPs) in the C site is observed (see Figure 4-8), which accounts for a certain degree of flexibility of the atoms in this site along the *a*-*b* plane, albeit less conspicuous than the Ga2 to $(Ga2)_{int}$ displacement in melilites. Another distinct feature is that in langasites, the alternating layers consisting of La and octahedra do not seem relaxed away for the accommodation of the interstitial, whereas in melilites the central atom within the same channel containing an oxygen interstitial moves to the new $(La/Sr)_{int}$. In langasites as in melilites, the oxygen propagation seems to occur within the tetrahedral layer, as the highly anisotropic displacement parameters (ADPs) of the C site, O1, O2 and O3 are flattened along this direction with the increase in temperature (see Figure 4-8 in page 100).

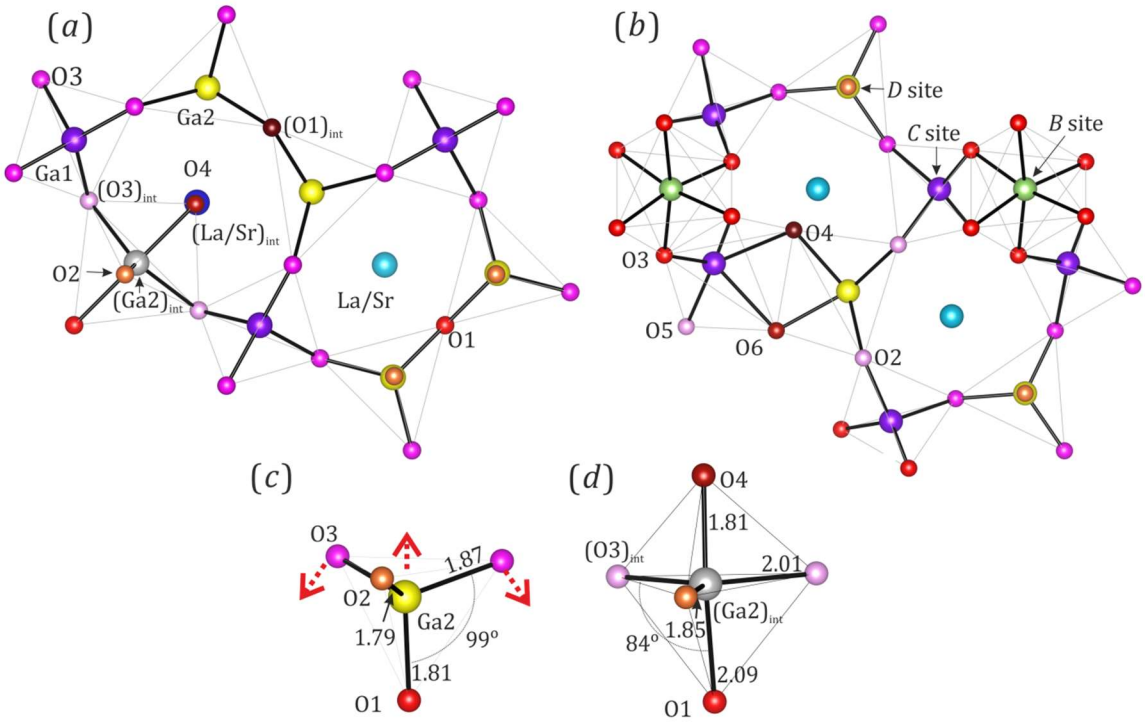

Figure 4-20 Differences in the local structure relaxation in langasites and melilites. The structural relaxation around the interstitial oxides in $La_{1.54}Sr_{0.46}Ga_3O_{7.27}$ melilite (*a*) and $La_3Ga_{3.5}Ge_{2.5}O_{14.75}$ langasite (*b*). (*a*) shows the structural relaxation around the interstitial oxygen in $La_{1.54}Sr_{0.46}Ga_3O_{7.27}$ along the channels parallel to [001]. The same colour coding: violet for 4-connected tetrahedra (Ga1) and yellow for the ones having a non-apical oxygen (Ga2) is used. The 5-coordinated Ga $(Ga2)_{int}$, bond to the maroon oxygen interstitial (O4) is highlighted in grey. O3 in magenta interconnects the distinct Ga sites and is able to relax to $(O3)_{int}$ in pale pink forming an equatorial plane with O2 in orange. This results in the formation the distorted trigonal bipyramidal polyhedra: $(Ga2)_{int}O5$. The split $(O1)_{int}$ site connecting two Ga2 sites (not directly bound to $(Ga2)_{int}O5$) relaxes away from the interstitial O4 and is plotted in mahogany to differentiate from the red bulk O1 site in red. Similarly, the $(La/Sr)_{int}$ site which displaced towards O4 by 0.45 Å is plotted in a darker blue in order to discriminate it from the bulk La/Sr site in the adjacent channel. Analogously a channel containing an interstitial oxygen adjacent to a channel with no interstitial is plotted for the langasite in (*b*). $Ga2O_4$ tetrahedal unit (*c*) and $(Ga2)_{int}O_5$ in $La_{1.54}Sr_{0.46}Ga_3O_{7.27}$ (*d*). The dashed red arrows represent the direction of the movement of the O3 and Ga2 sites for the incorporation of the O4 interstitial oxide.

4.2.3.2 Conductivity comparison

The mobility of the extra oxygen in the langasite and melilite structures is evaluated in Figure 4-21 where the variation of the conductivity at 500 °C is plotted as a function of the concentration of oxygen interstitials per channel '$C_{O_{int/chann}}$' (determined as $x/4$ for $La_{1+x}Sr_{1-x}Ga_3O_{7+x/2}$ and $x/6$ for $La_3Ga_{5-x}Ge_{1+x}O_{14+x/2}$). The increase in conductivity was fit to a power function for both structures (see caption in Figure 4-21).

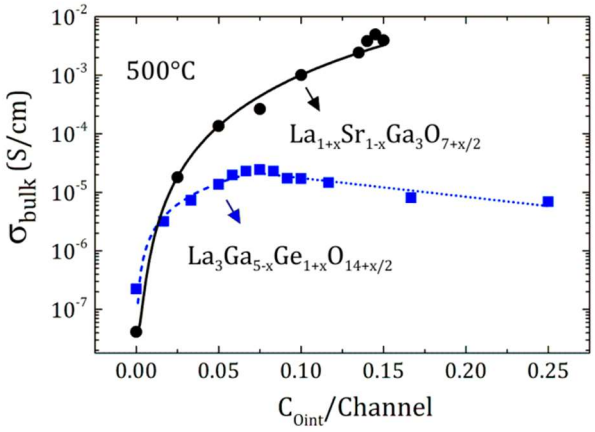

Figure 4-21 Conductivity at 500 °C for $La_{1+x}Sr_{1-x}Ga_3O_{7+x/2}$ (black circles) and $La_3Ga_{5-x}Ge_{1+x}O_{14+x/2}$ (blue squares) as a function of the concentration of extra oxygen introduced per channel. The black solid line is the fit to $\sigma = \sigma_0 + AC_{O_{int}/channel}^{n}$ where $\sigma_0 = 4.12 \times 10^{-8}$ S·cm^{-1}, A = 0.79 and n = 2.9 accounting for the increase in conductivity in melilites. The evolution of the conductivity as a function of the concentration of O_{int} in langasties was fit to two equations. The dash blue line denotes the fit of the data to $\sigma = A(C_{O_{int}/channel}-B)^{n}$ where A = 5.3×10^{-4} S·cm^{-1}, B = -3.54×10^{-10} S·cm^{-1} and n = 1.2 for $0 < x < 0.075$ whereas the dotted blue line accounts for the fit of the $0.075 < x < 0.25$ data to $\sigma = A + BC_{O_{int}/channel}$ where A = -9.42×10^{-5} S·cm^{-1} and B = 3×10^{-5} S·cm^{-1}.

The increase in conductivity as a function of the extra oxygen is less steep in langasites and the conductivity reaches a maximum value for langasites at a concentration of $C_{O_{int/channel}}$ ~0.075, whereas this value is doubled in melilites where the maxima is found at $C_{O_{int/channel}}$ ~0.15 showing a conductivity of 5×10^{-3} S·cm^{-1} at 500 °C, two orders of magnitude higher than the most conductive langasite ($C_{O_{int/chann}}$ ~0.075) having a conductivity of 2.3×10^{-5} S·cm^{-1} at the same temperature.

The less dramatic increase in conductivity as a function of the concentration of extra oxygen shown by $La_3Ga_{5-x}Ge_{1+x}O_{14+x/2}$ in comparison with other structure types based on interconnected tetrahedra incorporating extra oxygen such as melilites, could be explained on the basis of the differences in the local relaxation within the channels in the two structures. In melilites, the interstitial oxide ion is located in the center of the pengatonal channels where the large La cation lies (see Figure 4-20-a). The proposed interstitial migration pathway suggests that the O_{int} would move from one center of the pentagonal channel to a neighboring channel via the formation of an intermediate edge-sharing Ga_2O_9 unit between two Ga2 sites where the O_{int} becomes a bridging oxygen[42,61]. In langasites, the extra oxygen is displaced away from the center of the channel towards two neighboring tetrahedral C and D sites forming a $(Ga/Ge)_2O_8$ unit. In order for the extra oxygen to migrate along the tetrahedral layer into a neighboring $(Ga/Ge)_2O_7$ site, the most likely mechanism is a 'knock-on' type in which an O6 pushes O2 to O4 and this site hops across the channel to an O6 site where a new Ge_2O_8 unit is formed and so on. The displacement of the O_{int} further away from the middle of the channel into the $(Ga/Ge)_2O_8$ unit seems a plausible explanation for a more constrained mobility of the extra oxygen in langasites and it could also be the reason why the maximum in conductivity in langasites is found at $C_{O_{int/channel}}$ ~0.075 with the increase in the concentration of extra oxygen having no positive effect on the conductivity. The structural rigidity in langasites could be caused by the presence of octahedra interconnecting the top and bottom layers of tetrahedra.

In essence, the further relaxation required for the oxide ion accommodation in langasites in comparison with that of other interstitial oxide ion hosts with good ionic conducting properties such as apatites and melilites turns the $(Ga/Ge)_2O_8$ dimers into deeper trap for the interstitial oxides, thus preventing a fast oxide ion migration. The formation and de-formation of edge-sharing $(Ga/Ge)_2O_8$ units involve the breaking and creation of a higher number of bonds which in turn requires a higher energetic cost. This higher energetic cost can be correlated with the higher activation energies in $La_3Ga_{5-x}Ge_{1+x}O_{14+x/2}$ (~1.1 eV) with respect to $La_{1+x}Sr_{1-x}Ga_3O_{7+x/2}$ (~0.4 eV).

4.3 Summary and conclusion

The structure of doped langasites with a remarkable flexibility for the accommodation of up to 5.36 % of extra oxygen in $La_3Ga_{3.5}Ge_{2.5}O_{14.75}$ was introduced here. To reveal the local environment around the O_{int} combined DFT, NPD and ^{71}Ga and ^{17}O NMR studies were carried out that located the O_{int} in a Ge_2O_8 dimer. Such dimer is formed by two former C and D tetrahedral sites which simultaneously bind the interstitial to form a pseudo-square based pyramid like polyhedra sharing one edge. This provokes a rearrangement of the O2 framework oxygen which moves over 1 Å away from its original position.

Although a promising increase in the conductivity of over two orders of magnitude compared to the parent insulating material was observed for $La_3Ga_{4.5}Ge_{1.5}O_{14.25}$ (~10^{-3} S·cm^{-1} at 900 °C), the conductivity plateaus for those $La_3Ga_{5-x}Ge_{1+x}O_{14+x/2}$ compositions with $x > 0.5$. This was explained on the basis of the structural analysis presented. The creation and deformation of $(Ga/Ge)_2O_8$ dimers has a high energy cost (E_a ~1.1 eV) which could in turn be due to the restricted mobility of the tetrahedral C site which is locked in place by the binding of two octahedral B sites on the top and bottom layers.

5 ISOVALENT DOPING OF $La_3Ga_{5-x}Ge_{1+x}O_{14+x/2}$

This chapter comprises the study of isovalent dopings performed in $La_3Ga_{5-x}Ge_{1+x}O_{14+x/2}$ presented in Chapter 4. The aim of this doping strategy is to increase the disorder within the structure to enhance its conductivity. Two doping mechanisms were studied: one involved the substitution of La^{3+} on the A site for other lanthanides in $La_{3-y}Ln_yGa_{5-x}Ge_{1+x}O_{14+x/2}$where Ln = Pr, Nd, Sm and Gd and the second approach consisted of the replacement of the costly and scarce Ga^{3+} for Al^{3+} in $La_3Ga_{5-x-y}Al_yGe_{1+x}O_{14+x/2}$.

The doping of LaGaGeO langasites on the A site in $La_{3-y}Ln_yGa_{5-x}Ge_{1+x}O_{14+x/2}$ allowed us to correlate the effect of the A-cation size with the extra oxide ion incorporation capability and the resulting conductivity. Similar studies involving the co-doping of La for Ln were carried out in interstitial oxide ion conductors such as apatites [121,122] and melilites[142]. The cation radii for host and dopant cations are given in Table 5-1.

The isovalent doping of Ga for Al in $La_3Ga_{5-x-y}Al_yGe_{1+x}O_{14+x/2}$ and $La_3Al_{5-x}Ge_{1+x}O_{14+x/2}$ is discussed. Since the C and D tetrahedral sites are found to bind the extra oxygen incorporated in $La_3Ga_{5-x}Ge_{1+x}O_{14+x/2}$, this doping strategy constitutes an interesting approach to seek for an increase in conductivity as a consequence of the induced Ga, Al and Ge disorder in the M_2O_8 local environment. $La_3Ga_{5-x}Al_xSnO_{14}$ $(0 < x \leq 2)$[274], $La_3Nb_{0.5}Ga_{5.5-x}Al_xO14$ $(0 < x \leq 0.2)$[275], $La_3Ga_{5-x}Al_xSiO_{14}$ $(0 < x \leq 0.9)$[276] and $La_3Ta_{0.5}Ga_{5.5-x}Al_xO_{14}$ $(0 < x \leq 0.2)$[276] comprised previous $Ca_3Ga_2Ge_4O_{14}$-type structures where a partial substitution of Ga by Al is reported. The complete substitution of Ga by Al in $La_3Al_5GeO_{14}$ and $La_3Al_{5-x}Ge_{1+x}O_{14+x/2}$ introduced in this chapter are novel langasite compositions not reported up to date.

Table 5-1 Coordination, charge and ionic radii of the host and dopant cations for the systems studied in this chapter.

System	Site Doped	Coordination	Host		Dopant	
			Charge	Ionic radius (Å)	Charge	Ionic radius (Å)
$La_{3-y}Ln_yGa_{5-x}Ge_{1+x}O_{14+x/2}$	A	VIII	La^{3+}	1.16	Pr^{3+}	1.126
					Nd^{3+}	1.109
					Sm^{3+}	1.079
					Gd^{3+}	1.053
$La_3Ga_{5-x-y}Al_yGe_{1+x}O_{14+x/2}$	B, C and D	VI/IV	Ga^{3+}	0.62/ 0.47	Al^{3+}	0.535/ 0.39
$La_3Al_{5-x}Ge_{1+x}O_{14+x/2}$	B, C and D	VI/IV	Al^{3+}	0.535/ 0.39	Ge^{4+}	0.53/ 0.39

The ionic radii values are taken from [239]

5.1 Experimental Methods

5.1.1.1 Synthesis

Doped langasites were prepared *via* Pechini's method by mixing stoichiometric amounts of the various lanthanide (III) nitrates (Alfa Aesar 99.99 %) with gallium (III) nitrate (Alfa Aesar 99.999 %), aluminium (III) nitrate (Alfa Aesar 99.999 %) and germanium (IV) oxide (Sigma-Aldrich ≥99.99 %) in distilled water. In $La_{3-y}Ln_yGa_{5-x}Ge_{1+x}O_{14+x/2}$, the concentration of product formula in the initial solution ranged from 6.23×10^{-4} M to 6.23×10^{-3} M. Citric acid (Sigma-Aldrich ≥99.5 %) and ethylene glycol (Alfa Aesar 99 %) were added to the solution in a 1:1 ratio to the initial mixture of reagents. The mixture of reactants was dried for 15 hours at 175 °C in a hot plate. The dried polymerized precursors were ground and heated at 600 °C for 60 hours which allowed for the removal of the organic components. These steps were followed by a thorough mixing of the pre-calcined powders, pellet pressing and a final sintering of the $La_{3-y}Ln_yGa_{5-x}Ge_{1+x}O_{14+x/2}$ reactants at 850 °C for $x \leq 1$ and at 800 °C for $x > 1$. The Al-langasites $La_3Al_{5-x}Ge_{1+x}O_{14+x/2}$ and $La_3Ga_{5-x-y}Al_yGe_{1+x}O_{14+x/2}$ with $0 \leq x \leq 1$ were phase pure after one annealing cycle consisting of a 12 hours dwell at 900 °C with a heating-cooling rate of 3 ° min^{-1}. In $La_3Al_{3.5}Ge_{2.5}O_{14.75}$ (x = 1.5), the final temperature was lowered to 850 °C to avoid the formation of a $LaAlO_3$ impurity at 900 °C at this particular composition.

5.1.1.2 Characterization

5.1.1.2.1 XRD and NPD

The purity of the samples was analysed by means of powder X-ray diffraction in a PANalytical X'pert Pro diffractometer with a Co-source ($K_{\alpha 1,Co} = 1.7890$ Å) in reflection mode and in a Bruker D8 Discovery diffractometer with a Cu-source ($K_{\alpha 1,Cu} = 1.5406$ Å) .

Elemental analysis of $La_{1.5}Pr_{1.5}Ga_{4.5}Ge_{1.5}O_{14.25}$ specimens sintered at 800-1300 °C was carried out in the JEOL FX2000 Transmission Electron Microscope (TEM). The sample preparation and operation conditions are explained in the experimental chapter (see 2.3.2.1).

The interstitial location and structural relaxation in $La_{1.5}Pr_{1.5}Ga_4Ge_2O_{14.5}$ was studied at the high resolution TOF diffractometer HRPD at ISIS. These experiments were performed in a 5 g sized sample contained in a ∅ = 11 mm vanadium can covering the height of the beam of

~2 cm. The diffraction patterns at the banks 1-3 were acquired at room temperature and ambient pressure.

The structural characterization of $La_3Al_{5-x}Ge_{1+x}O_{14+x/2}$ with x = 0, 1 and 1.5 was carried out by means of a combined study of Synchrotron X-Ray Diffraction (SXRD) data collected at the I11 beamline in Diamond and high-intensity Neutron Diffraction data collected at the GEM diffractometer in ISIS. This study was carried out at room temperature.

5.1.1.2.2 Pellet sintering

Ln-langasites pellets for conductivity measurement purposes were sintered by means of two routes as follows:

- Conventional sintering was carried out in $La_{3-y}Ln_yGa_{5-x}Ge_{1+x}O_{14+x/2}$ with Ln = Pr, Nd, with y = 0 and 1.5 and with x = 0, 0.25 and 0.5. Mixtures of reagents were prepared by Pechini and 6.23×10^{-4} M solutions of the initial mixture of precursors were used. Carbon-free powders were obtained after an intermediate annealing step at 600 °C for 60 hours. Afterwards the powder were re-ground and pressed into ∅ = 8 mm sized pellets with in a uniaxial press at a pressure of 10 kPa. At the final steps, the pellets were heated at 1250 °C for 5 hours (x = 0.25 and 0.5) and 12 hours (x = 0) delivering $\rho \geq 80$ % specimens.

- Phase pure $La_{3-y}Ln_yGa_{5-x}Ge_{1+x}O_{14+x/2}$ with Ln = Pr Nd, Sm and Gd, with y = 1, 1.5 and 3 and with $x = 0.5$, 0.75 and 1 were synthesized by Pechini at 850 °C for 12 hours. Phase pure samples were mechanically milled and SPS-sintered as follows: 1.5-2 g were heated at temperatures ranging from 1000 to 1050 °C for 4 - 5 min in a ⌀ = 20 mm graphite die exerting a compressive force of 50 MPa along the z-axis. The ramp rate was held constant at 200 ° min^{-1} in all the experiments (see 2.2.3 for further details regarding the equipment used).

An alternative approach involving the simultaneous synthesis and sintering assisted by SPS were carried out for $La_3Al_{5-x}Ge_{1+x}O_{14+x/2}$ and $La_3Ga_{5-x-y}Al_yGe_{1+x}O_{14+x/2}$ with $0 \leq x \leq 1$. Stoichiometric mixtures of reactants prepared by Pechini were heated below their synthesis temperature at 800-850 °C for 12 hours and mechanically milled (see page 23 for milling conditions). 1.5-2g of un-reacted powders were SPS sintered at low temperatures 1000-1050 °C (slightly above T_{decomp} ~ 950 °C) that were held for 4-5 min in a ⌀ = 20 mm graphite die with an applied pressure of 50 MPa and a heating-cooling ramp rate of 200 ° min^{-1} delivering samples with a high purity and 60-90 % densities.

5.1.1.3 Conductivity determination

AC impedance measurements were carried out in two instruments: a Solartron 1255B frequency response analyser coupled to a Solartron 1287 electrochemical interface at 1 mHz-20 MHz (for the total conductivity determination introduced in page 137) and an E4980 LCR meter analyser at 1 Hz – 2 MHz (for the bulk conductivity introduced in page 141) while a 300 mV perturbation voltage was applied. The data was collected under cooling while commercial dry air (BOC) was circulated through a sealed environment. Commercial gold paste was used as electrodes. For further details on sample preparation and equipment see 2.3.3.

5.2 Results and Discussion

5.2.1 $La_{3-y}Ln_yGa_{5-x}Ge_{1+x}O_{14+x/2}$ for Ln=Pr, Nd, Sm and Gd

5.2.1.1 Synthetic Outcome

Phase pure $La_{3-y}Ln_yGa_{5-x}Ge_{1+x}O_{14+x/2}$ $0 \leq x \leq 0.3$ compositions were formed after one annealing cycle of the Pechini precursors at 1300 °C for 12 hours. The synthetic temperature was lowered to 800-850 °C in $La_{3-y}Ln_yGa_{5-x}Ge_{1+x}O_{14+x/2}$ with $x > 0.3$. Increasing the synthetic temperature above 850 °C or above 800 °C in $La_{1.5}Ln_{1.5}Ga_{3.5}Ge_{2.5}O_{14.75}$ with Ln = Pr and Nd or increasing the nominal composition to $x >$ 1.5 lead to the formation of $Ln_3Ga_5O_{12}$ with a garnet structure as an impurity.

The cell parameters for $La_{3-y}Ln_yGa_{5-x}Ge_{1+x}O_{14+x/2}$ obey Vegard's law within the $0 \leq x \leq 1.5$ region for y = 1.5 and Ln = Nd, Pr and Sm. For the complete substitution of La when y = 3, a lower doping of $0 \leq x \leq 1$ is achieved for all Ln studied: Nd, Pr, Sm and Gd. The trend in the lattice parameters of Pr and Nd containing systems is given in Figure 5-2.

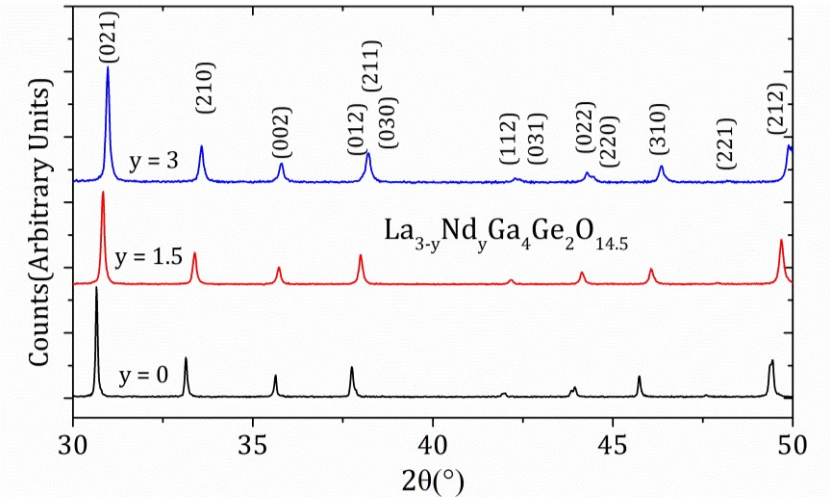

Figure 5-1 PXRD patterns measured in Bruker D8 Advance diffractometer ($K_{\alpha 1,Cu} = 1.5406$ Å) in $La_{3-y}Nd_yGa_4Ge_2O_{14.5}$ with $0 \leq y \leq 3$. The 2θ region 30-50° shows a shift in the Bragg peaks with the change in compositions and no presence of peaks attributed to impurity phases.

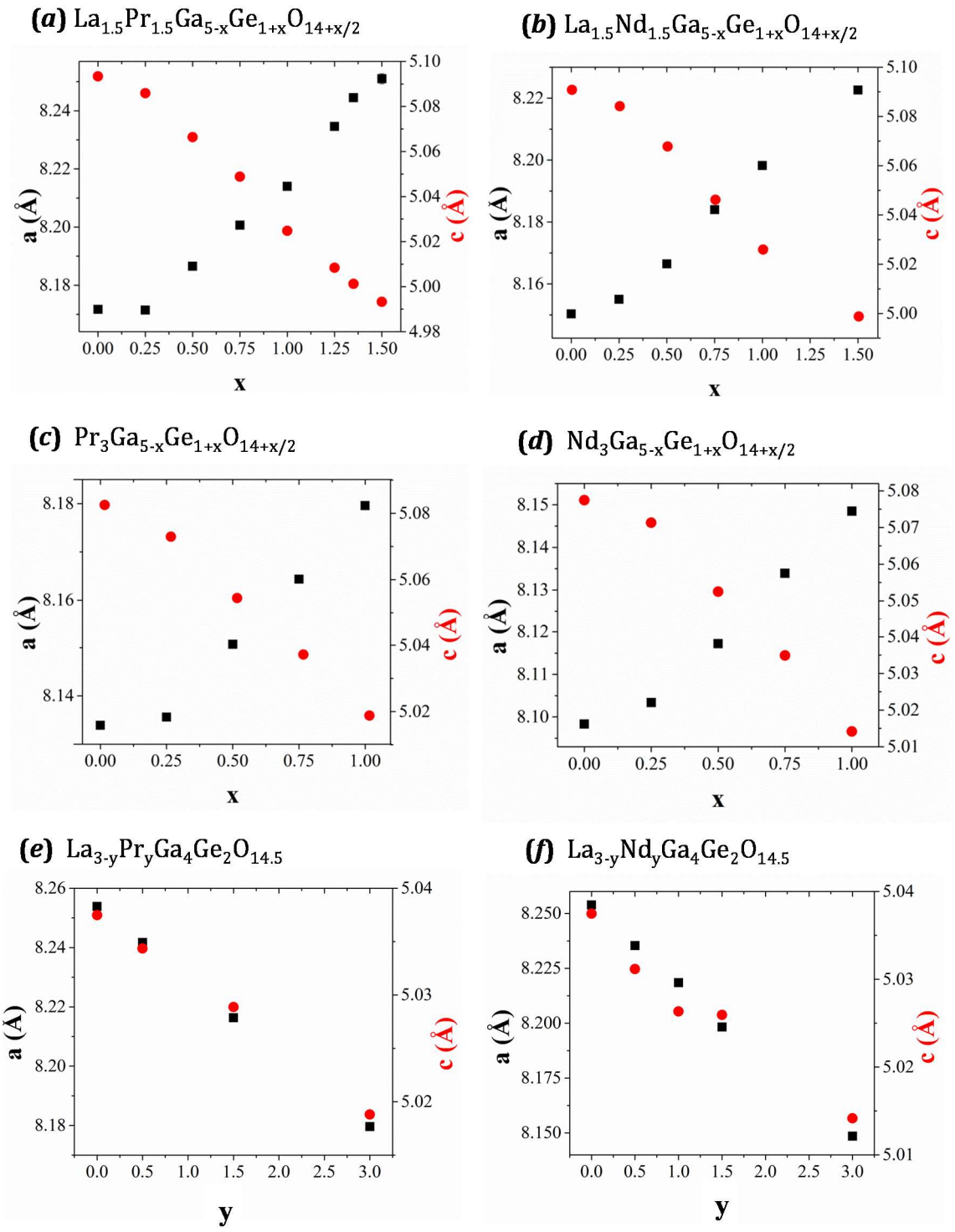

Figure 5-2 Trends of the lattice parameter evaluated by Pawley fitting in the Nd and Pr containing systems. The errors plotted correspond to 1 × e.s.d and are lying behing the symbols.

An EDX analysis in the TEM demonstrated the successful incorporation of extra oxygen in a sample with the $La_{1.5}Pr_{1.5}Ga_4Ge_2O_{14.5}$ nominal composition shown in Figure 5-3. The various crystallites analysed grouped into a tight cluster with an averaged composition of $La_{1.59(9)}Pr_{1.46(7)}Ga_{4.03(7)}Ge_{1.91(6)}O_{14.46(3)}$. This sample was analysed by NPD and the Rietveld refinement of the data is introduced hereafter.

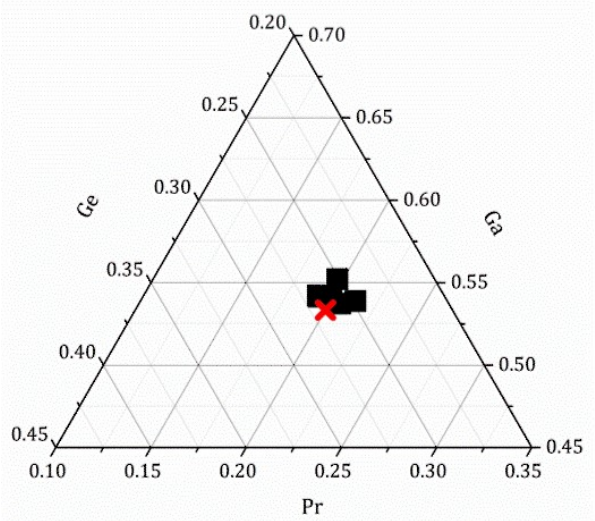

Figure 5-3 Ternary phase diagram of the EDX data collected in a sample with the $La_{1.5}Pr_{1.5}Ga_4Ge_2O_{14.5}$ nominal composition (denoted by a red cross), the data collected on eight crystallites (denoted by black squares) averaged to $La_{1.59(9)}Pr_{1.46(7)}Ga_{4.03(7)}Ge_{1.91(6)}O_{14.46(3)}$. The Rietveld refinement of the HRPD data of this sample is discussed in the next section 5.2.1.2.

5.2.1.2 Structural Characterization: Refinement of high resolution NPD data

The approach undertaken for the refinement of the high resolution $La_{1.5}Pr_{1.5}Ga_4Ge_2O_{14.5}$ data at 297 K is analogous to the one presented in the previous chapter for $La_3Ga_4Ge_2O_{14.5}$ and $La_3Ga_{3.5}Ge_{2.5}O_{14.75}$. Firstly the possibility of lowering the symmetry of the cell as a consequence of the accommodation of interstitial oxide ions was tested by a Pawley fit of the data in two different space groups: *P*321 and *P*1 (see Table 5-2). All the peaks present in the NPD pattern were indexed in a *P*321 space group having a very similar goodness of fit of $S \sim 1.9$ to the one obtained in a *P*1 geometry. Therefore *P*321 was retained for further refinement.

Table 5-2 Comparison of the fitting parameters for a Pawley fitting of the NPD $La_{1.5}Pr_{1.5}Ga_4Ge_2O_{14.5}$ in *P*321 and *P*1 space groups.

Composition	HPRD d-spacing	*P*321		*P*1	
		R_{wp} / R_{exp}	S	R_{wp} / R_{exp}	S
$La_{1.5}Pr_{1.5}Ga_4Ge_2O_{14.5}$	0.6-2.6 (b1) 0.8-3.7 (b2) 2.6-7.9 (b3)	1.98 / 1.06	1.88	1.53 / 0.82	1.86

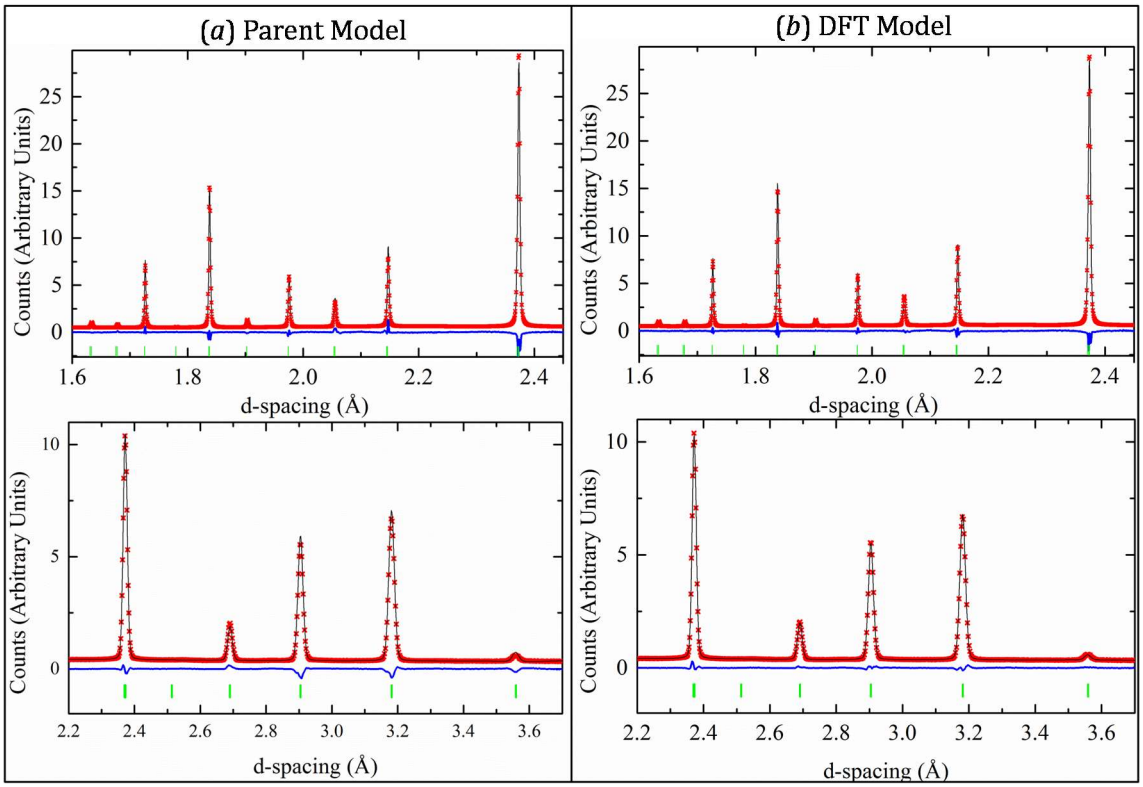

Figure 5-4 NPD Rietveld refinement of $La_{1.5}Pr_{1.5}Ge_4Ge_2O_{14.5}$ at 297 K using two different approaches: (a) Parent model ($R_{wp} = 4.659, R_{exp} = 1.028$ and $S = 4.530$) and (b) the initial refinement *via* a DFT model ($R_{wp} = 2.761, R_{exp} = 1.027$ and $S = 2.687$). Top figures account for the backscattering bank (b1) and the bottom figures for the detector at 90° (b2).

The initial model used for the refinement was the averaged DFT model calculated for $La_3Ga_4Ge_2O_{14.5}$ in which the A-site occupancy was fixed to 1/2 for La and Pr. At the early stages of the refinement, the occupancies for the framework oxygen sites O1-O3 and those for the new oxygen sites O4-O6 were freely refined so as to test the veracity of the model to describe $La_{1.5}Pr_{1.5}Ga_4Ge_2O_{14.5}$. The refined compositions at this early stage of the refinement were in good agreement to the values expected from the model. These results are a good indication supporting the fact that the extra oxygen in $La_{1.5}Pr_{1.5}Ga_4Ge_2O_{14.5}$ is also allocated within the pseudo-square based pyramid edge-sharing M_2O_8 units. Successive steps in the refinement involved fixing the occupancies of O1 and O3. The refinement indicated that these sites were indeed fully occupied and their occupancies were accordingly fixed to 1. On the other hand, restraints were introduced on the occupancies of O2 and O4-O6 with occ < 1, so as to maintain the expected ratios (see 4.2.1.2). Once the restrains were applied, the thermal parameters for all sites (excluding O4 and O6 due to their low occupancies) were refined anisotropically. At the final stage, once a stable refinement with sensible ADPs was achieved the occupancy restraints were removed and refined. The refined oxygen content of 14.37(4) is in good agreement with the nominal composition of 14.25.

The background was fitted using a Chebyshev function with eight polynomials. The peak shape was fitted using a pseudo-Voigt function for bank 3 with a lower resolution and an expanded pseudo-Voigt function to account for Stephens' model[208] for microstrain broadening for time-of-flight data in a trigonal geometry in high resolution banks 1 and 2. The refined atomic coordinates, occupancies and displacement parameters are introduced in Table 5-3 and Table 5-4.

Table 5-3 NPD refined fractional atomic coordinates and equivalent isotropic displacement (Å²) parameters in $La_{1.5}Pr_{1.5}Ga_4Ge_2O_{14.5}$ at 297 K.

*P*321	*a* = 8.22029(5) Å		$\boldsymbol{R_{wp}}$ = 2.475		
	c = 5.02713(3) Å		$\boldsymbol{R_{exp}}$ = 1.027		
	V = 294.188(4) Å³		$\boldsymbol{S}$ =2.410		
Site	x	y	z	B_{eq}	Occ.
La1	0.4171(1)	0	0	1.95	0.5
Pr1	0.4171(1)	0	0	1.95	0.5
Ga1	0	0	0	1.31	1/3
Ge1	0	0	0	1.31	2/3
Ga2	1/3	2/3	0.5286(3)	1.23	1/3
Ge2	1/3	2/3	0.5286(3)	1.23	2/3
Ga3	0.7606(1)	0	0.5	1.73	1/3
Ge3	0.7606(1)	0	0.5	1.73	2/3
O1	1/3	2/3	0.1788(3)	2.06	1
O2	0.4655(2)	0.3146(2)	0.3151(4)	1.19	0.653(2)
O3	0.2170(1)	0.0849(1)	0.7678(3)	2.70	1
O4	0.292(3)	0.865(2)	0.613(4)	2.9(3)	0.061(2)
O5	0.839(1)	0.5708(7)	0.285(1)	3.69	0.268(2)
O6	0.060(1)	0.551(2)	0.574(2)	2.6(2)	0.080(1)

Table 5-4 Atomic displacement parameters (Å²).

Sites	U^{11}	U^{22}	U^{33}	U^{12}	U^{13}	U^{23}
La1/Pr1	0.0229(5)	0.0200(7)	0.0304(8)	0.0100(3)	0	0
Ga1/Ge1	0.0205(5)	0.0205(5)	0.0089(9)	0.0102(2)	0	0
Ga2/Ge2	0.0174(3)	0.0174(3)	0.0120(6)	0.0087(2)	0	0
Ga3/Ge3	0.0241(4)	0.0224(4)	0.0186(6)	0.0121(2)	0	0
O1	0.0273(7)	0.0273(7)	0.024(1)	0.0137(3)	0	0
O2	0.0078(7)	0.0189(9)	0.0132(8)	0.0027(7)	0.0019(7)	0.0057(7)
O3	0.0250(6)	0.0474(8)	0.0298(7)	0.0177(6)	0.005(4)	0.0174(6)
O5	0.077(3)	0.028(2)	0.030(3)	0.022(2)	-0.006(3)	0.000(2)

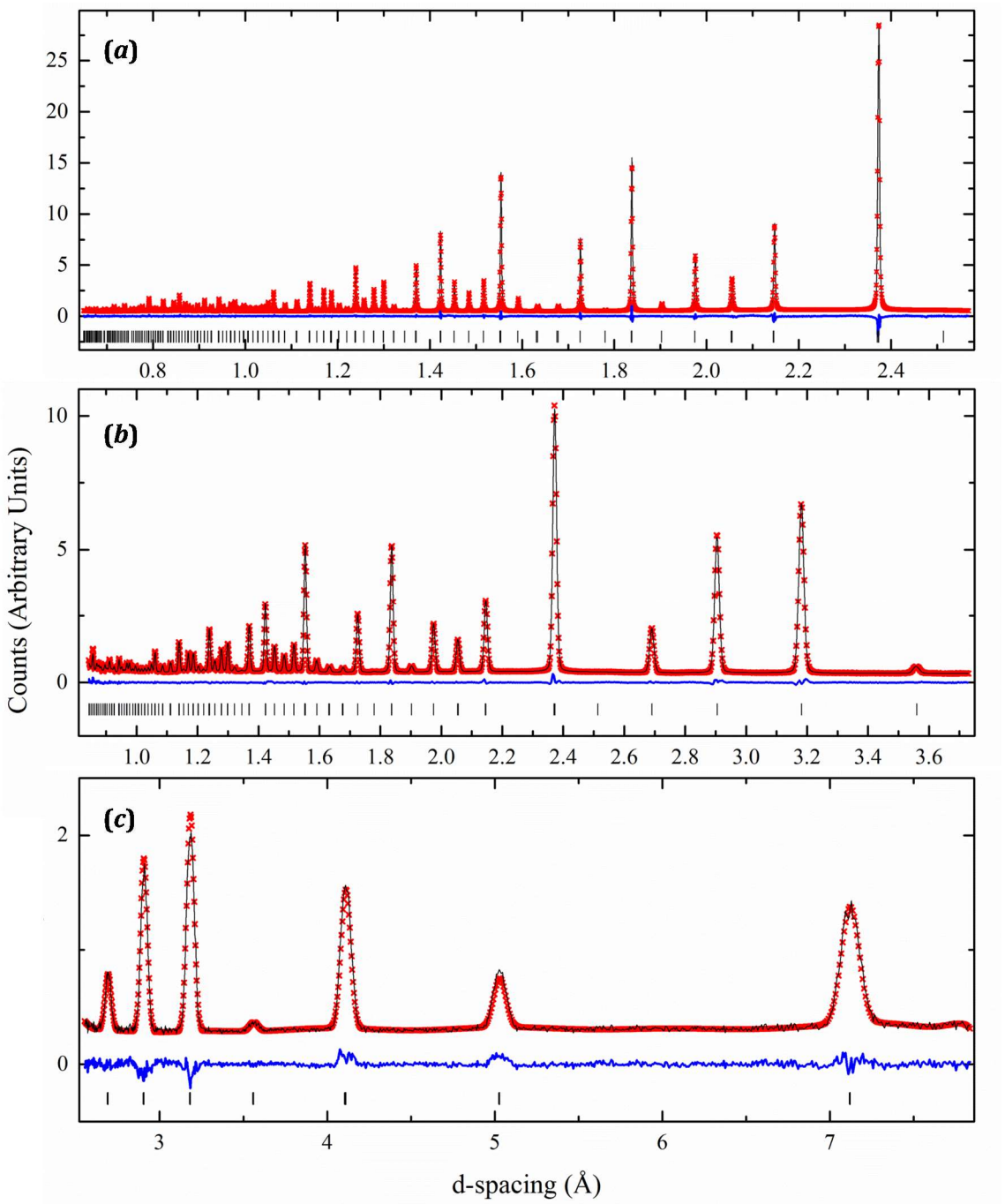

Figure 5-5 $La_{1.5}Pr_{1.5}Ga_4Ge_2O_{14.5}$ at 297 K. Fit of the combined Rietveld refined banks 1 (*a*), 2 (*b*) and 3 (*c*) for the detectors located at 170, 90 and 30 ° respectively.

Fitting of the refined model to the HRPD data b1-b3 presented in Figure 5-5 shows a good match between the observed and calculated profiles with no presence of impurities giving rise to unassigned peaks in the NPD pattern.

Figure 5-6 is showing the $La_{1.5}Pr_{1.5}Ga_4Ge_2O_{14.5}$ asymmetric unit cell along the *c* (*a*) and *a*-axes (*b*). In this figure, the M_2O_7 connectivity is given. The new oxygen sites O4-O6 originated as a consequence of incorporation of extra oxygen are also given in the figure, although no connectivity is shown for these atoms not to overcrowd the figures at a risk of losing perception of the shape and size of the refined ADPs.

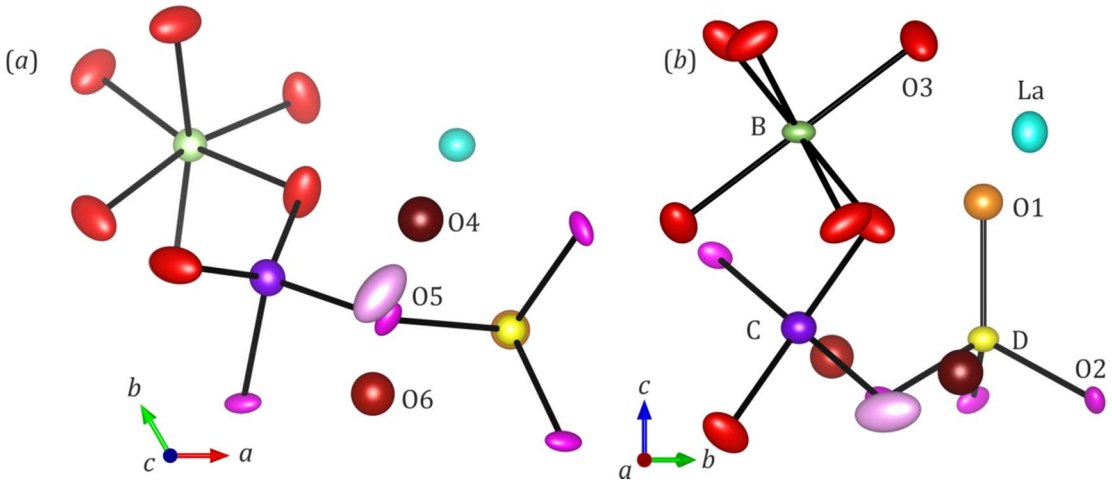

Figure 5-6 Plot of the asymmetric unit cell of the refined $La_{1.5}Pr_{1.5}Ga_4Ge_2O_{14.5}$ at 297 K along the *c* (*a*) and *a*-axes (*b*).

It is noticeable in Figure 5-6 the change in ADPs' shapes from the cations with a more circular shape to the oxygen sites, as the later show an elongation along the *a*-*b* plane. These characteristic shapes are in good agreement with those observed in $La_3Ga_{3.5}Ge_{2.5}O_{14.75}$ analysed at temperatures ranging from 9 to 873K (see 'VT NPD studies of $La_3Ga_{3.5}Ge_{2.5}O_{14.75}$' in page 98).

Due to the diffraction techniques limitations previously mentioned (see 4.2.1.3), impeding the clear determination of Ga and Ge distribution along the B-D sites in the refined model presented in Table 5-3 the occupancies of Ga and Ge were fixed to 2/3 and 1/3 values respectively. A more correct assessment of the relative occupancies of these cations is performed in base of the calculated Bond Valence Sum (*BVS*) values. The calculated *BVS* for Ga and Ge, in the B sites and in both M_2O_7 and M_2O_8 local environments in C and D sites is presented in Table 5-5. The calculated cations' *BVS* for the NPD refined $La_3Ga_4Ge_2O_{14.5}$ at 297K incorporating the same amount extra oxygen ($\%_{O_{int}} = 3.57$) is also given for comparison.

Table 5-5 Calculated BVS for all cations in $La_{1.5}Pr_{1.5}Ga_4Ge_2O_{14.5}$ in the b1-b3 combined HPRD refined model at 297 K. The BVS calculated values for $La_3Ga_4Ge_2O_{14.5}$ at 297 K are also given for comparison.

			$La_{1.5}Pr_{1.5}Ga_4Ge_2O_{14.5}$	$La_3Ga_4Ge_2O_{14.5}$
La			2.99	2.85
Pr			2.73	-
B (1a)	Ga		3.48	3.32
	Ge		3.51	3.48
C (3f)	Ga	M_2O_7	3.00	2.99
		M_2O_8	3.19	3.25
		Average	3.02	3.01
	Ge	M_2O_7	3.15	3.14
		M_2O_8	3.35	3.42
		Average	3.17	3.16
D (2d)	Ga	M_2O_7	3.71	3.46
		M_2O_8	3.15	3.53
		Average	3.66	3.46
	Ge	M_2O_7	3.90	3.64
		M_2O_8	3.31	3.70
		Average	3.57	3.64

From the inspection of the calculated *BVS* for the cations in the NPD refined models for $La_{1.5}Pr_{1.5}Ga_4Ge_2O_{14.5}$ and $La_3Ga_4Ge_2O_{14.5}$ at 297 K it is concluded that the C site would be preferably occupied by Ga in both $La_{1.5}Pr_{1.5}Ga_4Ge_2O_{14.5}$ and $La_3Ga_4Ge_2O_{14.5}$ as averaged *BVS* values for this site when fully occupied by Ga equals to 3.02 and 3.01 respectively. On the other hand, the octahedral and smaller 3-connected tetrahedral B and D sites with BVS of approximately ~3.5 suggest a Ga/Ge disorder. Fixing the fractional occupancy of B and D sites to ½, as suggested by BVS, yields $La_{1.5}Pr_{1.5}Ga_4Ge_2O_{14.5}$ and $La_3Ga_4Ge_2O_{14.5}$ matching their nominal compositions.

5.2.1.3 Conductivity Properties

5.2.1.3.1 Material processing

Similarly to the La-langasites introduced in Chapter 4, the Ge-richer $La_{3-y}Ln_yGa_{5-x}Ge_{1+x}O_{14+x/2}$ compositions show lower decomposition temperatures ranging from 1100 °C for $x = 0.5$ to 800 °C for $x = 1.5$. For this reason, two different approaches were carried out for the sintering of $La_{3-y}Ln_yGa_{5-x}Ge_{1+x}O_{14+x/2}$: conventional sintering was feasible for $0 \leq x \leq 0.3$, whereas a fast sintering technique such as Spark Plasma assisted Sintering (SPS) was needed for the Ge-richer $0.5 \leq x \leq 1$ range in order to avoid the decomposition of the main langasite phase.

- Conventional Sintering of $La_{3-y}Ln_yGa_{5-x}Ge_{1+x}O_{14+x/2}$ langasites

The sintering of $La_{3-y}Ln_yGa_{5-x}Ge_{1+x}O_{14+x/2}$ with Ln = Pr, Nd, Sm and Gd by conventional techniques consisting of prolonged firings at high temperatures close to their melting point (~1325-1350 °C) was not a trivial matter. The underlying cause to the added complexity in the densification of $La_{3-y}Ln_yGa_{5-x}Ge_{1+x}O_{14+x/2}$ was the formation of large voids during the

pellets sintering process. Figure 5-7 is showing the polished surface of an ø = 8 mm pellet with a $La_{1.5}Pr_{1.5}Ga_{4.5}Ge_{1.5}O_{14.25}$ nominal composition synthesized by the Pechini method, with a final annealing step at the high temperature of 1300 °C that was dwell for a duration of 12 hours. This phenomenon was observed for the sintering at T > 1100 °C for all Ln = Pr, Nd, Sm and Gd containing phases.

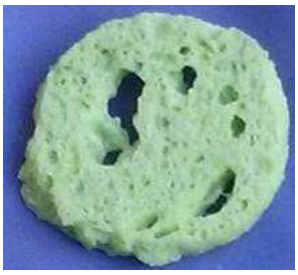

Figure 5-7 Presence of holes in an ø = 8 mm $La_{1.5}Pr_{1.5}Ga_{4.5}Ge_{1.5}O_{14.25}$ annealed for 12 hours at 1300 °C revealed after polishing its surface. The initial concentration of the solution of precursors was 6.23×10^{-3} M.

The morphology of the pellet in Figure 5-7 was investigated in a micron scale in the Scanning Electron Microscope (SEM) (see Figure 5-8). The microstructural SEM analysis revealed the existence of micropores in the $La_{1.5}Pr_{1.5}Ga_{4.5}Ge_{1.5}O_{14.25}$ pellet obtained by conventional sintering at 1300 °C. The pores are formed by the stacking of needle-like particles in parallel, resembling a staircase that ascends in circles that revolve around an axis. This particle arrangement can be clearly observed in the walls of tunnels running perpendicular to the folio plane (see Figure 5-8 ($b - f$)). Presumably, the stacking of micron-sized needle-like plates in parallel forming tunnels would ultimately generate visible mm-sized voids in Figure 5-7.

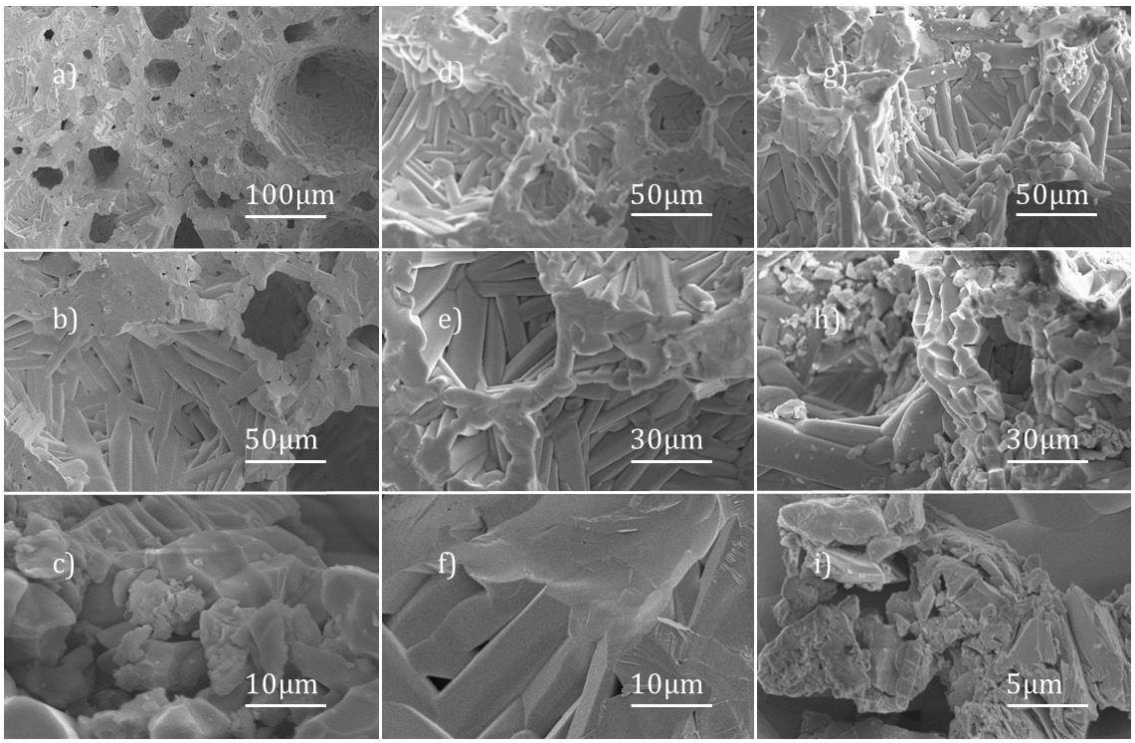

Figure 5-8 SEM images of a $La_{1.5}Pr_{1.5}Ga_{4.5}Ge_{1.5}O_{14.25}$ $\emptyset = 8\,mm$ pellet sintered at 1300 °C for 12 hours. The initial concentration of the Pechini precursors was $6.23 \times 10^{-3}\,M$.

Interestingly, a strong correlation between the concentration of the precursor solution and the final presence of voids in the sintered pellets was noticed. The more concentrated precursor solutions lead to the formation of larger voids in the final sintering step, *e*. *g*., the concentration of the precursor solution for the pellet in Figure 5-7 was the highest studied of 6.23 × 10^{-3} M. To account for this peculiar occurrence, precursor solution with various concentrations (*i*. *e*. 6.23 × 10^{-4}, 1.24 × 10^{-3} and 3.11 × 10^{-3} M) were produced and studied. The experiment consisted of carrying syntheses in parallel involving the polymerization of the precursor solution with different concentrations at 175 °C followed by the calcination at 600 °C for 60 hours. At this stage, prior to the sintering of the pellets at high temperatures, the particle size and morphology of the powder generated by each batch was studied on the SEM.

The images obtained for the resulting powders of 6.23 × 10^{-4} M (*a* and *d*), 1.24 × 10^{-3} M (*b* and *e*) and 3.11 × 10^{-3} M (*c* and *f*) starting concentration batches are given in Figure 5-9. An inspection of these images demonstrates an increment in the particle size of the precursor powders with the increase in concentration of the Pechini mother solution. After a 12 hours sintering step at 1300 °C those samples with initial concentrations of 1.24 × 10^{-3} and 3.11 × 10^{-3} M produced sintered pellets containing voids very much alike the ones in Figure 5-7. On the other hand, the more diluted mother solution with a concentration of 6.23 × 10^{-4} M produced a void-free pellet with a satisfactory 92 % density, making this a suitable candidate specimen for AC impedance analysis.

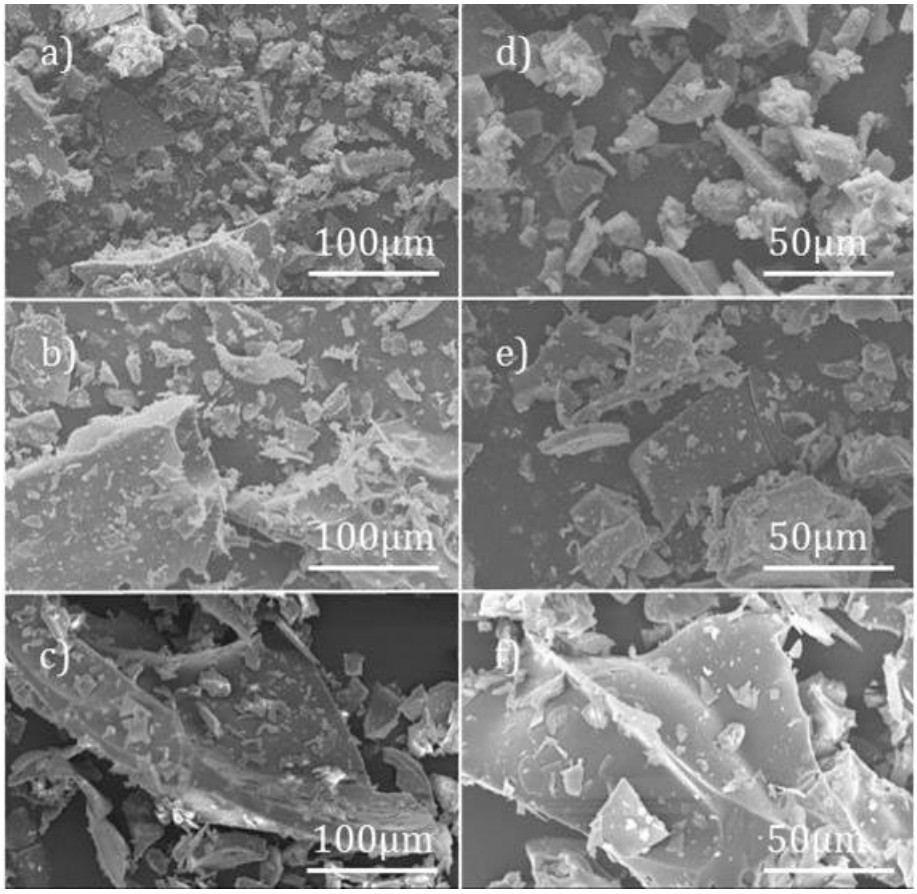

Figure 5-9 : SEM images of an initial mixture of reaction with a nominal $La_{1.5}Pr_{1.5}Ga_{4.5}Ge_{1.5}O_{14.25}$ composition. The initial concentration of the precursor of the reaction increases from 6.23 × 10^{-4} M (*a* and *d*), to 1.24 × 10^{-3} M (*b* and *e*) and 3.11 × 10^{-3} M (*c* and *f*). The SEM images were taken on C-free powders calcined at 600 °C for 60 hours. Voids were present in the sintered pellet of the powders *b*, *c*, *e* and *f* whereas *a* and *d* were 92 % dense after sintering at 1300 °C for several hours.

To further investigate this phenomenon and clarify whether the formation of voids is merely down to the crystallization process or it is also influenced by the formation of secondary phases, we investigated the phase purity and composition by powder diffraction and elemental analysis in the TEM in samples where the initial concentration of precursors equal to 6.23×10^{-3} and 6.23×10^{-4} M. After a final sintering stage involving the annealing of pressed powders at 1300 °C for 12 hours the initial concentrations of 6.23×10^{-3} and 6.23×10^{-4} M gave rise to large voids (similar to those shown in Figure 5-7) and a 92 % dense pellet respectively. Interestingly, the EDX and PXRD data collected on ground pellets produced with both 6.23×10^{-3} M (*b*) and 6.23×10^{-4} M (*c*) solutions introduced in Figure 5-10 revealed no presence of impurities. The composition of eight crystallites analysed per sample grouped into a tight cluster with an averaged compositions that rounded up to $La_{1.5}Pr_{1.5}Ga_{4.6}Ge_{1.4}O_{14.2}$ in both samples (*b*) and (*c*). These results support the fact that there are no variations in compositions correlated with the concentration of precursor in the initial mother solution.

The difference in content in Ge from $x = 0.5$ in the nominal targeted composition to $x \sim 0.4$ in the final analysed composition in samples (*b*) and (*c*), could be ascribed to the volatilization of Ge after the long sintering at the high temperature of 1300 °C. As mentioned earlier in this chapter a decrease in the decomposition temperature as the content of Ge 'x' increases was also observed in $y \neq 0$ compositions analogously to $La_{3-y}Ln_yGa_{5-x}Ge_{1+x}O_{14+x/2}$ where $y = 0$ (see page 77). To account for the volatilization of germanium with the increase in temperature, a sample belonging to the large batch produced with an initial concentration of 6.23×10^{-3} M was sintered at the lower temperature of 950 °C for 12 hours. The EDX and PXRD data collected in such sample named (*a*) are given in Figure 5-10. The analysed composition in (*a*) annealed at a lower temperature of 950 °C matches the $La_{1.5}Pr_{1.5}Ga_{4.5}Ge_{1.5}O_{14.25}$ nominal composition targeted. A summary of the lattice parameters, density and EDX data analysed is given in Table 5-6 for samples 6.23×10^{-3} M annealed at 950 °C (*a*) and at 1300 °C (*b*) and 6.23×10^{-4} M annealed at 950 °C (*c*).

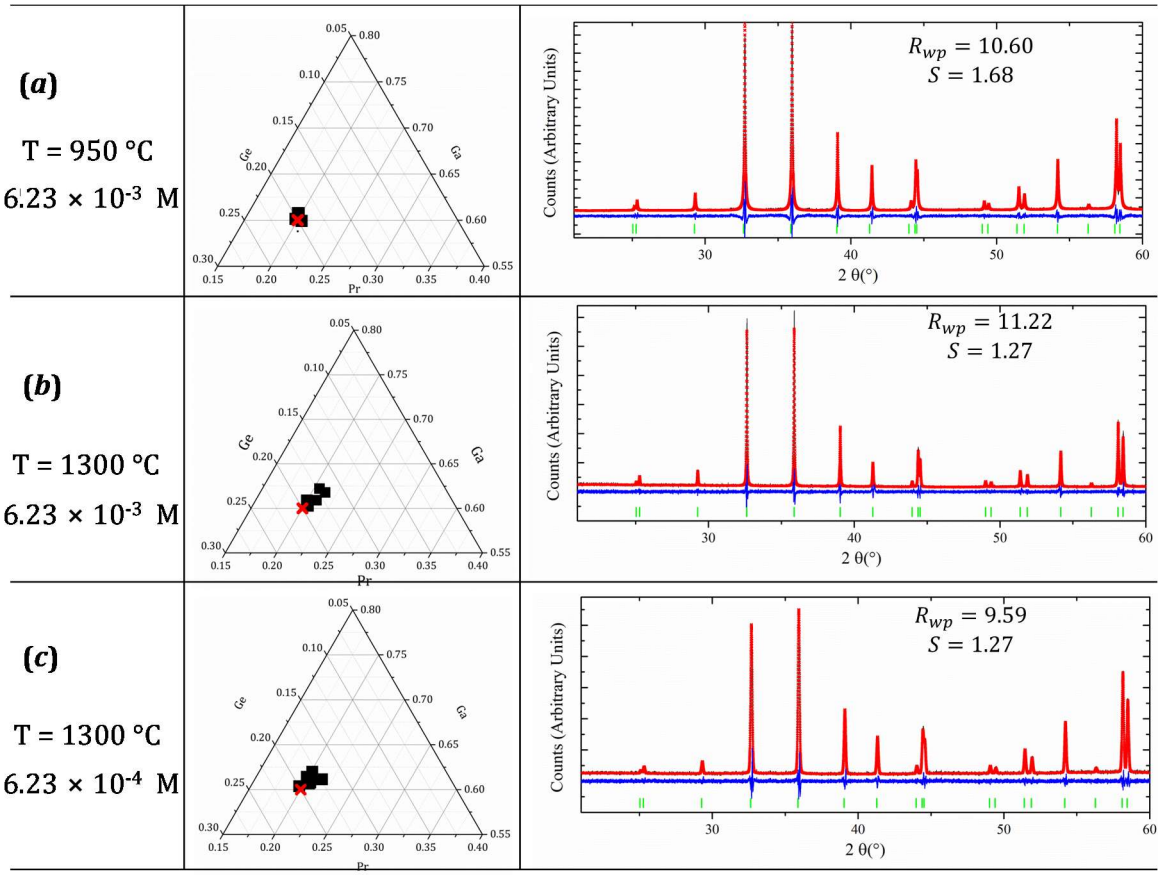

Figure 5-10 EDX and powder diffraction patterns of three samples with the $La_{1.5}Pr_{1.5}Ga_{4.5}Ge_{1.5}O_{14.25}$ nominal composition (denoted by a red cross in the phase diagram). Two concentrations of the initial precursor solution 6.23 × 10-3 (*a* and *b*) and 6.23 × 10-4 M (*c*) and two sintering temperatures 950 °C (*a*) and 1300 °C (*b* and *c*) were evaluated. The averaged EDX compositions are as follows: (*a*) $La_{1.50(7)}Pr_{1.5(1)}Ga_{4.5(1)}Ge_{1.50(5)}O_{14.20(3)}$, (*b*)$La_{1.56(4)}Pr_{1.50(4)}Ga_{4.59(8)}Ge_{1.36(7)}O_{14.18(2)}$ and (*c*) $La_{1.54(6)}Pr_{1.45(7)}Ga_{4.6(7)}Ge_{1.40(5)}O_{14.20(2)}$.

Table 5-6 Summary table with the analysed compositions and characteristics of the *a-c* samples in Figure 5-3.

	(*a*)	(*b*)	(*c*)
Stock solution conc. (M)	6.23 × 10-3	6.23 × 10-3	6.23 × 10-4
Annealing T (°C)	950	1300	1300
Nominal '*x*'	0.5	0.5	0.5
Actual (EDX) '*x*'	0.50(5)	0.36(7)	0.40(5)
Density (%)	-	-	92
a (Å)	8.18977(4)	8.18032(7)	8.1790(1)
c (Å)	5.06412(4)	5.075273(1)	5.07541(6)
Volume (Å3)	294.156(4)	294.124(5)	294.037(8)

From the inspection of the PXRD patterns presented in Figure 5-10 , there is no evidence for the formation of a secondary phase as a result of the GeO_2 volatilization from the mixture of reaction. In order to identify the presence of an amorphous impurity, quantitative X-ray analysis was carried out using $LaGaO_3$ (with similar absorption properties as the main phase and no overlapping peaks) as an internal standard. The quantitative phase

refinement revealed no significant amount of amorphous phase content (~2 %). Since such a small % value was obtained from the analysis it is difficult to discriminate whether it is a real value or within the error of the analysis. In any case, valuable insight was gained from these experiments which allowed us to design suitable densification routes for $La_{3-y}Ln_yGa_{5-x}Ge_{1+x}O_{14+x/2}$ ceramics with $y \neq 0$ and $0 \leq x \lesssim 0.4$.

The densification process in $La_{3-y}Ln_yGa_{5-x}Ge_{1+x}O_{14+x/2}$ was thus optimized by the preparation of initial mixtures of reaction with a concentration of 6.23×10^{-4} M within the $0 \leq x \leq 0.4$ region. The smaller particle size obtained by this route was found to avoid the formation of voids.

- Spark Plasma sintering of $La_{3-y}Ln_yGa_{5-x}Ge_{1+x}O_{14+x/2}$

The SPS protocol was optimized by decreasing the pellet thicknesses to 1-2 mm. Shortening the length of the pellets allowed us to decrease the temperature gradient generated across the length of the pellet during sintering which in turn allowed us to decrease the dwelling time and with it the risk of sample decomposition[277].

Some SPS sintered compositions such as $La_{1.5}Nd_{1.5}Ga_{4.5}Ge_{1.5}O_{14.25}$ and $Nd_3Ga_{4.5}Ge_{1.5}O_{14.25}$ had densities of 58 %, located at the border-line of the Heidinger approximation effectiveness (showing good results for porosity values of $P \sim 0.4$)[235]. Their conductivity was therefore compared to that of $La_{1.5}Nd_{1.5}Ga_{4.5}Ge_{1.5}O_{14.25}$ and $Nd_3Ga_{4.5}Ge_{1.5}O_{14.25}$ specimens sintered by conventional methods at 1250 °C for 5 hours having relative densities of 85 and 92 % respectively (see Appendix 7). It is therein demonstrated that the Heidinger corrected measured conductivities of samples with high and poor densities are in good agreement with each other. In $La_{1.5}Nd_{1.5}Ga_{4.5}Ge_{1.5}O_{14.25}$ the conductivities measured in both pellets only differ by 20 %, which lies within the reproducibility errors calculated for $La_3Ga_{4.7}Ge_{1.3}O_{14.15}$ (x = 0.3) and $La_3Ga_{4.5}Ge_{1.5}O_{14.25}$ (x = 0.5) that were reported in page 112. Moreover, the difference in conductivity between high and low porosity specimens in $Nd_3Ga_{4.5}Ge_{1.5}O_{14.25}$ at 500 °C is even smaller of 5 %. The comparison of the bulk conductivity data at the range of temperatures studied from 350 to 525 °C is given in Appendix 7.

The sintering conditions and PXRD patterns of the SPS-sintered specimens are introduced together with the conductivity results in the following section 5.2.1.3.2 in Table 5-7 and Figure 5-13 respectively. Additionally, the lattice parameters before and after SPS are presented in Appendix 8.

5.2.1.3.2 AC Impedance Spectroscopy

Two approaches were carried out for the determination of the conductivity. On the one side, the total conductivity at 500-900 °C was evaluated on fully densified specimens prepared by conventional sintering. On the other side, the bulk conductivity at the lower temperature range 350-500 °C was measured on SPS-sintered specimens with acceptable densities (>60 %). The dielectric constant of these materials with a lower density was corrected by means of the Heidinger approximation and used for the calculation of the conductivity from f_{max} at the Modulus plot.

- Total Conductivity

Conventionally sintered specimens with the compositions: $Ln_3Ga_{5-x}Ge_{1+x}O_{14+x/2}$ and $La_{1.5}Ln_{1.5}Ga_{5-x}Ge_{1+x}O_{14+x/2}$ with Ln = Pr and Nd and x = 0, 0.25 and 0.5 were analysed by AC impedance spectroscopy. The measured conductivities are introduced in Figure 5-11 (a) and (b) for $Ln_3Ga_{5-x}Ge_{1+x}O_{14+x/2}$ and $La_{1.5}Ln_{1.5}Ga_{5-x}Ge_{1+x}O_{14+x/2}$ respectively.

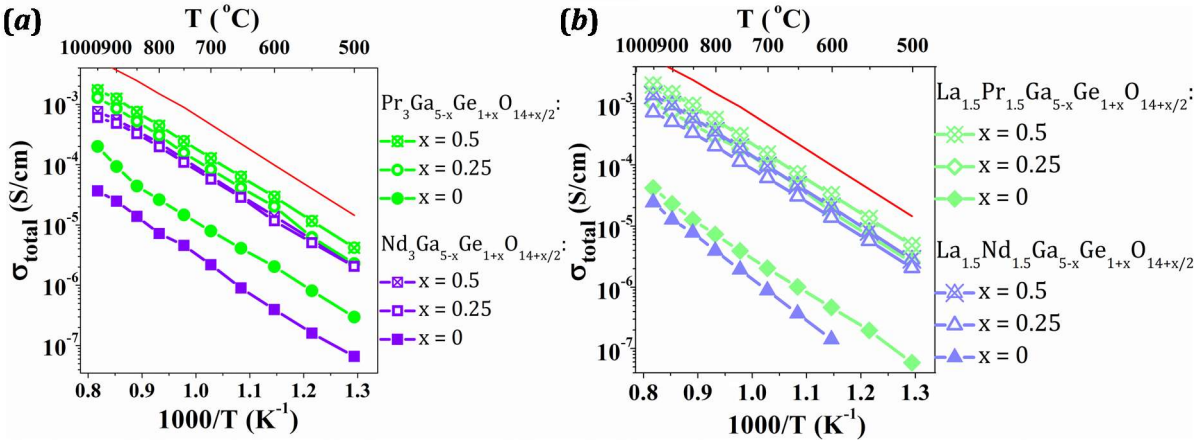

Figure 5-11 Arrhenius plot of the total conductivity for $Ln_3Ga_{5-x}Ge_{1+x}O_{14+x/2}$ (*a*) and $La_{1.5}Ln_{1.5}Ga_{5-x}Ge_{1+x}O_{14+x/2}$ (*b*) with Ln = Pr and Nd and x = 0, 0.25 and 0.5. The red line denotes the conductivity of $La_3Ga_{4.5}Ge_{1.5}O_{14.25}$.

Figure 5-11 demonstrates an increase in conductivity of approximately two orders of magnitude from $La_{3-y}Ln_yGa_5GeO_{14}$ (x = 0) to $La_{3-y}Ln_yGa_{4.75}Ge_{1.25}O_{14.125}$ (x = 0.25) for all compositions. However, and similarly to the trend in conductivity vs $C_{O_{int/channel}}$ observed for $La_3Ga_{5-x}Ge_{1+x}O_{14+x/2}$ (see page 120) the increase in conductivity is significantly attenuated from x = 0.25 to 0.5, where only a subtle rise of ~ 30 % is observed.

The total conductivity in Figure 5-11 was calculated from the corrected capacitance values extracted from the fitting of the arcs in the complex impedance plane. Figure 5-12 accounts for the complex impedance representations for $La_{1.5}Pr_{1.5}Ga_5GeO_{14}$ (*a*) and $La_{1.5}Pr_{1.5}Ga_{4.5}Ge_{1.5}O_{14.25}$ (*b*). Two arcs are visible in Figure 5-12-*a* for the parent insulating composition; one attributed to the bulk with a corrected capacitance (C_{corr}) of $\sim 10^{-12}\ F \cdot cm^{-1}$ and a second arc attributed to the grain boundary with C_{corr} $\sim 10^{-10}\ F \cdot cm^{-1}$. In $La_{1.5}Pr_{1.5}Ga_{4.5}Ge_{1.5}O_{14.25}$, the Warburg electrode response is visible at 500-950 °C (see Figure 5-12-*b*). At 500 °C, the semi-circular Warburg arc at lower frequencies has a large capacitance value of $C_{corr} \geq 10^{-6}\ F \cdot cm^{-1}$. At 900 °C and higher temperatures, the electrode response overtakes the bulk and grain boundary responses which are no longer visible. Thus, at $T \geq$ 900 °C resistivity values were read from the intercept with the Z'-axis.

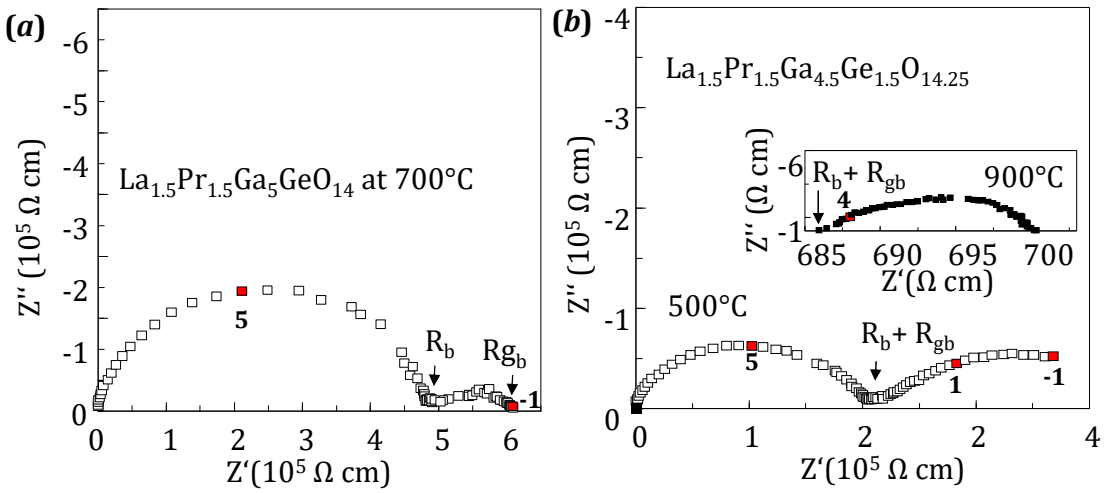

Figure 5-12 Complex impedance plots of $La_{1.5}Pr_{1.5}Ga_5GeO_{14}$ (*a*) and $La_{1.5}Pr_{1.5}Ga_{4.5}Ge_{1.5}O_{14.25}$ (*b*). The numbers in bold denotes the logarithm of the the frequency of the adjacent data points highlighted in red.

Activation energies were calculated from the slope of the linear fit to the conductivity in the Arrhenius plots for $La_{1.5}Ln_{1.5}Ga_{5-x}Ge_{1+x}O_{14+x/2}$ and $Ln_3Ga_{5-x}Ge_{1+x}O_{14+x/2}$ with Ln = Pr and Nd (see Figure 5-11). The calculated values are given in Table 5-7 as well as the pellet densities, sintering conditions, interstitial oxide content and the conductivity values measured at 700 °C.

Table 5-7 Sintering conditions used for the densification of $La_{3-y}Ln_yGa_{5-x}Ge_{1+x}O_{14+x/2}$, where Ln = Pr and Nd and $0 \leq x \leq 0.5$.

Nominal Composition	ρ (%)	Ea_{gb} (eV)	Conventional Sintering		$\%o_{int}$	$\sigma_{700\,°C}$ (S·cm^{-1})
			Temperature (°C)	Dwell (h)		
$Pr_3Ga_{4.5}Ge_{1.5}O_{14.25}$	96	1.10	1250	5	1.79	1.27×10^{-4}
$Pr_3Ga_{4.75}Ge_{1.25}O_{14.125}$	80	1.15	1250	5	0.89	8.31×10^{-5}
$Pr_3Ga_5GeO_{14}$	94	1.13	1300	12	-	7.92×10^{-6}
$Nd_3Ga_{4.5}Ge_{1.5}O_{14.25}$	92	1.08	1250	5	1.79	5.74×10^{-5}
$Nd_3Ga_{4.75}Ge_{1.25}O_{14.125}$	94	1.07	1250	5	0.89	5.64×10^{-5}
$Nd_3Ga_5GeO_{14}$	87	1.17	1300	12	-	2.18×10^{-6}
$La_{1.5}Pr_{1.5}Ga_{4.5}Ge_{1.5}O_{14.25}$	92	1.11	1250	5	1.79	1.50×10^{-4}
$La_{1.5}Pr_{1.5}Ga_{4.75}Ge_{1.25}O_{14.125}$	88	1.10	1250	5	0.89	9.55×10^{-5}
$La_{1.5}Pr_{1.5}Ga_5GeO_{14}$	80	1.15	1300	12	-	2.04×10^{-6}
$La_{1.5}Nd_{1.5}Ga_{4.5}Ge_{1.5}O_{14.25}$	85	1.13	1250	5	1.79	9.55×10^{-5}
$La_{1.5}Nd_{1.5}Ga_{4.75}Ge_{1.25}O_{14.125}$	85	1.07	1250	5	0.89	6.12×10^{-5}
$La_{1.5}Nd_{1.5}Ga_5GeO_{14}$	78	1.10	1300	12	-	8.84×10^{-7}

To ensure that the samples survived the experimental conditions, PXRD patterns of the powdered samples were collected and analysed which are introduced in Figure 5-11. These patterns show no formation of impurities during sintering and impedance experiments with the exception of $Nd_3Ga_5GeO_{14}$ and $La_{1.5}Nd_{1.5}Ga_5GeO_{14}$ where $Nd_3Ga_5O_{12}$ and an unidentified impurity phase (constituting 2-5 % of the relative intensity) were identified. A table with the lattice parameters determined by a Pawley fitting of the PXRD data collected in powdered samples before and after sintering and conductivity experiments are given in Appendix 8

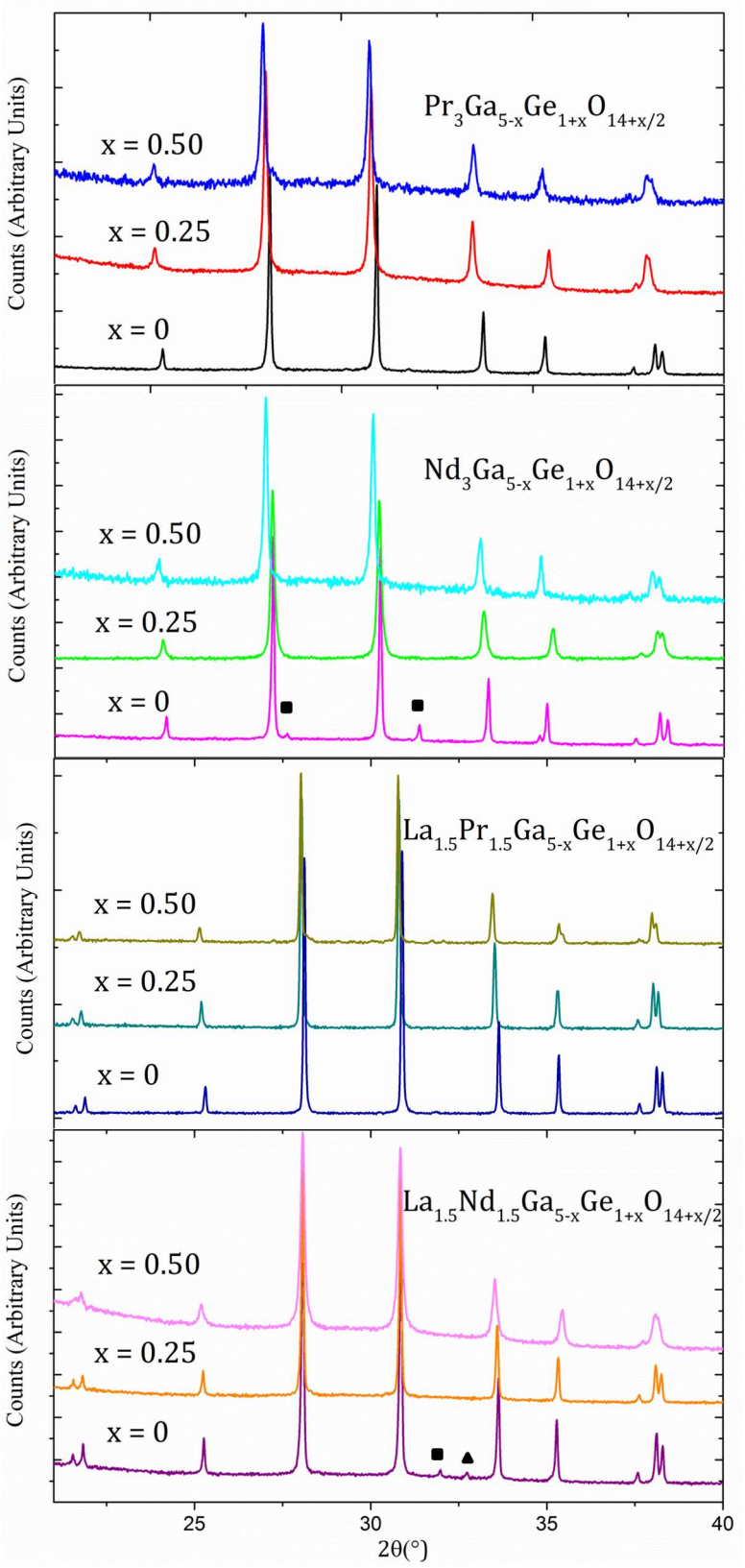

Figure 5-13 Post-Measurement PXRD patterns of those samples described in Table 5-7 collected in a Bruker diffractometer with a Cu source ($K_{\alpha 1,Cu}$= 1.5406 Å). The square and triangle symbols denote impurity phases. The square symbol accounts for $Nd_3Ga_5O_{14}$ with a garnet structure, and the phase denoted with a triangle was not identified.

- Bulk conductivity

As stated in the introduction, the analysis of the bulk conductivity was carried out using an Agilent E4980 LCR meter and the range of temperatures studied was determined by this instrument. Typically, the peak maximal at the *M''* plot was visible up to ~550 °C and the bulk conductivity was evaluated from 350 up to ~550 °C. Conductivity values calculated this way are represented in Figure 5-15

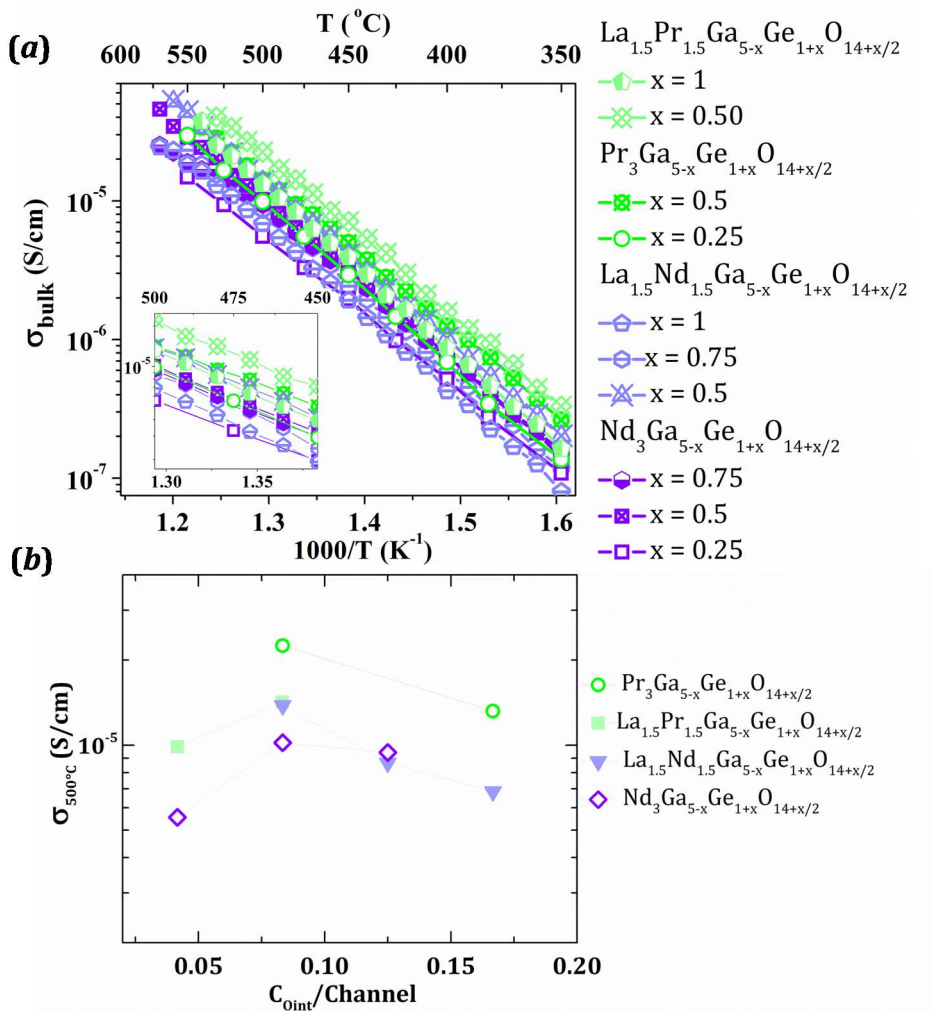

Figure 5-14 (*a*) Arrhenius plot of the bulk conductivity for several $La_{3-y}Ln_yGa_{5-x}Ge_{1+x}O_{14+x/2}$ where Ln = Pr and Nd sintered by SPS. (*b*) Bulk conductivity at 500 °C vs $C_{O_{int}/channel}$, where the maxima corresponds to $C_{O_{int}/channel} = 0.083$ in $La_{3-y}Ln_yGa_{4.5}Ge_{1.5}O_{14.25}$ ($x = 0.5$).

A significant contribution to the grain boundary was observed in the complex impedance plots of those samples in Figure 5-14 - see the elongation of the impedance arcs in Figure 5-15- *a*. Due to the fact that the arc associated to the bulk is masked by grain boundary contributions, the reading of the resistance value from the intercept with the *Z'*-axis is impeded. However, grain boundary and bulk contributions can be separated with the combined use of Z'' and M'' vs $log\ f$ plots as shown in Figure 5-15.

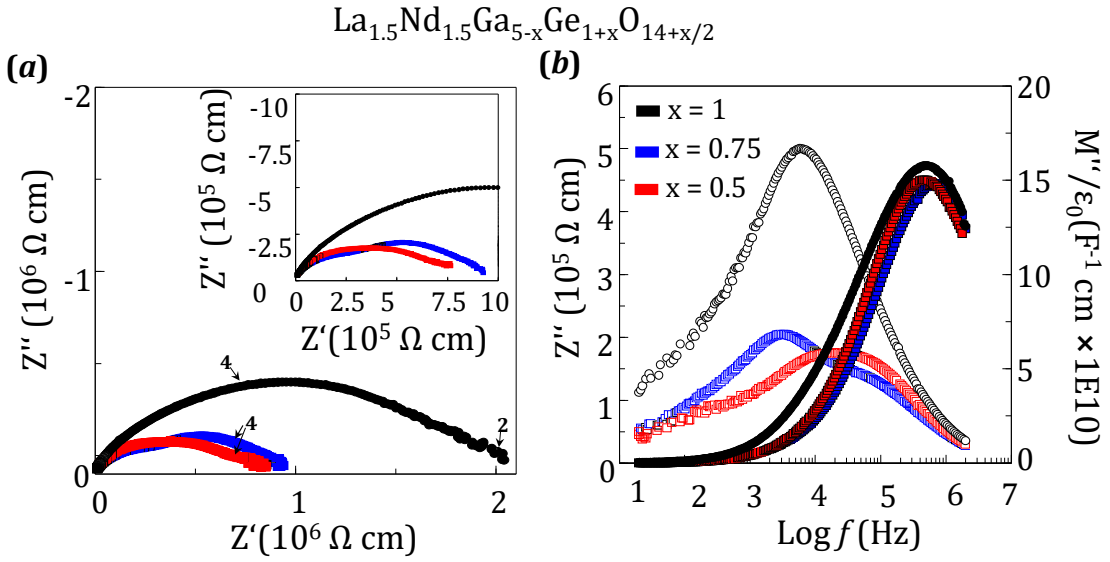

Figure 5-15 (*a*) Complex impedance plane for $La_{1.5}Nd_{1.5}Ga_{5-x}Ge_{1+x}O_{14+x/2}$ with x =1 (black), 0.75 (blue) and 0.5 (red) at 500 °C. The log values of the frequencies are indicated with arrows. (*b*) Impedance and modulus spectra are denoted by open and filled symbols respectively, also at 500 °C.

Table 5-8 Sintering conditions and conductivity for the samples presented in Figure 5-14.

Nominal Composition	ρ (%)	Ea_{bulk} (eV)	SPS Sintering		$\%O_{int}$	$\sigma_{500\,°C}$ (S·cm^{-1})
			T(°C)	Dwell (min)		
$La_{1.5}Pr_{1.5}Ga_4Ge_2O_{14.5}$	70	1.22	1000	5	3.57	1.32×10^{-5}
$La_{1.5}Pr_{1.5}Ga_{4.5}Ge_{1.5}O_{14.25}$	88	1.16	1000	5	1.79	2.25×10^{-5}
$Pr_3Ga_{4.5}Ge_{1.5}O_{14.25}$	74	1.10	1000	5	1.79	1.42×10^{-5}
$Pr_3Ga_{4.75}Ge_{1.25}O_{14.125}$	80	1.19	*		0.89	9.87×10^{-6}
$La_{1.5}Nd_{1.5}Ga_4Ge_2O_{14.5}$	72	1.20	1000	5	3.57	6.84×10^{-6}
$La_{1.5}Nd_{1.5}Ga_{4.25}Ge_{1.75}O_{14.375}$	81	1.18	1000	5	2.68	8.65×10^{-6}
$La_{1.5}Nd_{1.5}Ga_{4.5}Ge_{1.5}O_{14.25}$	58	1.18	1000	5	1.79	1.38×10^{-5}
$Nd_3Ga_{4.25}Ge_{1.75}O_{14.375}$	79	1.08	1000	5	2.68	9.42×10^{-6}
$Nd_3Ga_{4.5}Ge_{1.5}O_{14.25}$	58	1.18	1000	5	1.79	1.02×10^{-5}
$Nd_3Ga_{4.75}Ge_{1.25}O_{14.125}$	94	1.17	*		0.89	5.55×10^{-6}

* Dense samples where x = 0.25 were prepared by the conventional sintering method involving the heating at high temperatures specified in Table 5-7.

The Arrhenius plot of the bulk conductivity for $La_{3-y}Ln_yGa_{5-x}Ge_{1+x}O_{14+x/2}$ with Ln = Pr and Nd and y = 3 and 1.5 demonstrates a decrease in conductivity with the incorporation of smaller-sized Ln cations. For the same interstitial content of $\%O_{int} = 1.79$ the conductivity (in S·cm^{-1}) decrease as follows: $La_{1.5}Pr_{1.5}Ga_{4.5}Ge_{1.5}O_{14.25}$ (2.25×10^{-5}) > $Pr_3Ga_{4.5}Ge_{1.5}O_{14.25}$ (1.42×10^{-5}) ~$La_{1.5}Nd_{1.5}Ga_{4.5}Ge_{1.5}O_{14.25}$ (1.38×10^{-5}) > $Nd_3Ga_{4.5}Ge_{1.5}O_{14.25}$ (1.02×10^{-5}).

The change in conductivity at 500 °C as a function of the interstitial oxygen incorporated per channel ($C_{O_{int}/channel}$) is given in Figure 5-14-*b*. This plot is particularly useful to address the mobility of the oxide ions at different $C_{O_{int}/channel}$. Unfortunately, in

$La_{3-y}Ln_yGa_{5-x}Ge_{1+x}O_{14+x/2}$ systems as in $La_3Ga_{5-x}Ge_{1+x}O_{14+x/2}$ the conductivity is maximum at $C_{O_{int}/chann} = 0.0833$.

The samples studied by AC impedance were analysed after these experiments and the PXRD patterns are presented in Figure 5-18. A small amount of a $LaGaGeO_5$ impurity phase (5 % of the relative intensity) is present in those specimens with $x > 0.5$ due to the increase of the temperature above T_{decomp} during the sintering process, which took place at 1000 °C (see Table 5-8). The lattice parameters of the main langasite phase determined by Pawley fitting match the pre-sintering values suggesting that there is no change in composition in the majority phase and the reported values for the conductivity are ascribed to the compositions reported.

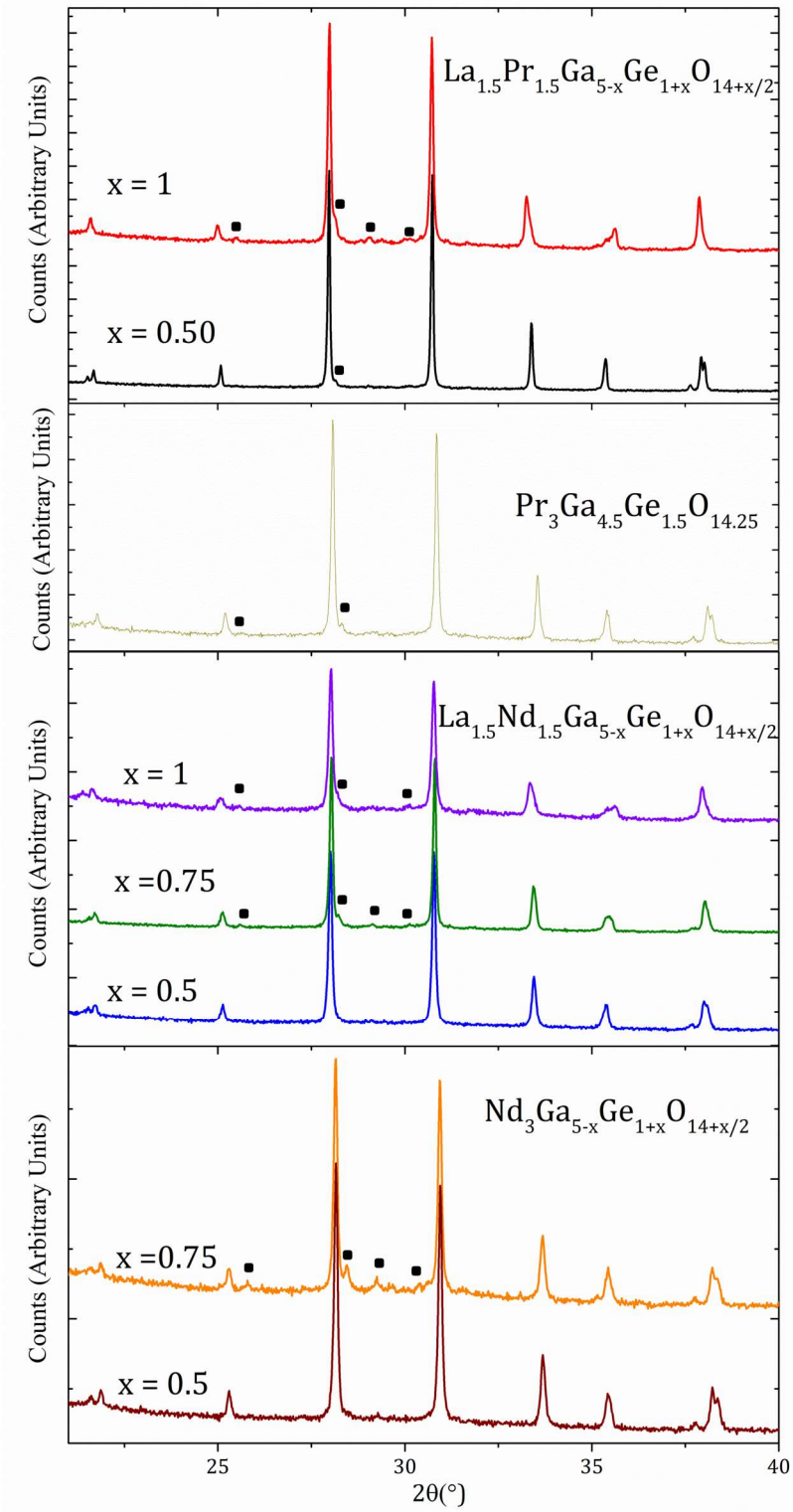

Figure 5-16 Post-Measurement PXRD patterns collected in a Bruker diffractometer with a Cu source ($K_{\alpha 1,Cu}$= 1.5406 Å). The square symbols denote a $LaGaGeO_5$ impurity (see page 75) formed during the sintering process.

- Characterization of the change in conductivity with the size of Ln for constant $C_{O_{int}/chann}$:

Herein, the conductivity of $La_{1.5}Ln_{1.5}Ga_{4.5}Ge_{1.5}O_{14.25}$ (Ln = La, Pr, Nd, Sm, Gd) and $La_2LnGa_4Ge_2O_{14.5}$ (Ln = La, Pr, Sm, Gd) is presented in Figure 5-17 and Table 5-9. Such a study allows us to further asses the decrease in conductivity coupled to the decrease in size of the Ln cation at two $C_{O_{int}/channel}$ concentrations of 0.083 and 0.167. In both Figure 5-17 and Table 5-9, the bulk conductivity for the formerly introduced $La_3Ga_{4.5}Ge_{1.5}O_{14.25}$ and $La_3Ga_4Ge_2O_{14.5}$ are also given for comparison.

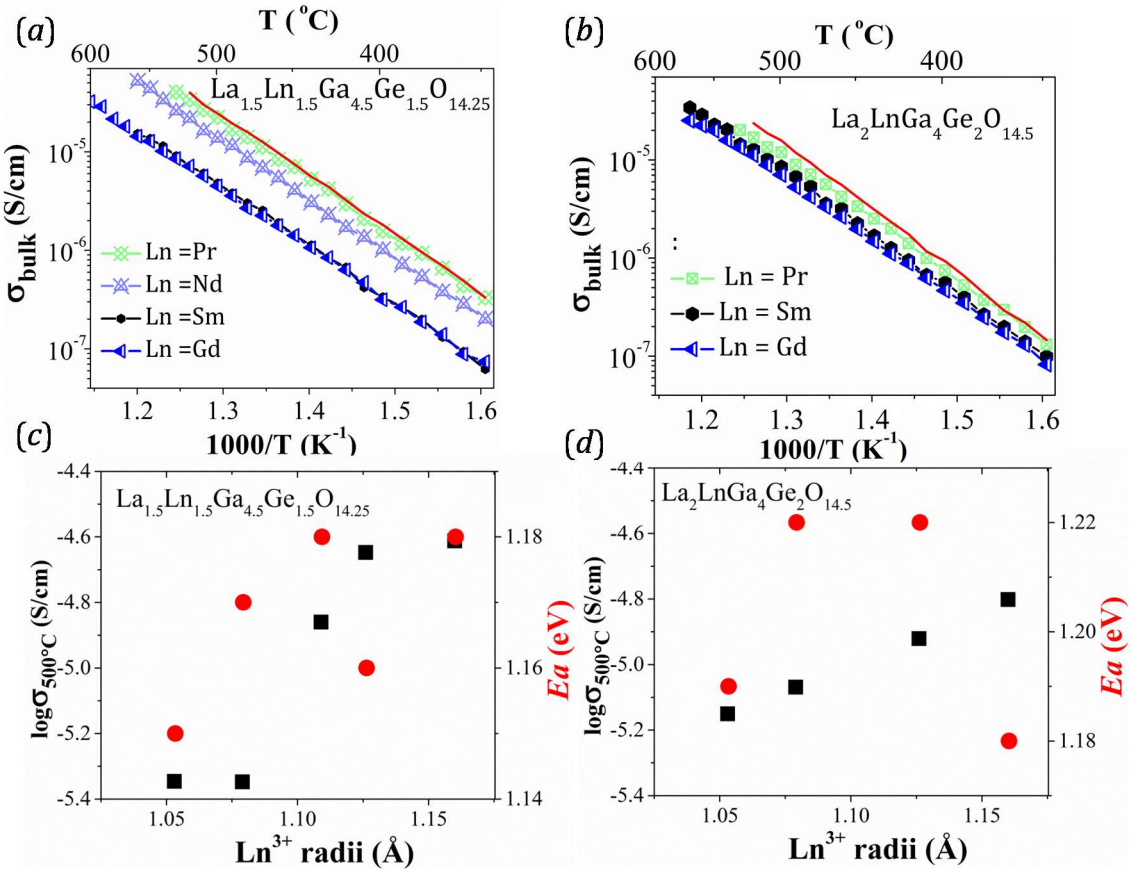

Figure 5-17 Arrhenius plot of the bulk conductivity in (*a*) $La_{1.5}Ln_{1.5}Ga_{4.5}Ge_{1.5}O_{14.25}$ (Ln = Pr, Nd, Sm, Gd) and (*b*) $La_2LnGa_4Ge_2O_{14.5}$ (Ln = Pr and Sm .The red lines denote the bulk conductivity of $La_3Ga_{4.5}Ge_{1.5}O_{14.25}$ and $La_3Ga_4Ge_2O_{14.5}$ in (*a*) and (*b*) respectively. The conductivity at 500 °C (black symbols) and activation energy in eV (red) as a function of the Ln^{3+} cation size is given in (*c*) and (*d*) for $La_{1.5}Ln_{1.5}Ga_{4.5}Ge_{1.5}O_{14.25}$ and $La_2LnGa_4Ge_2O_{14.5}$.

In $La_{1.5}Ln_{1.5}Ga_{4.5}Ge_{1.5}O_{14.25}$ (see Figure 5-17-*a*), the maximum conductivity is shown by the larger Ln = La and Pr atoms. A decrease in conductivity from $\sim 2 \times 10^{-5}$ S·cm^{-1} when Ln^{3+} = La-Nd to $\sim 5 \times 10^{-6}$ S·cm^{-1} for the smaller Sm and Gd is observed. The activation energies given in Figure 5-17-*c* remain constant for the compositions analysed, with the variation between values being of a negligible $\Delta E_a < 0.03\ eV$.

The correlation between conductivity and Ln^{3+} size was also investigated in $La_2LnGa_4Ge_2O_{14.5}$ with a higher concentration of interstitials of $C_{O_{int}/channel} = 0.167$. The Arrhenius plot of the conductivity given in Figure 5-17-*b* and the plot of the conductivity and activation energy as a function of the atomic radii at 500 °C in Figure 5-17-*d* demonstrate of a decrease in conductivity with the smaller Ln^{3+} size from 1.58×10^{-5} S·cm^{-1}

in $La_3Ga_4Ge_2O_{14.5}$ to 7.07 × 10^{-6} S·cm^{-1} in $La_2GdGa_4Ge_2O_{14.5}$ and no significant impact on the activation energy.

Table 5-9 SPS Sintering conditions activation energy in eV and conductivity of the compositions presented in Figure 5-17. For all samples a ramp rate of 200° min^{-1} was used and a pressure of 50 MPa with the exception of $La_3Ga_4Ge_2O_{14.5}$ where the pressure was increased up to 550 MPa.

Nominal Composition	ρ (%)	Ea_{bulk} (eV)	SPS Sintering T(°C)	SPS Sintering Dwell (min)	$\%_{O_{int}}$	$\sigma_{500\,°C}$ (S·cm^{-1})
$La_3Ga_{4.5}Ge_{1.5}O_{14.25}$	97	1.18	1100	10	1.78	2.44 × 10^{-5}
$La_{1.5}Pr_{1.5}Ga_{4.5}Ge_{1.5}O_{14.25}$	88	1.16	1000	5	1.78	2.25 × 10^{-5}
$La_{1.5}Nd_{1.5}Ga_{4.5}Ge_{1.5}O_{14.25}$	58	1.18	1000	5	1.78	1.38 × 10^{-5}
$La_{1.5}Sm_{1.5}Ga_{4.5}Ge_{1.5}O_{14.25}$	94	1.17	1000	5	1.78	4.49 × 10^{-6}
$La_{1.5}Gd_{1.5}Ga_{4.5}Ge_{1.5}O_{14.25}$	58	1.15	1000	5	1.78	4.51 × 10^{-6}
$La_3Ga_4Ge_2O_{14.5}$*	97	1.18	850	5	3.57	1.58 × 10^{-5}
$La_2PrGa_4Ge_2O_{14.5}$	92	1.22	1050	4	3.57	1.20 × 10^{-5}
$La_2SmGa_4Ge_2O_{14.5}$	61	1.22	1000	5	3.57	8.53 × 10^{-6}
$La_2GdGa_4Ge_2O_{14.5}$	81	1.19	1050	4	3.57	7.07 × 10^{-6}

* $La_3Ga_4Ge_2O_{14.5}$ was sintered in a double acting die at a pressure of 550 MPa. See 2.2.3.1 for details.

The post-AC impedance measurements purity checks carried out in powdered specimens are given in Figure 5-18. The PXRD patterns of the Ge-richer $La_2LnGa_4Ge_2O_{14.5}$ compositions with a lower decomposition temperature T_{decomp} ~900 ℃ show a minor impurity phase with a $LaGaGeO_5$ composition formed during the sintering process that took place at 1050 °C > T_{decomp}.

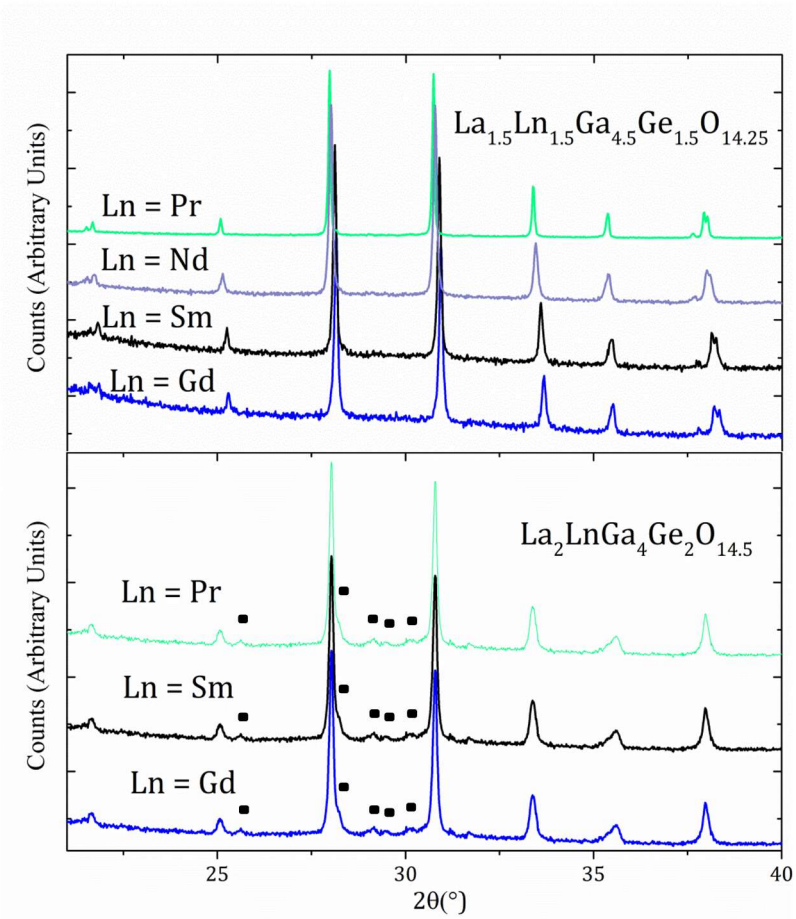

Figure 5-18 Post-Measurement PXRD patterns collected in a Bruker diffractometer with a Cu source ($K_{\alpha 1,Cu}$ = 1.5406 Å) in $La_{1.5}Ln_{1.5}Ga_{4.5}Ge_{1.5}O_{14.25}$ and $La_2LnGa_4Ge_2O_{14.5}$. The square symbols denote a $LaGaGeO_5$ impurity phase.

5.2.2 $La_3Ga_{5-x-y}Al_yGe_{1+x}O_{14+x/2}$ and $La_3Al_{5-x}Ge_{1+x}O_{14+x/2}$

5.2.2.1 Synthesis Outcome

The annealing temperature was optimized to 900 °C for those $La_3Al_{5-x}Ge_{1+x}O_{14+x/2}$ with $0 < x \leq 1$. Increasing the synthetic temperature from 900 °C to 950 °C lead to the formation of $LaAlO_3$ as an impurity. The decomposition temperature in $La_3Al_{5-x}Ge_{1+x}O_{14+x/2}$ was found to vary as a function of the dopant level 'x'. The Ge-richer systems for which $x > 1$ decomposed at 900 °C to form a langasite and a minority $LaAlO_3$ phase and the synthetic temperature was lowered to 850 °C in $1 < x \leq 1.5$. As shown in Figure 5-19 the cell parameters for $La_3Al_{5-x}Ge_{1+x}O_{14+x/2}$ obey Vegard's law within the $0 < x < 1.5$ region – incorporating the same amount of extra oxygen as the Ga analogue ($\%_{O_{int}} = 5.36$).

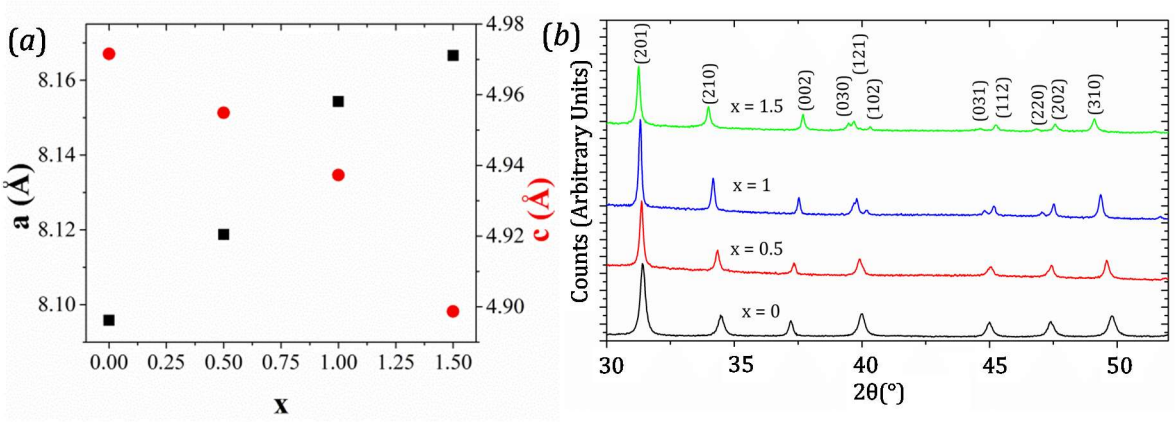

Figure 5-19 (a) Observed trend in the lattice parameters for $La_3Al_{5-x}Ge_{1+x}O_{14+x/2}$ ($0 \leq x \leq 1.5$). The a lattice parameter is denoted by black squares and c by red circles. (b) PXRD patterns measured in a Bruker D8 Advance diffractometer ($K_{\alpha 1,Cu} = 1.5406$ Å) show a shift in the Bragg peaks with the change in compositions with no presence of peaks attributed to impurity phases.

Several $La_3Ga_{5-x-y}Al_yGe_{1+x}O_{14+x/2}$ compositions were synthesized with various Ga:Al ratios with $0 \leq x \leq 1$. The mixing of Ga and Al on the B, C and D sites decrease the extent of the substitution of M^{3+} for Ge^{4+} with respect to $La_3Ga_{5-x}Ge_{1+x}O_{14+x/2}$ and $La_3Al_{5-x}Ge_{1+x}O_{14+x/2}$ with $0 \leq x \leq 1.5$. In $La_3Ga_{(5-x)/2}Al_{(5-x)/2}Ge_{1+x}O_{14+x/2}$ a $La_4Ge_4O_{14}$ ($P\bar{1}$) secondary phase was formed for $x > 1$.

5.2.2.2 Structural characterization: I11 and GEM combined refinement

This section deals with the characterization of $La_3Al_{5-x}Ge_{1+x}O_{14+x/2}$ with x=0, 1 and 1.5 by means of high-intensity neutron (GEM) and Synchrotron (I11) diffraction at room temperature. To test the lowering of the symmetry as a consequence of the interstitial accommodation the Pawley fitting of the data collected in I11 and GEM was performed in two different space groups: $P321$ and $P1$ which provided a good fit of the data (see Appendix 3). The calculated fitting parameters for both space groups (given in Table 5-10) are very similar between the two, therefore the geometry of the parent langasite $P321$ was retained for further refinement.

Table 5-10 Comparison of the R_{wp}, R_{exp} and S parameters for a Pawley fitting of $La_3Al_5GeO_{14}$, $La_3Al_4Ge_2O_{14.5}$ and $La_3Al_{3.5}Ge_{2.5}O_{14.75}$ at 297 K in $P321$ and $P1$ space groups with the high resolution SXRD data acquired at I11 and combined b5 and b6 NPD data acquired at GEM.

$La_3Al_{5-x}Ge_{1+x}O_{14+x/2}$ 'x'	$\%O_{int}$	*Data set*	$P321$		$P1$	
			R_{wp} / R_{exp}	S	R_{wp} / R_{exp}	S
$La_3Al_5GeO_{14}$ $x = 0$	-	I11	2.680 / 0.415	6.454	1.924 / 0.389	4.945
		b5-b6 (GEM)	2.148 / 1.140	1.883	2.322 / 1.055	2.200
$La_3Al_4Ge_2O_{14.5}$ $x = 1$	3.57	I11	1.092 / 0.246	4.431	0.930 / 0.236	3.937
		b5-b6 (GEM)	2.450 / 1.233	1.950	1.805 / 1.171	1.541
$La_3Al_{3.5}Ge_{2.5}O_{14.75}$ $x = 1.5$	5.36	I11	1.613 / 0.304	5.311	1.109 / 0.291	3.810
		b5-b6 (GEM)	2.294 / 1.237	1.854	1.902 / 1.260	1.524

The refinement of the GEM data in doped $La_3Al_4Ge_2O_{14.5}$ and $La_3Al_{3.5}Ge_{2.5}O_{14.75}$ from a DFT averaged model improved the goodness of the refinement ($e.g.$ the goodness of the fit for $La_3Al_{3.5}Ge_{2.5}O_{14.75}$ improved from $S = 3.07$ when using the parent model to $S = 2.43$, see Figure 5-20). On the other hand, the refinement of the I11 data in doped langasites show no differences when using the parent model or the DFT model as a starting point. This can be justified in terms of inefficiency of X-rays to locate oxygen in the presence of heavier elements. A comparison between the two fits is given in Figure 5-21.

The lattice parameters, and refined background and peak-shape functions used in the initial model of the Rietveld refinement were obtained via Pawley fitting of the data. The initial atomic positions were taken from the DFT averaged model for $La_3Ga_4Ge_2O_{14.5}$ where the Ga was replaced by Al for doped $La_3Al_4Ge_2O_{14.5}$ and $La_3Al_{3.5}Ge_{2.5}O_{14.75}$ compositions. The atomic positions used in the initial model of $La_3Al_5GeO_{14}$ were those of $La_3Ga_5GeO_{14}$ where again Ga was replaced by Al. At an initial stage of the refinement the distribution of Ge and Al was unknown and these two cations were evenly distributed amongst the B-D sites.

Initially, the NPD (combined refinement using the data collected on the 6 banks at GEM) and SXRD data sets were refined separately and once a good fit to the data was obtained both NPD and SXRD data sets were combined. Due to the fact that the goodness of fit of the model calculated by Rietveld using I11 data (S = 5.224 in $La_3Al_{3.5}Ge_{2.5}O_{14.75}$) approached the fit obtained with Pawley (S = 5.311 in $La_3Al_{3.5}Ge_{2.5}O_{14.75}$), we directed our efforts to first improve the refinement of GEM data. To this end, a parallel refinement strategy to the one followed in $La_3Ga_4Ge_2O_{14.5}$ (x = 1) and $La_3Ga_{3.5}Ge_{2.5}O_{14.75}$ (x = 1.5) based on the DFT model introduced in Chapter 4 was conducted for the refinement of $La_3Al_4Ge_2O_{14.5}$ and $La_3Al_{3.5}Ge_{2.5}O_{14.75}$ NPD data sets.

(*a*) Parent model. $R_{wp} = 4.930, R_{exp} = 1.607, S = 3.068$

- Bank 6. $R_{wp} = 4.248, R_{exp} = 1.628, S = 2.610$

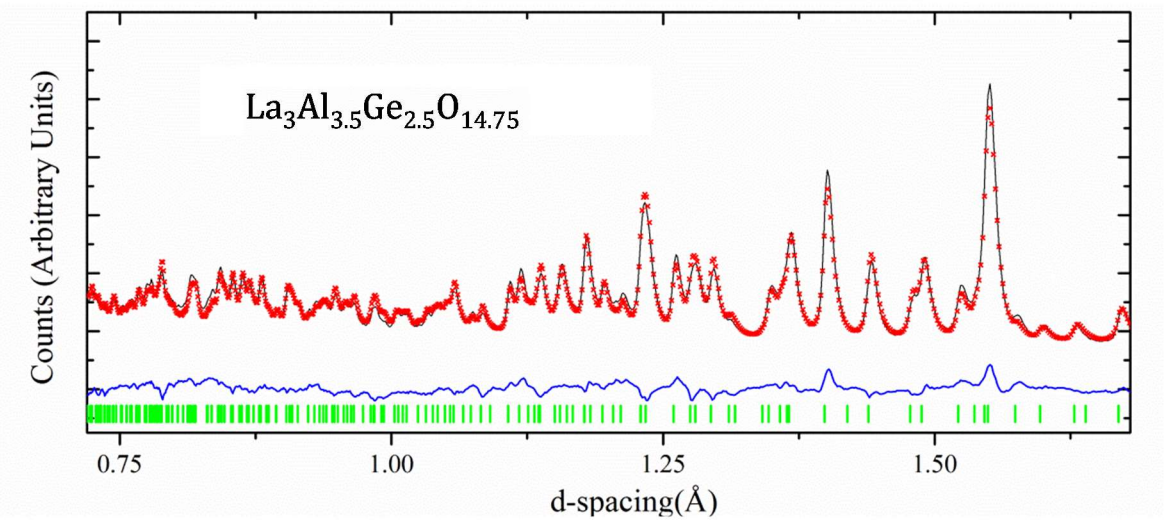

- Bank 5. $R_{wp} = 5.171, R_{exp} = 1.248, S = 4.145$

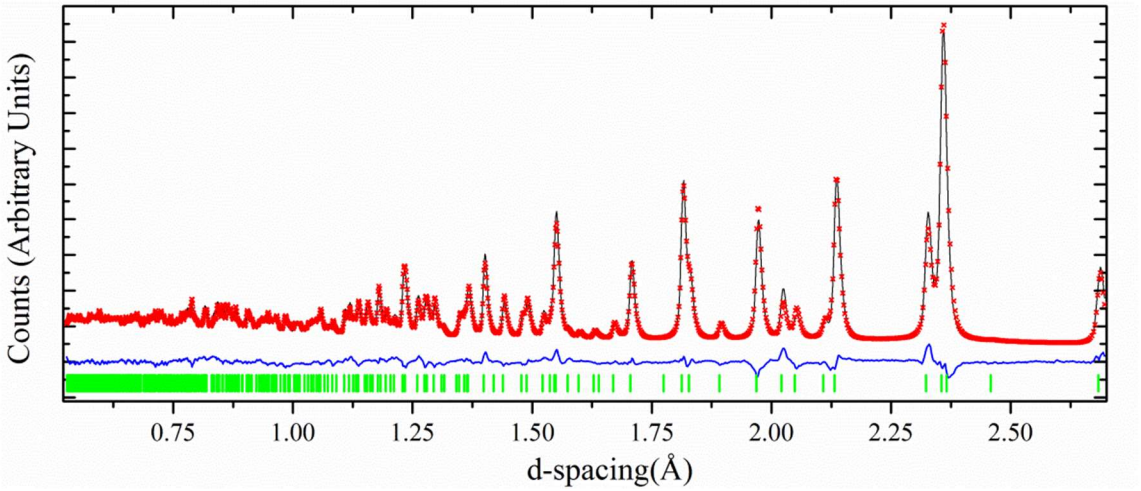

(b) DFT model (Initial Stage R_{wp}= 3.908, R_{exp} = 1.607, S = 2.432

- Bank 6. R_{wp} = 3.643, R_{exp} = 1.630, S = 2.234

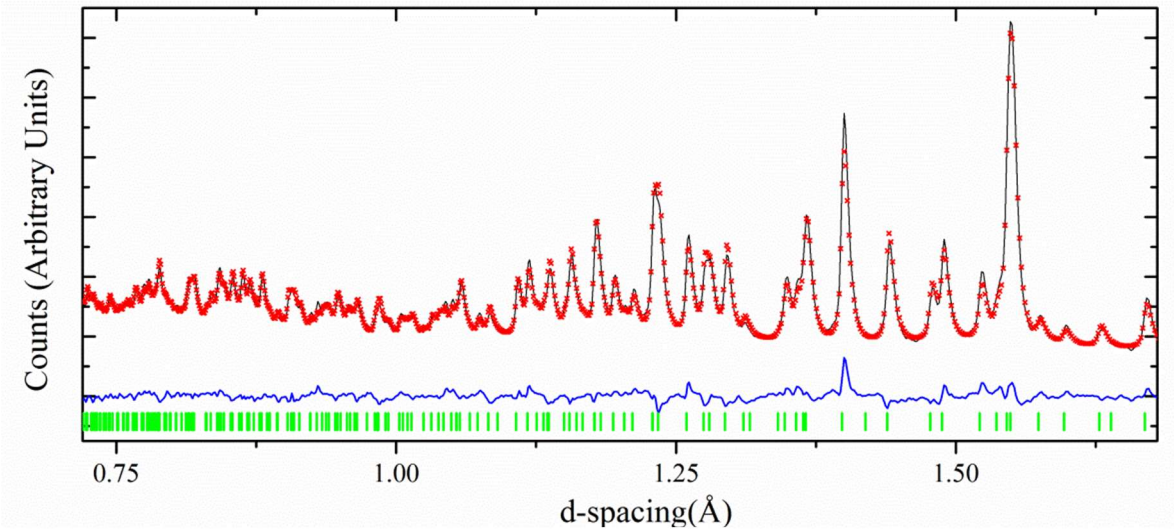

- Bank 5. R_{wp} = 4.414, R_{exp} = 1.249, S = 3.535

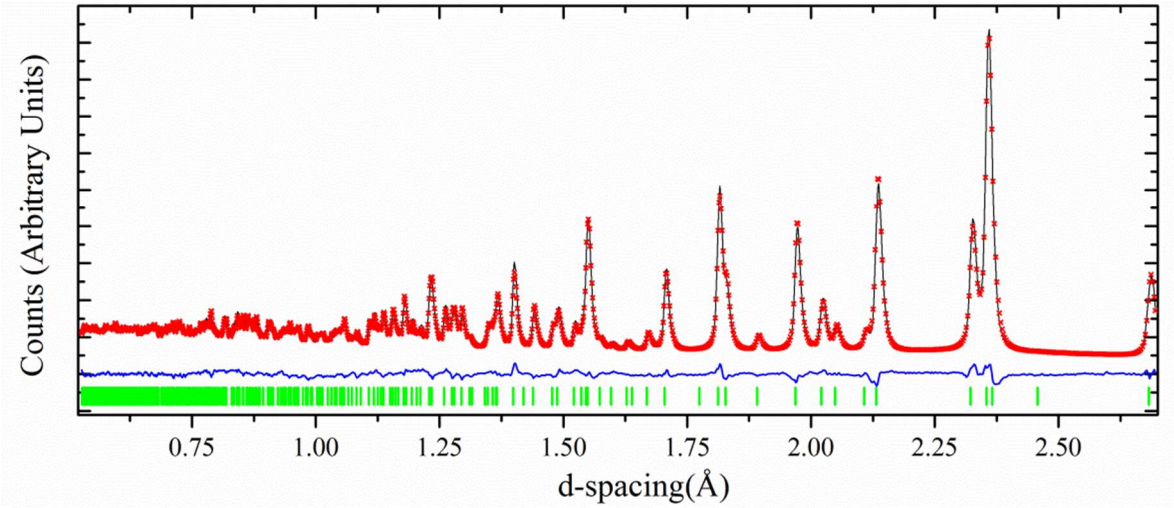

Figure 5-20 Comparison between the two fits of the banks 6 and 5 of GEM with the higher resolution obtained when using (a) the parent model and (b) the DFT averaged model as starting point of the Rietveld refinement of $La_3Al_{3.5}Ge_{2.5}O_{14.75}$ at 297 K. The errors given account for the combined refinement of banks 1-6 as well as the ones obtained separately for banks 5 and 6.

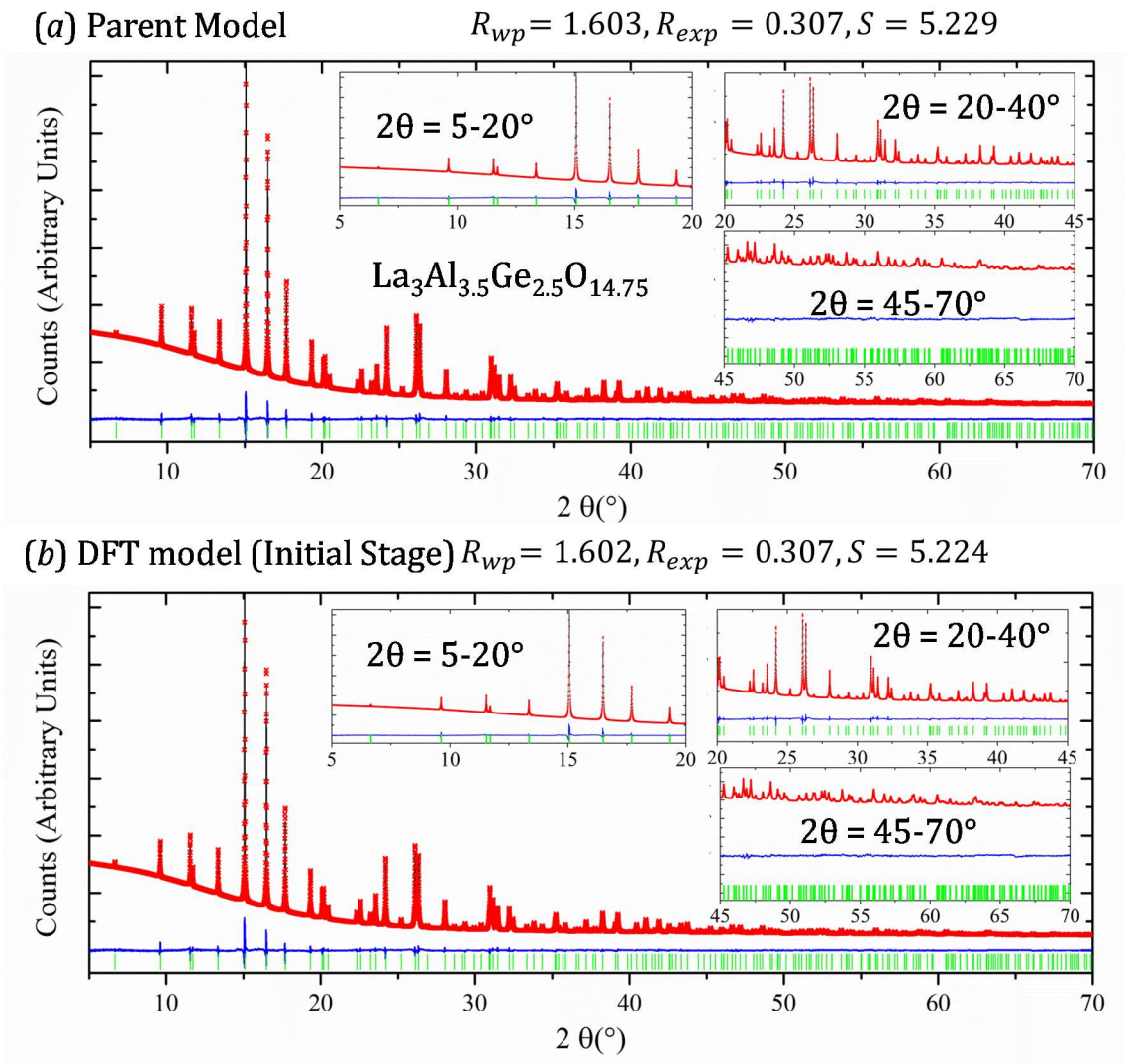

Figure 5-21 Comparison between the two fits of the I11 data of $La_3Al_{3.5}Ge_{2.5}O_{14.75}$ obtained when using (a) the parent model and (b) the DFT averaged model as starting points of the refinement.

Firstly, the scale factor, $Difc$ (for banks 1-5), $Difa$ (for banks 1-6) functions in GEM and zero shift in I11, and lattice parameters were refined. The refinement of La, Al and Ge atomic sites and occupancies was done on the first place and the oxygen atoms were included afterwards. Because of the lower resolution of the GEM diffractometer with respect to HRPD the split of the O2 site could not be carried out with the available data. In the refinements here presented for doped $La_3Al_{5-x}Ge_{1+x}O_{14+x/2}$ materials a total of five oxygen sites were identified which are: the framework oxygen O1-O3 and two new oxygen sites O4 and O5 which constitute the edges of the M_2O_8 unit. A chemically plausible environment was set with the inclusion of these two oxygen sites that account for the displaced O2 and the interstitial, as predicted by the DFT-averaged model. Moreover an oxygen saturated $La_3AlGe_5O_{16}$[258] langasite is also known having the same structure of $La_3GaGe_5O_{16}$ formerly introduced in Chapter 4. The geometry of the $(Al, Ge)_2O_8$ dimers found in $La_3Al_4Ge_2O_{14.5}$ and $La_3Al_{3.5}Ge_{2.5}O_{14.75}$ are introduced in Appendix 5.

Due to the Al/Ge disorder amongst the B, C and D sites their occupancies were enforced to add up to one so each site is fully occupied and their relative ratio was refined. The fractional occupancies of oxygen O3 and O1 refined to values close to unity so their occupancies were fixed to one. Further constraints inputted on an early stage of the refinement accounted for

the equalization of the refined extra oxygen to the incorporated germanium so that refined compositions were charge-balanced.

After refining each symmetry allowed atomic site, the thermal parameters for all cations as well and the framework oxygen (O1-O3) were refined anisotropically. The thermal parameters for the La, B and D cation sites were spherical and ADPs were reverted to B_{eq} in order to reduce the number of refined variables. An elongation of the refined ADP ellipsoid towards O5 was observed for the C site and U^{ij} were kept for this site in the final model. Due to the low occupancies of the oxygen sites conforming the shared edge within the M_2O_8 unit (O4 and O5) their thermal parameters were refined isotropically. The high refined B_{eq} values 2-4 Å^{-2} for O4 and O5 are an indication of the disorder associated to these sites[107]. At this stage the fit on the NPD refinement improved from the reported values in Figure 5-20: $R_{wp} = 3.908$, $R_{exp} = 1.607$, $S = 2.432$, to $R_{wp} = 3.457$, $R_{exp} = 1.607$, $S = 2.147$. Since a good fit to the data was achieved separately with both NPD and SXRD data sets (see Appendix 9), they were combined into one refinement. Other than the presence of O4 and O5 that SXRD data was unable to identify there were no differences between the two models. The combination of the two data sets in the refinement was followed by the elimination of the restraints that were forced into the refinement at an early stage. No other phases were added to the refinements as no extra peaks accounting for impurity phases or vanadium (the can used for the NPD experiments was made of this material) were observed. A Chebysev function with twelve polynomials was refined for each NPD bank and SXRD background and pseudo-Voigt functions were used to model the peak-shape.

The refined compositions are $La_3Al_{4.98(2)}Ge_{1.02(2)}O_{14}$, $La_3Al_{4.02(2)}Ge_{1.98(2)}O_{14.49(4)}$ and $La_3Al_{3.58(1)}Ge_{2.42(1)}O_{14.64(4)}$ which are in good agreement with the nominal values. The refined occupancies are given in Table 5-11. In this table, only the occupancies of aluminium sites are presented, since germanium occupancies are given by the difference to make the B, C and D sites fully occupied. Likewise, the occupancies of lanthanum, O1 and O3 fixed to 1 in the refinements are not given.

Table 5-11 Refined occupancies of the combined I11 and GEM (b1-b6) refinements of $La_3Al_{5-x}Ge_{1+x}O_{14+x/2}$ with x = 0, 1 and 1.5 at 297 K.

Refined occupancies						
Al1 (B site)	Al2 (D)	Al3 (C)	O2	O4	O5	**Refined compositions**
0.839(5)	0.843(5)	0.817(3)	1			$La_3Al_{4.98(2)}Ge_{1.02(2)}O_{14}$
0.787(4)	0.756(4)	0.578(3)	0.933(3)	0.081(2)	0.068(2)	$La_3Al_{4.02(2)}Ge_{1.98(2)}O_{14.49(4)}$
0.823(3)	0.713(3)	0.442(2)	0.888(2)	0.113(2)	0.104(2)	$La_3Al_{3.58(1)}Ge_{2.42(1)}O_{14.64(4)}$

The visual fits of the combined refinement for all three compositions are given in Figure 5-22 ($La_3Al_5GeO_{14}$), Figure 5-23 ($La_3Al_4Ge_2O_{14.5}$) and Figure 5-24 ($La_3Al_{3.5}Ge_{2.5}O_{14.75}$) and all the refined atomic parameters are introduced in Table 5-12.

(*a*) SXRD: I11

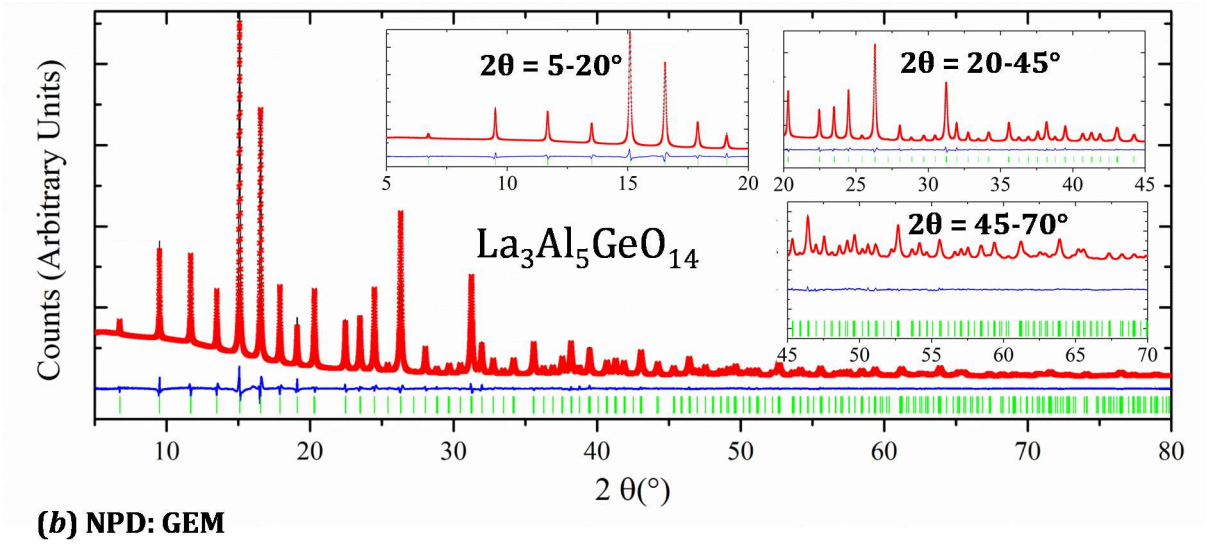

(*b*) NPD: GEM

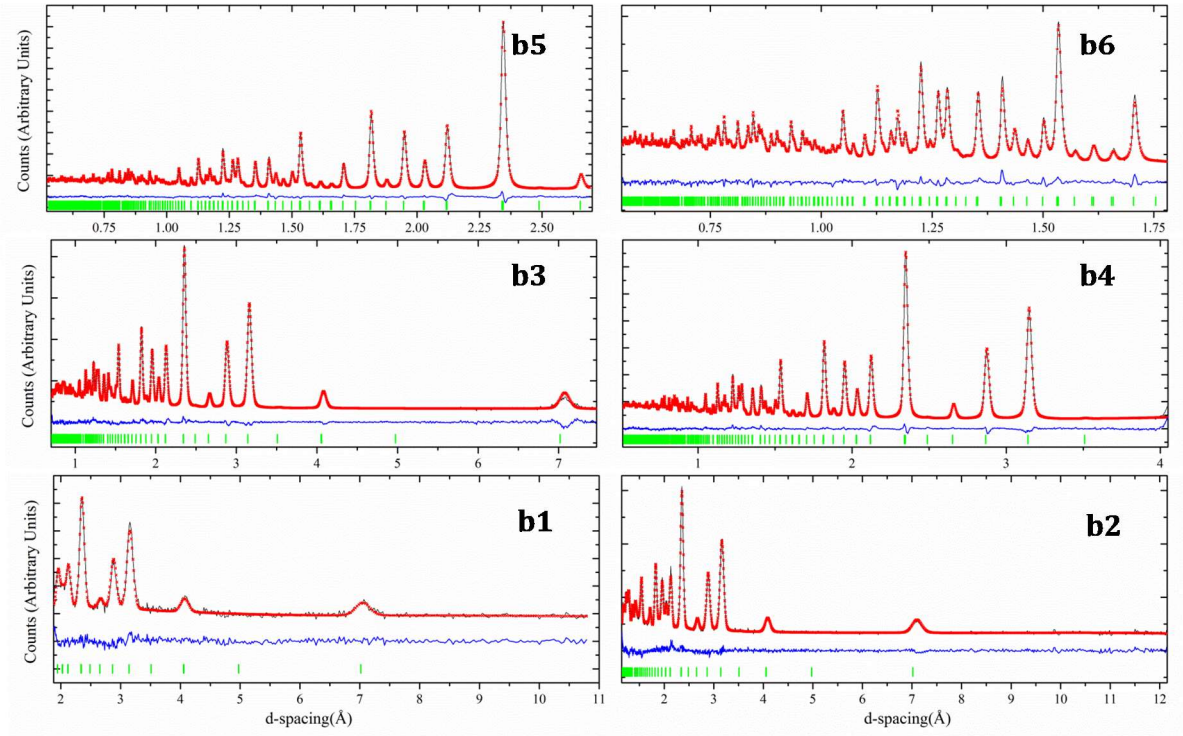

Figure 5-22 Fit of the combined SXRD (*a*) and NPD (*b*) refinement of $La_3Al_5GeO_{14}$ at 297 K. Three inset plots show expanded regions of the SXRD pattern in (*a*).

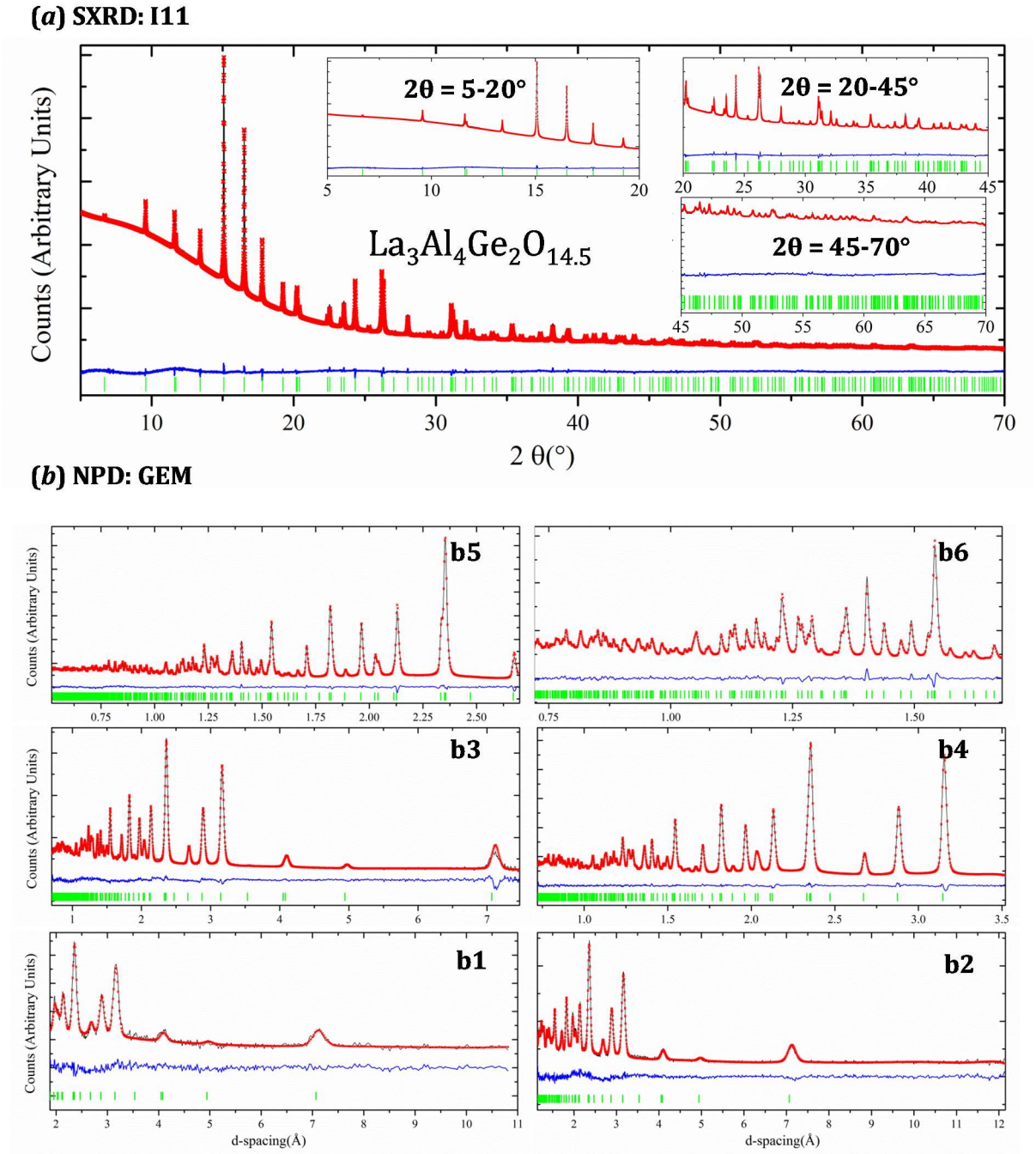

Figure 5-23 Fit of the combined SXRD (*a*) and NPD (*b*) refinement of $La_3Al_4Ge_2O_{14.5}$ at 297 K.

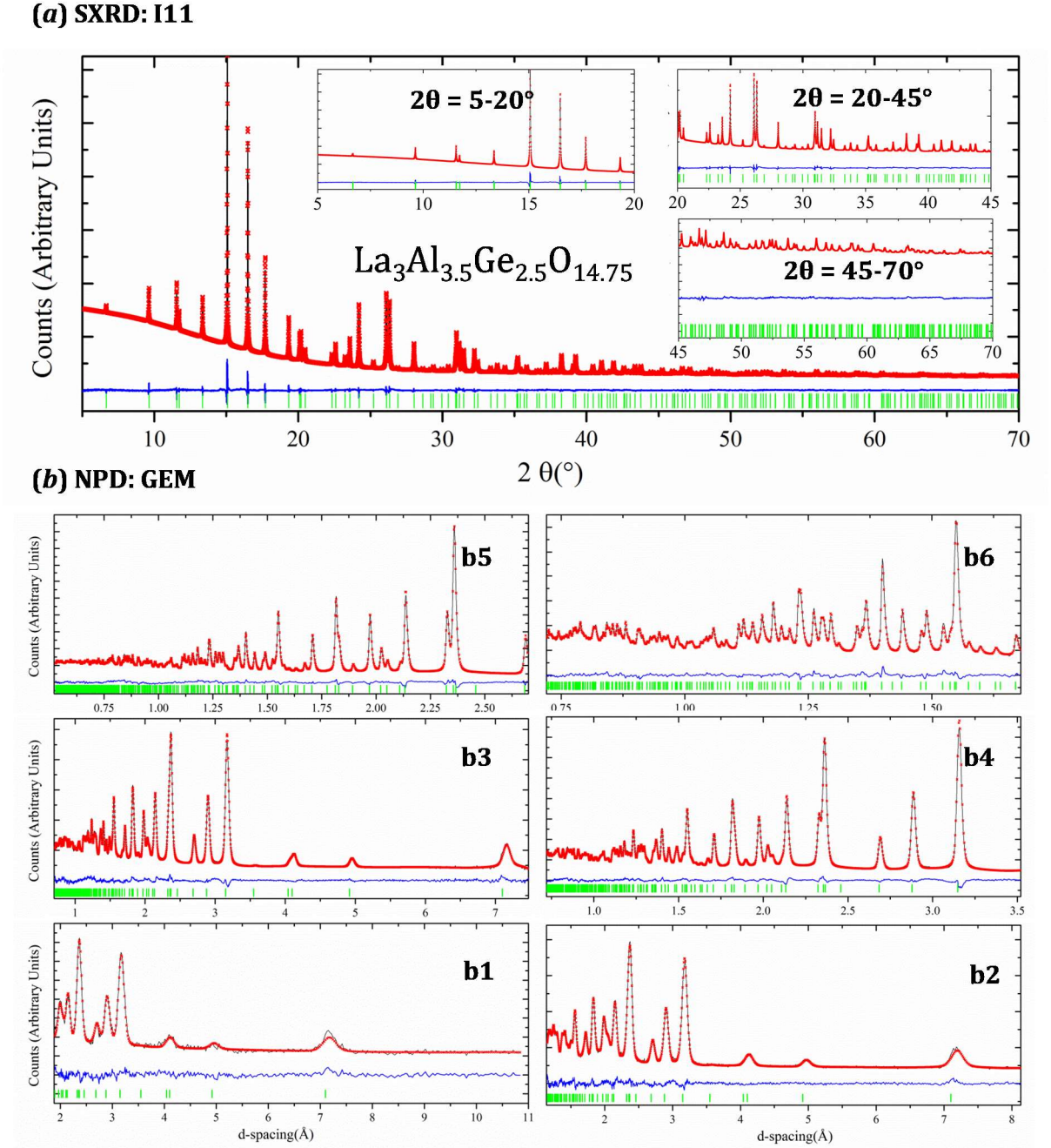

Figure 5-24 Fit of the combined SXRD (*a*) and NPD (*b*) refinement of $La_3Al_{3.5}Ge_{2.5}O_{14.75}$ at 297 K.

Table 5-12 Refined structural parameters for $La_3Al_{5-x}Ge_{1+x}O_{14+x/2}$ where x = 0, 1 and 1.5 at 297 K.

Parameter	$La_3Al_{5-x}Ge_{1+x}O_{14+x/2}$		
x	0	1	1.5
R_{wp}	2.432	1.321	1.663
R_{exp}	0.483	0.299	0.373
a (Å)	8.10288(5)	8.16048(5)	8.1974(3)
c (Å)	4.97459(4)	4.94172(4)	4.91674(2)
V (Å^3)	292.854(4)	284.997(4)	286.127(2)
La1 (3e),(x, 0, 0)			
x	0.41763(3)	0.4172(1)	0.41567(4)

OCC	1	1	1
B_{eq} (Å^2)	0.547(7)	0.80(1)	1.16(1)
Al1 (1a), (0, 0, 0)			
OCC	0.839(5)	0.787(4)	0.823(3)
B_{eq} (Å^2)	0.80(7)	1.13(7)	1.27(7)
Al2 (2d), (1/3,2/3,z)			
z	0.4694(8)	0.5278(5)	0.5269(6)
OCC	0.843(5)	0.756(4)	0.713(3)
B_{eq} (Å^2)	0.68(3)	1.25(5)	1.02(5)
Al3 (3f), (x, 0, 0.5)			
x	0.7618(2)	0.7555(2)	0.7528(1)
OCC	0.817(3)	0.578(3)	0.442(2)
U_{11}	0.0090(5)	0.0209(8)	0.0170(7)
U_{22}	0.0090(5)	0.0209(8)	0.0170(7)
U_{33}	0.010(1)	0.005(1)	0.017(1)
U_{12}	0.0045(2)	0.0209(8)	0.0085(3)
U_{13}	0	0	0
U_{23}	0	0	0
O1 (2d), (1/3,2/3,z)			
z	0.8209(7)	0.1739(4)	0.1694(4)
OCC	1	1	1
U_{11}	0.013(4)	0.0144(8)	0.0130(7)
U_{22}	0.013(4)	0.0144(8)	0.0130(7)
U_{33}	0.014(7)	0.009(1)	0.0039(9)
U_{12}	0.007(2)	0.0144(8)	0.0065(3)
U_{13}	0	0	0
U_{23}	0	0	0
O2 (6g), (x, y, z)			
x	0.4559(4)	0.4562(2)	0.4546(2)
y	0.3010(3)	0.3002(2)	0.2956(2)
z	0.6680(4)	0.3284(3)	0.32473()
OCC	1	0.933(3)	0.888(2)
U_{11}	0.003()1	0.0040(7)	0.006(1)
U_{22}	0.015(9)	0.0248(9)	0.021(2)
U_{33}	0.012(7)	0.0054(6)	0.012(1)
U_{12}	0.00255	0.0070(7)	0.003(1)
U_{13}	-0.002(8)	0.0022(6)	0.002(1)
U_{23}	0.000(6)	0.0092(7)	0
O3 (6g), (x, y, z)			
x	0.0863(2)	0.2156(1)	0.2154(2)
y	0.2153(2)	0.0899(1)	0.0922(2)
z	0.7687(3)	0.7662(3)	0.7671(3)
OCC	1	1	1
U_{11}	0.027(6)	0.0133(7)	0.007(1)
U_{22}	0.018(5)	0.0220(9)	0.022(1)
U_{33}	0.017(5)	0.0084(7)	0.005(1)
U_{12}	0.014(5)	0.0048(8)	-0.004(1)
U_{13}	0.008(4)	0.0047(5)	0.0031(7)
U_{23}	0.005(3)	0.0122(6)	0
O4(6g), (x,y, z)			

x	0.452(2)	0.447(2)
y	0.516(2)	0.528(2)
z	0.475(3)	0.501(2)
OCC	0.081(2)	0.113(2)
B_{eq} (Å²)	2.7(3)	2.4(2)
O5(6g), (x, y, z)		
x	0.388(2)	0.415(1)
y	0.140(2)	0.135(2)
z	0.426(3)	0.408(2)
OCC	0.068(2)	0.104(2)
B_{eq} (Å²)	3.4(7)	3.9(4)

The visual plot of the asymmetric unit cell of $La_3Al_5GeO_{14}$ (x = 0), $La_3Al_4Ge_2O_{14.5}$ (x = 1) and $La_3Al_{3.5}Ge_{2.5}O_{14.75}$ (x = 1.5) is given in Figure 5-25. It should be noticed that the ellipsoids of the oxygen atoms are elongated along the a-b plane. Furthermore, the increase in the dopant content from x = 0 to 1.5 seems to flatten the O1-O3 ellipsoids along this this direction.

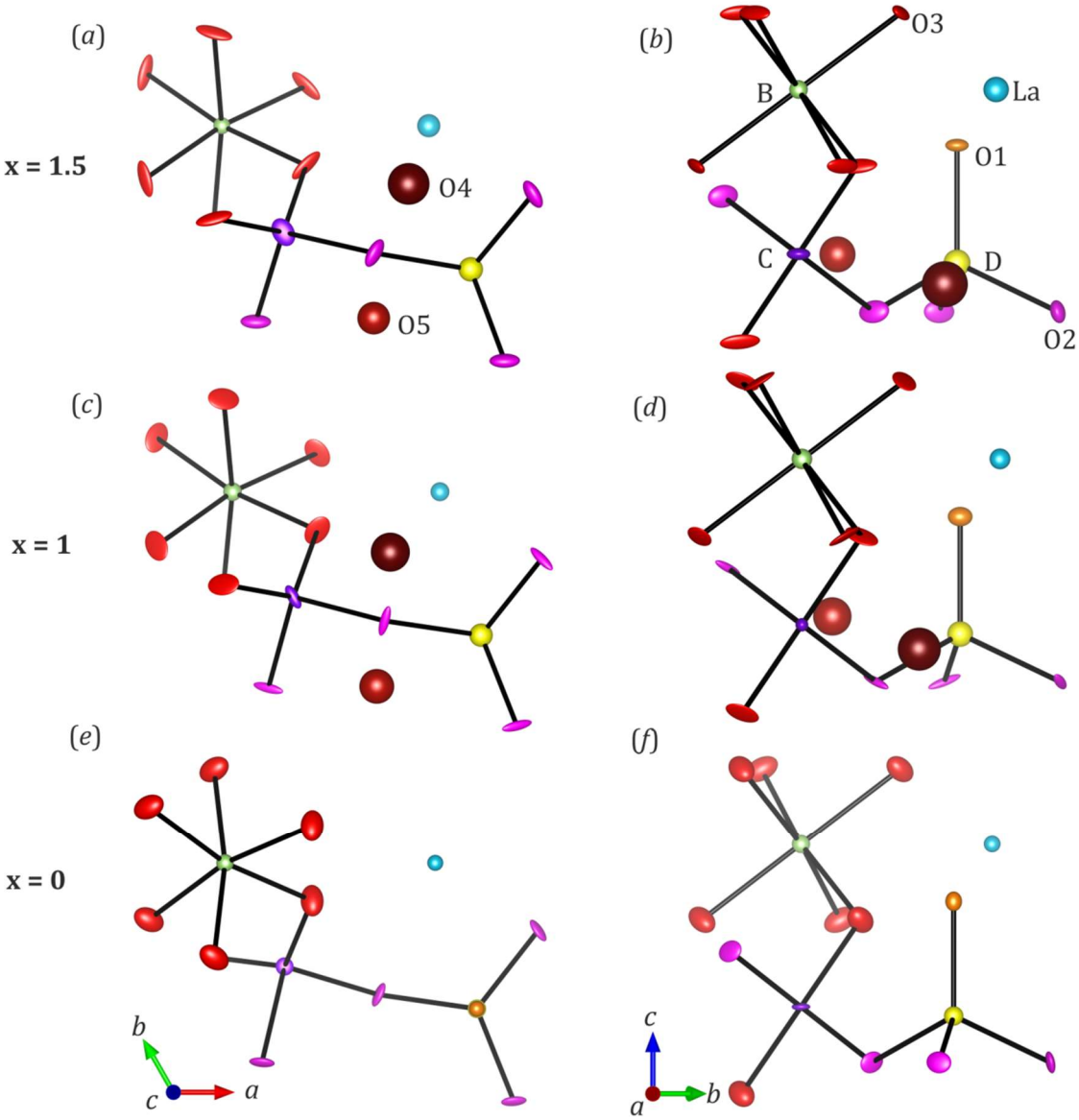

Figure 5-25 Asymmetric unit cell of $La_3Al_{5-x}Ge_{1+x}O_{14+x/2}$ for x = 0, 1 and 1.5 along c and a axes. The ellipsoids represent a 50 % of probability.

To validate the final models, the Bond Valence Sum (BVS) values for the cations were calculated, which are introduced in Table 5-13. The calculated BVS are in good agreement with the expected valences of 3 for La and Al and 4 for Ge.

In the parent $La_3Al_5GeO_{14}$ material there is an even distribution of Al and Ge in a 4:1 ratio amongst the three B-D sites. When an extra amount of germanium is incorporated in $La_3Al_4Ge_2O_{14.5}$ it is preferably substituted in the fully connected tetrahedral C site where the ratio between the two cations becomes 3:2 while it remains approximately equal to 4:1 in the remaining B and D sites. Further incorporation of Ge in $La_3Al_{3.5}Ge_{2.5}O_{14.75}$ substitutes Al^{3+} in C, where the ratio between Al:Ge is inverted with respect to x = 1 and becomes 2:3. This is opposite to the observation made in Ga-langasites, where upon doping Ge preferably substitutes Ga in the octahedral B and smaller tetrahedral D sites.

In both $La_3M^{3+}{}_{5-x}Ge_{1+x}O_{14+x/2}$ for M = Al and Ga, the M^{3+} cations alternate with Ge^{4+} to form a $(M/Ge)_2O_8$ unit so that M^{3+} and Ge^{4+} are intercalated amongst B-D sites rather than adjacent to each other.

Table 5-13 Calculated BVS for the combined GEM and I11 refinements of $La_3Al_5GeO_{14}$ (x = 0), $La_3Al_4Ge_2O_{14.5}$ (x = 1) and $La_3Al_{3.5}Ge_{2.5}O_{14.75}$ (x = 1.5) at room temperature.

Parameter			$La_3Al_{5-x}Ge_{1+x}O_{14+x/2}$		
x			0	1	1.5
A	La		2.81	2.87	2.94
B (1a)	Al		3.00	2.92	2.94
	Ge		3.90	3.79	3.82
C (3f)	Al	M_2O_7	3.01	2.96	2.98
		M_2O_8		3.30	2.64
		Average		3.00	2.94
	Ge	M_2O_7	3.92	3.86	3.88
		M_2O_8		4.29	3.43
		Average		3.91	3.82
D (2d)	Al	M_2O_7	3.17	3.06	2.96
		M_2O_8		3.13	3.28
		Average		3.07	3.00
	Ge	M_2O_7	4.11	3.98	3.85
		M_2O_8		4.07	4.28
		Average		3.99	3.90
$BVS_{Al_{TOTAL}}$			3.08	3.04	3.01
$BVS_{Ge_{TOTAL}}$			3.89	3.82	3.75

5.2.2.3 Conductivity Properties

The fact that Al-langasites formed a $LaAlO_3$ impurity when heated at $T \geq 950$ ° C demanded a careful processing of these materials into suitable specimens with acceptable densities ($\rho \gtrsim 60$ %) and high purities introduced in 5.2.2.3.1. The conductivity of these specimens was determined by AC impedance spectroscopy in 5.2.2.3.2.

5.2.2.3.1 Material processing: Reactive SPS-sintering

$La_3Al_{5-x}Ge_{1+x}O_{14+x/2}$ with x = 0, 0.1, 0.2, 0.3, 0.4, 0.5 and 1 were simultaneously synthesized and sintered by SPS[278,279]. Mixtures of $La_3Al_{5-x}Ge_{1+x}O_{14+x/2}$ precursors were routinely prepared by Pechini but the final sintering step was lowered below the optimal temperature T_{opt} = 900 °C to 850 °C for x = 0, 0.5 and 1 and to an even lower temperature of 800 °C for $0 \leq x \leq 0.4$. These routes led to samples with poor crystallinity at 850 °C (see Figure 5-28) and to amorphous mixture of reactants at 800 °C (see Figure 5-27). After SPS, the latter amorphous mixture of reactants produced pellets with higher densities (80-97 %) than the precursors pre-sintered at 850 °C, which produced lower density pellets (50-60 %). The cross section of a fractured 88 % dense pellet with a $La_3Al_{4.8}Ge_{1.2}O_{14.1}$ nominal composition was analysed in the Scanning Electron Microscope (SEM). Figure 5-26 shows good connectivity between small-sized grains (~1 μm) which are commonly obtained in SPS[174].

The sintering temperatures were lowered from 1050 to 1000 °C for Ge-richer $La_3Al_{5-x}Ge_{1+x}O_{14+x/2}$ compositions with $x \geq 0.4$. Additionally, a lower sintering temperature of 1000 °C was also used in $La_3Al_5GeO_{14}$ (x = 0). A small amount of a $LaAlO_3$ impurity (~4 % of the relative intensity) were observed in the PXRD patters of $La_3Al_{5-x}Ge_{1+x}O_{14+x/2}$ $0 \leq x \leq 0.3$ after SPS (see Figure 5-27 and Figure 5-28). The trend in the lattice parameters calculated by Pawley fitting of the PXRD patterns in Figure 5-27 and Figure 5-28 is depicted in Figure 5-29, which shows an increase in *a*, and decrease in *c* lattice parameters with an overall increase in the cell volume with the incorporation of Ge.

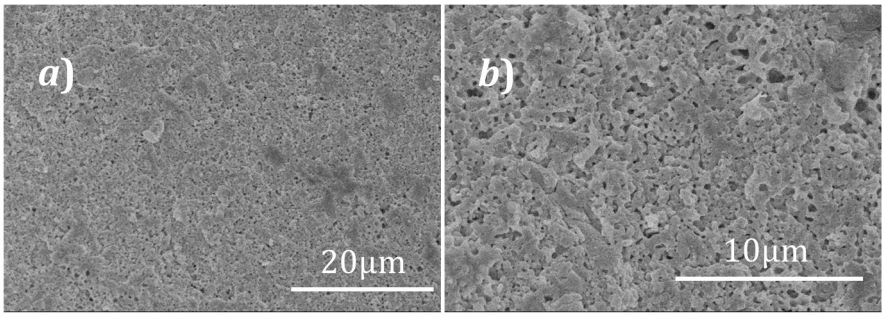

Figure 5-26 SEM images of the SPS synthesized and sintered 88 % dense pellet with a $La_3Al_{4.8}Ge_{1.2}O_{14.1}$ (x = 0.2) nominal composition coated with Au.

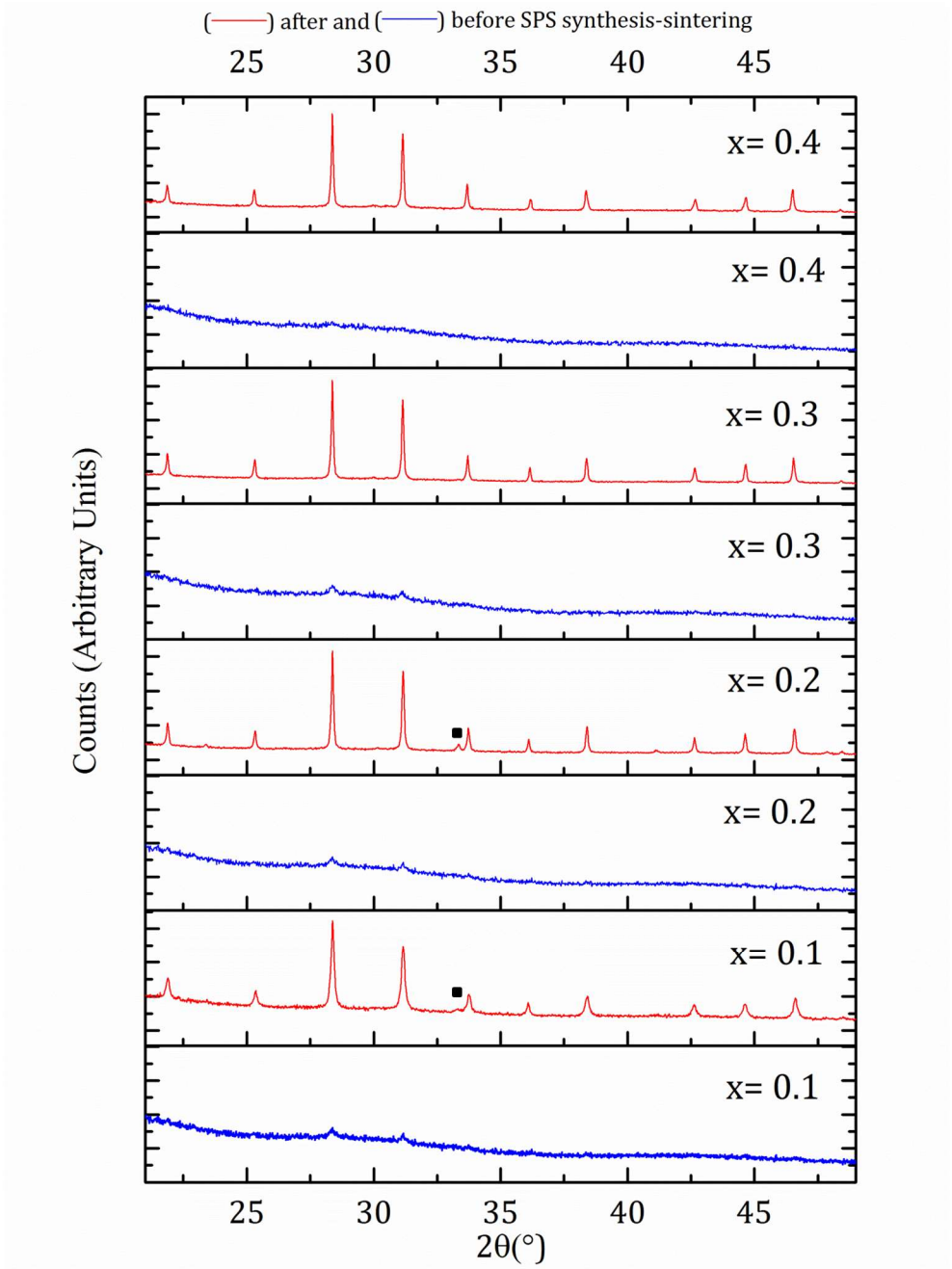

Figure 5-27 PXRD patterns of $La_3Al_{5-x}Ge_{1+x}O_{14+x/2}$ (x = 0.1, 0.2, 0.3 and 0.4) samples pre-treated at 800 °C for 12 h (blue) and after undergoing a combined SPS synthesis and sintering process (red). SPS cycles involved heating the samples at 1050 °C for 5 min for $0.1 \leq x \leq 0.3$ and at 1000 °C for 4 min for x = 0.4, while simultaneously applying a pressure of 50 MPa. Sintering conditions and densities are specified in Table 5-14. Black filled squares denote a $LaAlO_3$ impurity.

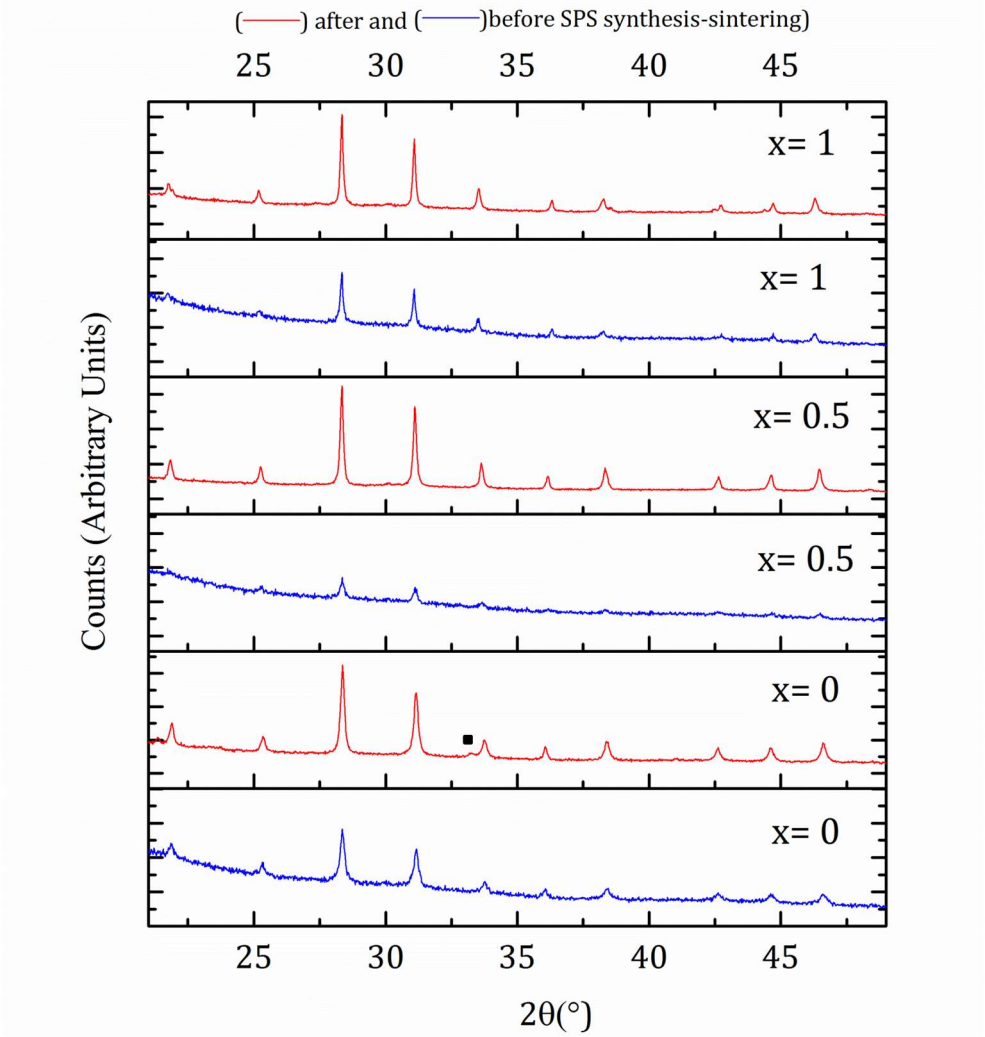

Figure 5-28 PXRD patterns of $La_3Al_{5-x}Ge_{1+x}O_{14+x/2}$ (x = 0, 0.5 and 1) samples pre-treated at 850 °C for 12 h (blue) and after undergoing a combined SPS synthesis and sintering process (red) involving heating at 1000 °C for 5 min under a pressure of 50 MPa. Sintering conditions and final densities are specified in Table 5-14. Black filled squares denote a $LaAlO_3$ impurity.

Additionally, $La_3Ga_{5-x-y}Al_yGe_{1+x}O_{14+x/2}$ compositions were prepared by Pechini at 850 °C and SPS sintered. All the sintering conditions and final densities for $La_3Al_{5-x}Ge_{1+x}O_{14+x/2}$ and $La_3Ga_{5-x-y}Al_yGe_{1+x}O_{14+x/2}$ are listed in Table 5-14 presented in the following section 5.2.2.3.2 along with their conductivity and activation energies in eV determined by AC impedance.

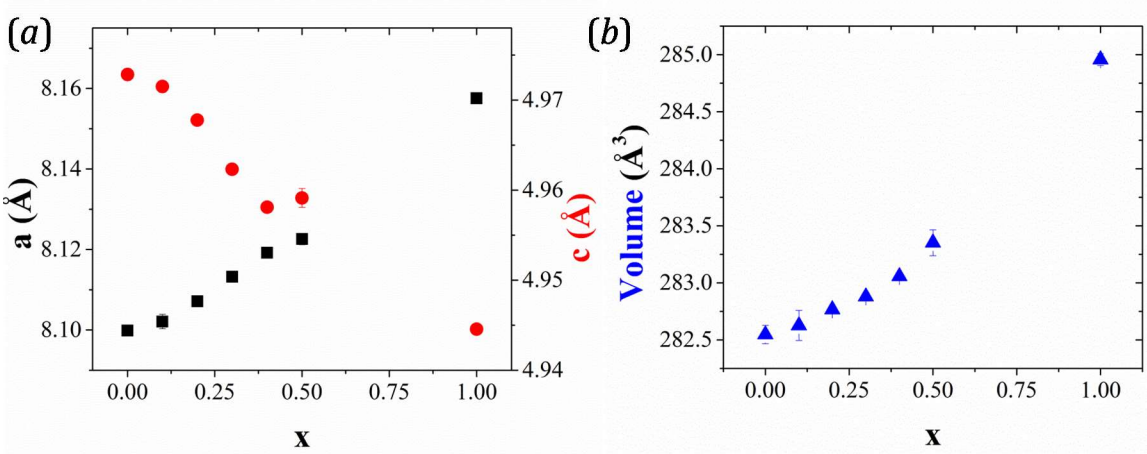

Figure 5-29 Trend in *a* and *c* lattice parameters (*a*) and cell volume (*b*) determined by Pawley fitting of SPS synthesized $La_3Al_{5-x}Ge_{1+x}O_{14+x/2}$ ($0 \leq x \leq 1$). The errors acccount for 1 × e.s.d.

5.2.2.3.2 AC Impedance Spectroscopy

- $La_3Al_{5-x}Ge_{1+x}O_{14+x/2}$

Figure 5-30-*a* shows the bulk conductivity data at 350-600 °C acquired in $La_3Al_{5-x}Ge_{1+x}O_{14+x/2}$ with $0 \leq x \leq 1$ (see 2.3.3.2 for details on the method used for the calculation of the bulk conductivity). This data allowed us to assess the mobility of the interstitial oxide ions in the Al-langasite by the representation of the bulk conductivity at 500 °C vs $C_{O_{int}/chann}$ in Figure 5-30-*b*. This figure demonstrates an increase in conductivity from 3.07×10^{-8} S·cm^{-1} in $La_3Al_5GeO_{14}$ ($x = 0$) to 2.94×10^{-6} S·cm^{-1} in $La_3Al_{4.8}Ge_{1.2}O_{14.1}$ ($x = 0.2$) at 500 °C. However, for $x > 0.2$ the conductivity slightly decreases to $\sim 1 \times 10^{-6}$ S·cm^{-1} and plateaus.

It is therefore demonstrated that the conductivity displayed by Al-langasites is lower than that of their Ga-analogues. The conductivity of $La_{4.5}Ga_{4.5}Ge_{1.5}O_{14.25}$ ($x = 0.5$) denoted by a red line in Figure 5-30-*a* lies one order of magnitude above the most conductive $La_3Al_{4.8}Ge_{1.2}O_{14.1}$ ($x = 0.2$). The interstitial saturation in Al-langasites is reached at $0.03 \leq C_{O_{int}/chann} < 0.05$, whereas this value corresponds to a higher 0.083 in Ga-langasites.

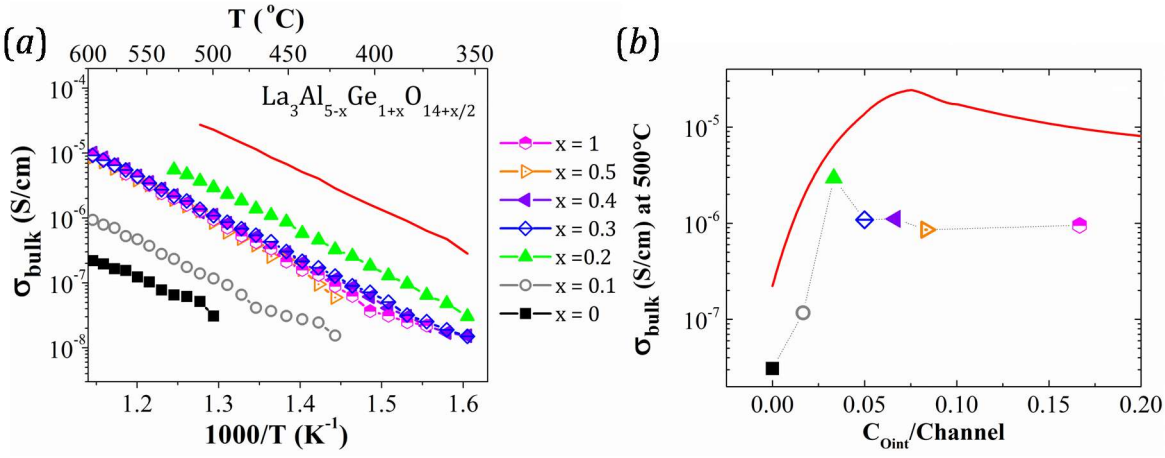

Figure 5-30 (*a*) Arrhenius plot of the bulk conductivity of $La_3Al_{5-x}Ge_{1+x}O_{14+x/2}$. The conductivity of $La_3Ga_{4.5}Ge_{1.5}O_{14.25}$ (x = 0.5) is given in a solid red line for comparison. (*b*) Bulk conductivity at 500 °C vs the concentration of oxygen interstitial per channel ($C_{O_{int}/channel} = x/6$). The red line in (*b*) accounts for $La_3Ga_{5-x}Ge_{1+x}O_{14+x/2}$.

The bulk conductivity values were extracted from the combined use of the *M''* and *Z''*vs frequency plots given in Figure 5-31-*b*. This plot allowed us to discriminate between the bulk and grain boundary components which are otherwise merged into one depressed semi-circle in the complex impedance plot (see Figure 5-31-*a*). Due to the poor density of these specimens the total conductivity values extracted from the arcs attributed to grain boundaries in the complex impedance plane are not meaningful.

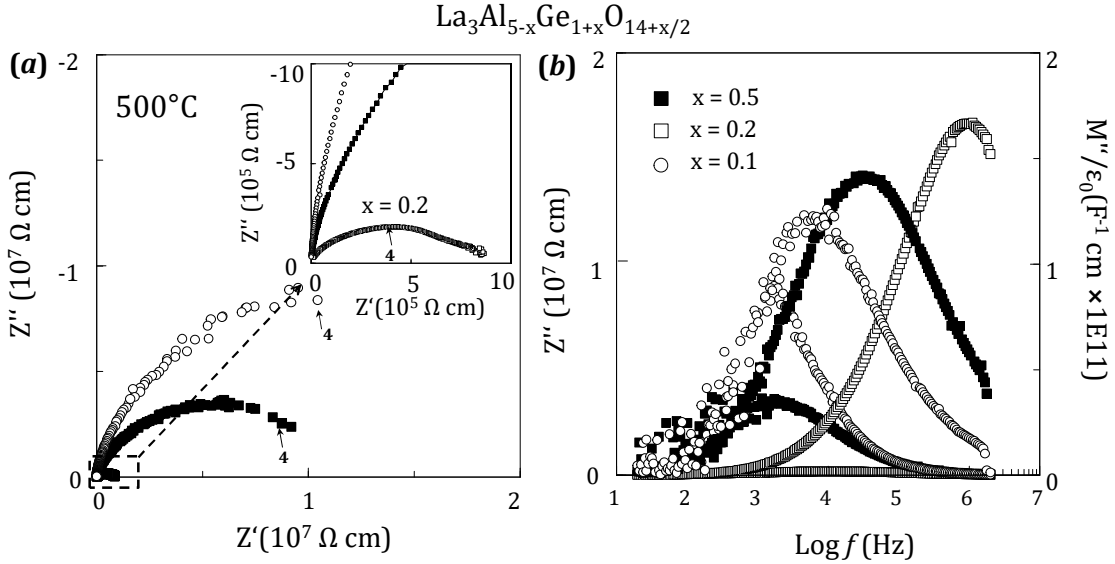

Figure 5-31 (*a*) Complex impedance plane for $La_3Al_{5-x}Ge_{1+x}O_{14+x/2}$ with x =0 (white circles), 0.2 (white squares) and 0.5 (black squares) at 500 °C, the numbers in bold accounts for $log\ f$ values. (*b*) Overlaid *Z''* and *M''* spectra at the same temperature. Due to the high noise at low frequencies (≲10³ Hz), $f_{max}$is only observed in the *Z''* spectra for x = 0.5.

- $La_3Ga_{5-x-y}Al_y\ Ge_{1+x}O_{14+x/2}$

Herein the bulk conductivities for various $La_3Ga_{5-x-y}Al_yGe_{1+x}O_{14+x/2}$ compositions is presented. This study seeks for an increase in conductivity as a consequence of the induced Ga, Al and Ge disorder in the M_2O_8 local environments.

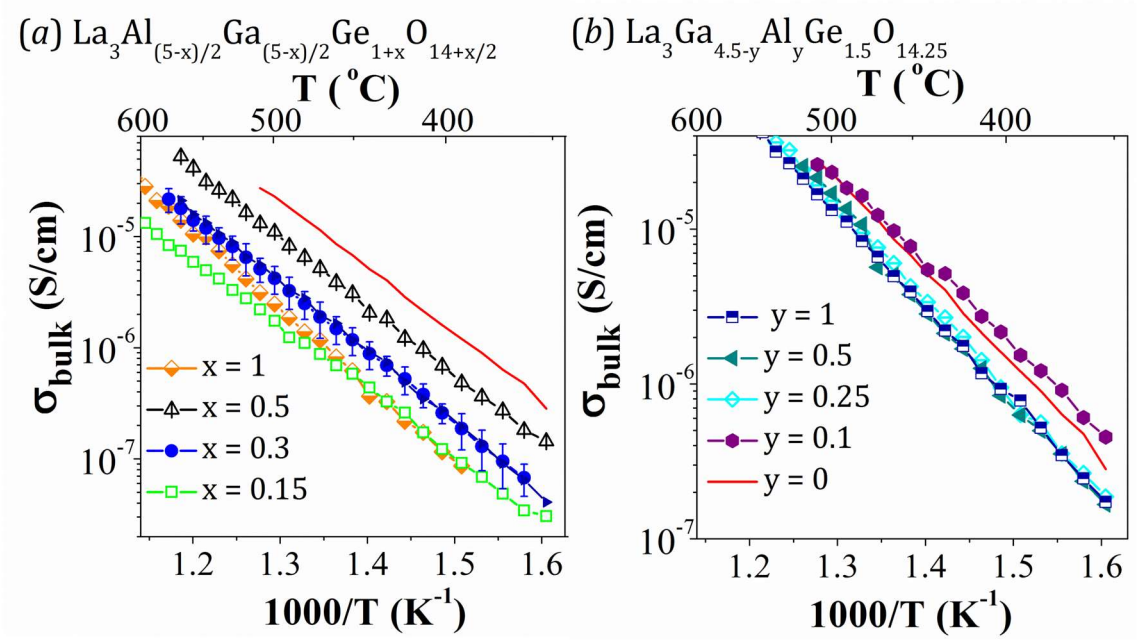

Figure 5-32 Arrhenius plot of the bulk conductivity of $La_3Al_{(5-x)/2}Ga_{(5-x)/2}Ge_{1+x}O_{14+x/2}$ (*a*) and $La_3Ga_{4.5-y}Al_yGe_{1.5}O_{14.25}$ (*b*). $La_3Ga_{4.5}Ge_{1.5}O_{14.25}$ is denoted by a soild red line in both graphs.

Firstly, the Al:Ga ratio was held constant and equal to 1:1 in $La_3Ga_{(5-x)/2}Al_{(5-x)/2}Ge_{1+x}O_{14+x/2}$ and the conductivity of four samples with different dopant content (x = 0.15, 0.3, 0.5 and 1) was investigated. The measured conductivities were found to gradually increase from x = 0.15 to 0.3 and up to the most conducting composition of $La_3Ga_{2.25}Al_{2.25}Ge_{1.5}O_{14.25}$ (x = 0.5) having a conductivity of 1.11 × 10^{-5} S·cm^{-1} at 500 °C, close to the maximum value of 2.29 × 10^{-5} S·cm^{-1} reached by $La_3Ga_{4.5}Ge_{1.5}O_{14.25}$, with also x = 0.5. In $La_3Ga_2Al_2Ge_2O_{14.5}$ (x = 1), where the concentration of oxygen interstitials is doubled, the conductivity is decreased by one order of magnitude to 2.48 × 10^{-6} S·cm^{-1} at 500 °C. The conductivity of $La_3Ga_2Al_2Ge_2O_{14.5}$ (x = 1) overlaps in most of the temperature range studied with $La_3Ga_{2.425}Al_{2.425}Ge_{1.15}O_{14.075}$ (x = 0.15) and $La_3Ga_{2.35}Al_{2.35}Ge_{1.3}O_{14.15}$ (x = 0.3).

With the focus placed on a dopant content of x = 0.5, a second study was carried out in which the Al:Ga ratio was varied and the dopant content was fixed at x = 0.5 in $La_3Ga_{4.5-y}Al_yGe_{1.5}O_{14.25}$. Several '$y$' values were studied (*i.e.* 0.1, 0.25, 0.5 and 1). Their bulk conductivity at 350-500 °C is introduced in Figure 5-32-*b*. The Arrhenius plot of the conductivity shows an overlap for $La_3Ga_{3.5}AlGe_{1.5}O_{14.25}$ (y = 1), $La_3Ga_4Al_{0.5}Ge_{1.5}O_{14.25}$ (y = 0.5) and $La_3Ga_{4.25}Al_{0.25}Ge_{1.5}O_{14.25}$ (y = 0.25) with a conductivity of approximately ~1.5 × 10^{-5} S·cm^{-1} at 500 °C. The best results were obtained for the Al-poorer $La_3Ga_{4.4}Al_{0.1}Ge_{1.5}O_{14.25}$ (y = 0.1) whose conductivity is equivalent to that of $La_3Ga_{4.5}Ge_{1.5}O_{14.25}$ of approximately ~2.3 × 10^{-5} S·cm^{-1} at 500 °C.

It can be noticed that the method used for the determination of the conductivity in this chapter is not frequently used for the characterization of electrolytes. Electrolyte materials are commonly studied at the cell's operating temperature, being a common procedure to report their total conductivities at 500-950 °C. However, for the systems studied in this chapter this is not feasible. This is because for one, these materials are unstable at 900-950 °C, and secondly, the pellets' densities are typically ~60 % and such low densities are not suitable for the determination of the total conductivity. For this reason, the bulk conductivities at 300-550 °C were reported; the peak maxima shifts to frequencies higher than 2 MHz (2 MHz being the maximum frequency reached by E4980 LCR meter analyser) at T > 550 °C and we were therefore unable to collect data at 550-850 °C.

Table 5-14 SPS sintering conditions for $La_3Al_{5-x}Ge_{1+x}O_{14+x/2}$ and $La_3Ga_{5-x-y}Al_yGe_{1+x}O_{14+x/2}$, a ramp rate of 200 ° min^{-1} and an applied pressure of 50 MPa were held constant in all the experiments carried out.

Nominal composition	ρ (%)	Ea_{bulk} (eV)	Sintering conditions		$\%_{O_{int}}$	$\sigma_{500\,°C}$ ($S{\cdot}cm^{-1}$)
			T(°C)	Dwell (min)		
$La_3Al_4Ge_2O_{14.5}$	58	1.35	1000	5	3.57	9.52×10^{-7}
$La_3Al_{4.5}Ge_{1.5}O_{14.25}$	56	1.36	1000	5	1.79	8.56×10^{-7}
$La_3Al_{4.6}Ge_{1.4}O_{14.2}$	97	1.28	1000	5	1.43	1.11×10^{-6}
$La_3Al_{4.7}Ge_{1.3}O_{14.15}$	83	1.24	1050	4	1.07	1.09×10^{-6}
$La_3Al_{4.8}Ge_{1.2}O_{14.1}$	88	1.25	1050	4	0.71	2.94×10^{-6}
$La_3Al_{4.9}Ge_{1.1}O_{14.05}$	79	1.22	1050	4	0.36	1.17×10^{-7}
$La_3Al_5GeO_{14}$	55	1.06	1000	5	-	3.07×10^{-8}
$La_3Al_2Ga_2Ge_2O_{14.5}$	57	1.39	1000	5	3.57	2.48×10^{-6}
$La_3Al_{2.25}Ga_{2.25}Ge_{1.5}O_{14.25}$	74	1.23	1000	5	1.79	1.11×10^{-5}
$La_3Al_{2.35}Ga_{2.35}Ge_{1.3}O_{14.15}$	79	1.18	1050	4	1.07	6.00×10^{-6}
$La_3Al_{2.35}Ga_{2.35}Ge_{1.3}O_{14.15}$	61	1.20	1000	5	1.07	4.25×10^{-6}
$La_3Al_{2.425}Ga_{2.425}Ge_{1.15}O_{14.075}$	57	1.16	1050	4	0.54	1.75×10^{-6}
$La_3Ga_{3.5}AlGe_{1.5}O_{14.25}$	58	1.20	1000	5	1.79	1.33×10^{-5}
$La_3Ga_4Al_{0.5}Ge_{1.5}O_{14.25}$	98	1.27	1050	4	1.79	1.70×10^{-5}
$La_3Ga_{4.25}Al_{0.25}Ge_{1.5}O_{14.25}$	64	1.23	1000	5	1.79	1.52×10^{-5}
$La_3Ga_{4.4}Al_{0.1}Ge_{1.5}O_{14.25}$	93	1.08	1050	4	1.79	2.29×10^{-5}
$La_3Ga_{4.5}Ge_{1.5}O_{14.25}$	97	1.18	1100	10	1.79	2.29×10^{-5}

To corroborate the validity of these experiments the pellets were ground and the PXRD patterns were recorded (see Figure 5-33). It is demonstrated that the samples retained their integrity during the course of these experiments as no presence of impurity phases was observed in the post-experimental patterns. For a comparison of the lattice parameters of these samples before and after AC impedance experiments determined by Pawley fitting, the reader is referred to Appendix 8.

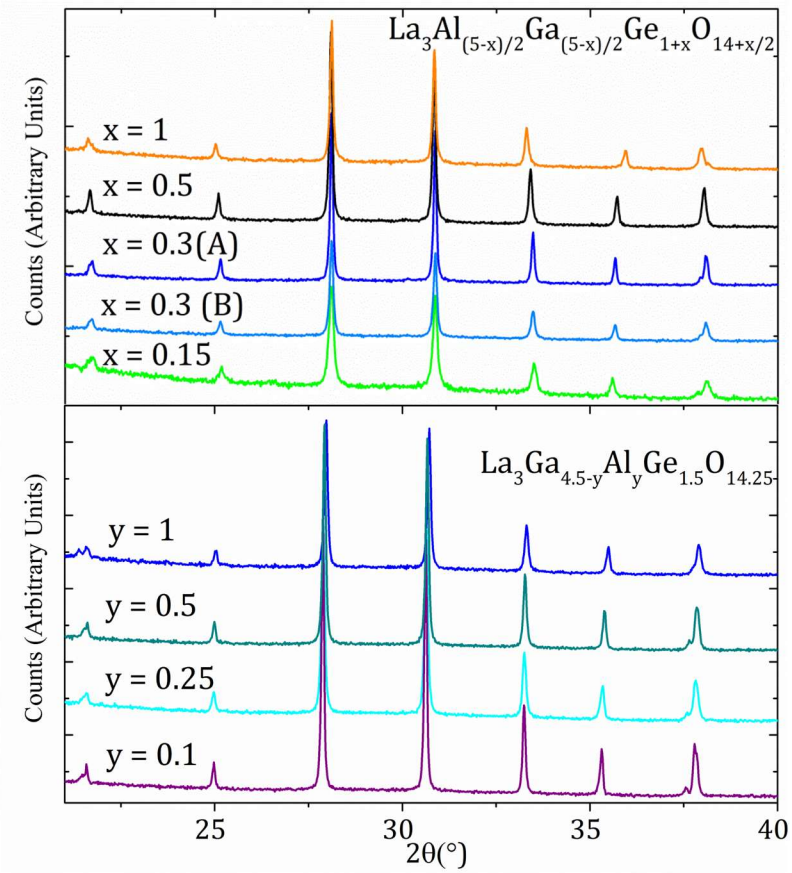

Figure 5-33 Post-Measurement PXRD patterns of $La_3Al_{(5-x)/2}Ga_{(5-x)/2}Ge_{1+x}O_{14+x/2}$ and $La_3Ga_{4.5-y}Al_yGe_{1.5}O_{14.25}$ collected in a Bruker diffractometer with a Cu source ($K_{\alpha 1,Cu}$ = 1.5406 Å) showing no evidence of sample decomposition or formation of impurity phases.

5.3 Summary and Conclusion

Herein, rare-earth langasite type-germanates $La_{3-y}Ln_yGa_{5-x}Ge_{1+x}O_{14+x/2}$ (Ln = Pr, Nd, Sm and Gd) were successfully prepared by the Pechini method incorporating up to ~3.57 % of interstitials in $Ln_3Ga_4Ge_2O_{14.5}$ (Ln = Pr, Nd, Sm and Gd) and a higher 5.36 % in $La_{1.5}Ln_{1.5}Ga_{3.5}Ge_{2.5}O_{14.75}$ (Ln = Pr and Nd). Additionally, a novel $La_3Al_5GeO_{14}$ langasite was synthesized by this sol-gel route, which also shows a great flexibility for the incorporation of interstitial oxides (up to 5.36 %) in $La_3Al_{3.5}Ge_{2.5}O_{14.75}$.

The structures of doped compositions were determined as follows: $La_{1.5}Pr_{1.5}Ga_4Ge_2O_{14.5}$ was characterized by high resolution NPD at HPRD whereas $La_3Al_4Ge_2O_{14.5}$ and $La_3Al_{3.5}Ge_{2.5}O_{14.75}$ compositions were analysed by a combined Rietveld refinement of synchrotron (I11) and high intensity neutrons (GEM). The Rietveld refinement of the data located the extra oxygen incorporated within M_2O_8 dimers resembling the one found in the saturated langasites: $La_3GaGe_5O_{16}$ and $La_3AlGe_5O_{16}$.

Pure fine-sized powders $La_{3-y}Ln_yGa_{5-x}Ge_{1-x}O_{14+x/2}$ with Ln = Pr and Nd, y = 1.5 and 3 and $0 \leq x < 0.5$ were sintered by conventional methods using a diluted (6.23×10^{-4} M) solution of reactants. This concentration produced particles with an averaged diameter $\bar{\emptyset}$ of $5-10\ \mu m$ after calcination at 600 °C, as determined by SEM. Smaller particle sized powders rendered 80-90 % dense specimens suitable for the determination of the conductivity. $La_{3-y}Ln_yGa_{5-x}Ge_{1-x}O_{14+x/2}$ with $x \geq 0.5$ were sintered by SPS assisted techniques due to a dramatic decrease in the decomposition temperature. In some instances, the sintering

process lead to the formation of a minor $LaGaGeO_5$ impurity while no significant change in composition of the main phase occurred, as evidenced by the constant value of the lattice parameters before and after sintering calculated by Pawley refinements. Impedance spectroscopy measurements shown a decrease in the bulk conductivity values as the Ln size decrease from 2.29×10^{-5} S·cm^{-1} in $La_3Ga_{4.5}Ge_{1.5}O_{14.25}$ to 1.05×10^{-5} S·cm^{-1} in $Nd_3Ga_{4.5}Ge_{1.5}O_{14.25}$ at 500 °C, whereas the activation energy was found constant throughout (E_a~1.1 eV).

Dense Al-langasites were prepared by reactive SPS-sintering and analysed by AC impedance spectroscopy. This study revealed a lower conductivity of Al-langasites with respect to their Ga-analogues. Furthermore, Al-langasites became saturated of interstitials at a lower concentration of defects per channel. The most conductive Al-langasite $La_3Al_{4.8}Ge_{1.2}O_{14.1}$ (x = 0.2) has a conductivity of 2.94×10^{-6} S·cm^{-1} at 500 °C, whereas $La_3Ga_{4.5}Ge_{1.5}O_{14.25}$ (x = 0.5) has a conductivity of 2.29×10^{-5} S·cm^{-1} of one order of magnitude higher. The interstitials mobility is again restrained by the trapping of the defects in the rigid M_2O_8 dimers, leading to high activation energies ~1.2 eV.

6 CONCLUSIONS AND OUTLOOK

The The solid solution range in $La_3Ga_{5-x}Ge_{1+x}O_{14+x/2}$ with a langasite structure extends up to $\boldsymbol{x}$ = 1.5 and demonstrates a remarkable flexibility in how it accommodates extra oxygen. This defect content is even higher than in other oxide ion conductors where the ionic conductivity is mediated *via* interstitial oxide ions such as apatite and melilites which incorporate ~3.9 and 4.6 % of extra oxygen respectively. In $La_3Ga_{5-x}Ge_{1+x}O_{14+x/2}$ the extra oxygen is located within the tetrahedral network forming a $(Ga/Ge)_2O_8$ dimer - resembling a similar unit found in $La_3GaGe_5O_{16}$. This position of the extra oxygen was predicted by DFT calculations and corroborated by high-resolution NPD, ^{71}Ga and ^{17}O NMR studies.

A promising increase in the bulk conductivity of two orders of magnitude with respect to the un-doped parent material is observed for $0.4 \leq x \leq 0.5$ (from 7.25×10^{-6} S·cm^{-1} in $La_3Ga_5GeO_{14}$ to 2.42×10^{-5} S·cm^{-1} at 500 °C). At this compositional range the conductivity reaches a plateau. For $x > 0.5$ a steady linear decrease in the bulk conductivity is observed down to 7.25×10^{-6} S·cm^{-1} for $x = 1.5$ at 500 °C. The impeded mobility of the extra oxygen at the higher concentration of O_{int}, could be caused by the higher rigidity of the $(Ga/Ge)_2O_8$ unit in comparison with other labile units such as the trigonal bipyramid coordinated $Ga2_{int}O_5$ in melilites.

Isovalent substitutions were carried out comprising the co-doping and full substitution of La^{3+} by other RE^{3+}($e.g.$ Pr, Nd, Sm and Gd) in $La_{3-y}Ln_yGa_{5-x}Ge_{1+x}O_{14+x/2}$. This approach resulted in a decrease in the conductivity with the smaller RE cations, with the highest conductivity being achieved by La-langasties. A second approach for isovalent substitution involved the substitution of Ga for the more abundant and inexpensive Al in $La_3Ga_{5-x-y}Al_yGe_{1+x}O_{14+x/2}$ and $La_3Al_{5-x}Ge_{1+x}O_{14+x/2}$. This again resulted in a decrease in the conductivity with respect to the originally studied $La_3Ga_{5-x}Ge_{1+x}O_{14+x/2}$ compositions. Moreover, the highest mobility of the interstitial was reached at an even lower concentration ($C_{O_{int}}/channel = 0.04$) being maximum at 2.94×10^{-6} S·cm^{-1} for $La_3Al_{4.8}Ge_{1.2}O_{14.1}$ at 500°C. A combined NPD and SXRD study reveals the location of the extra oxygen within a $(Al/Ge)_2O_8$ dimer.

Overall, the oxide ionic conductivity of the $La_3Ga_{5-x}Ge_{1+x}O_{14+x/2}$ langasite is modest and not competitive with other currently existing electrolytes which reach the desirable value of > 10^{-2} S·cm^{-1} at 600-1000 °C. However, this structure can accommodate a wide range of cations and over 140 langasites with different compositions have been reported up to

date. This discovery can open up exciting possibilities for the exploration of a large variety of compositions within this class of materials due to their flexibility towards chemical doping. This warrants further investigations into these systems.

6.1 Candidate structures containing a flexible M_2O_7 dimer

The structural insight into the doped langasite structure presented here constitutes a valuable knowledge base for the design of next generation electrolyte materials. Comparing the structures of langasites and melilites, one feature that could be hindering the oxide ion mobility in langasites is the presence of an octahedron interconnecting the layers of tetrahedra. This octahedron binds the tetrahedral C site which is fully connected and could in turn restrict the mobility of the M_2O_7 dimer; whereas in melilites the interconnected M_2O_7 units consist of two tetrahedra, each of which have one apical oxygen.

Some candidate structures fulfilling the aforesaid structural requirements suggested in ref.61 and more are introduced in the following sections. In the updated list those candidates in which the flexibility of the M_2O_7 unit is compromised are not considered and the list could be divided into the following categories:

- Structures based on flexible M_2O_7 dimers (*i.e.* two bridged non saturated tetrahedra): $Ba_2CuSi_2O_7$, $Ba_2TiSi_2O_8$ (fresnoites), $Ca_2ZnGe_{1.75}Si_{0.25}O_7$, $K_2MoAs_2O_9$ and $Sr_5Ga_6O_{14}$.

- Extended structures of interconnected MO_4: $LaSrNa_3ZnSi_6O_7$ (Nordite), $Ba_4Si_6O_{16}$, Na_2SiO_5 and $SrGa_2O_5$.

6.1.1 $Ba_2CuSi_2O_7$

The crystal structure shown in Figure 6-1 consists of layers of Si_2O_7 dimers (in yellow) connected by a 4-connected tetrahedra occupied by Cu(in violet). The layers of tetrahedra alternate with large Ba atoms (in cyan) along the *a*-direction which provides them with a separation of ~7 Å[280]. The view along the *c*-direction displays two rings where the Ba sits; a 4 and an 8-membered ring with potential for interstitial oxide ion accommodation.

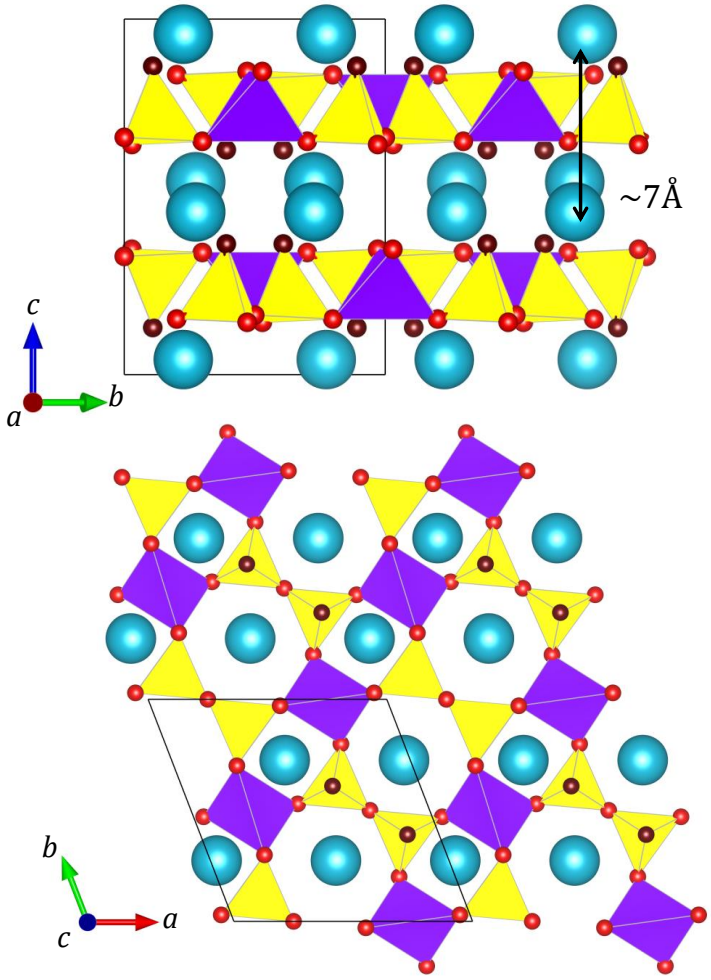

Figure 6-1 Structure of $Ba_2CuSi_2O_7$ where Ba is depicted in blue, Si_2O_7 dimers in yellow and the fully bridged tetrahedral sites occupied by Cu in violet. Bridging oxygens are coloured in red to differentiate them from the apical oxygens in mahogany.

6.1.2 $Ba_2TiSi_2O_8$ (fresnoites)

The crystal structure of fresnoites in Figure 6-2 displays the characteristics that presuppose ease of network deformation: there is a wide separation between the layers of tetrahedra provided by the large A = Ba cations as well as groups of Si_2O_7 linked by a square based pyramid occupied by titanium[281]. Although most commonly Ti^{4+} is found to occupy octrahedral sites, there are other reported compounds besides fresnoites where this cation is 5-coordinated, these are: Y_2TiO_5[282], the carnotite-type $Ba_2[(UO_2)_2Ti_2O_8]$[283], Ba_2TiO_4[284] and Li_4TiO_4[285] amongst others.

It can be observed how the connectivity of polyhedra is identical in melilites and fresnoites (although in the latter the fully connected tetrahedra is replaced by a 5-cooridnated Ti with an additional apical oxygen). Interestingly, and unlike melilites, all the apical oxygen atoms are pointing in the same direction.

Fresnoites do not constitute an extensive family of minerals in contrat to melilite and langasite materials. Compositions that are found to adopt a $A_2^{[10]}B^{[5]}C_2^{[4]}O_8$ fresnoite type structure are: $Ba_2TiM_2O_8$ where M = Si, Ge. $Sr_2Ti_2Si_2O_8$, $A_2V_3O_8$ where A = Rb[286], K[287] and $Ba_2VSi_2O_8$.

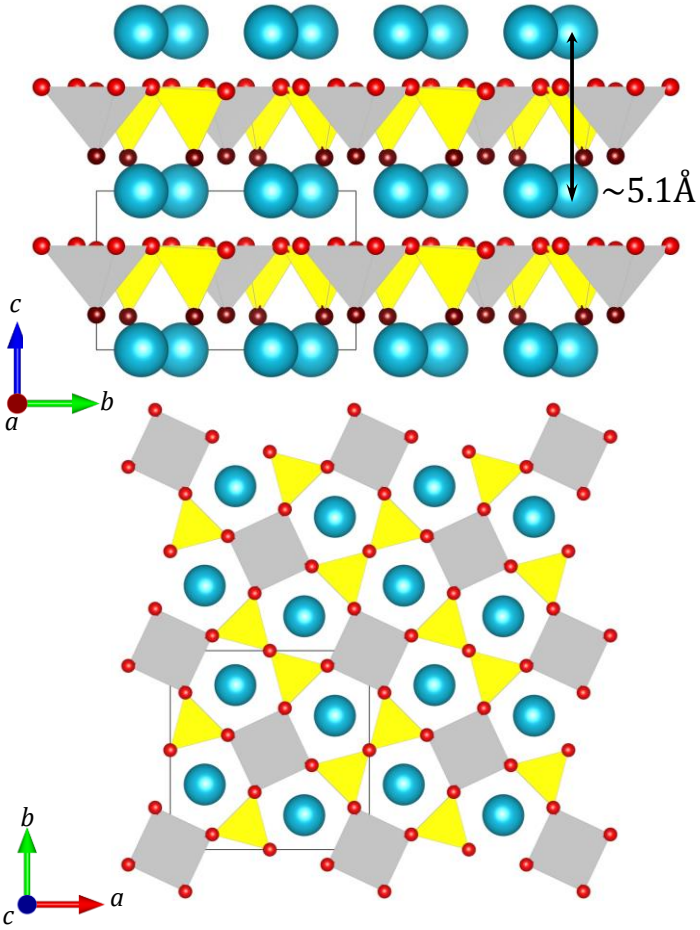

Figure 6-2 Polyhedral representation of a $A_2^{[10]}B^{[5]}C_2^{[4]}O_8$ fresnoite structure along *a* (top) and *c*-axes (bottom) A atoms are labelled in cyan B in grey and C in yellow.

6.1.3 2D: $Ca_2ZnGe_{1.75}Si_{0.25}O_7$

$Ca_2ZnGe_{1.75}Si_{0.25}O_7$ is another melilite-related material. In $Ca_2ZnGe_{1.75}Si_{0.25}O_7$, as in melilites, there are two types of tetrahedra present: a 3-connected site occupied by Si and Ge and a fully connected type occupied by Zn forming stacks of infinite layers of tetrahedra separated by ~5.1 Å.

$Ca_2ZnGe_{1.75}Si_{0.25}O_7$ contains three types of channels running parallel to the (101) direction where Ca lies: a 5-membered melilite-like rings, 4-membered rings, and elongated 6-membered[288] rings.

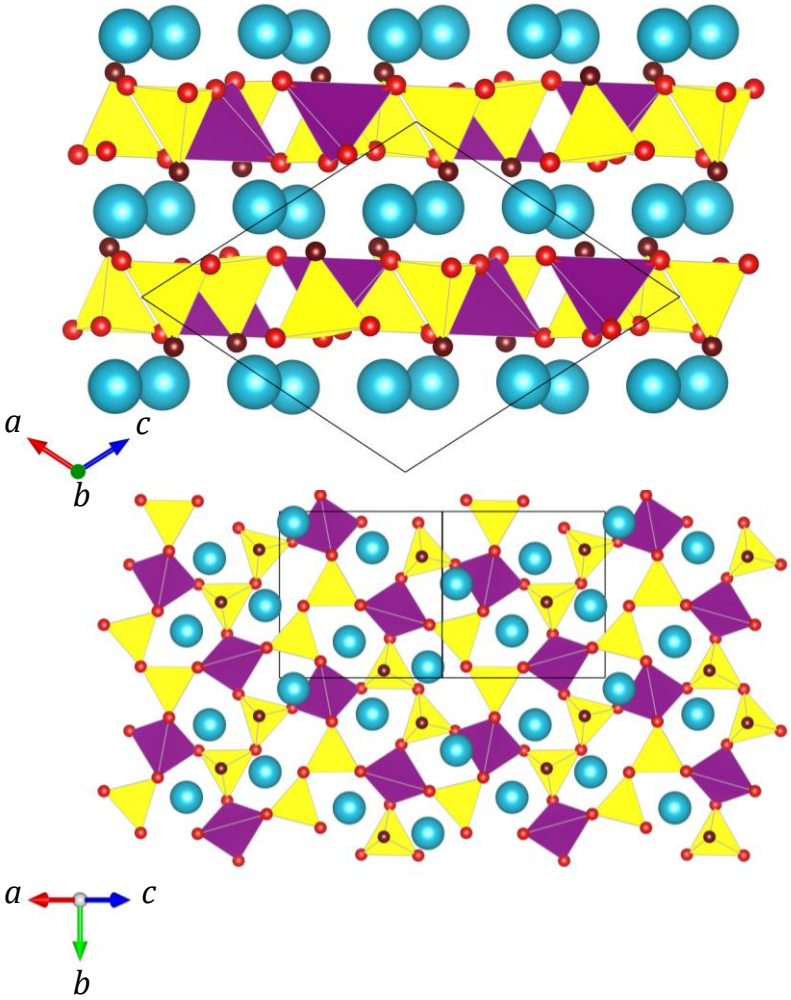

Figure 6-3 Polyhedral representation of $Ca_2ZnGe_{1.75}Si_{0.25}O_7$. Large Ca cations are depicted in cyan, 3 and 4-connected tetrahedra are given in yellow and violet respectively.

6.1.4 $K_2MoAs_2O_9$

$K_2MoAs_2O_9$ is built up from MoO_6 octahedra sharing corners with As_2O_7 dimers to form layers along the *a* -axis (see Figure 6-4 top). Besides the apical oxygen within the As_2O_7 dimers two oxygen atoms in MoO_6 remain unshared with short Mo-O distances that have an average of 1.704 Å[289]. The K^+ ions are located in the interlayer space providing the layers of tetrahedra with a ~5.8 Å separation.

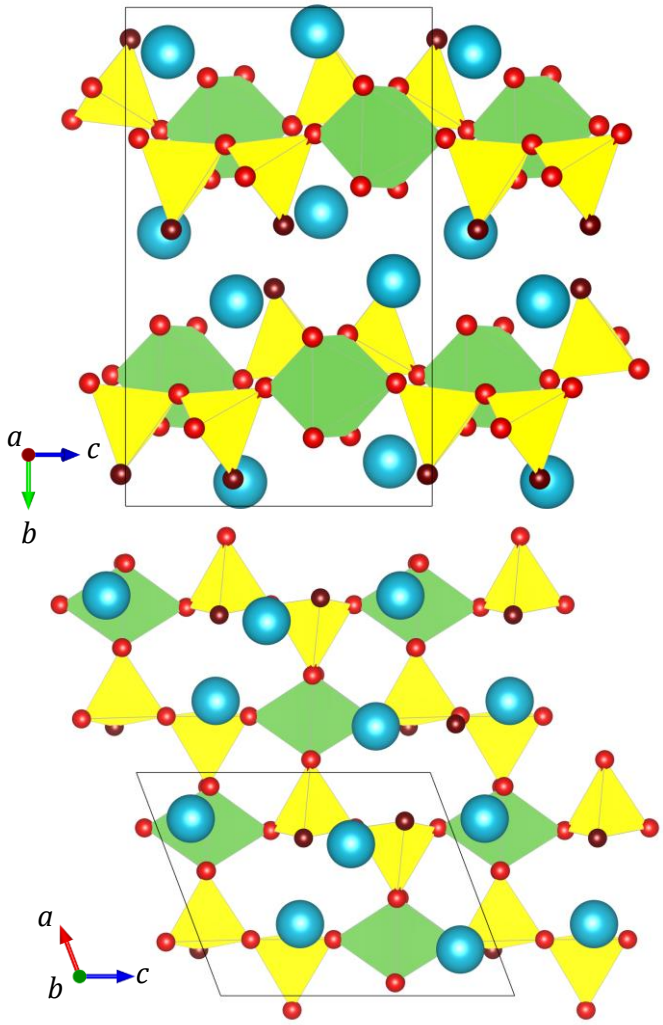

Figure 6-4 View of the $K_2MoAs_2O_9$ layered structure along the *a*-direction (top) and of the top layer along the *b*-direction in the bottom figure. K cations are represented by large blue spheres, MoO_6 are green octahedra and As_2O_7 units are displayed in yellow.

6.1.5 $Sr_5Ga_6O_{14}$

$Sr_5Ga_6O_{14}$ is a newly reported high pressure phase synthesized at 3 GPa and 1000 °C[290]. Its connectivity between constituent tetrahedral units is identical to that of the melilite structure. The infinite sheets of 3 and 4-connected tetrahedral sites are displayed along the *a*-axis in Figure 6-5 alternating with large Sr. These atoms lie in 5-membered rings but unlike in melilites, Sr is off-centered and three symmetrically independent sites are generated, whose coordination number range from six to eight oxygen atoms. In $Sr_5Ga_6O_{14}$, adjacent tetrahedral sheets do not overlap along the c-direction and the value of the *c* lattice parameter is doubled.

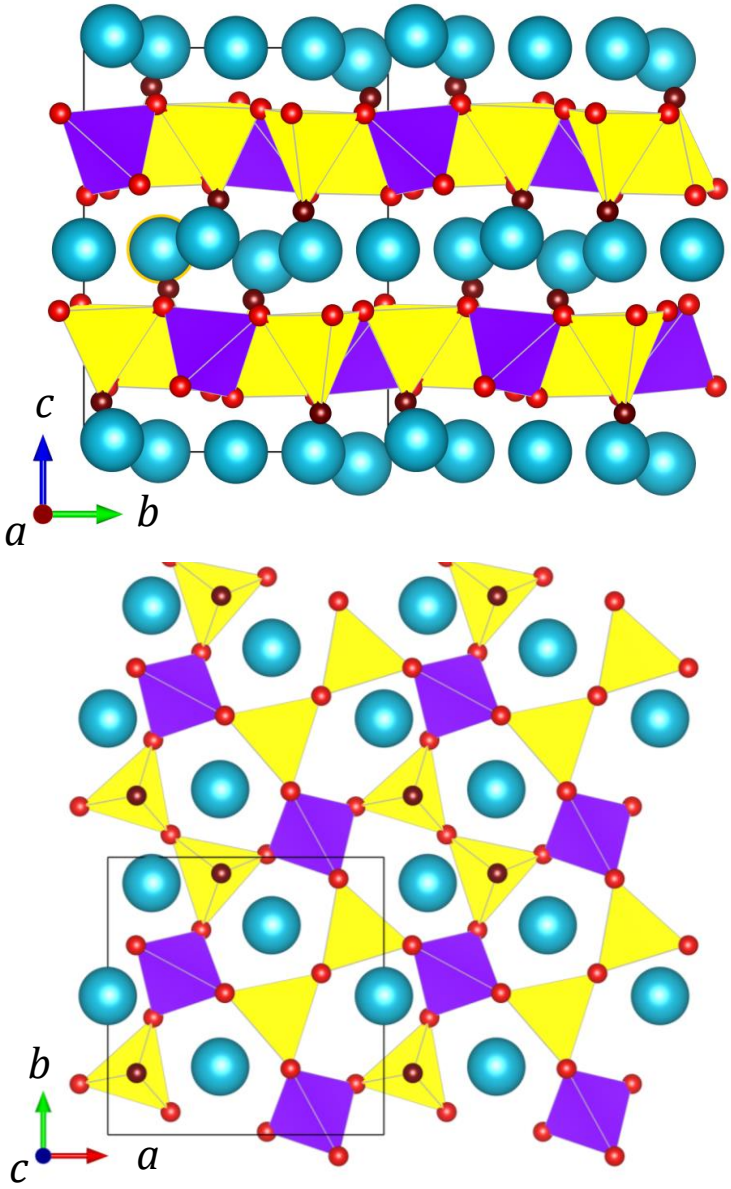

Figure 6-5 $Sr_5Ga_6O_{14}$. Top: view along the *a*-diretion. Bottom: view along the *c*-direction. For clarity, a single layer of tetrahedra is shown in order to avoid overlapping of different types of tetrahedral sites along the *c*-direction.

6.1.6 $Ba_4Si_6O_{16}$

In $Ba_4Si_6O_{16}$ the corner-sharing SiO_4 links to form zweier chains running along the *b*-direction. Three zweier chains are linked through every second tetrahedra giving rise to 6-membered rings with potential to accommodate interstitials[291] (see view along-*c* Figure 6-6 bottom). These triple chains running along *b* have a 2_1 symmetry (top figure) and intercalate with 8-coordinated Ba^{2+} providing a ~8.4 Å separation.

The co-doping of this phylosilicate with RE elements (*e. g.* Eu^{2+}, Dy^{3+}, Ce^{3+}, Tm^{3+}, Pr^{3+}) by the traditional solid-state reaction method has been investigated due to the exhibited long-lasting phosphorescence properties[292-295]. The fact that the Ba^{2+} can be partly substituted by RE elements with a higher valence and that this can be done by an easy solid-state reaction route, makes $Ba_4Si_6O_{16}$ an attractive candidate for exploratory doping investigations.

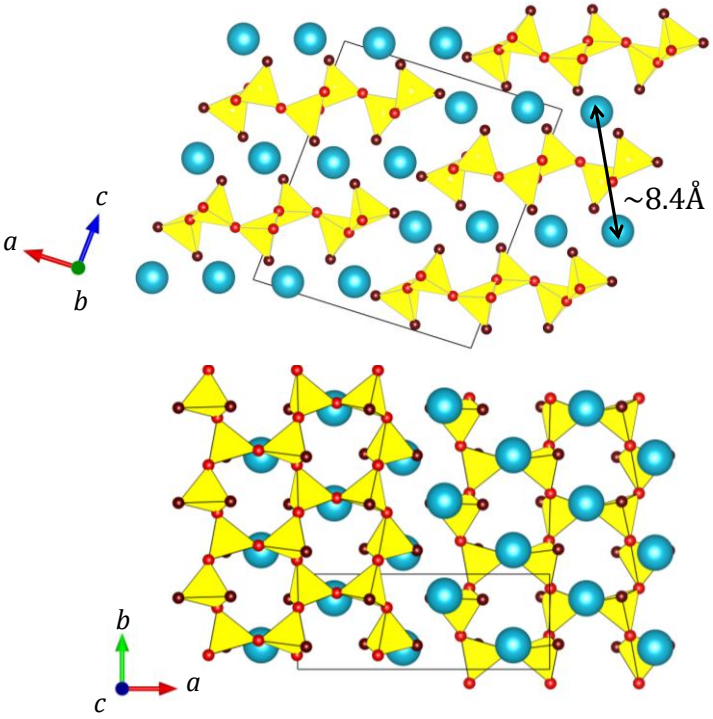

Figure 6-6 $Ba_4Si_6O_{16}$ based on interconnected tetrahedra (in yellow) occupied by Si containing one or two non-bridging oxygen denoted in maroon and intercalated with Ba in (in cyan).

6.1.7 $LaSrNa_3ZnSi_6O_7$ (Nordite)

The structure of nordite is often described as a combination of melilite and datolite[296] structure types due to their resemblance. Nordites consist of compact layers of large A cations connected by an infinite net of T_7O_{17} tetrahedra forming 4-, 5- and 8-membered rings along the *b*-direction (Figure 6-7, bottom)[297]. Si fully occupies 3-connected tetrahedral sites namely Si1-Si3, whereas Zn is found in the 4-connected sites. The layers of 3-connected tetrahedral sites alternate with fully connected tetrahedra and La along the *b*-directions (bottom figure).

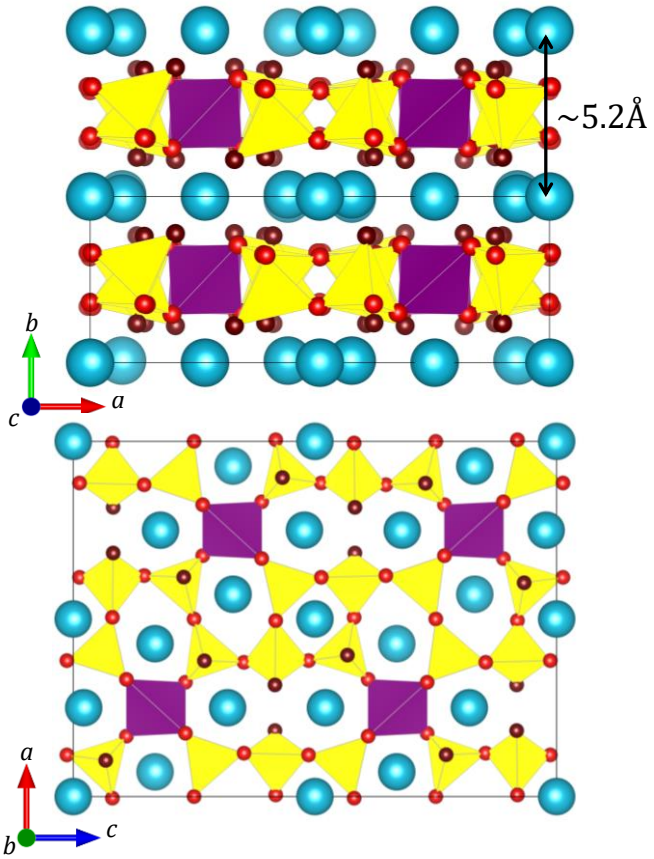

Figure 6-7 Nordite $LaSrNa_3ZnSi_6O_{17}$ structure viewed along *c* (top) and *b* -axes (bottom).

Although some analogues of this structure have been reported (*e. g*. ferronordite - CeSr $Na_3FeSi_6O_{17}$, manganonordite – $Na_3SrCeMnSi_5O_{17}$[298]) this is not an extensive family of minerals and not many compositions of nordites are known, which may call into question its ability to accommodate cations with different valences. Moreover, it is usually difficult to dope materials containing a large number of atoms due to the increased number of competing phases during the synthesis process.

6.1.8 $Na_2Si_2O_5$

ε-$Na_2Si_2O_5$[299] is the high pressure polymorph of $Na_2Si_2O_5$ synthesized at 7 GPa. Its structure consists of 6-membered rings occupied by large Na cations alternating with 2D infinite Si_2O_5 layers along the *c*-axis (see Figure 6-8).

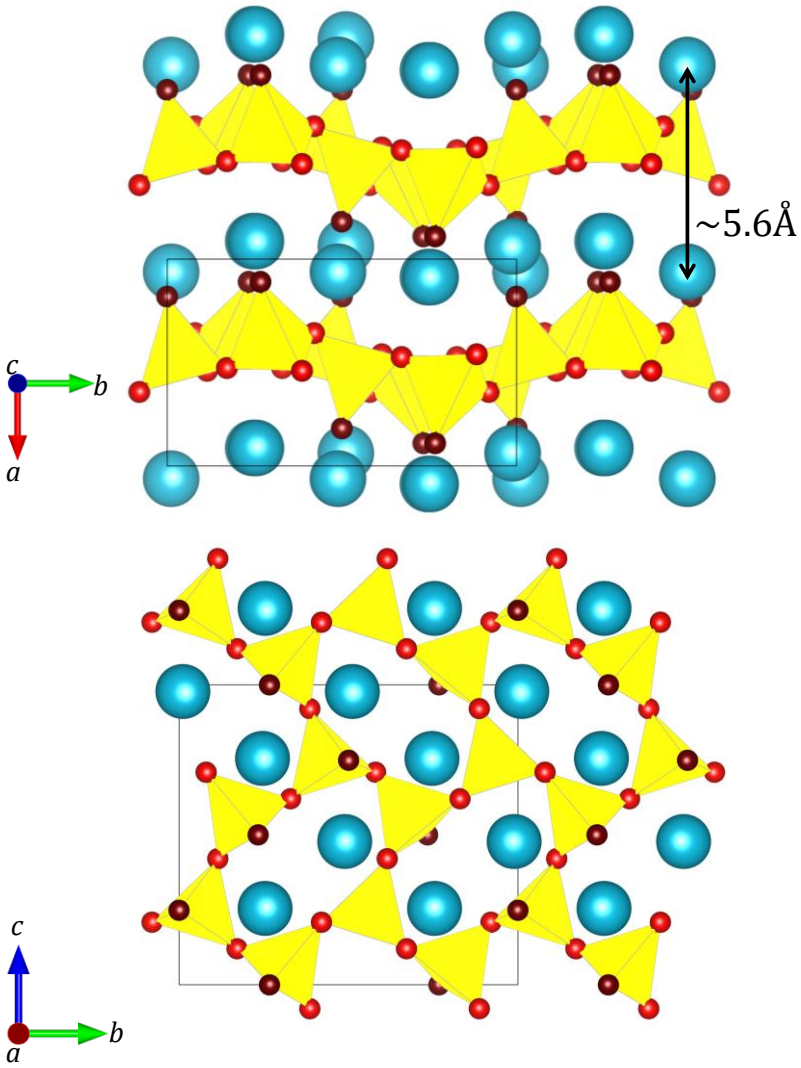

Figure 6-8 ε-$Na_2Si_2O_5$ structure viewed along *c* (top) and *a*-axes (bottom). Na cations are denoted in cyan and the chains of tetrahedra occupied by Si are given in yellow.

6.1.9 $Sr_2Ga_2O_5$

As well as $Sr_2Ga_2O_5$, $Sr_5Ga_6O_{14}$ is a high pressure phyllogallate which was first (and only) reported in ref. 290. Up until now, there are no applications known for this material with the exception of the use of its non-crystalline form as an additive for the densification of ionic conducting materials[300-302].

The crystal structure of $Sr_2Ga_2O_5$ consists of large 6 and 7-coordianted Sr atoms that provide a separation of ~5.3 Å between the infinite layers of GaO_4 tetrahedra. The view of a $Sr_2Ga_2O_5$'s single layer along the *c*-axis reveals the presence of two types of channels running parallel to this direction: a 4 and an 8-membered ring, where the latter has the shape of an elongated ellipsoid.

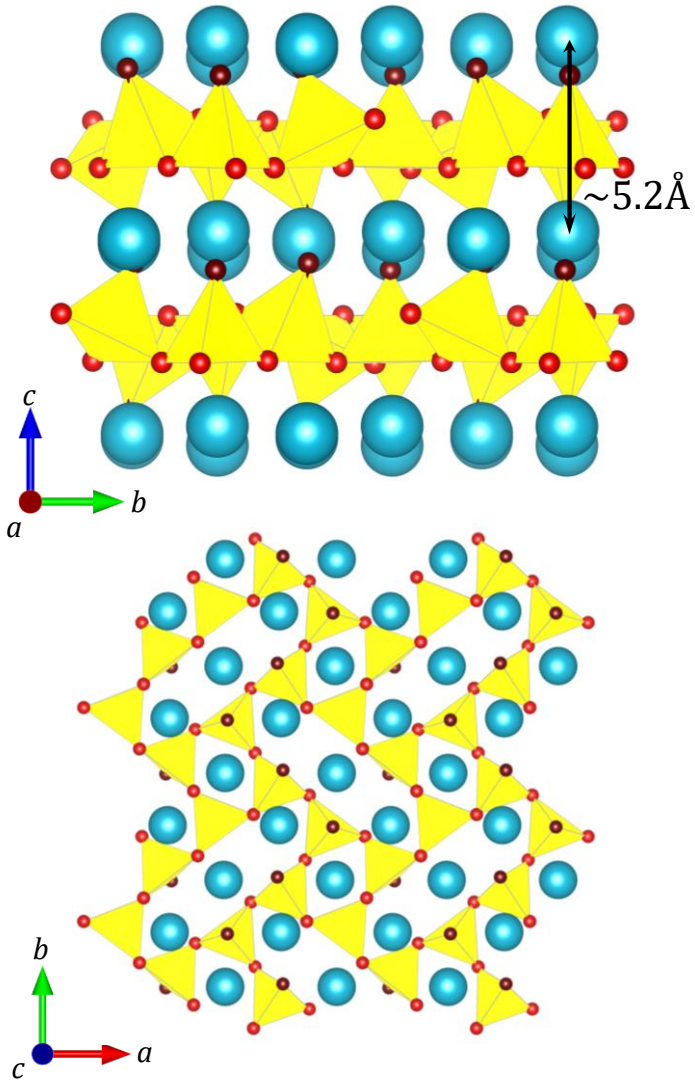

Figure 6-9 View of the layered structure of $Sr_2Ga_2O_5$ along the *a* (top) and *c*-axes (bottom). The large Sr cations are coloured in cyan and the extended chains of 3-connected tetrahedra are given in yellow.

7 APPENDICES

APPENDIX 1 LIST OF REPORTED MATERIALS WITH A LANGASITE STRUCTURE

Ga - Langasites										
A_3 Thomson Cube 3e			**B Octahedron 1a**				**C_3 Tetrahedron 3f**		**D_2 Tetrahedron 2d**	
A^+	**A^{2+}**	**A^{3+}**	**B^{3+}**	**B^{4+}**	**B^{5+}**	**B^{6+}**	**C^{3+}**	**C^{4+}**	**D^{3+}**	**D^{4+}**
1.1. $Na_2 A^{2+}Ge_6O_{14}$ (A = Ca, Sr)										
Na	Ca, Sr			Ge				Ge		Ge
1.2. $NaA^{2+}{}_2GaGe_5O_{14}$ (A = Ca, Sr, Pb)										
Na	Ca, Sr, Pb		Ga,	Ge			Ga	Ge		Ge
1.3. $A^{2+}{}_3Ga_2Ge_4O_{14}$ (A = Ca, Sr, Ba, Pb)										
	Ca, Ba		Ge				Ga	Ge		Ge
	Sr, Pb		Ga,	Ge			Ga	Ge		Ge
1.4. $A^{2+}{}_3X^{5+}Ga_3Z^{+}{}_2O_{14}$ (A=Ca, Sr, Ba, Pb, X=Sb, Nb, Ta, Z=Si, Ge)										
	Ca, Sr, Ba, Pb				Nb, Sb, Ta		Ga			Si
	Ca, Sr, Ba, Pb				Nb, Sb, Ta		Ga	Ge	Ga	Ge
1.5. $Ln_3Ga_5M^{4+}O_{14}$ (Ln = La, Pr, Nd; M = Si, Ge, Ti, Sn, Zr, Hf)										
La, Pr, Nd				Sn, Zr, Hf			Ga		Ga	
La, Pr, Nd			Ga				Ga		Ga	Si, Ge
La, Pr, Nd			Ga	Ti			Ga	Ti	Ga	
1.6. $Ln_3M^{5+}{}_{0.5}Ga_{5.5}O_{14}$ (Ln=La, Pr, Nd; M=Nb, Ta, Sb)										
		La, Pr, Nd	Ga+		Ta, Nb, Sb		Ga		Ga	
1.7. $La_3M^{6+}{}_{0.33}Ga_{5.67}O_{14}$ (Mo, W)										
		La	Ga			Mo, W	Ga		Ga	
1.8. $A^{2+}Ln_2SbGa_5O_{14}$ (A = Ba, Sr, Ln = La, Pr, Nd)										
	Ba, Sr	La, Pr, Nd			Sb		Ga		Ga	
Non-Ga containing Langasites										
A_3 Thomson Cube 3e			**B Octahedron 1a**			**C_3 Tetrahedron 3f**			**D_2 Tetrahedron 2d**	
A^+	**A^{2+}**	**A^{3+}**	**B^{3+}**	**B^{4+}**	**B^{5+}**	**C^{3+}**	**C^{4+}**		**D^{3+}**	**D^{4+}**
2.1 $NaA^{2+}{}_2M^{3+}Ge_5O_{14}$ (A = Ca, Sr, Pb, M = Al, Fe Sc, In)										
Na	Ca, Sr, Pb		Al, Fe Sc, In	Ge		Al, Fe Sc, In,	Ge			Ge
2.2. $A^{2+}{}_3B^{3+}{}_2Ge_4O_{14}$ (A = Ca, Sr, Ba, Pb, B = Al, Fe, Cr, In)										
	Ca, Ba		Ge			Ga	Ge			Ge
	Sr, Pb		Ga,	Ge		Ga	Ge			Ge
2.3. $Sr_3B^{2+}Ge_5O_{14}$ (B=Mg, Zn, Ni, Co, Fe, Mn)										
	Sr		Mg, Ni, Co, Fe, Mn				Ge			Ge
	Sr		Zn, Ge			Zn	Ge			Ge
2.4. $A^{2+}{}_3X^{5+}Y^{3+}{}_3Z^{+}{}_2O_{14}$ (A=Ca, Sr, Ba, Pb, X=Sb, Nb, Ta, Y= Al, Fe, In, Z=Si, Ge)										
	Ca, Sr, Ba, Pb				Nb, Sb, Ta	Al, Fe, In				Si
	Ca, Sr, Ba, Pb				Nb, Sb, Ta	Al, Fe, In	Ge		Al, Fe, In	Ge
2.5. $Ca_3Al_2Ti_{1.5}Si_{2.5}O_{14}$ – high pressure phase										
	Ca		Ti			Al	Ti, Si			Si
2.6. $La_3SbZn_3X^{4+}{}_2O_{14}$ (X=Si, Ge)										
		La			Sb		Zn			Si, Ge
2.7. $A^{2+}La_2SbAl_5O_{14}$ (A=Ca, Sr, Ba)										
	Ca, Sr, Ba	La			Sb		Al			Al

Ref: 152,241,303-311

APPENDIX 2 $La_3Ga_5MO_{14}$ WHERE M =Si AND Ti

Table 7-1 SXRD refined atomic positions and thermal parameters of $La_3Ga_5SiO_{14}$ and La_3GaTiO_{14} at 297K.

	$La_3Ga_5SiO_{14}$	$La_3Ga_5TiO_{14}$
La1 (3e),(x, 0, 0)		
x	0.41881(8)	0.4226(1)
occ	1	1
B_{eq} (Å^2)	0.41(2)	0.36(3)
Ga1 (1a), (0, 0, 0)		
occ	1	0.31(3)/occTi = 0.69(3)
B_{eq} (Å^2)	0.53(5)	0.3(1)
Ga2 (2d), (1/3,2/3,z)		
z	0.467(8)	0.5314(8)
occ	0.51(1)/occSi = 0.49(1)	1
B_{eq} (Å^2)	0.13(8)	0.21(6)
Ga3 (3f), (x, 0, 0.5)		
x	0.765(2)	0.7623(3)
occ	1	0.92(2)/occTi = 0.08(2)
B_{eq} (Å^2)	0.46(3)	0.37(6)
O1 (2d), (1/3,2/3,z)		
z	0.791(2)	0.187(3)
occ	1	1
B_{eq} (Å^2)	1.1(1)	0.8(1)
O2 (6g), (x, y, z)		
x	0.466(1)	0.459(2)
y	0.3113(9)	0.311(1)
z	0.678(1)	0.307(2)
occ	1	1
B_{eq} (Å^2)	1.1(1)	0.8(1)
O3 (6g), (x, y, z)		
x	0.221(1)	0.217(1)
y	0.0799(7)	0.074(1)
z	0.237(1)	0.762(2)
occ	1	1
B_{eq} (Å^2)	1.1(1)	0.8(1)

APPENDIX3 PAWLEY FITS

(a)

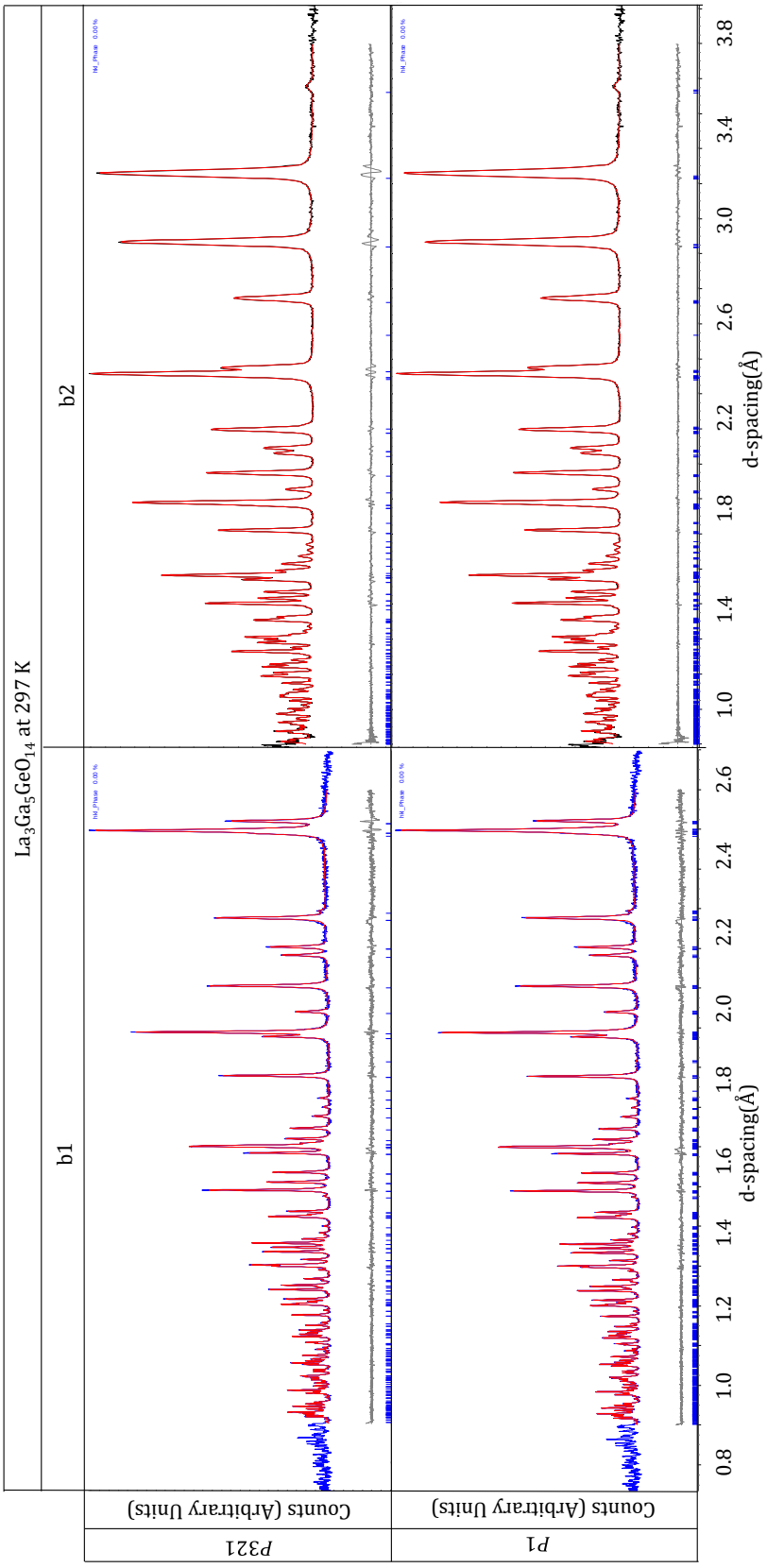

(*b*)

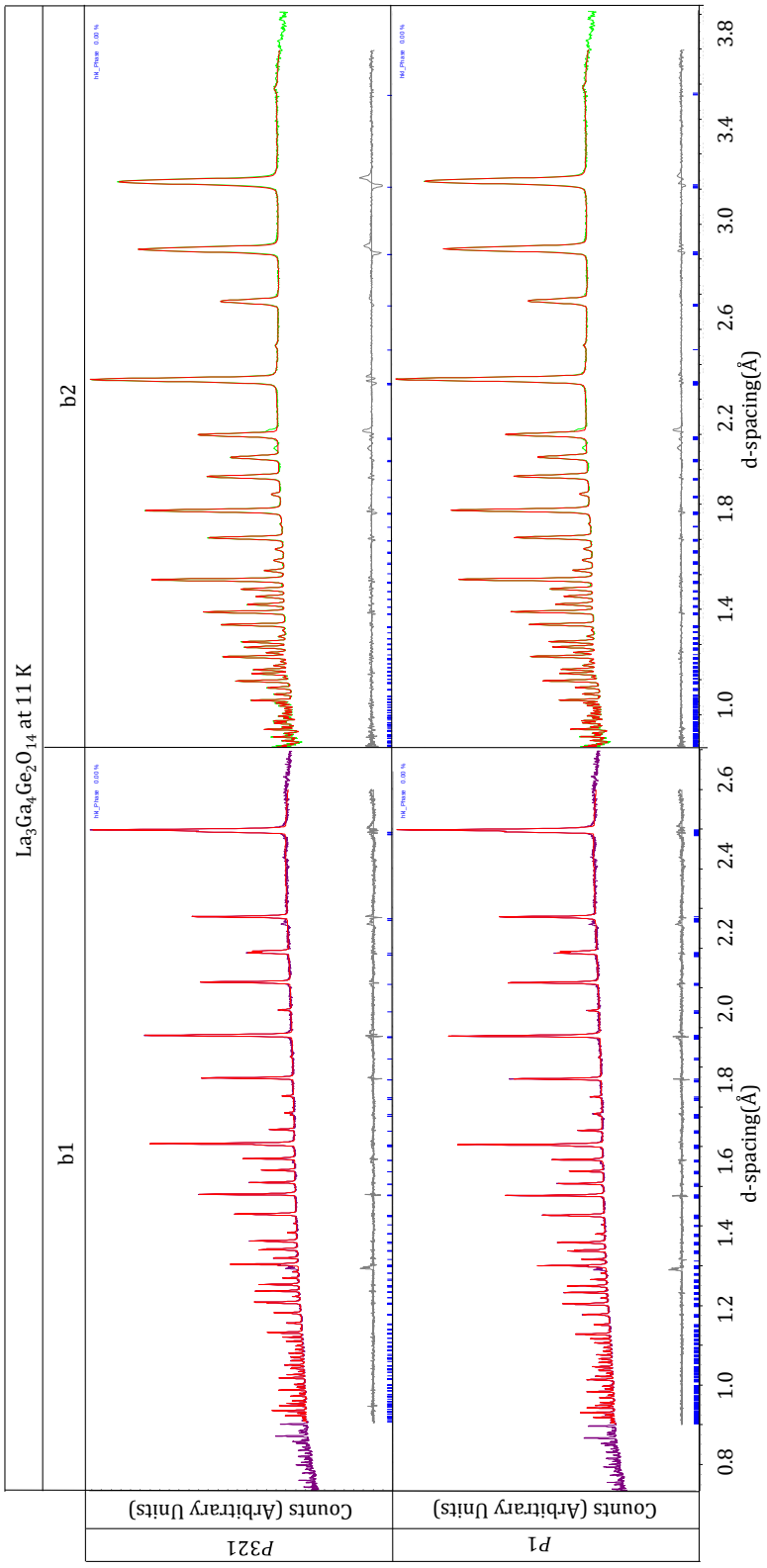
La3Ga4Ge2O14 at 11 K
b1
b2
P321
P1
Counts (Arbitrary Units)
d-spacing(Å)
0.8
1.0
1.2
1.4
1.6
1.8
2.0
2.2
2.4
2.6
3.0
3.4
3.8

(*c*)

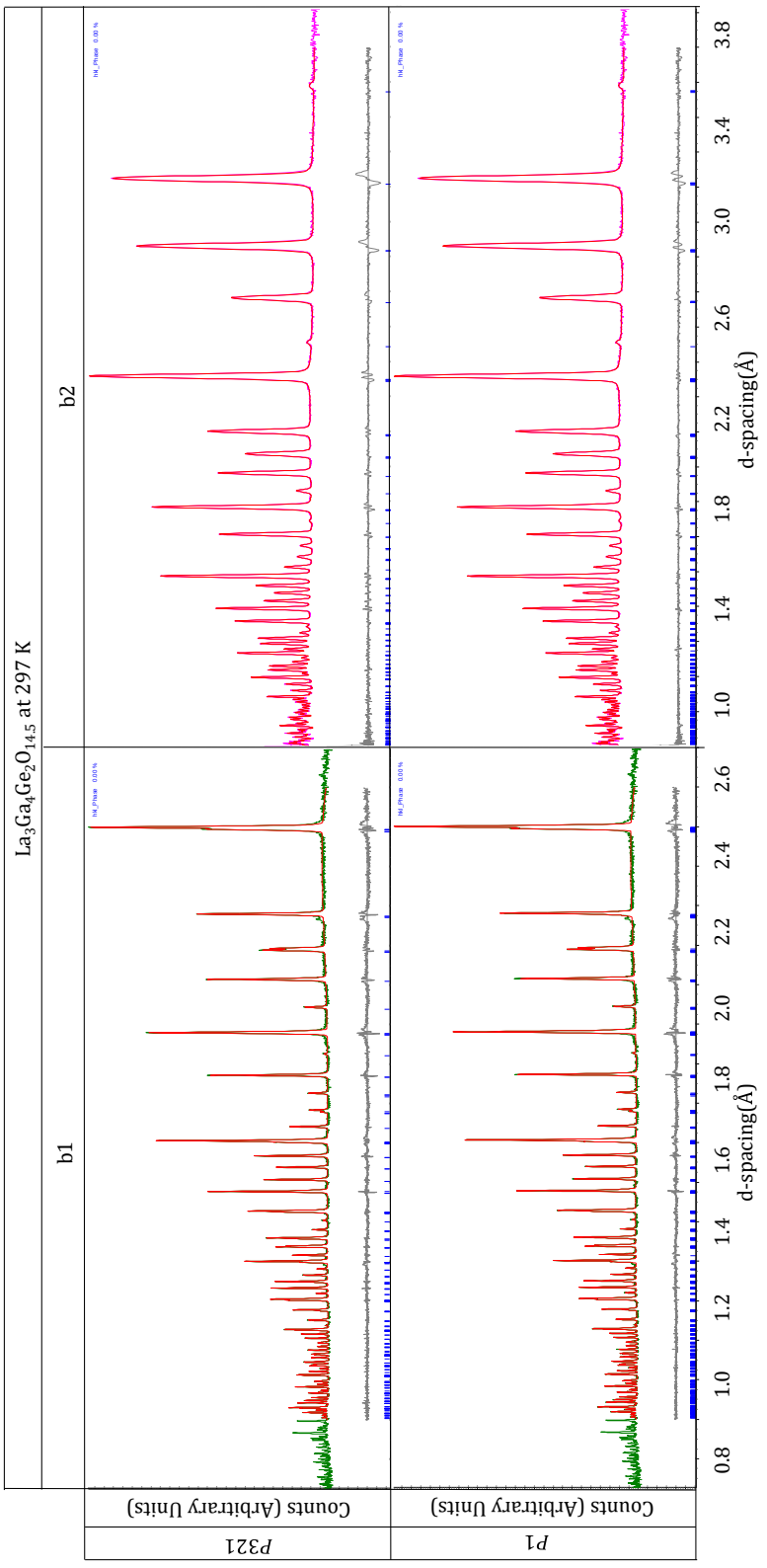
La3Ga4Ge2O14.5 at 297 K
b1
b2
P321
P1
Counts (Arbitrary Units)
d-spacing(Å)
0.8
1.0
1.2
1.4
1.6
1.8
2.0
2.2
2.4
2.6
3.0
3.4
3.8

(*d*)

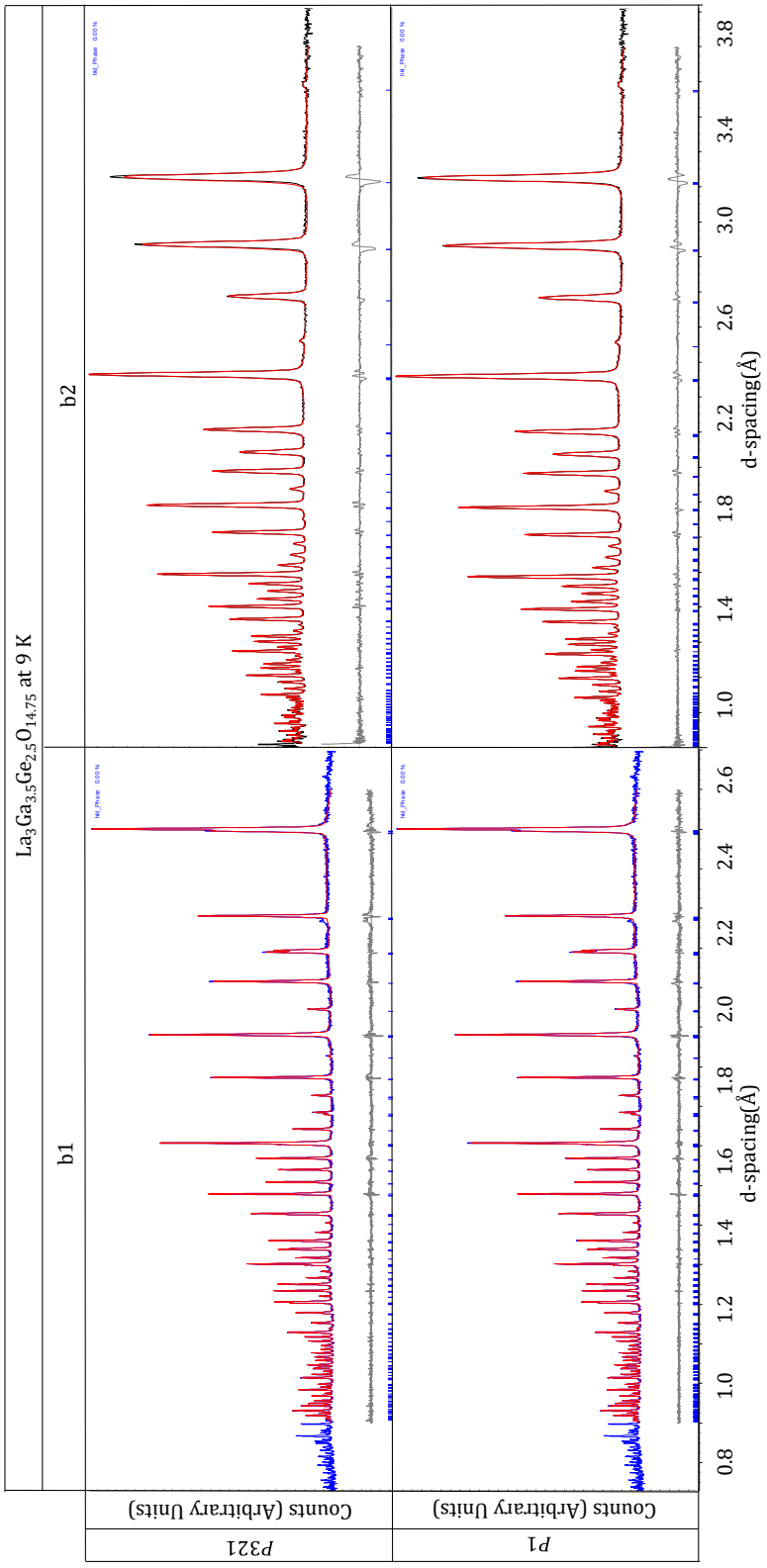
La3Ga3.5Ge2.5O14.75 at 9 K
b1
b2
P321
P1
Counts (Arbitrary Units)
d-spacing(Å)
0.8
1.0
1.2
1.4
1.6
1.8
2.0
2.2
2.4
2.6
3.0
3.4
3.8

(*e*)

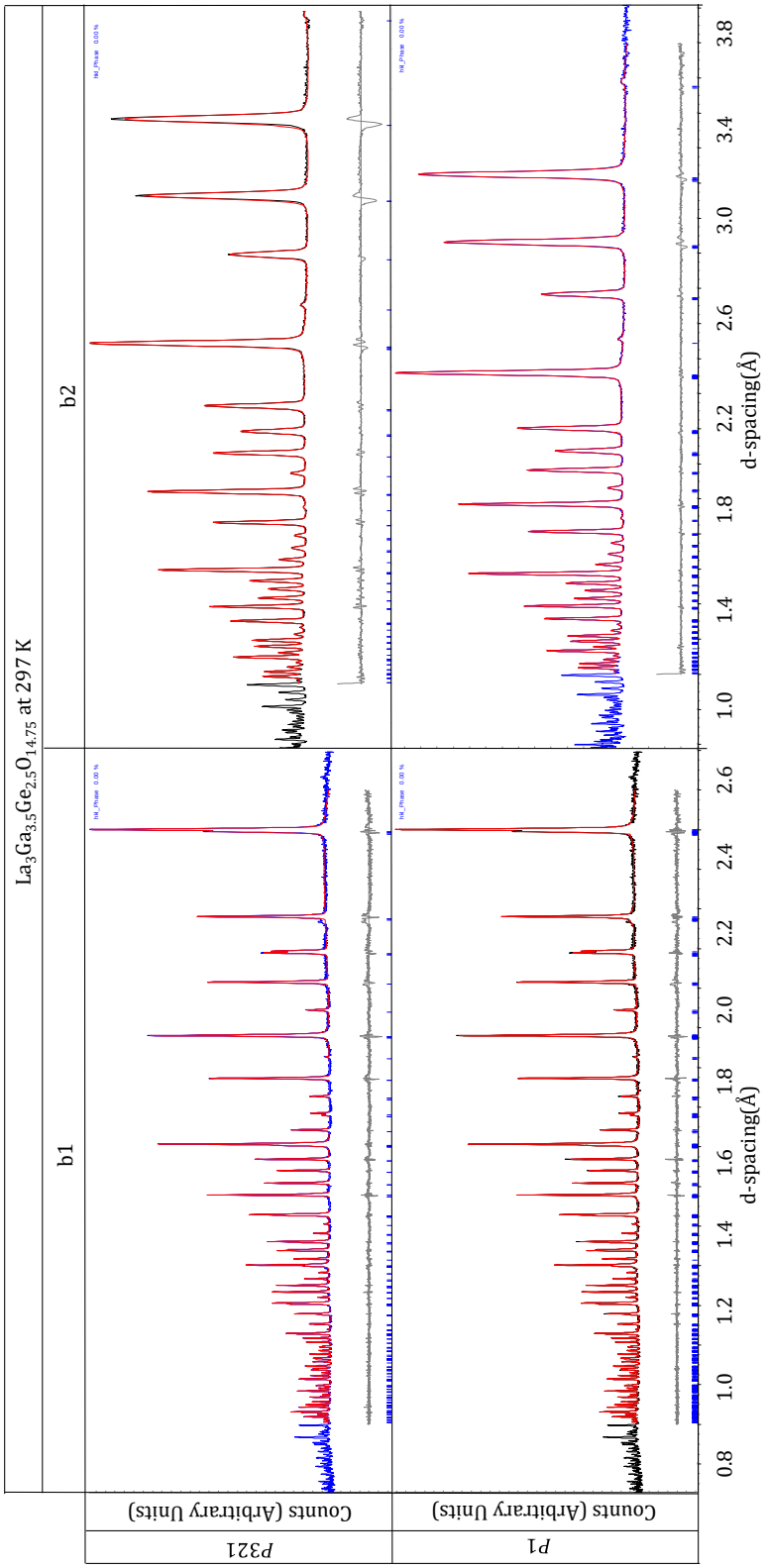
La3Ga3.5Ge2.5O14.75 at 297 K
b1
b2
P321
P1
Counts (Arbitrary Units)
d-spacing(Å)
0.8
1.0
1.2
1.4
1.6
1.8
2.0
2.2
2.4
2.6
3.0
3.4
3.8

(f)

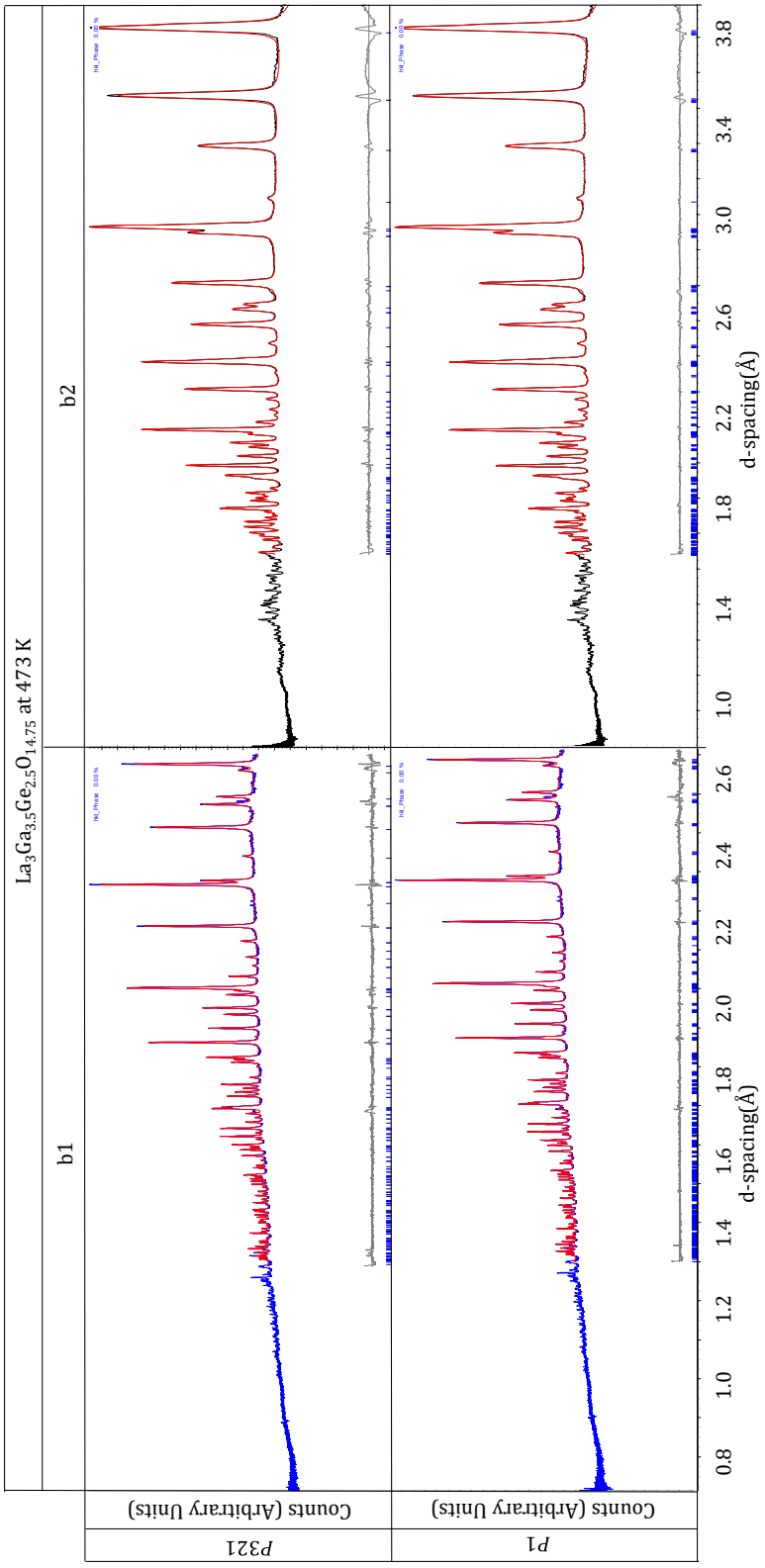
La3Ga3.5Ge2.5O14.75 at 473 K
b1
b2
P321
P1
Counts (Arbitrary Units)
d-spacing(Å)
0.8
1.0
1.2
1.4
1.6
1.8
2.0
2.2
2.4
2.6
3.0
3.4
3.8

(*g*)

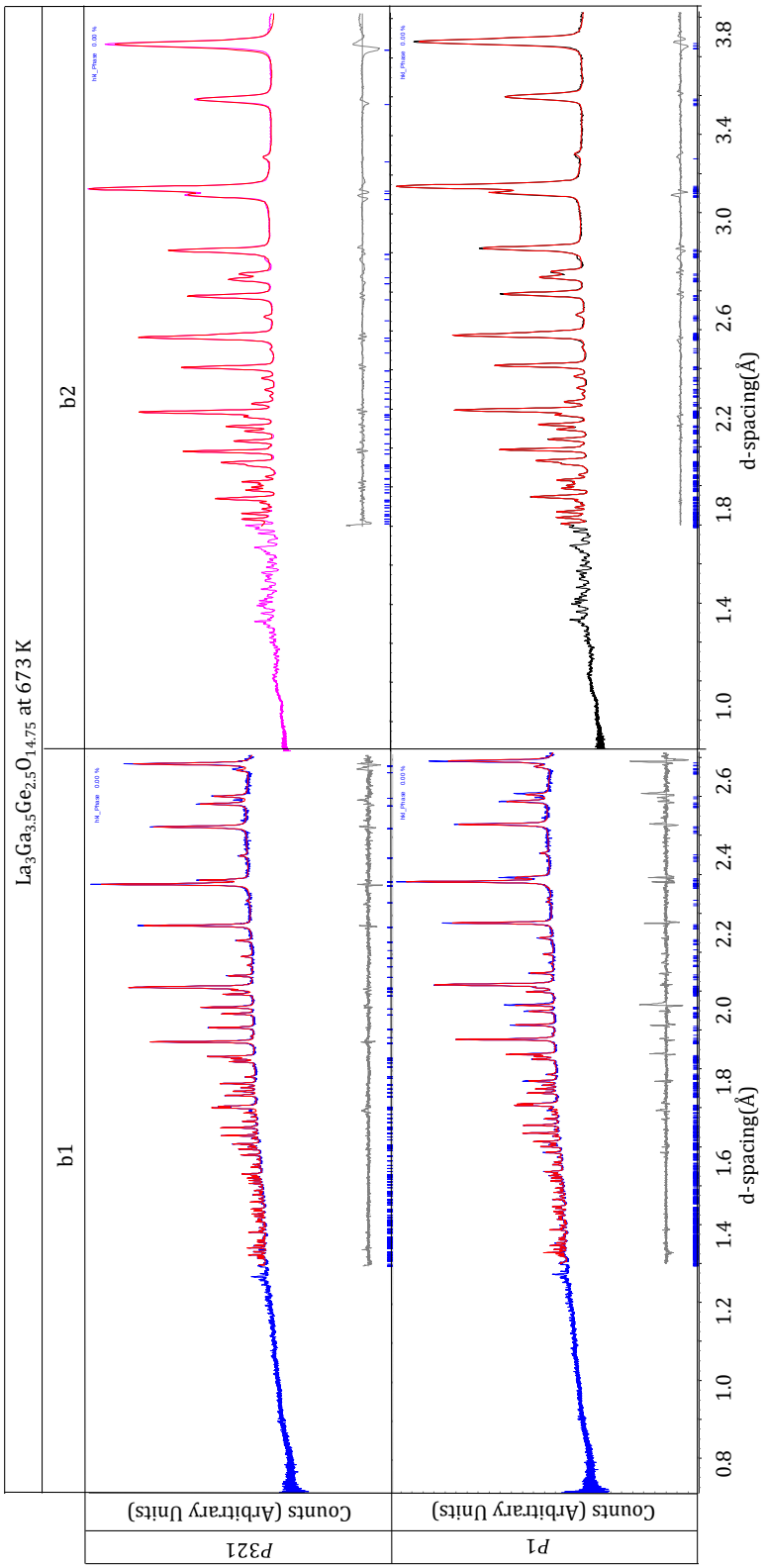
La3Ga3.5Ge2.5O14.75 at 673 K
b1
b2
P1
P321
Counts (Arbitrary Units)
d-spacing(Å)
0.8
1.0
1.2
1.4
1.6
1.8
2.0
2.2
2.4
2.6
3.0
3.4
3.8

(*h*)

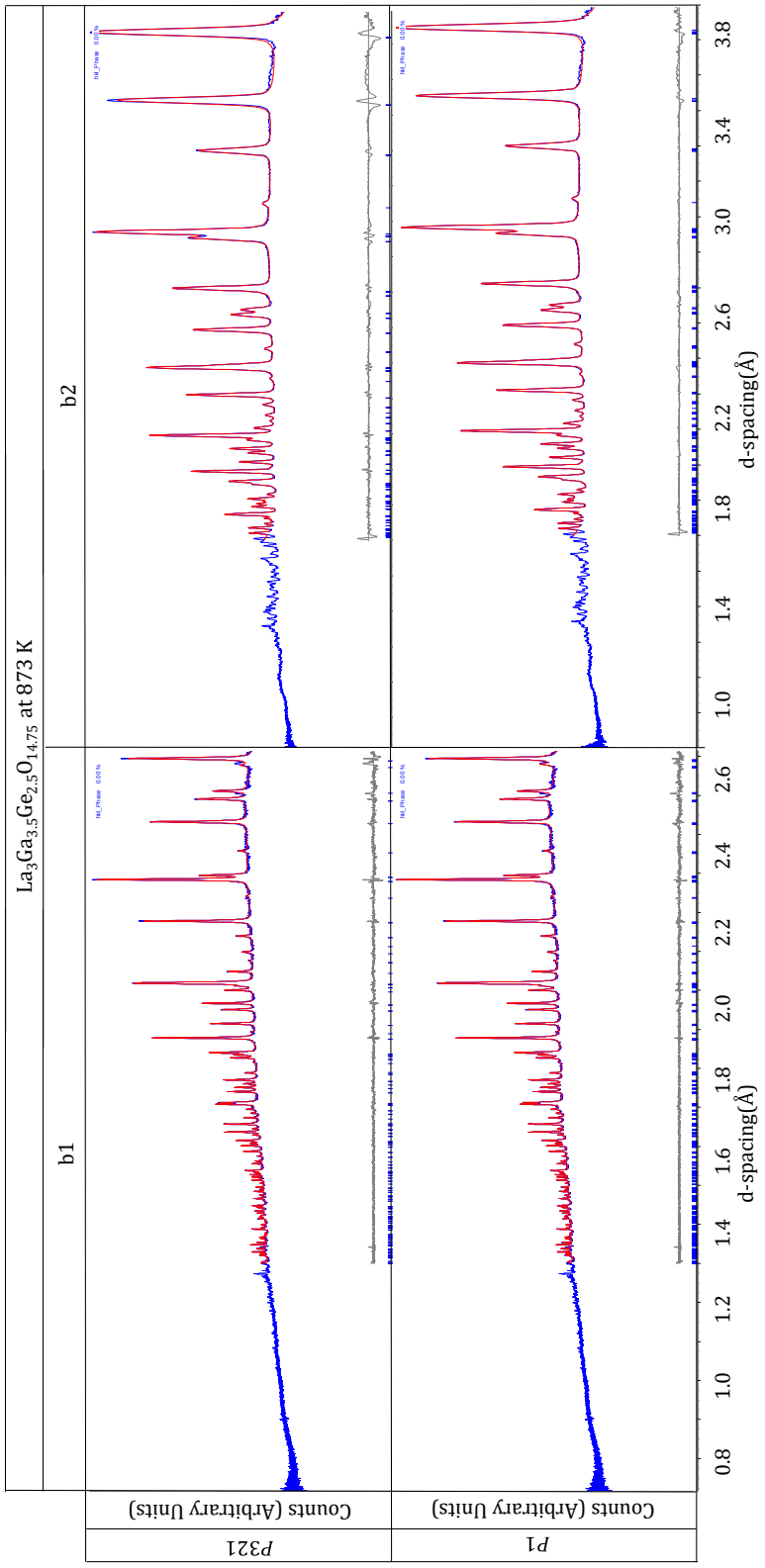
La3Ga3.5Ge2.5O14.75 at 873 K
b1
b2
P321
P1
Counts (Arbitrary Units)
Counts (Arbitrary Units)
d-spacing(Å)
d-spacing(Å)
0.8
1.0
1.2
1.4
1.6
1.8
2.0
2.2
2.4
2.6
1.0
1.4
1.8
2.2
2.6
3.0
3.4
3.8

(i)

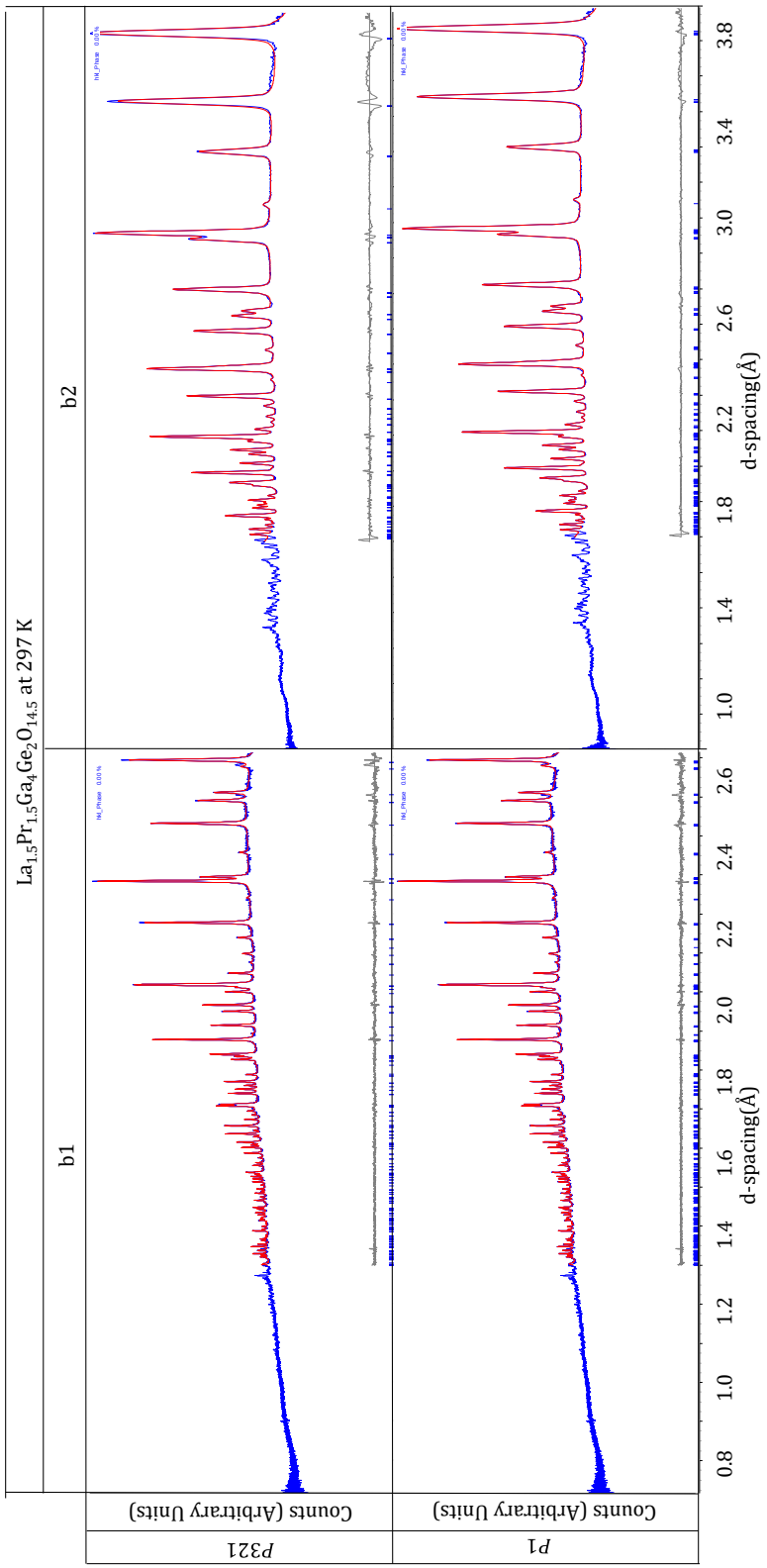
La1.5Pr1.5Ga4Ge2O14.5 at 297 K
b1
b2
P1
P3̄21
Counts (Arbitrary Units)
d-spacing(Å)
0.8
1.0
1.2
1.4
1.6
1.8
2.0
2.2
2.4
2.6
3.0
3.4
3.8

(*j*)

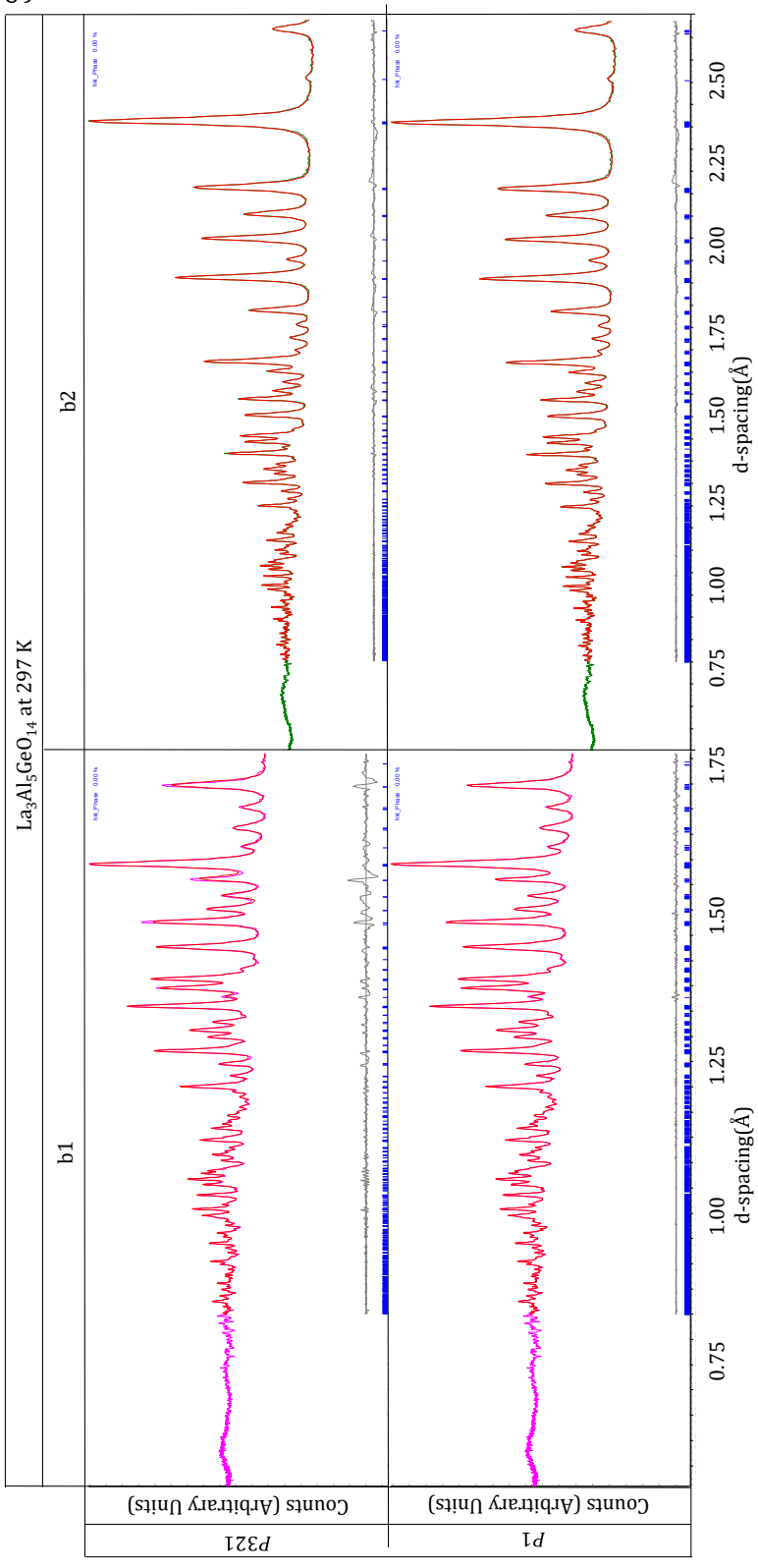
La3Al5GeO14 at 297 K
b1
b2
P321
P1
Counts (Arbitrary Units)
Counts (Arbitrary Units)
0.75
1.00
1.25
1.50
1.75
2.00
2.25
2.50
d-spacing(Å)
d-spacing(Å)

(k)

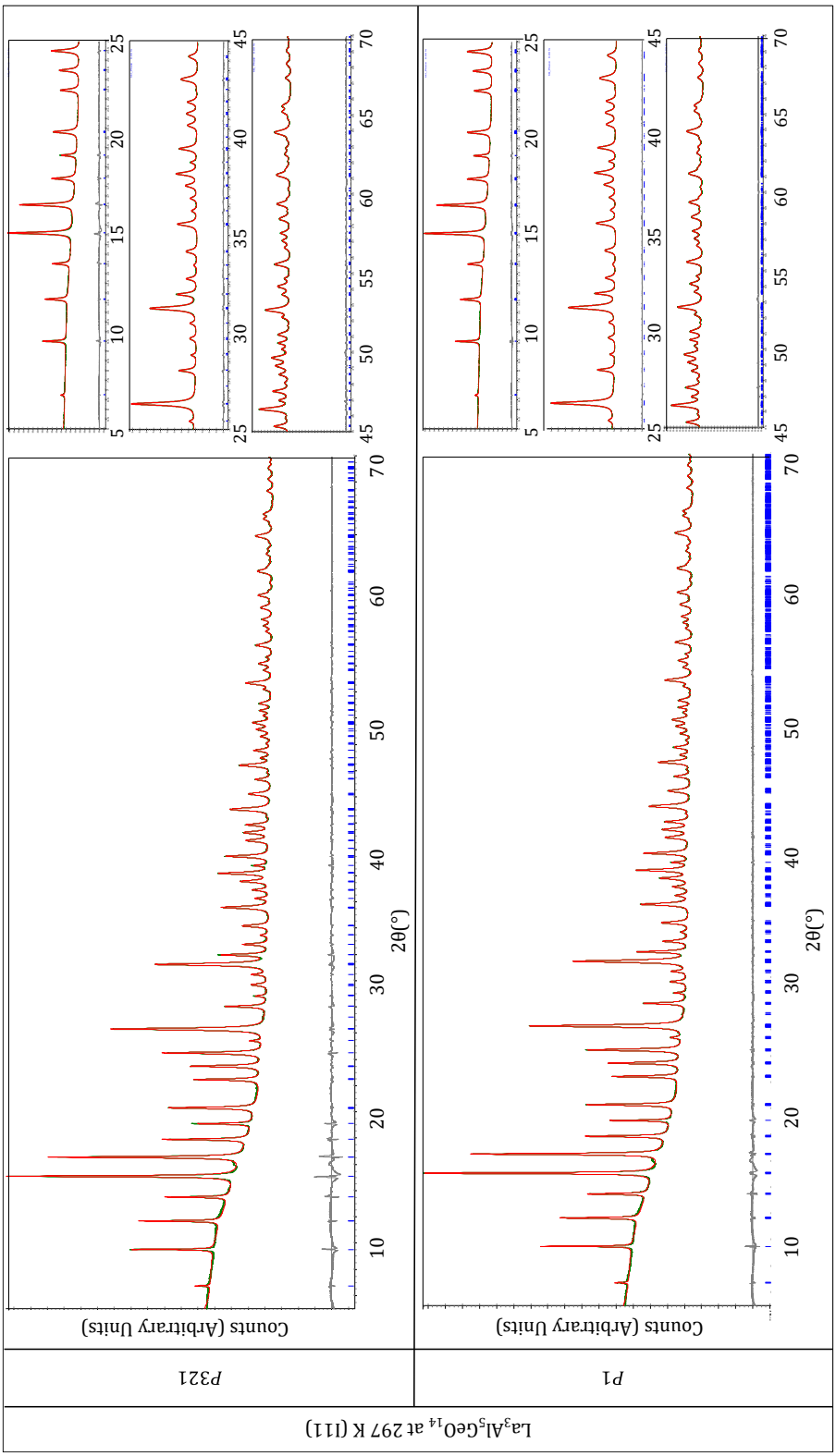

(*l*)

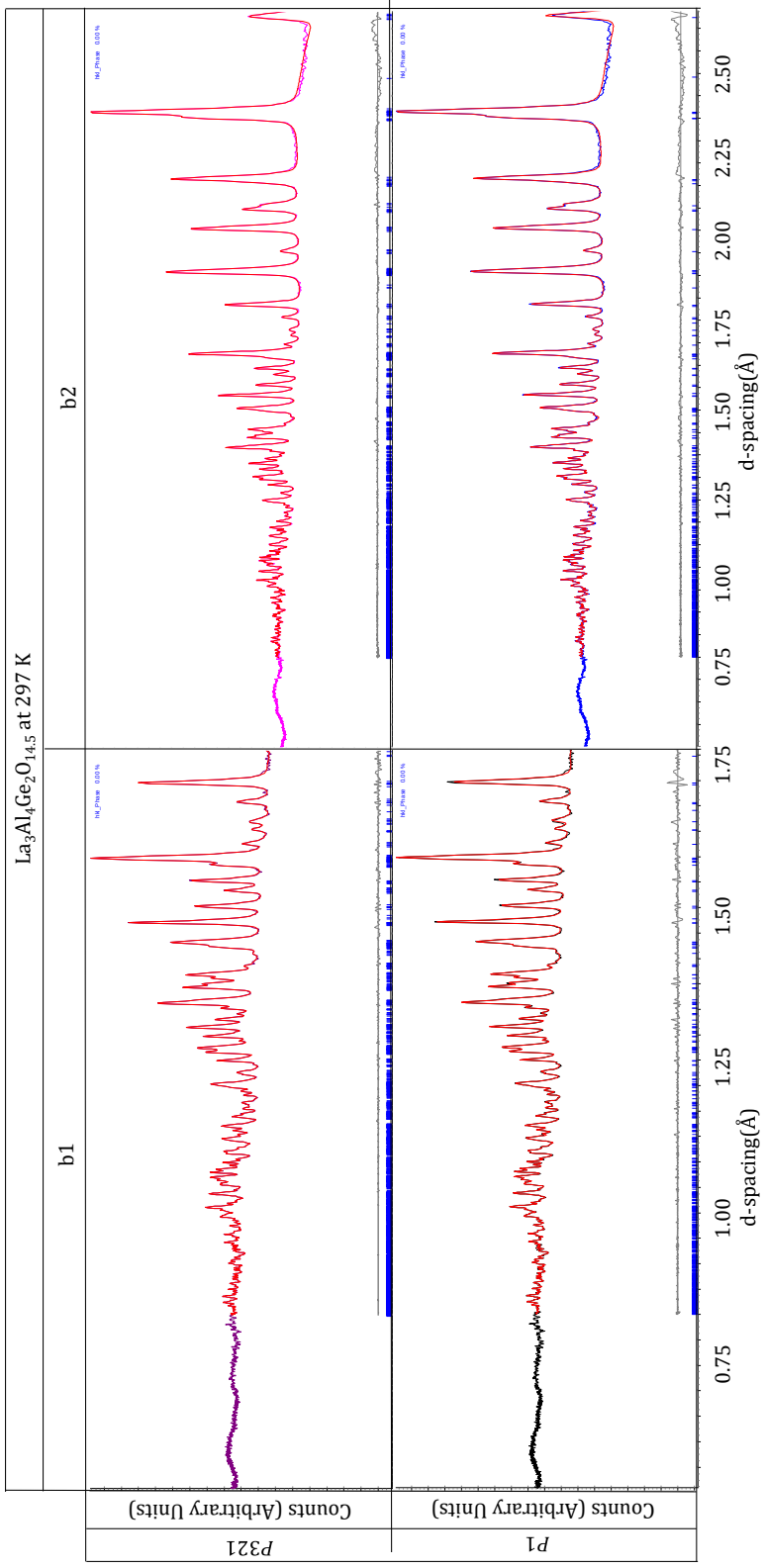
La3Al4Ge2O14.5 at 297 K
b1
b2
P321
P1
Counts (Arbitrary Units)
Counts (Arbitrary Units)
0.75
1.00
1.25
1.50
1.75
2.00
2.25
2.50
d-spacing(Å)
d-spacing(Å)

(m)

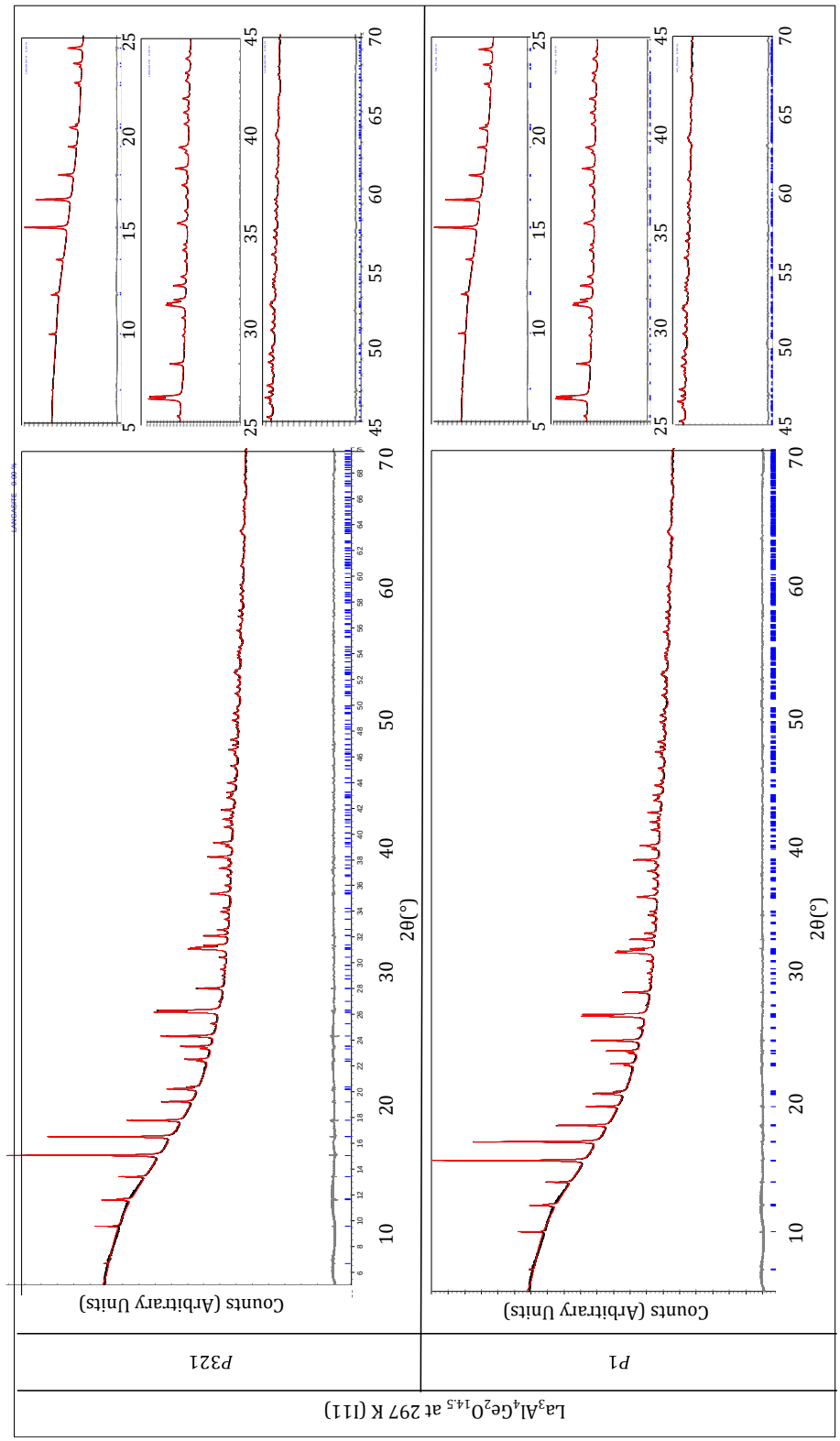
La3Al4Ge2O14.5 at 297 K (111)
P1
P321
Counts (Arbitrary Units)
2θ(°)

(n)

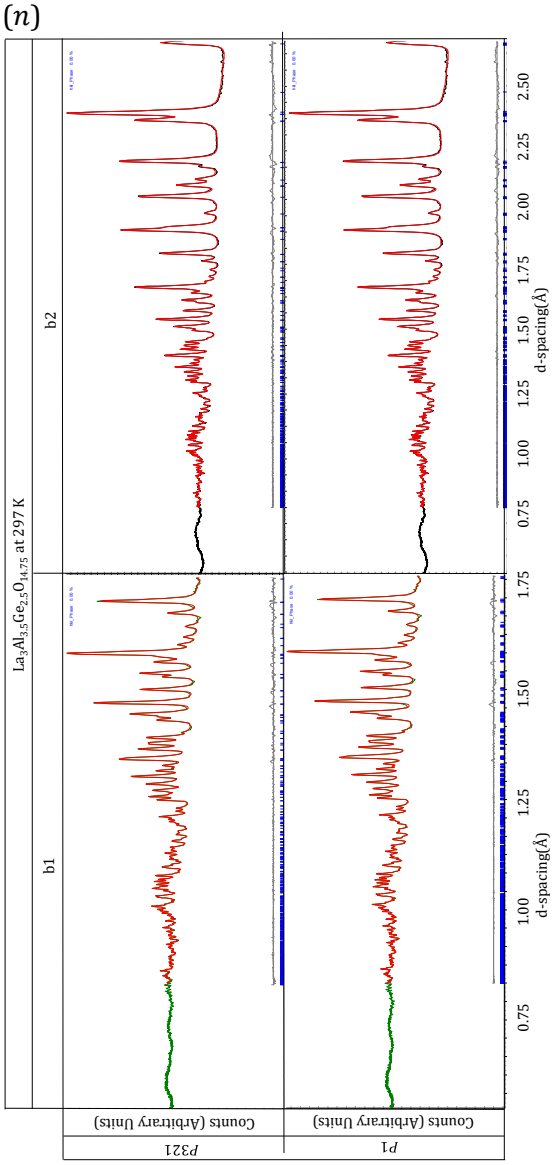
La3Al3.5Ge2.5O14.75 at 297 K
b2
b1
Counts (Arbitrary Units)
Counts (Arbitrary Units)
P1
P3̄21
d-spacing(Å)
d-spacing(Å)
0.75
1.00
1.25
1.50
1.75
2.00
2.25
2.50

(o)

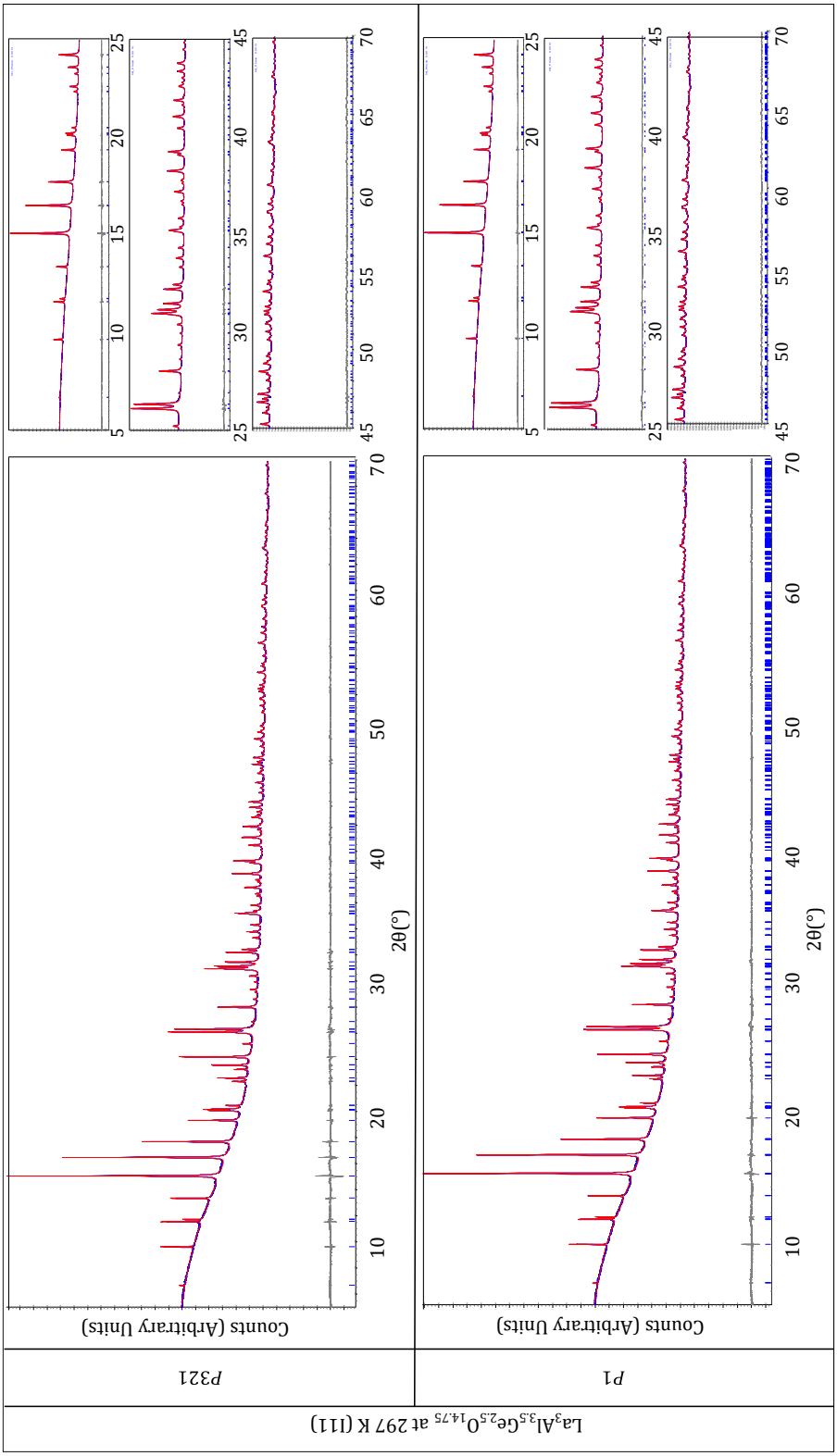

Figure 7-1 Pawley fits in *P*321 and *P*1 for (*a*) $La_3Ga_5GeO_{14}$ at 297 K, $La_3Ga_4GeO_{14}$ at 11 K (*b*) and at 297 K (*c*), $La_3Ga_{3.5}Ge_{2.5}O_{14.75}$ at 9 K (*d*), 297 K (*e*) 473 K (*f*), 673 K (*g*) and 873 K (*h*) $La_{1.5}Pr_{1.5}Ga_4Ge_2O_{14.5}$ at 297 K (*i*) $La_3Al_5GeO_{14}$ at 297 K (*j*) GEM and (*k*) I11 data, $La_3Al_4Ge_2O_{14}$ at 297 K (*l*) GEM and (*m*) I11 and $La_3Al_{3.5}Ge_{2.5}O_{14.75}$ at 297 K (*n*) GEM and (*o*) I11.

APPENDIX 4 NPD REFINED $La_3Ga_{3.5}Ge_{2.5}O_{14.75}$ FINAL MODELS

Table 7-2 Final NPD refined models for $La_3Ga_{3.5}Ge_{2.5}O_{14.75}$ from 9 to 873K, the given errors represent 1× e.s.d from the refinement output.

Parameter	$La_3Ga_{3.5}Ge_{2.5}O_{14.75}$				
Temperature (K)	9 K	297 K	473 K	673 K	873 K
a (Å)	8.27470(2)	8.28416(6)	8.29605(2)	8.31018(9)	8.32494(9)
c (Å)	4.99719(2)	5.00156(4)	5.00725(2)	5.01441(6)	5.02216(5)
V (Å^3)	296.320(2)	297.256(5)	298.450(2)	299.896(8)	301.428(7)
R_{wp}	1.763	2.447	1.558	1.695	1.435
R_{exp}	0.727	1.173	0.819	1.200	0.964
La1 (3e),(x, 0, 0)					
x	0.4149(1)	0.41515(9)	0.4148(1)	0.4148(1)	0.4151(1)
OCC	1	1	1	1	1
U_{11}	0.0126(3)	0.0185(3)	0.0240(4)	0.0296(5)	0.0343(5)
U_{22}	0.0104(4)	0.0164(3)	0.0195(4)	0.0243(5)	0.0278(5)
U_{33}	0.0156(4)	0.0209(3)	0.0229(4)	0.0264(5)	0.0301(5)
U_{12}	0.0052(2)	0.00819(2)	0.0097(2)	0.0122(3)	0.0139(3)
U_{13}	0	0	0	0	0
U_{23}	0	0	0	0	0
Ga1 (1a), (0, 0, 0)					
OCC	7/12	7/12	7/12	7/12	7/12
U_{11}	0.0115(4)	0.0164(4)	0.0192(5)	0.0232(6)	0.0255(6)
U_{22}	0.0115(4)	0.0164(4)	0.01923(5)	0.0232(6)	0.0255(6)
U_{33}	0.0027(3)	0.0073(5)	0.0089(7)	0.0125(9)	0.0176(9)
U_{12}	0.0058(2)	0.0082(2)	0.0096(2)	0.0116(3)	0.0127(3)
U_{13}	0	0	0	0	0
U_{23}	0	0	0	0	0
Ga2 (3f), (1/3,2/3,z)					
z	0.5274(2)	0.5268(2)	0.7572(1)	0.5268(3)	0.5266(3)
OCC	7/12	7/12	7/12	7/12	7/12
U_{11}	0.0072(3)	0.0130(3)	0.0275(5)	0.0205(4)	0.0238(4)
U_{22}	0.0072(3)	0.0130(3)	0.0238(6)	0.0205(4)	0.0238(4)
U_{33}	0.0100(3)	0.0126(5)	0.0125(9)	0.0214(7)	0.0236(7)
U_{12}	0.0036(1)	0.0065(1)	0.0138(2)	0.0103(2)	0.0119(2)
U_{13}	0	0	0	0	0
U_{23}	0	0	0	0	0
Ga3 (2d), (x, 0, 0.5)					
x	0.75727(5)	0.75712(9)	0.7572(1)	0.7576(1)	0.7577(1)
OCC	7/12	7/12	7/12	7/12	7/12
U_{11}	0.0184(4)	0.0245(4)	0.0276(5)	0.0318(6)	0.0367(6)
U_{22}	0.0132(5)	0.0204(4)	0.0238(6)	0.0269(7)	0.0298(7)
U_{33}	0.0096(5)	0.0151(4)	0.0188(5)	0.0219(7)	0.0231(6)
U_{12}	0.0066(3)	0.0102(2)	0.0119(3)	0.0135(4)	0.0149(4)
U_{13}	0	0	0	0	0

U_{23}	0	0	0	0	0
O1 (2d), (1/3,2/3,z)					
z	0.1733(3)	0.1740(2)	0.1742(3)	0.1748(3)	0.1754(3)
OCC	1	1	1	1	1
U_{11}	0.0178(5)	0.0244(4)	0.0300(5)	0.0357(8)	0.0442(9)
U_{22}	0.0177(5)	0.0244(4)	0.0300(5)	0.0357(8)	0.0442(9)
U_{33}	0.0049(7)	0.0115(7)	0.0125(9)	0.017(1)	0.016(1)
U_{12}	0.0089(2)	0.0122(2)	0.0150(3)	0.0178(4)	0.0221(4)
U_{13}	0	0	0	0	0
U_{23}	0	0	0	0	0
O2 (6g), (x, y, z)					
x	0.4638(5)	0.4623(8)	0.4628(7)	0.4632(8)	0.469(1)
y	0.3081(6)	0.3066(7)	0.3082(7)	0.3081(8)	0.314(1)
z	0.3114(4)	0.314(1)	0.315(1)	0.316(1)	0.320(1)
OCC	0.666(3)	0.570(3)	0.618(3)	0.624(3)	0.499(3)
U_{11}	0.004(1)	0.016(2)	0.014(2)	0.021(2)	0.023(3)
U_{22}	0.020(1)	0.034(2)	0.036(2)	0.039(2)	0.041(3)
U_{33}	0.013(1)	0.022(2)	0.027(2)	0.031(2)	0.045(3)
U_{12}	0.0059(1)	0.015(1)	0.013(1)	0.014(2)	0.014(2)
U_{13}	0	0.002(1)	-0.001(1)	-0.003(1)	-0.004(2)
U_{23}	0	0.017(1)	0.016(2)	0.017(2)	0.030(3)
O3 (6g), (x, y, z)					
x	0.2156(1)	0.2158(1)	0.2158(1)	0.2158(2)	0.2156(2)
y	0.0891(1)	0.0903(1)	0.0906(1)	0.0907(1)	0.0908(1)
z	0.7730(2)	0.7734(2)	0.7734(2)	0.7733(3)	0.7736(3)
OCC	1	1	1	1	1
U_{11}	0.0182(6)	0.0231(5)	0.0291(7)	0.0349(9)	0.0389(9)
U_{22}	0.0460(9)	0.0537(8)	0.060(1)	0.065(1)	0.068(1)
U_{33}	0.0162(6)	0.0226(6)	0.0227(7)	0.0257(9)	0.0296(9)
U_{12}	0.0150(7)	0.0185(6)	0.0231(8)	0.027(1)	0.028(1)
U_{13}	0.0069(5)	0.0068(4)	0.0085(5)	0.0099(7)	0.0105(7)
U_{23}	0.0172(5)	0.0177(5)	0.0187(6)	0.0204(7)	0.0215(7)
O4(6g), (x, y, z)					
x	0.297(1)	0.297(1)	0.292(2)	0.289(2)	0.281(2)
y	0.876(1)	0.875(2)	0.868(2)	0.868(3)	0.856(3)
z	0.589(1)	0.588(2)	0.586(2)	0.589(3)	0.590(3)
OCC	0.120(2)	0.110(3)	0.118(2)	0.114(2)	0.115(2)
B_{eq} (Å^2)	1.7(1)	2.7(2)	3.8(3)	4.7(4)	5.4(4)
O5(6g), (x, y, z)					
x	0.824(2)	0.832(1)	0.825(1)	0.821(2)	0.830(1)
y	0.565(2)	0.554(1)	0.560(2)	0.560(2)	0.558(1)
z	0.311(1)	0.312(2)	0.312(2)	0.312(3)	0.309(2)
OCC	0.247(4)	0.351(4)	0.294(2)	0.286(2)	0.410(2)
U_{11}	0.088(9)	0.085(5)	0.097(7)	0.097(9)	0.081(5)
U_{22}	0.008(3)	0.018(3)	0.024(4)	0.017(4)	0.015(3)
U_{33}	0.014(4)	0.022(3)	0.027(4)	0.036(6)	0.030(3)
U_{12}	0.025(4)	0.008(3)	0.021(4)	0.015(5)	0.007(3)

U_{13}	0	0.025(3)	-0.039(4)	-0.046(5)	-0.031(3)
U_{23}	0	0.004(2)	0.001(3)	-0.000(3)	0.002(2)
O6(6g), (x, y, z)					
x	0.0682(9)	0.0675(7)	0.0653(9)	0.064(1)	0.061(1)
y	0.537(1)	0.5348(9)	0.531(1)	0.530(2)	0.526(2)
z	0.551(1)	0.545(1)	0.541(2)	0.544(2)	0.540(2)
OCC	0.123(1)	0.121(2)	0.122(1)	0.123(1)	0.123(1)
B_{eq} (Å^2)	1.4(1)	2.3(1)	3.1(2)	3.6(2)	4.4(3)

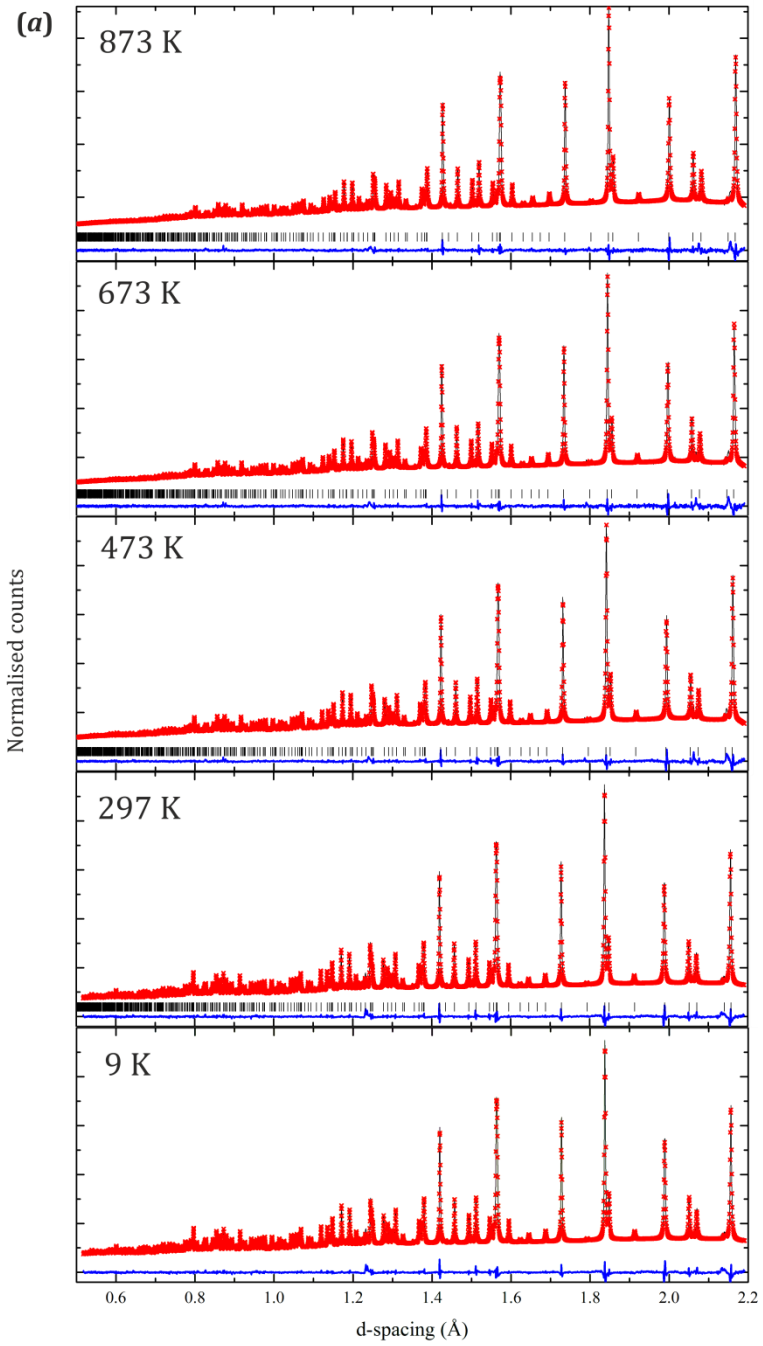

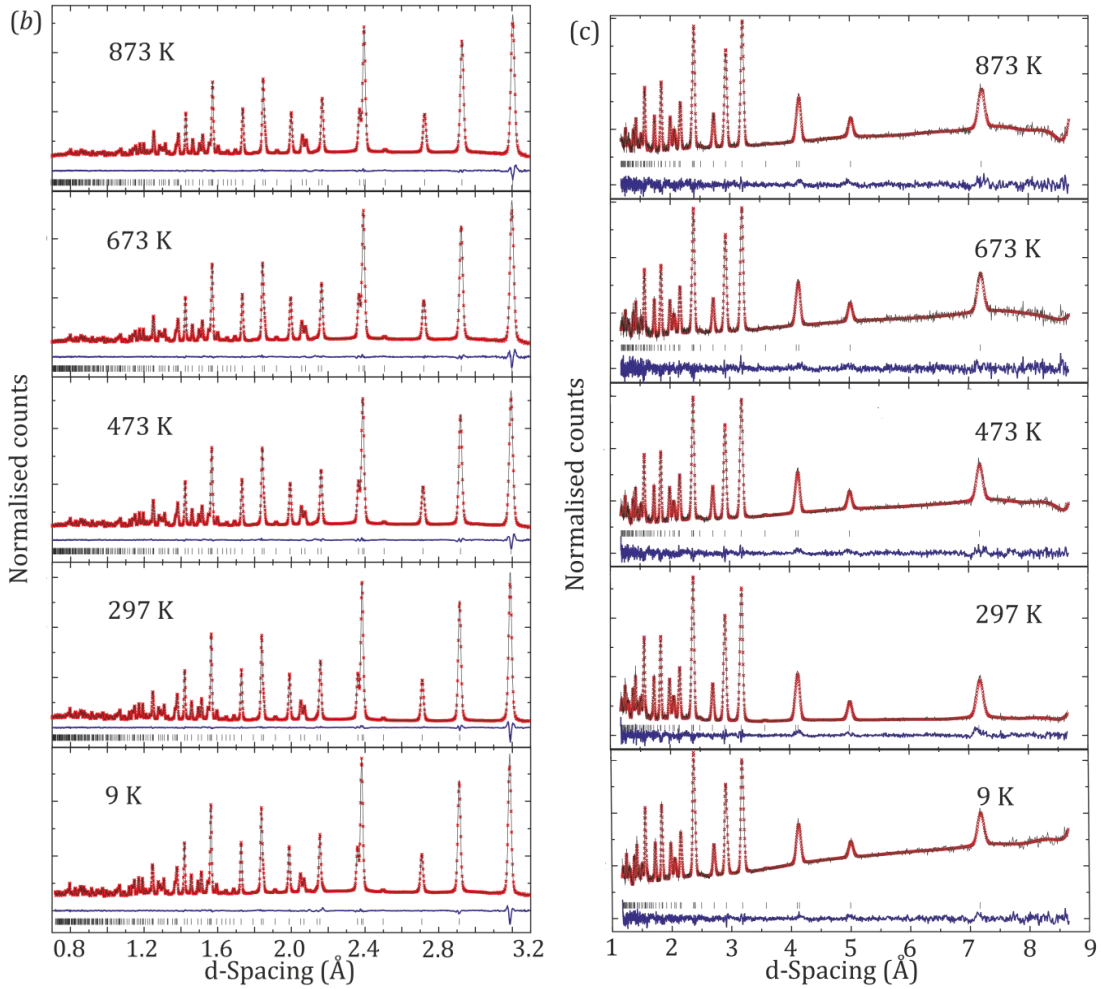

Figure 7-2 Fit of the combined b1(*a*), b2 (*b*) and b3 (*c*) refinement of $La_3Ga_{3.5}Ge_{2.5}O_{14.75}$ at 9-873K.

Table 7-3Final NPD refined model for the parent langasite $La_3Ga_5GeO_{14}$ (x=0) at 297K and $La_3Ga_4Ge_2O_{14.5}$ (x=1) at 11 and 297K.

Parameter	$La_3Ga_5GeO_{14}$	$La_3Ga_4Ge_2O_{14.5}$	
x	0	1	1
Temperature (K)	297	11	297
R_{wp}	2.667	1.992	2.809742
R_{exp}	1.789	1.002	1.847251
a (Å)	8.20885(2)	8.24442(5)	8.25387(4)
c (Å)	5.10535(2)	5.03419(4)	5.03841(3)
V (Å^3)	297.935(2)	296.333(4)	297.262(4)
La1 (3e),(x, 0, 0)			
x	0.41920(9)	0.4162(1)	0.4168(1)
OCC	1	1	1
U_{11}	0.01344(3)	0.0115(5)	0.0172(4)
U_{22}	0.01417(4)	0.0072(6)	0.0172(4)
U_{33}	0.01255(4)	0.01621(6)	0.0090(8)
U_{12}	0.0071(2)	0.0036(3)	0.0086(2)

U_{13}	0	0	0
U_{23}	0	0	0
Ga1 (1a), (0, 0, 0)			
OCC	1	2/3	2/3
U_{11}	0.01655(5)	0.0093(6)	0.0171(5)
U_{22}	0.01655(5)	0.0093(6)	0.0171(5)
U_{33}	0.0075(7)	0.006(1)1	0.0090(8)
U_{12}	0.0082(2)	0.0047(3)	0.0085(3)
U_{13}	0	0	0
U_{23}	0	0	0
Ga2 (2d), (1/3,2/3,z)			
z	0.5277(2)	0.5273(4)	0.5261(3)
OCC	1	02-Mar	02-Mar
U_{11}	0.01651(3)	0.0061(4)	0.0143(3)
U_{22}	0.01651(3)	0.0061(4)	0.0143(3)
U_{33}	0.01070(5)	0.0068(8)	0.0120(6)
U_{12}	0.00825(2)	0.0030(2)	0.0072(2)
U_{13}	0	0	0
U_{23}	0	0	0
Ga3 (3f), (x, 0, 0.5)			
x		0.7606(2)	0.7603(1)
OCC	0.5	2/3	2/3
U_{11}	0.0125(4)	0.0150(6)	0.0226(5)
U_{22}	0.0110(5)	0.0101(7)	0.0191(5)
U_{33}	0.0124(5)	0.0123(7)	0.018(6)
U_{12}	0.0055(3)	0.0051(3)	0.0096(3)
U_{13}	0	0	0
U_{23}	0	0	0
O1 (2d), (1/3,2/3,z)			
z	0.1787(3)	0.1763(4)	0.1778(3)
OCC	0.998(6)	1	1
U_{11}	0.0185(6)	0.0061(4)	0.0230(6)
U_{22}	0.0185(6)	0.0061(4)	0.0229(6)
U_{33}	0.0131(1)	0.0068(8)	0.020(1)
U_{12}	0.0092(3)	0.0030(2)	0.0115(3)
U_{13}	0	0	0
U_{23}	0	0	0
O2 (6g), (x, y, z)			
x	0.4584(1)	0.4610(4)	0.4636(2)
y	0.3098(1)	0.3100(3)	0.3131(2)
z	0.3112(2)	0.3119(8)	0.3132(5)
OCC	0.982(3)	0.660(4)	0.646(2)

U_{11}	0.0148(5)	0.007(1)	0.0093(8)
U_{22}	0.0247(7)	0.015(1)	0.017(1)
U_{33}	0.0153(5)	0.008(1)	0.0094(7)
U_{12}	0.0086(5)	0.005(1)	0.0050(8)
U_{13}	0.0038(5)	-0.004(1)	0.0063(9)
U_{23}	0.0084(5)	0.0014(9)	0.0113(8)
O3 (6g), (x, y, z)			
x	0.2204(1)	0.2174(2)	0.2168(1)
y	0.08018(9)	0.0855(2)	0.0861(1)
z	0.7642(2)	0.7691(3)	0.7682(2)
OCC	1.001(3)	1	1
U_{11}	0.0198(6)	0.0188(9)	0.0229(6)
U_{22}	0.0241(7)	0.037(1)	0.0476(9)
U_{33}	0.0187(6)	0.020(1)	0.0261(7)
U_{12}	0.0124(5)	0.0149(9)	0.0187(7)
U_{13}	0.0035(4)	0.0079(7)	0.0060(5)
U_{23}	0.0103(4)	0.0156(7)	0.0151(6)
O4(6g), (x, y, z)			
x		0.062(2)	0.063(1)
y		0.536(2)	0.546(2)
z		0.559(2)	0.561(2)
OCC		0.083(1)	0.085(1)
B_{eq} (Å^2)		0.9(2)	2.6(2)
O5(6g), (x, y, z)			
x		0.831(2)	0.833(1)
y		0.559(1)	0.5690(8)
z		0.307(2)	0.312(1)
OCC		0.261(4)	0.262(2)
U_{11}		0.077(6)	0.061(3)
U_{22}		0.029(4)	0.026(2)
U_{33}		0.008(4)	0.02(3)
U_{12}		0.023(5)	0.013(4)
U_{13}		-0.026(4)	0
U_{23}		-0.011(3)	0
O6(6g), (X, Y, Z)			
x		0.297(3)	0.290(3)
y		0.864(3)	0.856(2)
z		0.594(4)	0.597(4)
OCC		0.089(2)	0.084(2)
B_{eq} (Å^2)		2.5(3)	4.7(4)

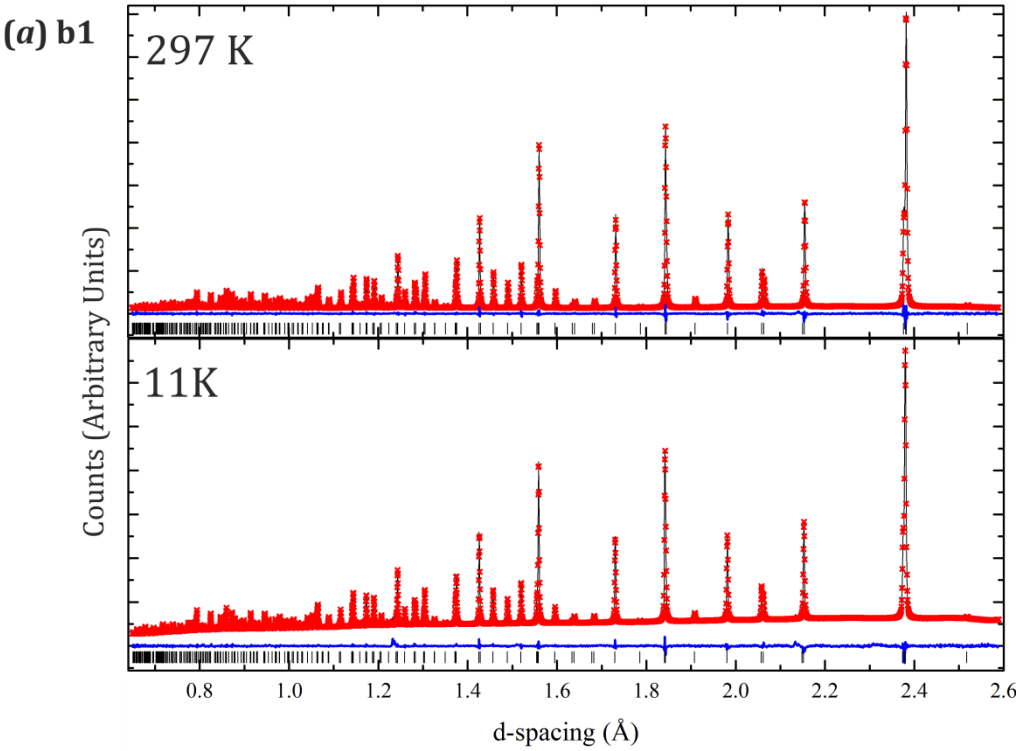
(a) b1
297 K
11K
Counts (Arbitrary Units)
0.8
1.0
1.2
1.4
1.6
1.8
2.0
2.2
2.4
2.6
d-spacing (Å)

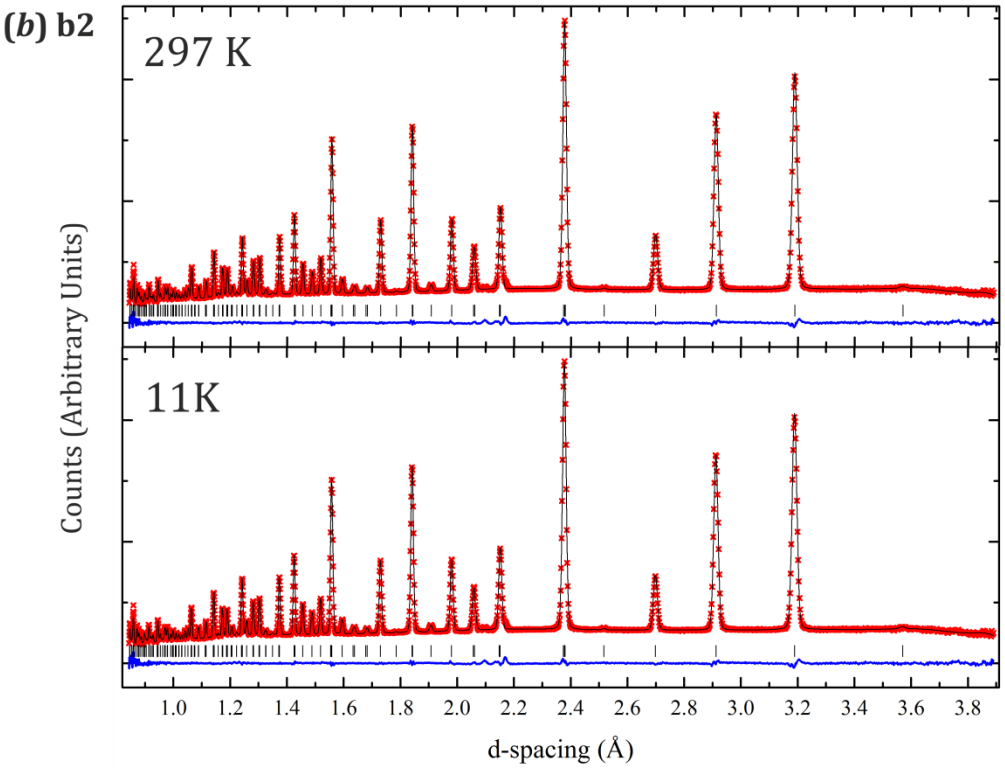
(b) b2
297 K
11K
Counts (Arbitrary Units)
1.0
1.2
1.4
1.6
1.8
2.0
2.2
2.4
2.6
2.8
3.0
3.2
3.4
3.6
3.8
d-spacing (Å)

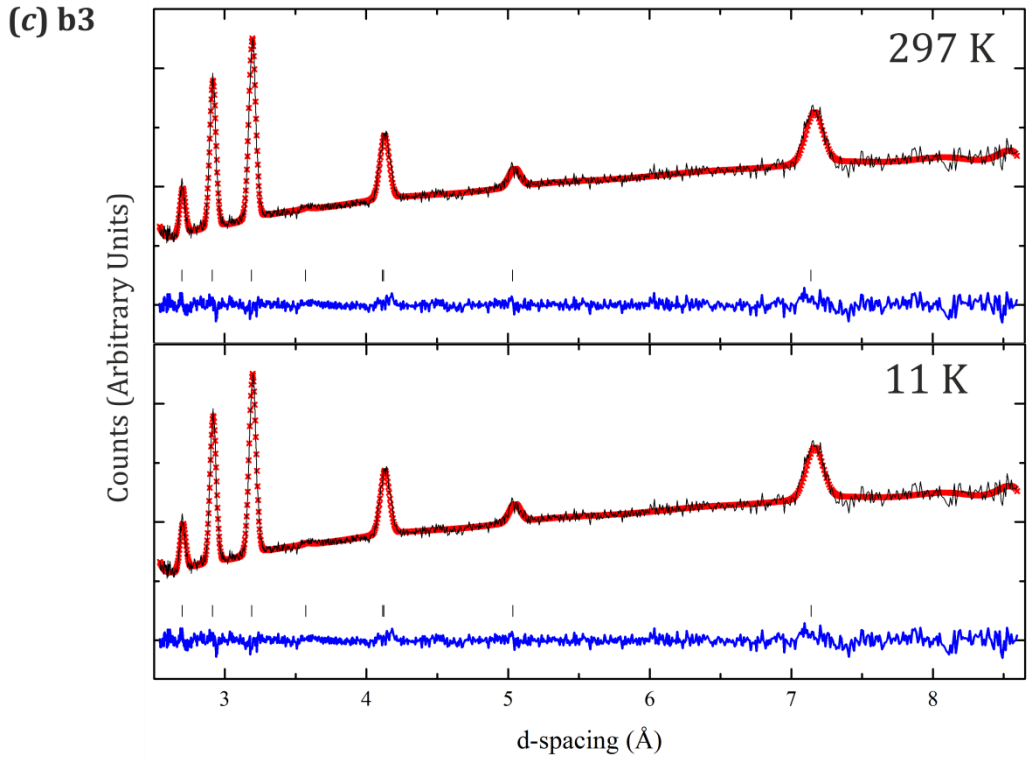

Figure 7-3 Fit of the combined b1 (*a*), b2 (*b*) and b3 (*c*) refinement of $La_3Ga_4Ge_2O_{14.5}$ at 11 and 297K.

APPENDIX 5 Ge_2O_8 LOCAL ENVIRONMENTS

Ge_2O_{10} local environments in 2 × 2 × 2 $La_3Ga_4Ge_2O_{14.5}$ DFT calculated supercell $a-d$ (numbered 1-4 in the figure below) and collapsed $P321$ cell used as the starting points for the refinement (e). (f) $La_3Ga_5GeO_{14}$, (g) $La_3Ga_4Ge_2O_{14.5}$, (h) $La_3Ga_{3.5}Ge_{2.5}O_{14.75}$, ($i$) $La_3GaGe_5O_{16}$, (j) $La_{1.5}Pr_{1.5}Ga_4Ge_2O_{14.5}$, ($k$) $La_3Al_5GeO_{14}$, (l) $La_3Al_4Ge_2O_{14.5}$ and (m) $La_3Al_{3.5}Ge_{2.5}O_{14.75}$. All refined models presented in this appendix accounts to data collected at 297K.

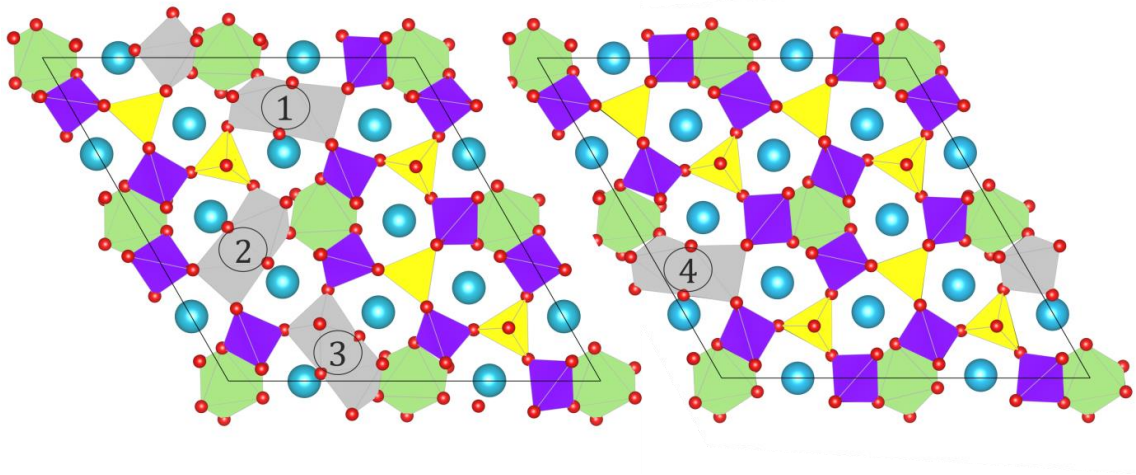

(a) 1

Bond length (Å)

C-	1	1.79301	D-	4	2.03347
	2	1.78354		5	1.82400
	3	1.95933		6	1.83725
	4	1.87532		7	1.78397
	5	1.92632		8	1.85652

Angles (°)

1-C-	2	128.75	2-C-	3	93.4514	3-C-	4	82.3513	4-C-	5	79.0691
	3	92.9469		4	111.8871		5	159.5796	4-D-	5	77.5087
	4	119.3623		5	101.2562	5-D-	6	130.1532		6	84.5862
	5	88.8469	6-D-	7	90.3445		7	108.1425		7	94.1602
7-D-	8	109.9832		8	119.3552		8	86.9706		8	154.4991

(b) 2

Bond length (Å) dO4-5 2.42

C-	1	1.78418	D-	4	2.01701
	2	1.77395		5	1.84633
	3	2.02476		6	1.87045
	4	1.88219		7	1.77898
	5	1.93767		8	1.84177

Angles (°)

1-C-	2	122.4923	2-C-	3	99.4038	3-C-	4	79.6521	4-C-	5	78.5166
	3	89.6151		4	114.2056		5	151.8886	4-D-	5	77.3414
	4	123.2815		5	105.5851	5-D-	6	85.9434		6	150.4506
	5	87.7338	6-D-	7	111.2221		7	106.5855		7	96.9448
7-D-	8	115.4684		8	89.6789		8	136.2578		8	85.9686

(c) 3

Bond length (Å)												
C-	1	1.79345	D-	4	2.09135							
	2	1.77412		5	1.83169							
	3	1.97712		6	1.82348							
	4	1.87676		7	1.78238							
	5	1.94322		8	1.86667							
Angles (°)												
1-C-	2	127.7156	2-C-	3	96.3740	3-C-	4	82.4806	4-C-	5	78.6155	
	3	90.1294		4	102.5151		5	157.2343		5	75.8705	
	4	119.6590		5	102.5151		6	134.1360		6	86.7827	
	5	88.3050	6-D-	7	115.8996	5-D-	7	107.1059	4-D-	7	92.4937	
7-D-	8	111.0254		8	91.9417		8	134.1360		8	154.2307	

(d) 4

Bond length (Å)												
C-	1	1.80586	D-	4	2.01872							
	2	1.80486		5	1.83212							
	3	1.88467		6	1.84511							
	4	1.93328		7	1.78956							
	5	1.95182		8	1.88070							
Angles (°)												
1-C-	2	119.2854	2-C-	3	100.0854	3-C-	4	81.2773	4-C-	5	75.8743	
	3	95.5082		4	119.5437		5	155.9482		5	76.5023	
	4	120.6972		5	97.6524		6	127.2799	4-D-	6	86.2355	
	5	89.8097	6-D-	7	117.6259	5-D-	7	113.4231		7	95.5850	
7-D-	8	106.9388		8	90.8611		8	86.3817		8	95.5850	

(e) **Collapsed model**

Bond length (Å)

I(O4-O5) = 2.4376(10) Å

C-	1	1.806(5)	D-	4	1.9532(5)		
	2	1.806(5)		5	1.8890(4)		
	3	1.8950(4)		6	1.7990(8)		
	4	2.1587(5)		7	1.795(5)		
	5	2.1448(9)		8	1.7990(5)		

Angles (°)

1-C-	2	134.7(2)	2-C-	3	99.20(14)	3-C-	4	71.98(2)	4-C-	5	69.00(6)
	3	102.23(12)		4	116.52(12)		5	136.88(8)		5	78.735(14)
	4	107.95(14)		5	114.07(12)		6	131.53(8)	4-D-	6	73.00(6)
	5	73.70(13)	6-D-	7	116.2(2	5-D-	7	101.40(13)		7	88.75(9)
7-D-	8	116.22(11)		8	101.95(7)		8	86.25(8)		8	153.13(10)

(f) $La_3Ga_5GeO_{14}$ at 297K

Bond length (Å)

C-	1	1.8070(8)	D-	4	1.8129(12)		
	2	1.8070(11)		5			
	3	1.8824(9)		6	1.8129(8)		
	4	1.8824(11)		7	1.779(2)		
	5			8	1.8129(8)		

Angles (°)

1-C-	2	134.64(9)	2-C-	3	108.70(10)	3-C-	4	98.35(8)	4-C- 5
	3	100.57(7)		4	100.57(7)		5		5
	4	108.70(12)		5			6		4-D- 6 101.62(11)
	5		6-D-	7	116.49(13)	5-D-	7		7 116.49(7)
7-D-	8	116.49(12)		8	101.62(10)		8		8 101.62(11)

(g) $La_3Ga_4Ge_2O_{14.5}$ at 297K

Bond length (Å)

I(O4-O5) = = 2.30(2) Å

C-	1	1.7969(13)	D-	4	1.945(8)		
	2	1.7969(13)		5	1.805(13)		
	3	1.765(6)		6	1.914(6)		
	4	2.098(7)		7	1.755(2)		
	5	2.17(2)		8	1.914(5)		

Angles (°)

1-C-	2	132.17(11)	2-C-	3	104.9(2)	3-C-	4	74.7(2)	4-C- 5 65.2(2)
	3	98.7(2)		4	113.1(2)		5	132.3(3)	5 75.6(3)
	4	113.0(2)		5	113.8(2)		6	135.0(3)	4-D- 6 76.0(2)
	5	75.4(2)	6-D-	7	115.3(2)	5-D-	7	101.4(3)	7 95.2(2)
7-D-	8	115.3(2)		8	103.1(2)		8	82.2(3)	8 145.4(2)

(h) $La_3Ga_{3.5}Ge_{2.5}O_{14.75}$ at 297K

Bond length (Å)

l(O4-05) = 2.498(14) Å

C-	1	1.7984(9)	D-	4	1.909(4)								
	2	1.7984(10)		5	1.915(7)								
	3	1.817(9)		6	1.835(10)								
	4	2.188(4)		7	1.7645(14)								
	5	2.194(9)		8	1.835(6)								

Angles (°)

1-C-	2	131.10(9)	2-C-	3	109.82(15)	3-C-	4	71.2(2)	4-C-	5	69.5(2)		
	3	99.4(2)		4	115.67(12)		5	133.4(2)		5	81.6(2)		
	4	111.68(13)		5	112.47(13)		6	138.8(2)	4-D-	6	76.3(2)		
	5	73.44(13)	6-D-	7	116.0(2)	5-D-	7	99.3(2)		7	92.8(2)		
7-D-	8	116.0(2)		8	102.2(2)		8	78.8(2)		8	147.3(2)		

(i) $La_3GaGe_5O_{16}$

Bond length (Å)

l(O4-05) = 2.45(6) Å

C-	1	1.796(15)	D-	4	1.85(6)								
	2	1.719(15)		5	1.91(11)								
	3	1.86(2)		6	1.796(15)								
	4	1.91(11)		7	1.719(15)								
	5	1.85(6)		8	1.86(2)								

Angles (°)

1-C-	2	119.1(3)	2-C-	3	102.5(3)	3-C-	4	92.9(6)	4-C-	5	81.3(9)		
	3	89.2(3)		4	105.0(3)		5	162.6(2)		5	81.3(9)		
	4	134.2(3)		5	94.8(2)		6	134.2(3)	4-D-	6	83.4(6)		
	5	83.4(6)	6-D-	7	119.1(3)	5-D-	7	105.0(3)		7	94.8(2)		
7-D-	8	102.5(3)		8	89.2(3)		8	92.9(6)		8	162.6(2)		

(j) $La_{1.5}Pr_{1.5}Ga_4Ge_2O_{14.5}$ at 297K

Bond length (Å)

I(O4-O5) = 2.33(3) (14) Å

C-	1	1.7956(13)	D-	4	1.968(10)	
	2	1.7956(13)		5	1.882(14)	
	3	1.814(6)		6	1.7666(16)	
	4	2.048(8)		7	1.982(5)	
	5	2.182(19)		8	1.982(5)	

Angles (°)

1-C-	2	132.25(12)	2-C-	3	108.43(19)	3-C-	4	76.3(3)	4-C-	5	66.9(3)
	3	94.87(16)		4	111.22(16)		5	133.1(3)		5	74.6(3)
	4	114.60(18)		5	111.3(3)	5-D-	6	132.2(3)	4-D-	6	77.8(3)
	5	76.1(3)	6-D-	7	118.20(19)		7	118.20(19)		7	96.64(18)
7-D-	8	118.20(17)		8	99.5(2)		8	79.2(3)		8	140.3(3)

(k) $La_3Al_5GeO_{14}$ at 297K

Bond length (Å)

C-	1	1.7580(18)	D-	4	1.737(3)	
	2	1.7580(18)		5		
	3	1.7930(16)		6	1.7369(13)	
	4	1.793(3)		7	1.740(4)	
	5			8	1.7369(12)	

Angles (°)

1-C-	2	133.16(11)	2-C-	3	107.28(12)	3-C-	4	100.39(12)	4-C-	5	
	3	102.23(11)		4	102.23(10)		5			5	
	4	107.28(10)		5		5-D-	6		4-D-	6	104.86(12)
	5		6-D-	7	113.76(13)		7			7	113.76(8)
7-D-	8	113.76(11)		8	104.86(12)		8			8	104.86(12)

(l) $La_3Al_4Ge_2O_{14.5}$ at 297K

Bond length (Å)

l(O4-05) = 2.26808(0) Å

C-	1	1.739(3)	D-	4	1.92521(0)		
	2	1.739(3)		5	2.03185(0)		
	3	1.772(3)		6	1.749(3)		
	4	2.01267(0)		7	1.728(5)		
	5	1.79178(0)		8	1.7489(18)		

Angles (°)

1-C-	2	129.17(13)	2-C-	3	106.63(14)	3-C-	4	61.42(12)	4-C-	5	72.9303(0)
	3	103.61(13)		4	125.46(9)		5	131.26(12)		5	69.8839(0)
	4	104.75(8)		5	113.42(8)	5-D-	6	139.82(11)	4-D-	6	88.35(12)
	5	71.28(8)	6-D-	7	114.17(15)		7	96.39(9)		7	82.20(6)
7-D-	8	114.17(14)		8	104.39(14)		8	84.43(11)		8	151.30(11)

(m) $La_3Al_{3.5}Ge_{2.5}O_{14.75}$ at 297K

Bond length (Å)

l(O4-05) = 2.519(4) Å

C-	1	1.75277(5)	D-	4	1.79160(6)		
	2	1.75277(5)		5	2.0110(19)		
	3	1.76471(6)		6	1.76332(6)		
	4	2.05340(4)		7	1.75690(8)		
	5	2.257(8)		8	1.76332(3)		

Angles (°)

1-C-	2	127.92(10)	2-C-	3	107.90(7)	3-C-	4	67.2085(0)	4-C-	5	75.09(13)
	3	102.37(7)		4	124.05(7)		5	134.86(10)		5	82.74(18)
	4	106.39(6)		5	105.16(16)	5-D-	6	141.95(5)	4-D-	6	85.97(10)
	5	72.817(9)	6-D-	7	114.07(13)		7	100.88(3)		7	85.95(5)
7-D-	8	114.07(11)		8	104.50(12)		8	71.54(18)		8	149.58(10)

APPENDIX 6 POST-AC IMPEDANCE $La_3Ga_{5-x}Ge_{1+x}O_{14+x/2}$ PXRD PATTERNS

Purity checks were carried out for $La_3Ga_{5-x}Ge_{1+x}O_{14+x/2}$ specimens with x = 0, 0.1, 0.2, 0.3 (A and B), 0.35, 0.4, 0.45, 0.5 (A and B), 0.6, 0.7, 1 and 1.5 after AC impedance measurements were carried out to ensure the estability of these samples in under the experimental conditions. These consisted on scraping off the gold contacts with a scalpel and grinding the pellets into a fine powder that could be analysed by PXRD.

The PXRD patternrs were collected in X'Pert Pro PANanalytical diffractometer equiped with a Co-source ($K_{\alpha 1}$ = 1.7890 Å) in a 10-100° 2θ range. The magnified 20-60° region is shown in Figure 7-4 where no extra peaks associated to impurities are observed.

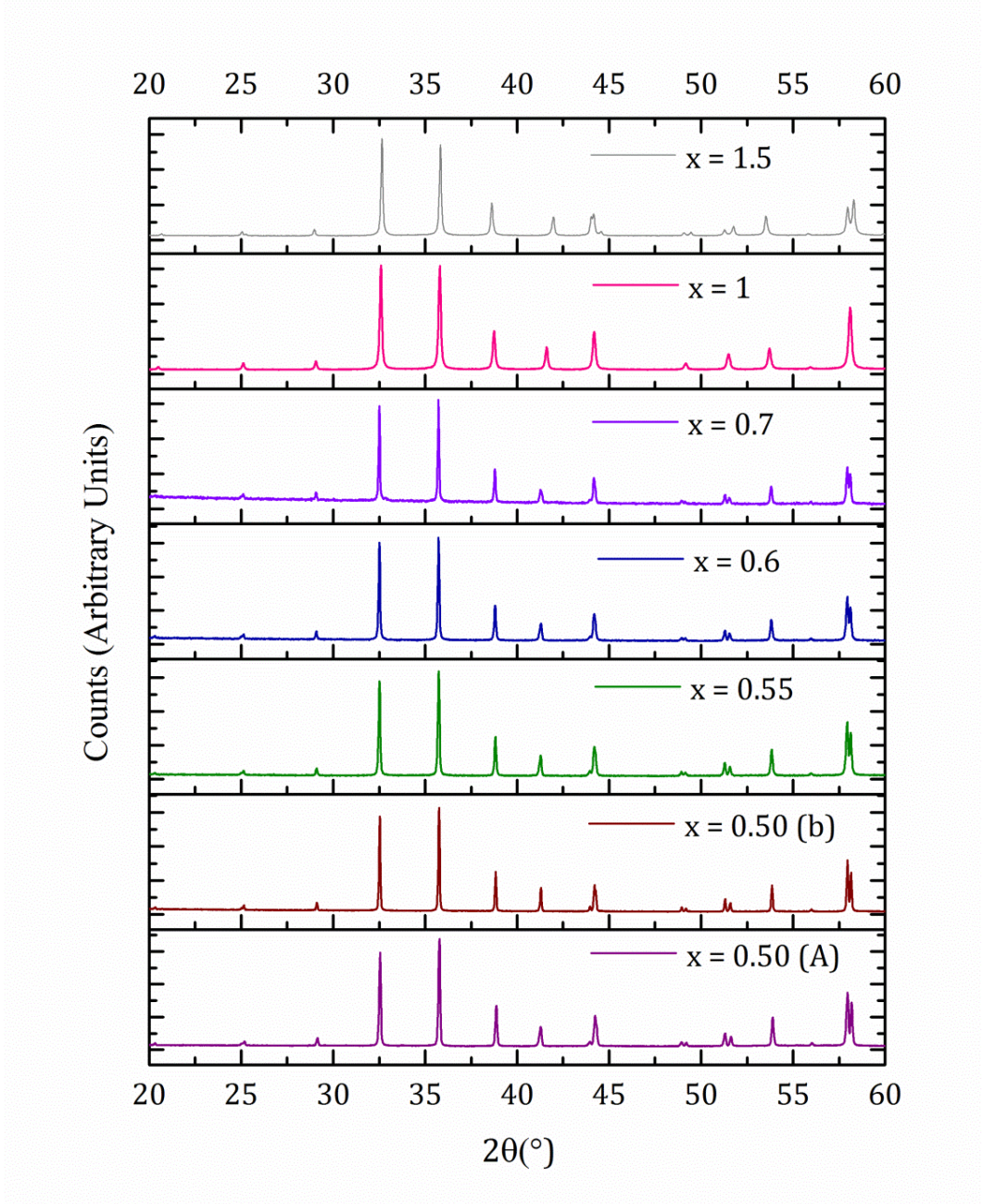

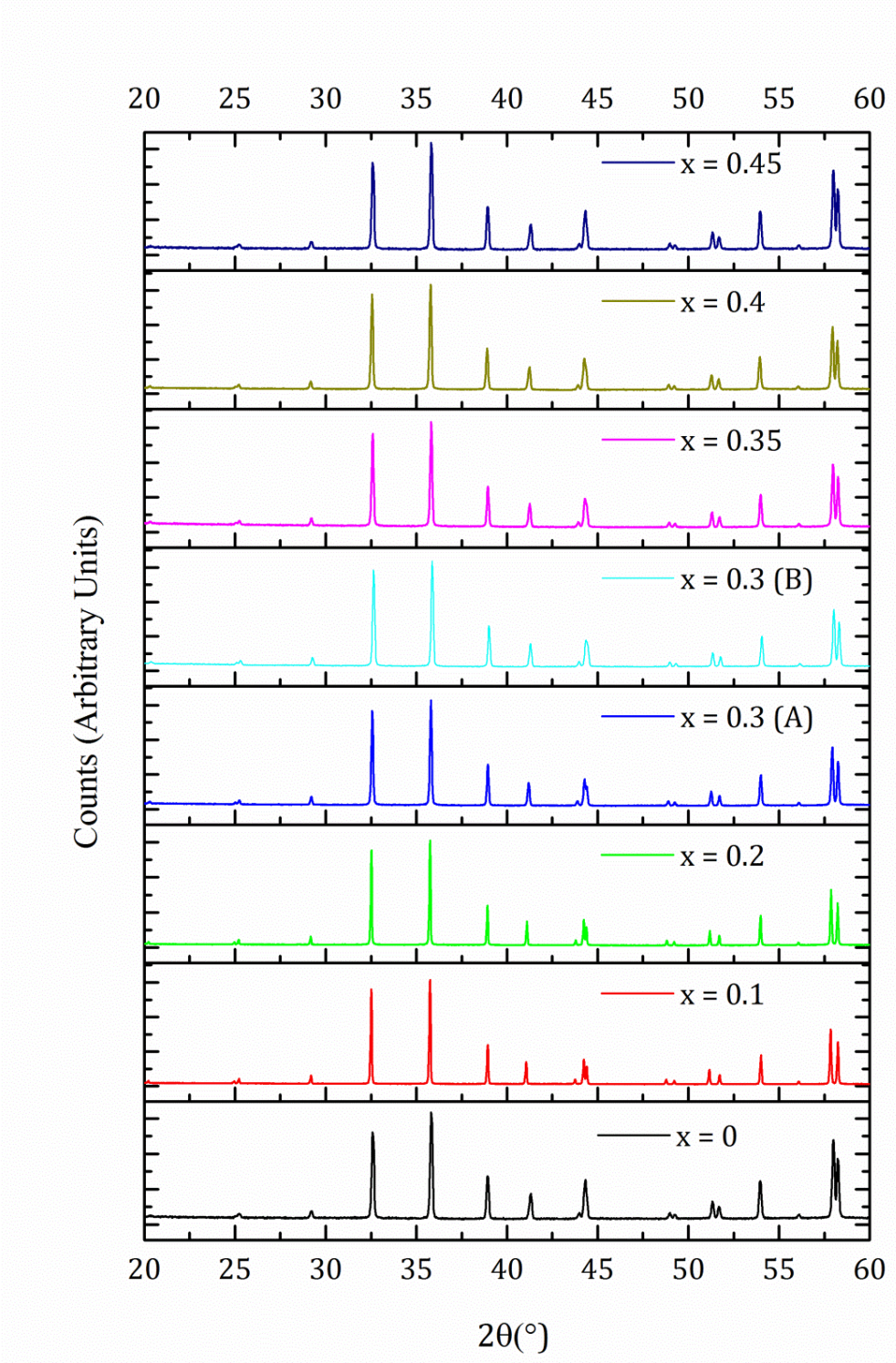

Figure 7-4 XRD patterns of $La_3Ga_{5-x}Ge_{1+x}O_{14+x/2}$ for x 0-1.5 after the AC impedance measurements were carried out.

APPENDIX 7 COMPARISON OF THE BULK CONDUCTIVITY OF SPECIMENS WITH DIFFERENT DENSITIES

The aim of this discussion is to compare the Heidinger corrected bulk conductivity calculated for two different compositions: $La_{1.5}Nd_{1.5}Ga_{4.5}Ge_{1.5}O_{14.25}$ and $Nd_3Ga_{4.5}Ge_{1.5}O_{14.25}$ (incorporating 1.79 % of extra oxygen) prepared by two different methods: conventional and SPS sintering techniques. The permittivity values corrected by Heidinger (ε_H) are included in the tables below Table 7-4 and Table 7-5.

The conventional sintering of $La_{1.5}Nd_{1.5}Ga_{4.5}Ge_{1.5}O_{14.25}$ and $Nd_3Ga_{4.5}Ge_{1.5}O_{14.25}$ involved the mechanical milling of the powders which allow for particle size reduction, followed by a 5 hours heating program at t a high temperature of 1250 °C. The sintering temperature was shortened from 12 hours (typically used for most of the materials prepared in this work) to 5 hours. The decrease in dwelling time was aimed at minimize the GeO_2 volatilization from the reaction mixture that was observed by EDX elemental analysis of $La_{1.5}Pr_{1.5}Ga_{4.5}Ge_{1.5}O_{14.25}$ annealed for 12 hours at 950 °C and 1300 °C (below and above T_{decomp}~1100 °C respectively), see section 5.2.1.3.1.

Table 7-4 Density, sintering conditions and conductivity of conventionally sintered $Nd_3Ga_{4.5}Ge_{1.5}O_{14.25}$ and $La_{1.5}Nd_{1.5}Ga_{4.5}Ge_{1.5}O_{14.25}$

Nominal Composition	ρ (%)	Ea_{bulk} (eV)	Conventional Sintering T (°C)	Dwell (h)	ε_H	$\sigma_{500\,°C}$ (S·cm^{-1})
$Nd_3Ga_{4.5}Ge_{1.5}O_{14.25}$	92	1.08	1250	5	38	1.10×10^{-5}
$La_{1.5}Nd_{1.5}Ga_{4.5}Ge_{1.5}O_{14.25}$	85	1.13	1250	5	38	1.05×10^{-5}

Spark plasma assisted sintering was carried out in mechanically milled powders that were pressed in a ⌀ = 20 mm graphite die at a pressure of 50 MPa and a heating-cooling ramp rate of 200 ° min^{-1}.

Table 7-5 Density, sintering conditions and conductivity of SPS sintered $Nd_3Ga_{4.5}Ge_{1.5}O_{14.25}$ and $La_{1.5}Nd_{1.5}Ga_{4.5}Ge_{1.5}O_{14.25}$

Nominal Composition	ρ (%)	Ea_{bulk} (eV)	SPS Sintering T(°C)	Dwell (min)	ε_H	$\sigma_{500\,°C}$ (S·cm^{-1})
$Nd_3Ga_{4.5}Ge_{1.5}O_{14.25}$	58	1.18	1000	5	49	1.02×10^{-5}
$La_{1.5}Nd_{1.5}Ga_{4.5}Ge_{1.5}O_{14.25}$	58	1.18	1000	5	52	1.38×10^{-5}

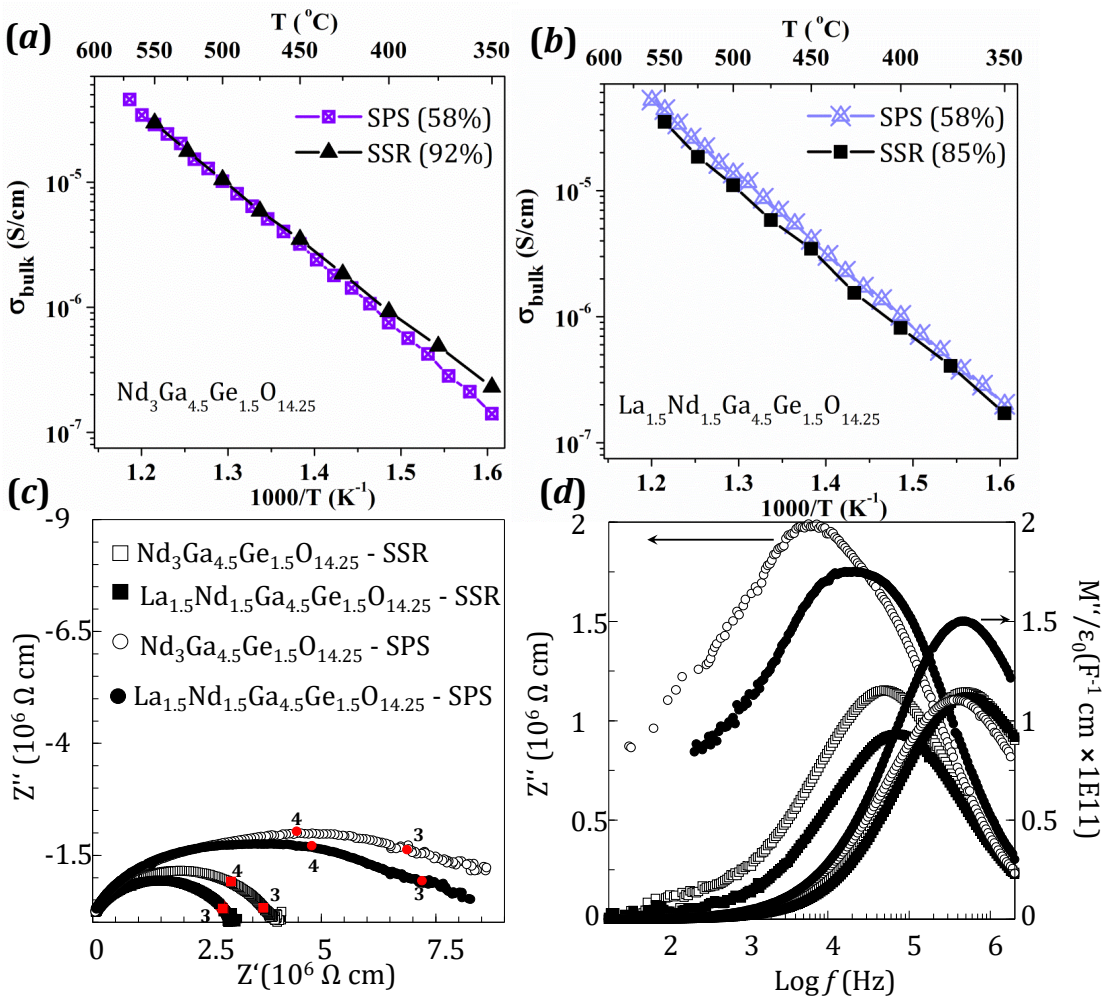

Figure 7-5 Arrhenius plot of the bulk conductivity of SPS and conventionally (denoted as SSR) sintered $Nd_3Ga_{4.5}Ge_{1.5}O_{14.25}$ (*a*) and $La_{1.5}Nd_{1.5}Ga_{4.5}Ge_{1.5}O_{14.25}$ (*b*) specimens. (*c*) Complex impedance plane for all four samples where the log of the frequency is denoted by red symbols and bold characters. (*d*) Combined *Z''* and *M''* plot.

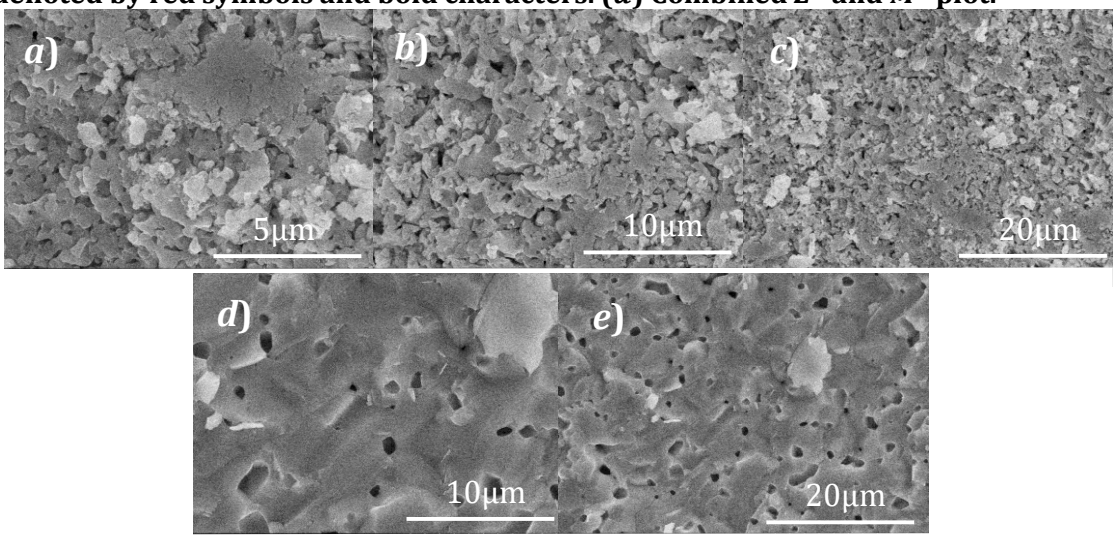

Figure 7-6 SEM images of $Nd_3Ga_{4.5}Ge_{1.5}O_{14.25}$ samples sintered by SPS (*a-c*) and a conventional sintering method (*d* and *e*).

APPENDIX 8 POST-MEASUREMENT PURITY CHECKS

Here, the lattice parameters determined by the Pawley fitting of PXRD patterns collected on powdered specimens of those samples whose conductivities are reported in this thesis are presented.

- $La_3Ga_{5-x}Ge_{1+x}O_{14+x/2}$

$La_3Ga_{5-x}Ge_{1+x}O_{14+x/2}$ 'x'	Before-SPS sintering					Post-Measurement					Sintering Conditions	Conductivity
	R_{wp}	S	a (Å)	c (Å)	V (Å^3)	R_{wp}	S	a (Å)	c (Å)	V (Å^3)		
0	Samples sintered by a conventional method					6.03	1.58	8.20477(3)	5.10655(2)	297.708(2)	Table 4-7	Figure 4-17
0.1						6.22	2.72	8.20765(5)	5.10522(4)	297.840(4)	Table 4-7	Figure 4-17
0.2						5.80	2.47	8.20958(3)	5.09967(3)	297.656(3)	Table 4-7	Figure 4-17
0.3 (A)	4.00	1.88	8.21374(2)	5.09148(3)	297.479(2)	3.89	1.59	8.21325(3)	5.09320(2)	297.544(3)	Table 4-7	Figure 4-17
0.3 (B)	4.67	1.92	8.214764(8)	5.09057(2)	297.501(1)	3.75	1.47	8.21500(3)	5.09000(3)	297.484(3)	Table 4-7	Figure 4-17
0.35	10.91	3.13	8.21880(5)	5.08798(4)	297.641(4)	7.26	2.76	8.21822(6)	5.08952(6)	297.689(6)	Table 4-7	Figure 4-17
0.4	6.60	1.33	8.22011(4)	5.0839(3)	297.498(3)	4.39	1.87	8.21911(3)	5.08710(5)	297.612(3)	Table 4-7	Figure 4-17
0.45	7.56	1.34	8.22207(2)	5.08072(2)	297.453(2)	9.79	2.44	8.2227(1)	5.084664(8)	297.732(8)	Table 4-7	Figure 4-17
0.5(A)	7.14	2.41	8.22274(6)	5.07402(5)	297.109(5)	4.08	1.53	8.22597(3)	5.07620(2)	297.470(3)	Table 4-7	Figure 4-17
0.5 (B)	6.70	2.05	8.22611(4)	5.07638(3)	297.491(3)	8.58	3.88	8.22357(8)	5.08052(2)	297.550(6)	Table 4-7	Figure 4-17
0.55	7.12	1.28	8.22727(4)	5.07453(3)	297.467(3)	5.70	1.39	8.22696(6)	5.07753(3)	297.62(1)	Table 4-7	Figure 4-17
0.6	5.60	1.68	8.23020(4)	5.06963(3)	297.391(4)	6.98	1.52	8.22813(6)	5.07444(7)	297.523(6)	Table 4-7	Figure 4-17
0.7	7.88	1.32	8.23597(5)	5.06382(3)	297.467(4)	7.12	1.31	8.2294(1)	5.07313(7)	297.541(9)	Table 4-7	Figure 4-17
1	7.52	1.65	8.2538(2)	5.03748(7)	297.21(1)	7.16	3.68	8.24950(9)	5.0428(4)	297.207(7)	Table 4-7	Figure 4-17
1.5	9.96	1.13	8.28546(3)	5.00089(6)	297.311(4)	3.98	1.92	8.28033(8)	5.00513(3)	297.195(6)	Table 4-7	Figure 4-17

- $La_{3-y}Ln_yGa_{5-x}Ge_{1+x}O_{14+x/2}$

The samples listed below were synthesized by Pechini and sintered by a conventional method involving the heating of pellets at 1250 °C for 12 hours for the parent materials and for 5 hours for the doped Ge-richer compositions.

Nominal compositions	Post-Measurement					Sintering Conditions	Conductivity
	R_{wp}	S	a (Å)	c (Å)	V (Å^3)		
$Pr_3Ga_{4.5}Ge_{1.5}O_{14.25}$	5.60	1.05	0.000586	5.0653(5)	290.38(5)	Table 5-7	Figure 5-11-*a*
$Pr_3Ga_{4.75}Ge_{1.25}O_{14.125}$	11.98	1.28	0.000086	5.0760(1)	290.934(8)	Table 5-7	Figure 5-11-*a*
$Pr_3Ga_5GeO_{14}$	5.64	1.87	0.000288	5.0808(1)	290.21(2)	Table 5-7	Figure 5-11-*a*
$Nd_3Ga_{4.5}Ge_{1.5}O_{14.25}$	6.58	1.05	0.000279	5.0525(2)	288.30(2)	Table 5-7	Figure 5-11-*a*
$Nd_3Ga_{4.75}Ge_{1.25}O_{14.125}$	4.02	1.26	0.00012	5.06829(7)	287.945(9)	Table 5-7	Figure 5-11-*a*
$Nd_3Ga_5GeO_{14}$	5.96	2.00	0.000119	5.0740(1)	287.70(1)	Table 5-7	Figure 5-11-*a*
$La_{1.5}Pr_{1.5}Ga_{4.5}Ge_{1.5}O_{14.25}$	14.45	1.62	0.000228	5.0761(2)	294.27(2)	Table 5-7	Figure 5-11-*a*
$La_{1.5}Pr_{1.5}Ga_{4.75}Ge_{1.25}O_{14.125}$	10.33	1.03	0.000137	5.0869(1)	294.19(1)	Table 5-7	Figure 5-11-*a*
$La_{1.5}Pr_{1.5}Ga_5GeO_{14}$	11.55	1.39	0.000094	5.09511(7)	294.234(8)	Table 5-7	Figure 5-11-*a*
$La_{1.5}Nd_{1.5}Ga_{4.5}Ge_{1.5}O_{14.25}$	2.17	1.09	0.000139	5.0665(1)	292.60(1)	Table 5-7	Figure 5-11-*a*
$La_{1.5}Nd_{1.5}Ga_{4.75}Ge_{1.25}O_{14.125}$	5.35	1.71	0.000079	5.08160(8)	292.268(7)	Table 5-7	Figure 5-11-*a*
$La_{1.5}Nd_{1.5}Ga_5GeO_{14}$	5.25	1.92	0.000085	5.08728(8)	292.052(8)	Table 5-7	Figure 5-11-*a*

- The compositions listed below underwent a fast SPS densification process in order to avoid their decomposition.

Nominal compositions	Before-SPS sintering					Post-Measurement					Sintering Conditions	Conductivity
	R_{wp}	S	a (Å)	c (Å)	V (Å^3)	R_{wp}	S	a (Å)	c (Å)	V (Å^3)		
$La_{1.5}Pr_{1.5}Ga_4Ge_2O_{14.5}$	4.59	1.17	8.2249(3)	5.0308(3)	294.73(3)	6.15	1.61	8.2200(2)	5.0431(1)	295.10(1)	Table 5-8	Figure 5-14
$La_{1.5}Pr_{1.5}Ga_{4.5}Ge_{1.5}O_{14.25}$	4.56	1.16	8.1907(3)	5.0648(3)	294.26(3)	5.16	1.40	8.1891(1)	5.07021(7)	294.46(1)	Table 5-8	Figure 5-14
$Pr_3Ga_{4.5}Ge_{1.5}O_{14.25}$	4.36	1.22	8.1561(7)	5.0589(3)	291.44(2)	5.63	1.37	8.1521(1)	5.06522(4)	291.518(9)	Table 5-8	Figure 5-14
$La_{1.5}Nd_{1.5}Ga_4Ge_2O_{14.5}$	4.51	1.17	8.2007(1)	5.0267(2)	292.76(1)	5.67	1.34	8.19287(4)	5.0431(2)	293.16(1)	Table 5-8	Figure 5-14
$La_{1.5}Nd_{1.5}Ga_{4.25}Ge_{1.75}O_{14.375}$	4.45	1.17	8.18805(5)	5.0462(1)	292.990(7)	6.12	1.59	8.17360(7)	5.05843(9)	292.666(7)	Table 5-8	Figure 5-14
$La_{1.5}Nd_{1.5}Ga_{4.5}Ge_{1.5}O_{14.25}$	4.53	1.16	8.17748(3)	5.0649(1)	293.318(8)	5.16	1.32	8.17595(6)	5.07020(7)	293.517(6)	Table 5-8	Figure 5-14
$Nd_3Ga_{4.25}Ge_{1.75}O_{14.375}$	4.16	1.18	8.1409(1)	5.03645(9)	289.06(1)	5.26	1.36	8.12141(6)	5.06151(6)	289.117(5)	Table 5-8	Figure 5-14
$Nd_3Ga_{4.5}Ge_{1.5}O_{14.25}$	4.48	1.21	8.12538(9)	5.0541(1)	288.978(9)	5.23	1.24	8.11905(2)	5.0598(1)	288.853(8)	Table 5-8	Figure 5-14

Nominal compositions	Before-SPS sintering					Post-Measurement					Sintering Conditions	Conductivity
	R_{wp}	S	a (Å)	c (Å)	V (Å^3)	R_{wp}	S	a (Å)	c (Å)	V (Å^3)		
$La_{1.5}Pr_{1.5}Ga_{4.5}Ge_{1.5}O_{14.25}$	4.56	1.16	8.1907(3)	5.0648(3)	294.26(3)	5.16	1.40	8.1891(1)	5.07021(7)	294.46(1)	Table 5-9	Figure 5-17-*a*
$La_{1.5}Nd_{1.5}Ga_4Ge_2O_{14.5}$	4.51	1.17	8.2007(1)	5.0266(2)	292.76(1)	5.67	1.34	8.19287(4)	5.0431(2)	293.16(1)	Table 5-9	Figure 5-17-*a*
$La_{1.5}Sm_{1.5}Ga_{4.5}Ge_{1.5}O_{14.25}$	4.21	1.14	8.14795(5)	5.0538(1)	290.566(8)	5.10	1.15	8.1429(1)	5.0583(2)	290.47(1)	Table 5-9	Figure 5-17-*a*
$La_{1.5}Gd_{1.5}Ga_{4.5}Ge_{1.5}O_{14.25}$	4.37	1.19	8.1274(1)	5.0504(1)	288.91(1)	4.69	1.20	8.12723(7)	5.0553(3)	289.17(2)	Table 5-9	Figure 5-17-*a*
$La_2PrGa_4Ge_2O_{14.5}$	4.95	1.30	8.23111(1)	5.03301(5)	295.308(3)	6.50	1.41	8.22398(3)	5.0399(1)	295.198(8)	Table 5-9	Figure 5-17-*a*
$La_2SmGa_4Ge_2O_{14.5}$	4.38	1.19	8.20413(8)	5.0235(1)	292.82(1)	5.44	1.38	8.1886(1)	5.0425(2)	292.82(2)	Table 5-9	Figure 5-17-*a*
$La_2GdGa_4Ge_2O_{14.5}$	5.22	1.40	8.2271(2)	5.0308(4)	294.90(3)	6.49	1.48	8.2122(2)	5.0455(2)	294.69(2)	Table 5-9	Figure 5-17-*a*

- $La_3Ga_{5-x-y}Al_yGe_{1+x}O_{14+x/2}$ and $La_3Al_{5-x}Ge_{1+x}O_{14+x/2}$

Nominal compositions	Before-SPS sintering					Post-Measurement					Sintering Conditions	Conductivity
	R_{wp}	S	a (Å)	c (Å)	V (Å^3)	R_{wp}	S	a (Å)	c (Å)	V (Å^3)		
$La_3Al_5GeO_{14}$	4.36	1.11	8.101(1)	4.9731(4)	282.66(9)	4.71	1.24	8.0999(3)	4.9728(2)	282.53(3)	Table 5-14	Figure 5-30
$La_3Al_{4.9}Ge_{1.1}O_{14.05}$	Non-crystalline (see Figure 5-23)					5.20	1.13	8.1021(6)	4.9715(2)	282.63(4)	Table 5-14	Figure 5-30
$La_3Al_{4.8}Ge_{1.2}O_{14.1}$						6.22	1.38	8.10714(8)	4.9678(2)	282.77(1)	Table 5-14	Figure 5-30
$La_3Al_{4.7}Ge_{1.3}O_{14.15}$						5.45	1.20	8.1132(2)	4.9623(1)	282.88(1)	Table 5-14	Figure 5-30
$La_3Al_{4.6}Ge_{1.4}O_{14.2}$						5.58	1.21	8.1192(1)	4.9581(1)	283.06(1)	Table 5-14	Figure 5-30
$La_3Al_{4.5}Ge_{1.5}O_{14.25}$	4.65	1.17	8.169(2)	5.1586(4)	298.1(1)	4.65	1.18	8.1226(5)	4.9591(3)	283.35(4)	Table 5-14	Figure 5-30
$La_3Al_4Ge_2O_{14.5}$	4.52	1.15	8.1618(5)	4.9430(5)	285.16(4)	4.87	1.27	8.1574(8)	4.9444(7)	284.94(7)	Table 5-14	Figure 5-30
$La_3Al_{2.425}Ga_{2.425}Ge_{1.15}O_{14.075}$	5.10	1.10	8.1607(4)	5.03649(6)	290.48(3)	5.11	1.12	8.1603(1)	5.0390(2)	290.59(2)	Table 5-14	Figure 5-32-*a*
$La_3Al_{2.35}Ga_{2.35}Ge_{1.3}O_{14.15}$ (A)	4.90	1.17	8.1709(2)	5.0292(4)	290.78(3)	5.71	1.25	8.16843(5)	5.02910(7)	290.602(6)	Table 5-14	Figure 5-32-*a*
$La_3Al_{2.35}Ga_{2.35}Ge_{1.3}O_{14.15}$ (B)						5.35	1.18	8.16759(3)	5.0288(1)	290.526(7)	Table 5-14	Figure 5-32-*a*
$La_3Al_{2.25}Ga_{2.25}Ge_{1.5}O_{14.25}$	3.24	1.03	8.177(1)	5.017(1)	290.5(1)	4.90	1.22	8.17878(2)	5.01973(4)	290.796(3)	Table 5-14	Figure 5-32-*a*
$La_3Al_2Ga_2Ge_2O_{14.5}$	4.49	1.16	8.2088(2)	4.9890(1)	291.14(1)	4.57	1.20	8.20740(7)	4.9918(3)	291.20(2)	Table 5-14	Figure 5-32-*a*
$La_3Ga_{4.4}Al_{0.1}Ge_{1.5}O_{14.25}$	5.00	1.21	8.22469(8)	5.07521(5)	297.319(6)	5.70	1.28	8.2225(1)	5.07815(3)	297.337(8)	Table 5-14	Figure 5-32-*a*
$La_3Ga_{4.25}Al_{0.25}Ge_{1.5}O_{14.25}$	4.61	1.18	8.2211(1)	5.0715(2)	296.85(2)	5.33	1.28	8.2199(1)	5.07359(4)	296.88(1)	Table 5-14	Figure 5-32-*a*
$La_3Ga_4Al_{0.5}Ge_{1.5}O_{14.25}$	4.83	1.17	8.2194(4)	5.0662(3)	296.41(3)	5.48	1.20	8.21562(8)	5.06611(8)	296.133(8)	Table 5-14	Figure 5-32-*a*
$La_3Ga_{3.5}AlGe_{1.5}O_{14.25}$	5.46	1.21	8.2050(2)	5.05195(9)	294.54(1)	5.32	1.25	8.20608(3)	5.0527(1)	294.666(9)	Table 5-14	Figure 5-32-*a*

APPENDIX 9 SEPARATE AND COMBINED GEM AND I11 REFINEMENTS OF $La_3Al_{3.5}Ge_{2.5}O_{14.75}$ AT 297 K

Parameter	$La_3Al_{3.5}Ge_{2.5}O_{14.75}$		
Data sets	GEM	I11	Combined
R_{wp}	2.432	1.321	1.663
R_{exp}	0.483	0.299	0.373
a (Å)	8.1946(3)	8.19750(3)	8.1974(3)
c (Å)	4.9157(2)	4.916789(2)	4.91674(2)
V (Å^3)	285.87(3)	286.138(3)	286.127(2)
La1 (3e),(x, 0, 0)			
x	0.4163(1)	0.41528(6)	0.41567(4)
OCC	1	1	1
B_{eq} (Å^2)	0.88(2)	1.08(1)	1.16(1)
Al1 (1a), (0, 0, 0)			
OCC	0.824(9)	0.760(7)	0.823(3)
B_{eq} (Å^2)	0.60(8)	1.38(9)	1.27(7)
Al2 (2d), (1/3,2/3,z)			
z	0.5258(5)	0.5262(1)	0.5269(6)
OCC	0.770(7)	0.769(6)	0.713(3)
B_{eq} (Å^2)	0.46(6)	0.96(8)	1.02(5)
Al3 (3f), (x, 0, 0.5)			
x	0.7538(2)	0.7530(2)	0.7528(1)
OCC	0.452(4)	0.386(5)	0.442(2)
Beq (Å^2)		1.51(4)	
U_{11}	0.0221(6)		0.0170(7)
U_{22}	0.0134(6)		0.0170(7)
U_{33}	0.00355(6)		0.017(1)
U_{12}	0.0067(6)		0.0085(3)
U_{13}	0		0
U_{23}	0		0
O1 (2d), (1/3,2/3,z)			
z	0.1685(4)	0.169(1)	0.1694(4)
OCC	1	1	1
Beq (Å^2)		1.6(2)	
U_{11}	0.0129(7)		0.0130(7)
U_{22}	0.0129(7)		0.0130(7)
U_{33}	0.0062(9)		0.0039(9)
U_{12}	0.0645(7)		0.0065(3)
U_{13}	0		0
U_{23}	0		0
O2 (6g), (x, y, z)			
x	0.4547(2)	0.4562(2)	0.4546(2)
y	0.2953(2)	0.3002(2)	0.2956(2)
z	0.3258(3)	0.3284(3)	0.32473()
OCC	0.901(3)	1	0.888(2)
U_{11}	0.0039(7)		0.006(1)
U_{22}	0.035(1)		0.021(2)
U_{33}	0.0051(6)		0.012(1)
U_{12}	0.0028(7)		0.003(1)
U_{13}	0		0.002(1)
U_{23}	0		0

O3 (6g), (x, y, z)			
x	0.2157(2)	0.2174(6)	0.2154(2)
y	0.0927(1)	0.0900(5)	0.0922(2)
z	0.7679(3)	0.7713(7)	0.7671(3)
OCC	1	1	1
Beq (Å^2)		1.8(1)	
U_{11}	0.0083(6)		0.007(1)
U_{22}	0.0259(7)		0.022(1)
U_{33}	0.0045(6)		0.005(1)
U_{12}	0		-0.004(1)
U_{13}	0		0.0031(7)
U_{23}	0		0
O4(6g), (x,y, z)			
x	0.448(1)		0.447(2)
y	0.531(2)		0.528(2)
z	0.503(2)		0.501(2)
OCC	0.115(2)		0.113(2)
B_{eq} (Å^2)	2.5(2)		2.4(2)
O5(6g), (x, y, z)			
x	0.430(2)		0.415(1)
y	0.129(2)		0.135(2)
z	0.397(3)		0.408(2)
OCC	0.112(3)		0.104(2)
B_{eq} (Å^2)	4.1(4)		3.9(4)

8 References

(1) Monthly Energy Review, U.S. Energy Information Administration, June **2015**.
(2) Quadrennial Energy Review: Energy Transmission, Storage, and Dsitribution Infrastructure, April **2015**.
(3) World Energy Resources: 2013 Survey, World Energy Council **2013**.
(4) Irvine, J. T. S.; Connor, P. Solid Oxide Fuels Cells: Facts and Figures: Past Present and Future Perspectives for SOFC Technologies; Springer, **2013**.
(5) Minh, N. Q. Journal of the American Ceramic Society **1993**, 76, 563.
(6) Patil, D. S.; Venkatramani, N.; Rohatgi, V. K.; Mutsuddy, B. C. Solid state ionics **1992**, 1-3, 189.
(7) Haile, S. M. Acta Materialia **2003**, 51, 5981.
(8) Larminie, J.; Dicks, A. Fuel Cell Systems Explained England, **2003.**
(9) Iulianelli, A.; Basile, A. International Journal of Hydrogen Energy **2012**, 37, 15241.
(10) Villa, D. C.; Angioni, S.; Quartarone, E.; Righetti, P. P.; Mustarelli, P. Fuel Cells **2013**, 13, 98.
(11) Devrim, Y.; Erkan, S.; Baç, N.; Eroglu, I. International Journal of Hydrogen Energy **2012**, 37, 16748.
(12) Crabtree, G. W.; Dresselhaus, M. S.; Buchanan, M. V. Print edition **2004**, 57, 39.
(13) Cooper, H. W. Chemical Engineering Progress **2007**, 34.
(14) Park, S.; Vohs, J. M.; Gorte, R. J. Nature **2000**, 404, 265.
(15) Murray, E. P.; Tsai, T.; Barnett, S. A. Nature **1999**, 400, 649.
(16) Kulkarni, A.; Giddey, S. J Solid State Electrochem **2012**, 16, 3123.
(17) Brett, D. J. L.; Atkinson, A.; Brandon, N. P.; Skinner, S. J. Chemical Society Reviews **2008**, 37, 1568.
(18) Surdoval, W. A. ECS Transactions **2009**, 25, 21.
(19) Hibino, T.; Hashimoto, A.; Inoue, T.; Tokuno, J.-i.; Yoshida, S.-i.; Sano, M. Science **2000**, 288, 2031.
(20) Kobayashi, Y.; Tomida, K.; Nishiura, M.; Hiwatashi, K.; Kishizawa, H.; Takenobu, K. Mitsubishi Heavy Industries Technical Review **2015**, 52, 110.
(21) Kreuer, K. D. Annu. Rev. Mater. Res. **2003**, 33, 333.
(22) Ding, C.; Hashida, T. Energy & Environmental Science **2010**, 3, 1729.
(23) Shaikh, S. P. S.; Muchtar, A.; Somalu, M. R. Renewable and Sustainable Energy Reviews 2015, 51, 1.
(24) Ge, X.-M.; Chan, S.-H.; Liu, Q.-L.; Sun, Q. Advanced Energy Materials **2012**, 2, 1156.
(25) Huijsmans, J. P. P.; van Berkel, F. P. F.; Christie, G. M. Journal of Power Sources **1998**, 71, 107.
(26) Atkinson, A.; Barnett, S.; Gorte, R. J.; Irvine, J. T. S.; McEvoy, A. J.; Mogensen, M.; Singhal, S. C.; Vohs, J. Nat Mater **2004**, 3, 17.
(27) Adler, S. B. Chem. Rev. **2004**, 104, 4791.
(28) Hashimoto, T.; Ishizawa, N.; Mizutani, N.; Kato, M. Journal of Crystal Growth **1987**, 84, 207.
(29) Jiang, S. Journal of Materials Science **2008**, 43, 6799.
(30) Tu, H. Y.; Takeda, Y.; Imanishi, N.; Yamamoto, O. Solid State Ionics **1999**, 117, 277.
(31) Teraoka, Y.; Zhang, H.-M.; Furukawa, S.; Yamazoe, N. Chemistry Letters **1985**, 14, 1743.
(32) Shao, Z.; Haile, S. M. Nature **2004**, 431, 170.

(33) Chiba, R.; Yoshimura, F.; Sakurai, Y. Solid State Ionics **1999**, 124, 281.
(34) Tarancón, A.; Marrero-López, D.; Peña-Martínez, J.; Ruiz-Morales, J. C.; Núñez, P. Solid State Ionics **2008**, 179, 611.
(35) Tarancón, A.; Peña-Martínez, J.; Marrero-López, D.; Morata, A.; Ruiz-Morales, J. C.; Núñez, P. Solid State Ionics **2008**, 179, 2372.
(36) Ruddlesden, S. N.; Popper, P. Acta Crystallographica **1957**, 10, 538.
(37) Solak, N.; Zinkevich, M.; Aldinger, F. Solid State Ionics **2006**, 177, 2139.
(38) Sayers, R.; Liu, J.; Rustumji, B.; Skinner, S. J. Fuel Cells **2008**, 8, 338.
(39) Kharton, V. V.; Yaremchenko, A. A.; Naumovich, E. N. J Solid State Electrochem **1999**, 3, 303.
(40) Adler, S. B.; Lane, J. A.; Steele, B. C. H. Journal of The Electrochemical Society **1996**, 143, 3554.
(41) Jacobson, A. J. Chem. Mater. **2010**, 22, 660.
(42) Malavasi, L.; Fisher, C. A. J.; Islam, M. S. Chem. Soc. Rev. **2010**, 39, 4370.
(43) Sun, C.; Hui, R.; Roller, J. J Solid State Electrochem **2010**, 14, 1125.
(44) Ding, D.; Li, X.; Lai, S. Y.; Gerdes, K.; Liu, M. Energy & Environmental Science **2014**, 7, 552.
(45) Chen, D.; Yang, G.; Ciucci, F.; Tade, M. O.; Shao, Z. Journal of Materials Chemistry A **2014**, 2, 1284.
(46) Chao, C.-C.; Hsu, C.-M.; Cui, Y.; Prinz, F. B. ACS Nano **2011**, 5, 5692.
(47) Riess, I. Solid State Ionics **1992**, 52, 127.
(48) Liu, Q.; Qin, H.; Raza, R.; Fan, L.; Li, Y.; Zhu, B. RSC Advances **2012**, 2, 8036.
(49) Guo, Y.; Bessaa, M.; Aguado, S.; Steil, M. C.; Rembelski, D.; Rieu, M.; Viricelle, J.-P.; Benameur, N.; Guizard, C.; Tardivat, C.; Vernoux, P.; Farrusseng, D. Energy & Environmental Science **2013**, 6, 2119.
(50) Guo, Y. M.; Largiller, G.; Guizard, C.; Tardivat, C.; Farrusseng, D. Journal of Materials Chemistry A **2015**, 3, 2684.
(51) Goodenough, J. B. Nature **2000**, 404, 821.
(52) Bruce, P. G. Solid state electrochemistry; Cambridge University Press: UK, **1995**.
(53) Badwal, S. P. S. Solid State Ionics **1992**, 52, 23.
(54) Huang, K.; Feng, M.; Goodenough, J. B. Journal of the American Ceramic Society **1998**, 81, 357.
(55) Sammes, N. M.; Tompsett, G. A.; Näfe, H.; Aldinger, F. Journal of the European Ceramic Society **1999**, 19, 1801.
(56) Huang, K.; Tichy, R. S.; Goodenough, J. B. Journal of American Ceramic Society **1998**, 81, 2565.
(57) Zhang, G. B.; Smyth, D. M. Solid State Ionics **1995**, 82, 161.
(58) Fuierer, P.; Maier, R.; Roeder-Roith, U.; Moos, R. Journal of Materials Science 2011, 46, 5447.
(59) Arikawa, H.; Nishiguchi, H.; Ishihara, T.; Takita, Y. Solid State Ionics **2000**, 136–137, 31.
(60) León-Reina, L.; Losilla, E. R.; Martínez-Lara, M.; Martín-Sedeño, M. C.; Bruque, S.; Núñez, P.; Sheptyakov, D. V.; Aranda, M. A. G. Chemistry of Materials **2005**, 17, 596.
(61) Kuang, X.; Green, M. A.; Niu, H.; Zajdel, P.; Dickinson, C.; Claridge, J. B.; Jantsky, L.; Rosseinsky, M. J. Nat Mater **2008**, 7, 498.
(62) Li, M.-R.; Kuang, X.; Chong, S. Y.; Xu, Z.; Thomas, C. I.; Niu, H.; Claridge, J. B.; Rosseinsky, M. J. Angewandte Chemie International Edition **2010**, 49, 2362.
(63) Orera, A.; Slater, P. R. Chemistry of Materials **2010**, 22, 675.
(64) Chroneos, A.; Yildiz, B.; Tarancon, A.; Parfitta, D.; Kilner, J. A. Energy Environmental Science **2011**, 4, 2774.
(65) Skinner, S. J.; Kilner, J. A. Materials Today **2003**, 6, 30.

(66) Materials for Energy Conversion Devices; Woodheard Publishing Limited: Cambridge, UK, Sorrell, C. C.
(67) Möbius, H.-H. J Solid State Electrochem **1997**, 1, 2.
(68) Goodenough, J. B.; Ruiz-Diaz, J. E.; Zhen, Y. S. Solid State Ionics **1990**, 44, 21.
(69) Fergus, J.; Hui, R.; Li, X.; Wilkinson, D. P.; Zhang, J. Solid Oxide Fuel Cells: Materials Properties and Performance, **2009**.
(70) Weppner, W. Solid State Ionics **1992**, 52, 15.
(71) Eguchi, K.; Setoguchi, T.; Inoue, T.; Arai, H. Solid State Ionics **1992**, 52, 165.
(72) Steele, B. C. H. Solid State Ionics **2000**, 129, 95.
(73) Yahiro, H.; Eguchi, K.; Arai, H. Solid State Ionics **1989**, 36, 71.
(74) Steele, B. C. H. Journal of Materials Science **2001**, 36, 1053.
(75) Verkerk, M. J.; Burggraaf, A. J. Journal of The Electrochemical Society **1981**, 128, 75.
(76) Kruidhof, H.; Bouwmeester, H. J. M.; de Vries, K. J.; Gellings, P. J.; Burggraaf, A. J. Solid State Ionics **1992**, 50, 181.
(77) Drache, M.; Conflant, P.; Obbade, S.; Wignacourt, J. P.; Watanabe, A. Journal of Solid State Chemistry **1996**, 129, 98.
(78) Takahashi, T.; Esaka, T.; Iwahara, H. J Appl Electrochem **1977**, 7, 299.
(79) Weng, C.-H.; Wei, W.-C. J. Journal of the American Ceramic Society **2010**, 93, 3124.
(80) Zhou, D.; Wang, H.; Yao, X.; Pang, L.-X.; Zhou, H.-F. Journal of the American Ceramic Society **2008**, 91, 139.
(81) Watanabe, A.; Sekita, M. Solid State Ionics **2005**, 176, 2429.
(82) Watanabe, A.; Ono, A. Solid State Ionics **2004**, 174, 15.
(83) Lee, K. T.; Yoon, H. S.; Wachsman, E. D. Materials Research Society **2012**, 27, 2063.
(84) Bhalla, A. S.; Guo, R.; Roy, R. Mat Res Innovat **2000**, 4, 3.
(85) Huang, P.; Horky, A.; Petric, A. Journal of the American Ceramic Society **1999**, 82, 2402.
(86) Goodenough, J. B.; Manthiram, A.; Kuo, J. F. Materials Chemistry and Physics **1993**, 35, 221.
(87) Goodenough, J. B.; Manthiram, A.; Paranthaman, P.; Zhen, Y. S. Solid State Ionics **1992**, 52, 105.
(88) Jankovic, J.; Wilkinsona, D. P.; Hu, R. Journal of Power Sources **2012**, 201, 49.
(89) Sun, Y.; Yang, C.; Shu, T.; Li, G.; Liao, F.; Lin, J. Inorganic Chemistry Communications **2013**, 33, 151.
(90) Jankovic, J.; Wilkinson, D. P.; Hui, R. Journal of The Electrochemical Society **2011**, 159, B109.
(91) Tarasova, N. A.; Animitsa, I. E. Russ J Electrochem **2013**, 49, 698.
(92) Yoshinaga, M.; Fumoto, T.; Hashimoto, T. Journal of The Electrochemical Society **2005**, 152, A1221.
(93) El-Masri, T.; Li, Q.; Thangadurai, V. Ionics **2010**, 16, 581.
(94) Jankovic, J.; Wilkinson, D. P.; Hui, R. Journal of The Electrochemical Society **2011**, 158, B61.
(95) Zhang, G. B.; Smyth, D. M. Solid State Ionics **1995**, 82, 153.
(96) Lee, C. K.; Sinclair, D. C.; West, A. R. Solid State Ionics **1993**, 62, 193.
(97) Abraham, F.; Debreuille-Gresse, M. F.; Mairesse, G.; Nowogrocki, G. Solid State Ionics **1988**, 28–30, Part 1, 529.
(98) Yasuda, N.; Miyayama, M.; Kudo, T. Materials Research Bulletin **2001**, 36, 323.
(99) Abraham, F.; Boivin, J. C.; Mairesse, G.; Nowogrocki, G. Solid State Ionics **1990**, 40–41, Part 2, 934.
(100) Yan, J.; Greenblatt, M. Solid State Ionics **1995**, 81, 225.

(101) Kendall, K. R.; Navas, C.; Thomas, J. K.; Loye, H.-C. Chem. Mater. **1996**, 8, 642.

(102) Fuierer, P.; Maier, M.; Exner, J.; Moos, R. Journal of the European Ceramic Society **2014**, 34, 943.

(103) Morozova, M. V.; Buyanova, E. S.; Petrova, S. A.; Khisametdinova, V. V.; Emel'yanova, Y. V.; Shatokhina, A. N.; Zhukovskii, V. M. Russ J Electrochem **2011**, 47, 448.

(104) Fuierer, P.; Maier, R.; Röder-Roith, U.; Moos, R. Journal of Materials Science **2011**, 46, 5447.

(105) Nadir, S.; Steinfink, H. Journal of Solid State Chemistry **1999**, 143, 9.

(106) K. Huang, R. S. T., J. B. Goodenough Journal of American Ceramic Society **1998**, 81, 2565.

(107) Sansom, J. E. H.; Richings, D.; Slater, P. R. Solid State Ionics **2001**, 139, 205.

(108) Leon-Reina, L.; Losilla, E. R.; Martinez-Lara, M.; Bruque, S.; Aranda, M. A. G. Journal of Materials Chemistry **2004**, 14, 1142.

(109) Takai, S.; Touda, S.; Oikawa, K.; Mori, K.; Torii, S.; Kamiyama, T.; Esaka, T. Solid State Ionics **2002**, 148, 123.

(110) Packer, R. J.; Skinner, S. J. Advanced Materials **2010**, 22, 1613.

(111) Haugsrud, R.; Norby, T. Nat Mater **2006**, 5, 193.

(112) Martín-Sedeño, M. C.; Losilla, E. R.; León-Reina, L.; Bruque, S.; Marrero-López, D.; Núñez, P.; Aranda, M. A. G. Chemistry of Materials **2004**, 16, 4960.

(113) Martin-Sedeno, M. C.; Marrero-Lopez, D.; Losilla, E. R.; Bruque, S.; Nunez, P.; Aranda, M. A. G. Journal of Solid State Chemistry **2006**, 179, 3445.

(114) Joubert, O.; Magrez, A.; Chesnaud, A.; Caldes, M. T.; Jayaraman, V.; Piffard, Y.; Brohan, L. Solid State Sciences **2002**, 4, 1413.

(115) Boysen, H.; Lerch, M.; Stys, A.; Senyshyn, A. Acta Crystallographica Section B **2007**, 63, 675.

(116) Van Brutzel, L.; Chartier, A.; Crocombette, J. P. Physical Review B **2008**, 78, 024111.

(117) Wang, J.; Ewing, R. C.; Becker, U. Scientific Reports **2014**, 4, 4216.

(118) Skinner, S. J. Solid State Sciences **2003**, 5, 419.

(119) Aguadero, A.; Alonso, J. A.; Martinez-Lope, M. J.; Fernandez-Diaz, M. T.; Escudero, M. J.; Daza, L. Journal of Materials Chemistry **2006**, 16, 3402.

(120) White, T. J.; ZhiLi, D. Acta Crystallographica Section B **2003**, B59, 1.

(121) Nakayama, S.; Sakamoto, M. Journal of the European Ceramic Society **1998**, 18, 1413.

(122) Nakayama, S.; Kageyama, T.; Hiromichi, A.; Yoshihiko, S. Journal of Materials Chemistry **1995**, 5, 1801.

(123) Kilo, M.; Taylor, M. A.; Argirusis, C.; Borchardt, G.; Lesage, B.; Weber, S.; Scherrer, S.; Scherrer, H.; Schroeder, M.; Martin, M. Journal of Applied Physics **2003**, 94, 7547.

(124) Abram, E. J.; Sinclair, D. C.; West, A. R. Journal of Materials Chemistry **2001**, 11, 1978.

(125) Huang, Z. X.; Li, B. Y.; Liu, J. Key Engineering Materials **2010**, 434-435.

(126) Shaula, A. L.; Kharton, V. V.; Marques, F. M. B. Journal of Solid State Chemistry **2005**, 178, 2050.

(127) Zhou, J.; Ye, X. F.; Li, J. L.; Wang, S. R.; Wen, T. L. Solid State Ionics **2011**, 201, 81.

(128) Jones, A.; Slater, P. R.; Islam, M. S. Chem. Mater. **2008**, 20, 5055.

(129) Tolchard, J. R.; Slater, P. R. Journal of Physics and Chemistry of Solids **2008**, 69, 2433.

(130) Kendrick, E.; Orera, A.; Slater, P. R. Journal of Materials Chemistry **2009**, 19, 7955.

(131) Panchmatia, P. M.; Orera, A.; Rees, G. J.; Smith, M. E.; Hanna, J. V.; Slater, P. R.; Islam, M. S. Angewandte Chemie International Edition **2011**, 50, 9328.

(132) León-Reina, L.; Martín-Sedeño, M. C.; Losilla, E. R.; Cabeza, A.; Martínez-Lara, M.; Bruque, S.; Marques, F. M. B.; Sheptyakov, D. V.; Aranda, M. A. G. Chemistry of Materials **2003**, 15, 2099.

(133) Jo, S. H.; Muralidharan, P.; Kim, D. K. Electrochimica, Acta. **2009**, 54, 7495.

(134) Kharton, V. V.; Marques, F. M. B.; Atkinson, A. Solid-State Ionics **2004**, 174, 135.

(135) Gorshkov, M. Y.; Neuimin, A. D.; Bogdanovich, N. M.; Danilov, Y. V.; Dunyushkina, L. A. Russ J Electrochem **2007**, 43, 721.

(136) Mauvy, F.; Lalanne, C.; Bassat, J. M.; Grenier, J. C.; Brisse, A.; Sauvet, A. L.; Barthet, C.; Fouletier, J. Solid State Ionics **2009**, 180, 1183.

(137) Nakao, T.; Mineshige, A.; Kobune, M.; Yazawa, T.; Yoshioka, H. Solid State Ionics **2008**, 179, 1567.

(138) Tealdi, C.; Mustarelli, P.; Islam, M. S. Advanced Functional Materials **2010**, 20, 3874.

(139) Mancini, A.; Tealdi, C.; Malavasi, L. International Journal of Hydrogen Energy **2012**, 37, 8073.

(140) Wei, F.; Gasparyan, H.; Keenan, P. J.; Gutmann, M.; Fang, Y.; Baikie, T.; Claridge, J. B.; Slater, P. R.; Kloc, C. L.; White, T. J. Journal of Materials Chemistry A **2015**, 3, 3091.

(141) Tealdi, C.; Mustarelli, P.; Islam, M. S. Advanced Functional Materials **2010**, 20, 3874.

(142) Liu, B.; Ding, D.; Liu, Z.; Chen, F.; Xia, C. Solid State Ionics 2011, 191, 68.

(143) Wei, F.; Baikie, T.; An, T.; Schreyer, M.; Kloc, C.; White, T. J. Journal of the American Chemical Society **2011**, 133, 15200.

(144) Xu, J.; Kuang, X.; Véron, E.; Allix, M.; Suchomel, M. R.; Porcher, F.; Liang, C.; Pan, F.; Wu, M. Inorganic Chemistry **2014**, 53, 11589.

(145) Tealdi, C.; Chiodelli, G.; Pin, S.; Malavasi, L.; Flor, G. Journal of Materials Chemistry A **2014**, 2, 907.

(146) Mancini, A.; Felice, V.; Natali Sora, I.; Malavasi, L.; Tealdi, C. Journal of Solid State Chemistry **2014**, 213, 287.

(147) Stade, J.; Bohaty, L.; Hengst, M.; Heimann, R. B. Cryst. Res. Technol. **2002**, 37, 1113.

(148) Fritze, H.; Tuller, H. L. Appl. Phys. Lett. **2001**, 78, 976.

(149) Krizan, J. W.; de la Cruz, C.; Andersen, N. H.; Cava, R. J. Journal of Solid State Chemistry **2013**, 203, 310.

(150) Lee, C.; Kan, E.; Xiang, H.; Whangbo, M.-H. Chemistry of Materials **2010**, 22, 5290.

(151) Bjørheim, T. S.; Haugsrud, R.; Norby, T. Solid State Ionics **2014**, 264, 76.

(152) Maksimov, B. A.; Kazantsev, S. S.; Molchanov, V. N.; Verin, I. A.; Mill, B. V. Crystallography Reports **2004**, 49, 585.

(153) Mill, B. V.; Maksimov, B. A.; Pisarevskiœ, Y. V.; Danilova, N. P. A.; Werner, P. S.; Schneider, J. Crystallography Reports **2004**, 49, 65.

(154) Eysel, W.; Lambert, U.; Mayer, B. E.; Renkenberger, C. Zeitschrift fur Kristallographie **1992**, 201, 235.

(155) Carter, C. B.; Norton, M. G. In Ceramic Materials; Springer New York: **2007**, p 139.

(156) Carter, C. B.; Norton, M. G. In Ceramic Materials; Springer New York: **2007**, p 444.

(157) Baláž, P. In Mechanochemistry in Nanoscience and Minerals Engineering; Springer Berlin Heidelberg: **2008**, p 103.

(158) Pechini, M. P.; Patent, U., Ed. US, **1967**; Vol. 3,330,697.

(159) Zha, J.; Roggendorf, H. Advanced Materials **1991**, 3, 522.

(160) Sakka, S. Handbook of sol-gel science and technology. 1. Sol-gel processing; Kluwer Academic Publishers Group, **2005**; Vol. Springer US.

(161) Ring, T. A. Fundamentals of ceramic powder processing and synthesis California, USA, **1995**.

(162) Carter, C. B.; Norton, M. G. In Ceramic Materials; Springer New York: **2007**, p 427.

(163) Carter, C. B.; Norton, M. G. In Ceramic Materials; Springer New York: **2007**, p 412.

(164) Ring, T. A. Fundamental of Ceramic Powder Processing and Synthesis; Academic Press: London, **1995**.

(165) Masia, S.; Calvert, P.; Rhine, W.; Bowen, H. K. Journal of Materials Science **1989**, 24, 1907.

(166) Tanaka, S.; Pin, C. C.; Uematsu, K. Journal of the American Ceramic Society **2006**, 89, 1903.

(167) Chabert, F.; Dunstan, D. E.; Franks, G. V. Journal of the American Ceramic Society **2008**, 91, 3138.

(168) Hoffmann, M. J.; Funfschilling, S.; Kahraman, D. In Ceramics Science and Technology; Wiley-VCH, Ed. **2012**; Vol. 3, p 171.

(169) Nygren, M. S., Z. In Ceramics Science and Techonology; Wiley-VCH: **2012**, p 189.

(170) Li, W. B.; Easterling, K. E.; Ashby, M. F. Metallurgical Transactions A **1991**, 22, 1071.

(171) Li, B.; Wang, X.; Han, X.; Qi, X.; Li, L. Journal of Materials Science **2004**, 39, 2621.

(172) Hong, J.; Gao, L.; Torre, S. D. D. L.; Miyamoto, H.; Miyamoto, K. Materials Letters **2000**, 43, 27.

(173) Kumar, R.; Prakash, K. H.; Cheang, P.; Khor, K. A. Acta Materialia **2005**, 53, 2327.

(174) Tan, Y.; Zhang, J.; Wu, Y.; Wang, C.; Koval, V.; Shi, B.; Ye, H.; McKinnon, R.; Viola, G.; Yan, H. Sci. Rep. **2015**, 5.

(175) Liu, J.; Shen, Z.; Nygren, M.; Su, B.; Button, T. W. Journal of the American Ceramic Society **2006**, 89, 2689.

(176) Hungria, T.; Galy, J.; Castro, A. Advanced Engineering Materials **2009**, 11, 615.

(177) Kali, R.; Mukhopadhyay, A. Journal of Power Sources **2014**, 247, 920.

(178) Delaizir, G.; Manafi, N.; Jouan, G.; Rozier, P.; Dollé, M. Solid State Ionics **2012**, 207, 57.

(179) Aboulaich, A.; Bouchet, R.; Delaizir, G.; Seznec, V.; Tortet, L.; Morcrette, M.; Rozier, P.; Tarascon, J.-M.; Viallet, V.; Dollé, M. Advanced Energy Materials **2011**, 1, 179.

(180) Suárez, M.; Fernández, A.; Menéndez, J. L.; Torrecillas, R.; Kessel, H. U.; Hennicke, J.; Kirchner, R.; Kessel, T. Challenges and Opportunities for Spark Plasma Sintering: A Key Technology for a New Generation of Materials, **2013**.

(181) Hulbert, D. M. 2008, *Lawrence Berkeley National Laboratory*. Retrieved from: http://escholarship.org/uc/item/2c14z63t

(182) Shen, Z.; Nygren, M. The Chemical Record **2005**, 5, 173.

(183) Carney, C. M.; Mah, T.-I. Journal of the American Ceramic Society **2008**, 91, 3448.

(184) Grasso, S.; Sakka, Y.; Maizza, G.; Hu, C. Journal of the American Ceramic Society **2009**, 92, 2418.

(185) Anselmi-Tamburini U., G. J. E., Munir Z. A. Scripta Materialia **2006**, 54, 828.

(186) David, W. I. F.; Shankland, K.; McCusker, L. B.; Bärlocher, C. Structure Determination from Powder Diffraction Data; University Press: UK, **2010**.

(187) Dinnebier, R. E.; Billinge, S. J. L. Powder Diffraction Theory and Practice; RSCPublishing: Cambridge CB4 0WF, UK, **2008**.

(188) Pecharsky, V. K.; Zavalij, P. Y. Fundamentals of Powder Diffraction and Structural Characterization of Materials; Springer: USA, **2009**.
(189) Source, D. L. 2015; Vol. **2015**.
(190) Tartoni, N.; Thompson, S. P.; Tang, C. C.; Willis, B. L.; Derbyshire, G. E.; Wright, A. G.; Jaye, S. C.; Homer, J. M.; Pizzeyc, J. D.; Bell, A. M. T. Journal of Synchrotron Radiation **2007**, 15, 43.
(191) Attwood, D. Soft X-rays and Extreme Ultraviolet Radiation; Cambridge University Press: UK, **2000**.
(192) Thompson, S. P.; Parker, J. E.; Potter, J.; Hill, T. P.; Birt, A.; Cobb, T. M.; Yuan, F.; Tang, C. C. Review of Scientific Instruments **2009**, 80, 075107.
(193) Toby, B. H.; Von Dreele, R. B. Journal of Applied Crystallography **2013**, 46, 544.
(194) Sears, V.F. Neutron News **1992**, 3, 29.
(195) Ibberson, R. M.; Bill, D.; Knight, K. Rutherford Appleton Laboratory, Oxfordshire, UK.
(196) Hannon, A. C. Nuclear Instruments and Methods in Physics Research Section A: Accelerators, Spectrometers, Detectors and Associated Equipment **2005**, 551, 88.
(197) Williams, W. G.; Ibberson, R. M.; Day, P.; Enderby, J. E. Physica B: Condensed Matter **1997**, 241–243, 234.
(198) Kabekkodu, S. Powder Diffraction File Inorganic and Organic Data International Centre for Diffraction Data: USA, **2010**.
(199) Degen, T.; Sadki, M.; Bron, E.; König, U.; Nénert, G. Powder Diffraction **2014**, 29, S13.
(200) Coelho, A. In General profile and structure analysis software for powder diffraction data; Coelho Software: Brisbane, Australia, **2012**.
(201) Coelho, A. Journal of Applied Crystallography **2003**, 36, 86.
(202) de Wolff, P. M. Journal of Applied Crystallography **1972**, 5, 243.
(203) Pawley, G. S. Journal of Applied Crystallography **1981**, 14, 357.
(204) Rietveld, H. M. Journal of Applied Crystallography **1969**, 2, 65.
(205) Young, R. A.; Wiles, D. B. Journal of Applied Crystallography **1982**, 15, 430.
(206) Coelho, A. Technical reference Topas Academic. V5. **2013**.
(207) Von Dreele, R. B.; Jorgensen, J. D.; Windsor, C. G. Journal of Applied Crystallography **1982**, 15, 581.
(208) Stephens, P. W. Journal of Applied Crystallography **1999**, 32, 281.
(209) McCusker, L. B.; Von Dreele, R. B.; Cox, D. E.; LoueÈrd, D.; Scardie, P. Journal of Applied Crystallography **1999**, 32, 36.
(210) Toby, B. H. Powder Diffraction **2006**, 21, 67.
(211) Watkin, D. Acta Crystallographica Section A **1994**, 50, 411.
(212) Brown, I. D. The Chemical Bond in Inorganic Chemistry: The Bond Valence Model; Oxford University Press: UK, **2006**.
(213) Collins, D. M. Nature **1982**, 298, 49.
(214) Main, P. In Crystal Structure Analysis: Principles and Practice; Oxford University Press: **2009**.
(215) Samy, A.; Dinnebier, R. E.; Smaalen, S.; Jansena, M. Acta Crystallographica Section B **2010**, B66, 184.
(216) Oldag, T.; Aussieker, T.; Keller, H.-L.; Preitschaft, C.; Pfitzner, A. Powder Diffraction **2013**, 631, 184.
(217) Bindzus, N.; Iversen, B. B. Acta Crystallogr A **2012**, 68, 752.
(218) Dinnebier, R.; Schneider, M.; Smaalen, S.; Olbrich, F.; Behrensc, U. **1999**, 55, 35.
(219) Ali, R.; Yashima, M.; Matsushita, Y.; Yoshioka, H.; Izumi, F. Journal of Solid State Chemistry **2009**, 182, 2846.

(220) Ali, R.; Yashima, M.; Matsushita, Y.; Yoshioka, H.; Ohoyama, K.; Izumi, F. Chemistry of Materials **2008**, 20, 5203.
(221) Petricek, V.; Dusek, M.; Palatinus, L. Z.Kristallographic **2014**, 229, 345.
(222) Egerto, R. F. Physical Principles of Electron Microscopy **2005**.
(223) www.jeol.co.jp.
(224) Knoll, M.; Ruska, E. Zeitschrift für Physik **1932**, 78, 318.
(225) Egerton, R. F. Physical Principles of Electron Microscopy USA, **2005**.
(226) Walter, G. W. Corrosion Science **1986**, 26, 681.
(227) Olivier, M.-G.; Poelman, M. Use of Electrochemical Impedance Spectroscopy (EIS) for the Evaluation of Electrocoatings Performances, Recent Researches in Corrosion Evaluation and Protection, **2012**.
(228) Tena-Zaera, R.; Elias, J.; Lévy-Clément, C.; Mora-Seró, I.; Luo, Y.; Bisquert, J. physica status solidi (a) **2008**, 205, 2345.
(229) Barsoukov, E.; Macdonald, J. R. Impedance Spectroscopy Theory, Experiment, and Applications, **2005**.
(230) Sinclair, D. C.; West, A. R. Journal of Applied Physics **1989**, 66, 3850.
(231) John T. S. Irvine, D. C. S., Anthony R. West Advanced Materials **1990**, 2, 132
(232) Liu, M.; Khandkar, A. Solid State Ionics **1992**, 52, 3.
(233) Dellis, J. L.; Carpentier, J. L. Solid State Ionics **1993**, 62, 119.
(234) MacDonald, J. R. Electrochimica, Acta. **1997**, 35, 1486.
(235) Heidinger, R. N., S. Powder Metallurgy International **1988**, 20, 30.
(236) Anna-Karin, A.; Pan, Y.; Valant, M.; Alford, N. Journal of American Ceramic Society **2009**, 92, 1773.
(237) Penn, S. J.; Alford, N. M.; Templeton, A.; Wang, X.; Xu, M.; Reece, M.; Schrapel, K. Journal of American Ceramic Society **1997**, 80, 1885.
(238) Maier, J. Angewandte Chemie International Edition in English **1993**, 32, 313.
(239) Shannon, R. D. Acta Crystallographica **1976**, A32, 751.
(240) Santibanez-Mendieta, A. B., Licoccia, E. F.; Traversaa, E. Journal of The Electrochemical Society **2011**, 158, B1.
(241) Takeda, H.; Soichiro, R. A.; Shiosaki, T. Ferroelectric **2002**, 295, 67.
(242) Takeda, H.; Kato, T.; Chani, V. I.; Shimamura, K.; Fukuda, T. Journal of Alloys and Compounds **1999**, 290, 244.
(243) Robinson, K.; Gibbs, G. V.; Ribbe, P. H. Science **1971**, 172, 567.
(244) Kresse, G.; Furthmüller, J. Phys. Rev. B **1996**, 54, 11169.
(245) Stewart, J. C.; Segall, M. D.; Pickard, C. J.; Hasnip, P. J.; Probert, M. J.; Refson, K.; Payne, M. C. Zeitschrift für Kristallographie **2005**, 220, 567.
(246) Perdew, J. P.; Burke, K.; Ernzerhof, M. Phys. Rev. Lett. **1996**, 77, 3865.
(247) Kresse, G.; Joubert, D. Physical Review B **1999**, 59, 1758.
(248) Pickard, C. J.; Mauri, F. 63 **2001**, 245101.
(249) Yates, J. R.; Pickard, C. J.; Mauri, F. Physical Review B **2007**, 76, 024401.
(250) Ferrage, F.; Zoonens, M.; Warschawski, D. E.; Popot, J.-L.; Bodenhausen, G. Journal of the American Chemical Society **2003**, 125, 2541.
(251) Ashbrook, S. E.; Smith, M. E. Chemical Society Reviews **2006**, 35, 718.
(252) Medek, A.; Harwood, J. S.; Frydman, L. Journal of the American Chemical Society 1995, 117, 12779.
(253) Frydman, L.; Harwood, J. S. Journal of the American Chemical Society **1995**, 117, 5367.
(254) Amoureux, J.-P.; Fernandez, C.; Steuernagel, S. Journal of Magnetic Resonance, Series A **1996**, 123, 116.
(255) Ashbrook, S. E. Physical Chemistry Chemical Physics **2009**, 11, 6892.
(256) Millot, Y.; Man, P. P. Solid state nuclear magnetic resonance **2002**, 21, 21.
(257) Iuga, D.; Schäfer, H.; Verhagen, R.; Kentgens, A. P. M. Journal of Magnetic Resonance **2000**, 147, 192.

(258) Adiwidjaja, G. B., M.; Claus, C.; Friese, K.; Klaska, K. H.; Jarchow, O.; Ruks, M.; Wozniak, I. Zeitschrift fuer Kristallographie **1998**, 213, 223.

(259) Smith, R. Refinement of time-of-flight Profile Parameters in GSAS, Crystallography Group, Isis Facility, Rutherford Appleton Laboratory.

(260) Sears, V. F. Neutron News **1992**, 3, 29.

(261) Blanc, F.; Middlemiss, D. S.; Gan, Z.; Grey, C. P. Journal of the American Chemical Society **2011**, 133, 17662.

(262) Kiyono, H.; Matsuda, Y.; Shimada, T.; Ando, M.; Oikawa, I.; Maekawa, H.; Nakayama, S.; Ohki, S.; Tansho, M.; Shimizu, T.; Florian, P.; Massiot, D. Solid State Ionics **2012**, 228, 64.

(263) Ashbrook, S. E.; Dawson, D. M. Accounts of Chemical Research **2013**, 46, 1964.

(264) Middlemiss, D. S.; Blanc, F.; Pickard, C. J.; Grey, C. P. Journal of Magnetic Resonance **2010**, 204, 1.

(265) Michaelis, V. K.; Kroeker, S. The Journal of Physical Chemistry C **2010**, 114, 21736.

(266) Bonhomme, C.; Gervais, C.; Babonneau, F.; Coelho, C.; Pourpoint, F.; Azaïs, T.; Ashbrook, S. E.; Griffin, J. M.; Yates, J. R.; Mauri, F.; Pickard, C. J. Chemical Reviews **2012**, 112, 5733.

(267) Massiot, D.; Bessada, C.; Coutures, J. P.; Taulelle, F. Journal of Magnetic Resonance **1990**, 90, 231.

(268) Begg, B. D.; Vance, E. R.; Hunter, B. A.; Hanna, J. V. Journal of Materials Research **1998**, 13, 3181.

(269) Massiot, D.; Vosegaard, T.; Magneron, N.; Trumeau, D.; Montouillout, V.; Berthet, P.; Loiseau, T.; Bujoli, B. Solid state nuclear magnetic resonance **1999**, 15, 159.

(270) Michaelis, V. K.; Aguiar, P. M.; Terskikh, V. V.; Kroeker, S. Chemical Communications **2009**, 4660.

(271) Sinclair, D.; Li, M. Journal of Applied Physics **2013**, 114.

(272) Hodge, I. M.; Ingram, M. D.; West, A. R. Journal of Electroanalythical Chemistry **1976**, 74, 125.

(273) Shannon, R. D. Journal of Applied Physics **1992**, 73, 348.

(274) Park, S.; Keszler, D. A. Solid State Sciences **2002**, 4, 799.

(275) Takeda, H.; Kuze, T.; Nishida, T.; Uchiyama, K.; Shiosaki, T. Materials Research Bulletin **2008**, 43, 1731.

(276) Takeda, H.; Yamaura, J.; Hoshina, T.; T., T. In IOP Conference Series: Materials Science and Engineering; IOP Publishing Ltd: **2011**; Vol. 18, p 1.

(277) Nanko, M.; Sato, M.; Matsumaru, K.; Ishizaki, K. In Novel Materials Processing (MAPEES'04): Proceedings of the International Symposium on Novel Materials Processing by Advanced Electromagnetic Energy Sources; Technology, E. S., Ed. **2005**.

(278) Munir, Z. A.; Anselmi-Tamburini, U.; Ohyanagi, M. Journal of Materials Science **2006**, 41, 763.

(279) Wong-Ng, W.; Xie, W.; Yan, Y.; Liu, G.; Kaduk, J.; Thomas, E.; Tritt, T. Journal of Applied Physics **2011**, 110, 113706.

(280) Malinovskii, Y. A. Doklady Akademii Nauk SSSR **1984**, 279, 616.

(281) Moore, P. B. Science **1967**, 156, 1361.

(282) Mumme, W. G.; Wadsley, A. D. Acta Crystallographica Section B **1968**, 24, 1327.

(283) Wallwork, K. S.; James, M. The Canadian Mineralogist **2006**, 44, 433.

(284) Wu, K. K.; Brown, I. D. Acta Crystallographica B **1973**, 24, 1969.

(285) Izquierdo, G.; West, A. R. Materials Research Bulletin **1980**, 15, 1655.

(286) Withers, R. L.; Hoche, T.; Liu, Y.; Esmaeilzadeh, S.; Keding, R.; Salese, B. journal of Solid State Chemistry **2004**, 177, 3316.

(287) Liu, G.; Greedan, J. E. Journal of Solid State Chemistry **1995**, 114, 499.

(288) Armbruster, T.; Roethlisberger, F.; Seifert, F. American Mineralogist **1990**, 75, 847.

(289) Zid, M. F.; Jouini, T. Acta Crystallographica Section C **1996**, 52, 1334.

(290) Kahlenberg, V.; Goettgens, V.; Mair, P.; Schmidmair, D. Journal of Solid State Chemistry **2015**, 228, 27.

(291) Hesse, K.; Liebau, F. In Zeitschrift für Kristallographie **1980**; Vol. 153, p 3.

(292) Wang, P. Wuli Xuebao **2014**, 63, 7.

(293) Gong, Y.; Wang, Y.; Li, Y.; Xu, X.; Zeng, W. Opt. Express **2011**, 19, 4310.

(294) Ishigaki, T.; Sato, K.; Kamei, S.; Uematsu, K.; Toda, K.; Sato, M. MRS Proceedings **2012**, 1471.

(295) Zhang, X.; Xu, X.; He, Q.; Qiu, J.; Yu, X. ECS Journal of Solid State Science and Technology **2013**, 2, R225.

(296) Foit, F. F.; Phillips, M. W.; Gibbs, G. V. American Mineralogist **1973**, 58, 909.

(297) Bakakin, V. V.; Belov, N. V.; Borisov, S. V.; Solovyeva, L. P. The American Mineralogist **1970**, 55, 1167.

(298) Pekov, I. V.; Chukanov, N. V.; Kononkova, N. N.; Belakovskii, D. I.; Pushcharovskii, D. Y.; Vinogradova, S. A. Zapiski Vserossiiskogo Mineralogicheskogo Obshchestva **1998**, 127, 32.

(299) Fleet, M. E.; Henderson, G. S. Journal of Solid State Chemistry **1995**, 119, 400.

(300) Seo, S.-W.; Jung, S.-J.; Park, M.-W.; Yu, S.-M.; Lee, K.-T.; Lee, J.-S. Electron. Mater. Lett. **2014**, 10, 213.

(301) Lee, J.-S. J. Electroceram **2006**, 17, 709.

(302) Lee, J.-S.; Choi, K.-H.; Park, M.-W.; Choi, Y.-G.; Mun, J.-H. Journal of Alloys and Compounds **2009**, 474, 219.

(303) Mil, B. V. LANGASITE-TYPE MATERIALS: FROM DISCOVERY TO PRESENT STATE, **2000**.

(304) Belokoneva, E. L.; Simonov, M. A.; Batushin, A. V.; Mill, B. V.; Belov, N. V. Doklady Akademii Nauk SSSR **1980**, 255, 1099.

(305) Takeda, H.; Uecker, R.; Kumatoriya, M.; Shimamura, K.; Reiche, P.; Fukuda, T. Crystal Research and Technology **1997**, 32, 939.

(306) Takeda, H.; Sato, J.; Morikoshi, H.; Kato, T.; Shimamura, K.; Fukuda, T. Materials Letters **1999**, 41, 104.

(307) Belokoneva, E. L.; Stefanovich, S. Y.; Pisarevskii, Y. V.; Mosunov, A. V. Zhurnal Neorganicheskoi Khimii **2000**, 45, 1786.

(308) Takeda, H.; Nishida, T.; Okamura, S.; Shiosaki, T. Transaction of the Material Research Society of Japan **2003**, 28, 1891.

(309) Klimenkova, A. A.; Maximov, B. A.; Molchanov, V. N.; Mill, B. V.; Rabadanov, M. H.; Pisarevsky, Y. V.; Pushcharovsky, D. Y. Kristallografiya **2007**, 52, 238.

(310) Chitra, R.; Choudhury, R. R. Acta Crystallographica Section B **2010**, B66, 497.

(311) Bordet, P.; Gelard, I.; Marty, K.; Ibanez, A.; Robert, J.; Simonet, V.; Canals, B.; Ballou, R.; Lejay, P. Journal of Physics: Condensed Matter **2006**, 18.